FACULTY OF SCIENCE
UNIVERSITY OF COPENHAGEN

Subgap states in proximitized full-shell nanowires

Ida Egholm Nielsen

Center for Quantum Devices
Niels Bohr Institute
University of Copenhagen

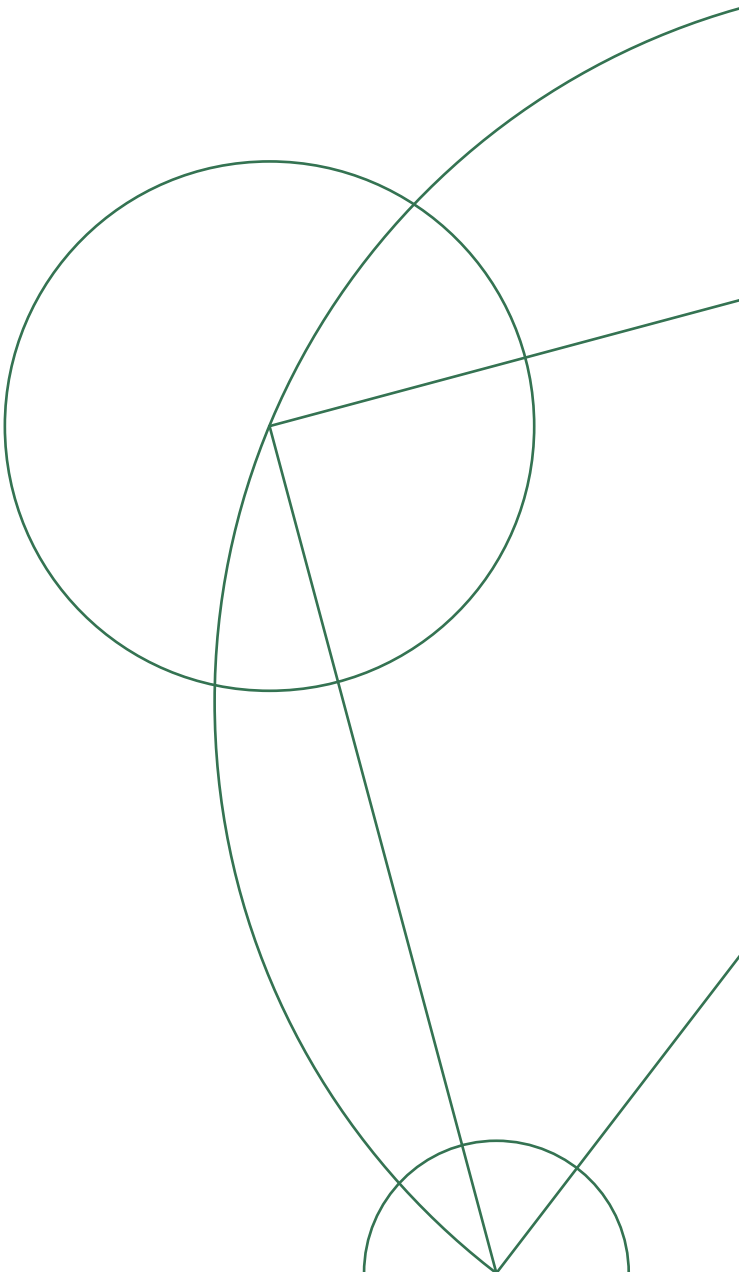

Master's thesis in Physics

Supervisors: Karsten Flensberg and Jens Paaske
Dated: September 3, 2019

Abstract

The endeavour for low-decoherence quantum computing has over the past decades lead to an intense search for Majorana zero-energy modes as they provide a platform for topologically protected quantum information processing. Hybrid semiconductor-superconductor nanowires have been proposed as a possible realisation of these modes and have shown signatures consistent with the theory of Majorana modes. Tunnelling spectroscopy of the recently designed full-shell wires has revealed a zero-energy state in certain intervals of an applied axial magnetic field.

In this thesis we expand a simple model for full-shell wires by introducing different perturbations. These include impurities treated within the first-order Born approximation, as well as deformations that break the angular symmetry. Different concepts that are relevant for the understanding of full-shell wires will be introduced, and through appropriate approximations we will make predictions to be held up against the experimental observations. A central prediction is our calculation of the differential conductance by use of the scattering matrix formalism. We will also question the stability of a possible non-trivial topological phase and search for trivial zero-energy states that present an alternative interpretation of the experimental results.

Acknowledgements

I would like to express my gratitude to Jens Paaske and Karsten Flensberg for their valuable supervision on this project as well as for my education in condensed matter physics and related subjects. I am fascinated by your deep understanding and knowledge of physics, and our discussions have been very inspiring. Many of the results in this thesis would neither exist if it was not for the computer wizard Jannis N. Bouchikas and his patience in learning me the basics of operating on a remote server. For their thorough proof reading and helpful suggestions, I would like to thank Signe F. Simonsen, Hano M. Sura, Clara N. Breiø, and Morten K. Munk.

Contents

1 Introduction

Hybrid semiconductor-superconductor devices have received a vast amount of attention following the theoretical proposals by Oreg et al. [1] and Lutchyn et al. [2] of a configuration that could realise Majorana zero-energy modes as quasiparticle excitations in the semiconductor [3–7]. The suggested setup includes a semiconducting wire with strong spin-orbit interaction, coupled to an s-wave superconductor and placed in an external magnetic field. The search for these modes is partly motivated by their non-Abelian braiding statistics which makes them a basis for topologically protected quantum computation [8, 9].

One of the compositions used so far is a semiconductor nanowire placed on top of an s-wave superconductor [4], or a hexagonal wire with one or two facets covered by an epitaxial superconducting shell [5, 6]. This study in nanowires is focusing on the recently introduced full-shell nanowire in which the semiconducting core is covered by an s-wave superconductor on all six facets. We were inspired to consider this new configuration following the experiments performed by Vaitiekėnas et al. and presented in the article *Flux-induced Majorana modes in full-shell nanowires* [10]. As seen from Fig. 1.1, differential conductance measurements on this type of wire have shown signatures of a zero-energy state when a magnetic field parallel to the wire results in a flux around one superconducting flux quantum $\Phi_0 = h/2e$. The question is now how stable the observed zero-energy state is, and whether it really is a Majorana zero-energy mode, or if there is some other explanation to the peak at zero bias voltage. To describe the system, Lutchyn et al. [11] presented a model Hamiltonian in their article *Topological superconductivity in full-shell proximitized nanowires* that will also be the basis Hamiltonian in this thesis. The model predicts that for an odd winding number of the phase of the superconducting order parameter, topologically non-trivial phases of the nanowire are possible, allowing Majorana zero-energy modes, in agreement with the measurements in [10].

At this point, full-shell wires are not completely understood. The contribution of this thesis is a thorough analysis and expansion of the hollow-cylinder model from [11] to better describe the new type of nanowires. We will start with an explanation of the parabolic variations that have been observed in the superconducting transition temperature and spectral gap when varying the magnetic flux through the wire [10]. We then present the model Hamiltonian for a full-shell nanowire and develop a method for distinguishing trivial and non-trivial topological phases of the system. In [11], they find that a breaking of the angular symmetry of the wire can enlarge the parameter space for the non-trivial phase. This has inspired us to investigate deformations of the wire that are periodic in the angular coordinate. We examine if the effect of those is also an extension of the non-trivial phase to a larger parameter range. Furthermore, the stability of the non-trivial phase to variations in the system parameters will be questioned. Since a zero-bias peak in the differential conductance is not necessarily an indication of a Majorana zero-energy mode we will also test if the model predicts a trivial zero-energy state that may present an alternative explanation. After this we will try to learn about the perturbing effects of impurities in the semiconductor. In [11] disorder in the superconducting shell was seen to influence the topological phase. Finally, we will consider finite-size effects and through the scattering matrix formalism calculate the differential conductance in a setup similar to the one used in [10] and compare with the experimental results.

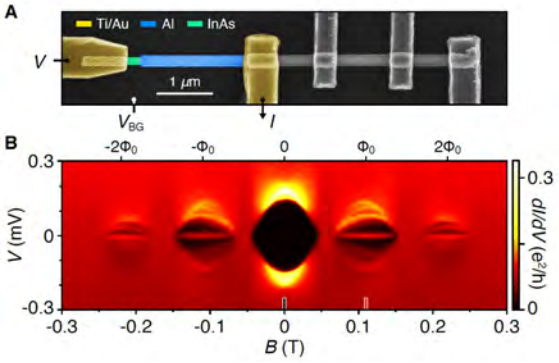

Figure 1.1: Part of Fig. 1 in Vaitiekėnas et al. [10] showing **A** the device for measuring the tunnelling spectrum of the full-shell Al-InAs nanowire and **B** the resulting differential conductance as function of axial magnetic field, B, and source-drain bias voltage, V. The zero-bias signal suggesting existence of a MZM is seen in the lobe around ± 0.1 T.

For this construction of a full-shell nanowire model, some of our statements are accompanied by several figures. The full documentation of our findings is placed in the appendices and only the salient plots are included in the main text.

Before starting our study of full-shell nanowires, we will briefly present the main features of Majorana zero-energy modes in nanowires and the reason for the large interest in detecting them.

1.1 Majorana zero-energy modes

Majorana zero-energy modes (MZMs) are quasiparticle excitations which are expected to exist at zero energy in topological superconductors. They are wanted for their intrinsically non-local nature and their non-Abelian exchange statistics, which makes them appropriate for low-decoherence topological quantum computation [7, 9]. A MZM is described by the annihilation operator $\gamma = uc_\sigma^\dagger + u^* c_\sigma$ where c_σ annihilates an electron with spin σ and u is a coefficient. We observe that the operator is Hermitian, meaning that a MZM is in a sense its own antiparticle. Two MZMs represent together one fermionic (quasiparticle) excitation. This can be seen by dividing the electron creation and annihilation operators into their real and imaginary parts: $c_\sigma = (\gamma_{\sigma,a} + i\gamma_{\sigma,b})/2$. Each part is then proportional to a MZM operator and the electron is thereby expressed as a superposition of two MZMs [9]. From Kitaev's tight-binding model for a one-dimensional p-wave superconductor we expect to find MZMs at each end of the nanowire [8].[1] If the wire is long enough that the wave functions of the two modes do not overlap, they together constitute a highly delocalised fermionic state and are therefore immune to local sources of decoherence [1]. The state of MZMs can be manipulated by exchanging the different quasiparticles, and with four modes or more the effects of braiding operations become non-trivial and can be used to encode information. Exchanging the MZMs is a global operation which can be done over macroscopic distances, ensuring protection from local perturbations. This is known as low-decoherence topological quantum computing [2, 9].

[1] In general the MZMs exist on transition points between trivial and non-trivial topological regions, a concept which we will consider in more detail later [12].

2 Little-Parks effect

In their 1962 article, *Observation of quantum periodicity in the transition temperature of a superconducting cylinder* [13], Little and Parks demonstrated phase winding of the superconducting order parameter in a hollow tin cylinder. This section will review the theory of what is now called the Little-Parks effect, based on chapter 17 in Abrikosov [14], together with the results of the original experiment as well as more recent research. We will then use this to interpret the parabolic variations in transition temperature and spectral gap with magnetic flux, observed in the experiments on full-shell nanowires [10].

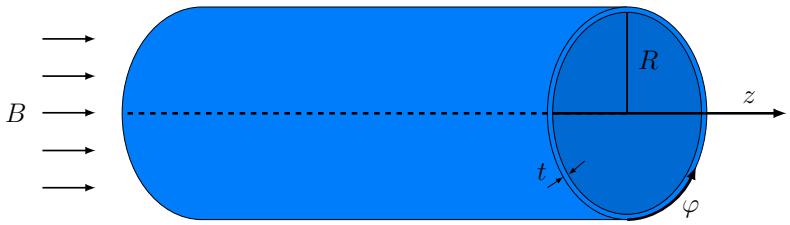

Figure 2.1: Thin, doubly connected superconducting cylinder and its orientation with respect to the magnetic field in the Little-Parks experiment.

The system considered is a thin superconducting cylinder of thickness t much smaller than the London penetration depth $t \ll \lambda_\mathrm{L}$ and a radius $R \gg \lambda_\mathrm{L}$ (see Fig. 2.1). A magnetic field B is applied along the cylinder axis and provokes a screening current in the superconductor. However, due to the system dimensions ($t \ll \lambda_\mathrm{L}$) the current cannot exclude the magnetic field from the superconductor and the field is assumed constant across the cylinder wall. This means that there will be no requirement on quantisation of the magnetic flux[2] through the cavity, $\Phi = \pi R^2 B$. We use cylindrical coordinates $\boldsymbol{r} = (z, r, \varphi)$ and choose the vector potential to be $\boldsymbol{A} = A\hat{\boldsymbol{\varphi}}$ and the order parameter of the superconductor to have a constant norm $\Delta(\boldsymbol{r}) = |\Delta| e^{-i\chi(\boldsymbol{r})}$. It is required that $\chi(\boldsymbol{r} + 2\pi\hat{\boldsymbol{\varphi}}) = \chi(\boldsymbol{r}) + 2\pi n$, where $n \in \mathbb{Z}$, to ensure that the Cooper pair wave function (and hence the order parameter [16]) is single valued. In a magnetic field the difference in free energy between the superconducting phase and the normal phase is then

$$\int dV\ (\Omega_\mathrm{s} - \Omega_\mathrm{n}) = \int dV \left(a\tau|\Delta|^2 + \frac{b}{2}|\Delta|^4 + \frac{1}{4m}\left(\nabla\chi - 2e\boldsymbol{A}\right)^2 |\Delta|^2 \right). \tag{2.1}$$

Here we have used the Ginzburg-Landau theory for the free energy density of the superconductor, Ω_s, valid near the transition between the metallic and superconducting phases for smooth variation of $\Delta(\boldsymbol{r})$ in space. Ω_n is the free energy density of the normal phase, $a, b > 0$ are constants, m is the electron mass, e is the electron charge. Finally, $\tau = \frac{T - T_\mathrm{c}^0}{T_\mathrm{c}^0}$ is the deviation in temperature T from the critical value T_c^0 where the transition takes place in absence of a field, i.e. the temperature at which the free energy of the superconducting state and the normal state are the same. The last term on the right hand side of Eq. (2.1) is the kinetic energy cost of the induced supercurrent[3] and the integration is

[2] as opposed to the fluxoid which is always an integer times $h/2e$ [15].

[3] The supercurrent density is [16, 17] $\boldsymbol{j}_\mathrm{s} = \frac{-e}{4mi}\left(\Delta^*(\boldsymbol{r})\boldsymbol{\nabla}\Delta(\boldsymbol{r}) - \Delta(\boldsymbol{r})\boldsymbol{\nabla}\Delta^*(\boldsymbol{r})\right) - \frac{2e^2}{2m}\boldsymbol{A}|\Delta(\boldsymbol{r})|^2 = \frac{e}{2m}|\Delta|^2\left(\nabla\chi(\boldsymbol{r}) - 2e\boldsymbol{A}\right)$.

over the entire volume of the superconductor. In equilibrium, $\nabla\chi$ is constant along the wire circumference so we use instead the average value of the last term from Eq. (2.1):

$$\nabla\chi - 2e\boldsymbol{A} = \frac{1}{2\pi R}\oint d\boldsymbol{l}\,(\nabla\chi - 2e\boldsymbol{A}) = \frac{1}{2\pi R}\,(2\pi n - 2e\Phi) = \frac{1}{R}\left(n - \tilde{\Phi}\right), \tag{2.2}$$

where the contour of integration is the cylinder cross-section perpendicular to z. $\tilde{\Phi} = \Phi/\Phi_0$ is the flux in units of the superconducting magnetic flux quantum $\Phi_0 = h/2e$ (where $\hbar = 1$). As mentioned, the total change in the phase $\chi(\boldsymbol{r})$ must be an integer times 2π when taking one turn around the cylinder. The integer n appearing in the second equality is therefore called the winding number. The integrand of the free energy difference can then instead be written as

$$\Omega_\mathrm{s} - \Omega_\mathrm{n} = a\tau|\Delta|^2 + \frac{1}{4mR^2}\left(n - \tilde{\Phi}\right)^2|\Delta|^2 + \frac{b}{2}|\Delta|^4.$$

To minimize the free energy of the superconductor, the winding number is n' when the flux through the cavity is in the interval $n' - \frac{1}{2} < \tilde{\Phi} < n' + \frac{1}{2}$. The superconductor free energy is thus periodic in flux by Φ_0 and so must the transition temperature be. By collecting terms of order $|\Delta|^2$ and introducing a new parameter τ' which changes sign at the phase transition, one finds an expression for the flux-dependent critical temperature T_c,

$$\begin{aligned} &\tau' = \tau + \frac{1}{4mR^2a}\left(n - \tilde{\Phi}\right)^2, \quad \tau'(T = T_\mathrm{c}) = 0 \implies \\ &\frac{\delta T_\mathrm{c}}{T_\mathrm{c}^0} = \frac{T_\mathrm{c} - T_\mathrm{c}^0}{T_\mathrm{c}^0} = -\frac{1}{4mR^2a}\left(n - \tilde{\Phi}\right)^2. \end{aligned}$$

This shows that the transition temperature indeed varies periodically with the enclosed flux in recurring parabolas centred on integer flux units $n\Phi_0$ in intervals each corresponding to a certain n. $T_\mathrm{c} \leq T_\mathrm{c}^0$ and the transition temperature oscillation reaches the minimum value at half integer flux and the maximum value at integer flux where $T_\mathrm{c} = T_\mathrm{c}^0$. These are the Little-Parks lobes that demonstrate the winding of the superconducting order parameter and they are illustrated in Fig. 2.2a.

In the original experiment by Little and Parks, they investigated a thin cylinder of tin with wall thickness 37.5 nm and a radius around 1.4 μm, for which the resistance was measured while varying an axial magnetic field at temperatures near T_c^0. The result is displayed in Fig. 2.2b showing small periodic variations in the resistance in form of a series of parabolas regularly spaced by one flux quantum, all superimposed on a quadratic background. Subtracting the background, seven of such parabolas with strictly periodic spacing were observed. This was interpreted as representing a similar series of parabolic oscillations in the transition temperature with magnetic field since lowering T_c with a magnetic field will raise the resistance at a given temperature around the transition point. The transition temperature was determined from the slope of resistance versus temperature curves and the maximum deviation was found to be $\delta T_\mathrm{c} = 5 \cdot 10^{-4}$ K. The energy cost of the supercurrent is also compensated by a decrease in the binding energy $|\Delta|$ of a Cooper pair. Since $|\Delta|^2$ is equal to the number density of Cooper pairs [16], n_s, the supercurrent is reduced by lowering smaller $|\Delta|$. Therefore $|\Delta|(\Phi)$ follows the same parabolic variation as T_c with a period $\Phi_0 = h/2e$. The quadratic background behaviour of the variations in resistance (shown in Fig. 2.2b) is due to a non-periodic weakening of

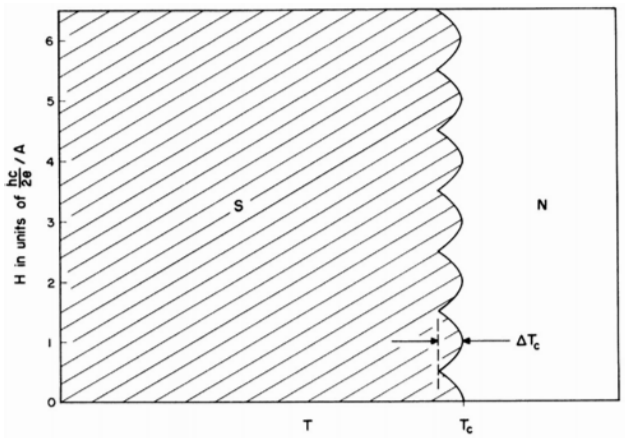

(a) Phase diagram illustrating Little-Parks lobes. Each parabola is centred around integer units of Φ_0 and the largest reduction in critical temperature is at odd half-integer values of the flux in units of Φ_0.

(b) Photograph from figure 2 in [13]. The upper trace is a magnetic field sweep and the lower trace shows variations of resistance at T_c as a function of magnetic field.

Figure 2.2: Figures from the original 1962 paper by Little and Parks [13].

the electron pairing parameter in a magnetic field [15]. We will present an expression for the pair-breaking further down.

Since the original experiment, the Little-Parks effect has been experimentally reproduced [10, 15, 18, 19] and the theory expanded [20–23] especially in regard to dividing the effect into two different regimes which we will review next in order to give a thorough characterisation of full-shell nanowires and explain the measurements in [10].

2.1 Destructive and non-destructive regimes

In an article from 1981 by de Gennes [20], the linearised Ginzburg-Landau equation for the superconducting order parameter was analysed. The system considered was an infinitely thin, uniform, and superconducting ring of radius R with a single branch of length L, all in a magnetic field perpendicular to the system plane. The solution to the Ginzburg-Landau equation predicted two different regimes; a non-destructive one where T_c remained finite for all strengths of the magnetic field B below the critical value B_c as observed in the Little-Parks experiment. The other was a destructive regime where, in certain intervals of B around what corresponds to odd multiples of half a flux quantum through the ring, the maximal reduction in the critical temperature would exceed T_c^0 and the system become normal even at $T = 0$ K. In these intervals, the kinetic energy of the supercurrent exceeds the condensation energy (the first term in Eq. (2.1)) resulting in destruction of superconductivity. In the case $L = 0$, the two regimes were found to be characterised by the ratio between R and the superconducting coherence length at zero temperature $\xi(0)$; For $2R < \xi(0)$ a normal phase would persist around odd half-integer flux quanta even at $T = 0$ K and for $2R > \xi(0)$ the Little-Parks oscillations would be non-destructive. Indeed we see in Eq. (2.2) that a smaller radius increases the kinetic energy and hence the maximal reduction in T_c is size dependent. The critical flux at $T = 0$ in the destructive regime (not to be confused with B_c) where the phase first shifts

to normal was calculated to be $\Phi_c = R/\xi(0)$ and the ring would remain normal in the interval $[\Phi_c, \Phi_0 - \Phi_c]$, centred around $\tilde{\Phi} = 1/2$, before re-entering into the superconducting phase. This behaviour would be repeated in higher Little-Parks lobes as well. The phase diagram in the non-destructive regime is like the one in Fig. 2.2a with a single superconducting region with a slightly modulated phase boundary up to the critical field B_c. The destructive regime phase diagram should instead consist of disconnected lobes of superconductivity separated by a normal resistive phase around odd multiples of $\Phi_0/2$.

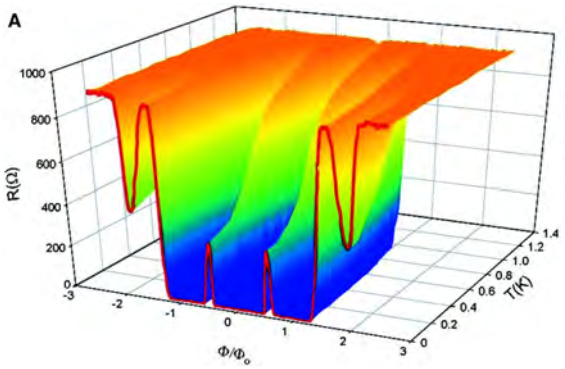

Figure 2.3: Figure 1A from [18] displaying resistance, R, measured for varying temperature, T, and magnetic flux, Φ/Φ_0.

Twenty years later Liu et al. [18] published results of an experiment on cylinders in the destructive regime, according to the de Gennes calculations for a ring [20].[4] One of the samples was an Al cylinder of diameter $d = 150$nm and thickness $t = 30$ nm. From the parallel critical field B_c they estimated the coherence length to be $\xi(20\text{ mK}) = 161$nm, meaning $2R = d < \xi(0\text{ K})$. The measured resistance as function of temperature and flux is duplicated in Fig. 2.3 which shows finite-resistance peaks around $\tilde{\Phi} = \pm 1/2$ and $\tilde{\Phi} = \pm 3/2$. The peaks at $\tilde{\Phi} \pm 1/2$ are only about a third of the normal state resistance R_N at temperatures much lower than the zero-field critical temperature T_c^0. Furthermore, the resistance in the second lobes remains finite even at $\tilde{\Phi} = \pm 2$. The same type of behaviour was observed for a cylinder of $Au_{0.7}In_{0.3}$ with $d = 154$ nm, $t = 30$ nm, and $\xi(20\text{ mK}) = 160$ nm and so $d < \xi(0\text{ K})$ for that sample as well. Even though the two cylinders were predicted to be in the destructive regime, the phase diagrams for the two materials were not distinctive lobes of superconducting phases separated by the normal phase. Instead, some intermediate phase with resistance $0 < R(\Phi) < R_N$ was observed between the zeroth and first lobes and a finite resistance phase was seen in the second lobes where a superconducting phase was expected. For a larger Al cylinder with $d = 257$ nm, $t = 30$ nm, and an estimated $\xi(0\text{ K}) < 60\text{ nm} < d$, non-destructive Little-Parks oscillations of period Φ_0, similar to the original experiment [13], were observed. Hence, the results from Liu et al. [18] did agree to some extent with the prediction by de Gennes [20], but there was still need for an explanation of the irregularities in the destructive regime phase diagrams.

In 2009 Dao et al. [21] suggested that inhomogeneities modulated at a long-range scale

[4]The theory should also hold for a cylinder that is equivalently orientated with respect to the magnetic field (as in the Little-Parks experiment).

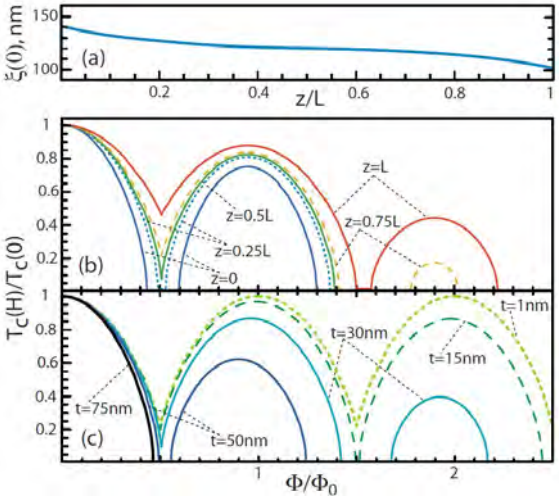

Figure 2.4: Figure 1 from [21] showing how a varying coherence length, $\xi(0)$, along a cylinder with constant radius **(a)** affects the flux-temperature phase diagram at different positions z along a cylinder of length L **(b)**. In **(c)** it is shown how a finite cylinder thickness results in a quadratic deviation of the phase transition line superimposed on the periodic behaviour of $T_c(\Phi)$ for a fixed z. This effect vanishes in the limit $t \ll R$.

compared to $\xi(0)$ could result in the reported behaviour of the resistance in [18]. That would separate the cylinder into normal and superconducting regions around the transition point and thereby yield a finite resistance lower than R_N. Such inhomogeneities could e.g. be variations in the thickness, radius or the electron diffusivity along the cylinder, causing phase transitions to occur only locally with different $T_c(\Phi, z)$.

They solved the linearised self-consistent equation of the superconducting order parameter for $t \ll \xi$ in the dirty limit where $\xi(0) = \sqrt{\pi\hbar v_F l_{el}/24 k_B T_c^0}$ [16]. Here $\hbar$ is the reduced Planck constant, v_F is the Fermi velocity, l_{el} is the mean free path, and k_B is the Boltzmann constant. They found that the finite field transition temperature should be the largest of the solutions $T_c(n, \Phi)$ to the equation

$$\ln\left(\frac{T_c(n,\Phi)}{T_c^0}\right) = \psi\left(\frac{1}{2}\right) - \psi\left(\frac{1}{2} + \frac{\alpha(n,\Phi)}{2\pi T_c(n,\Phi)}\right). \tag{2.3}$$

Here $\psi(x) = \frac{\Gamma'(x)}{\Gamma(x)}$ is the digamma function, n is the winding number introduced in Eq. (2.2), and $\alpha(n, \phi)$ is the pair-breaking parameter:

$$\alpha(n,\Phi) = \frac{\xi^2(0)}{\pi R^2} T_c^0 \left\{ 4(n-\tilde{\Phi})^2 + \tilde{t}^2\tilde{\Phi}^2 + 4n^2 \left[\frac{1}{\tilde{t}} \ln\left(\frac{2+\tilde{t}}{2-\tilde{t}}\right) - 1 \right] \right\},$$

with $\tilde{t} = t/R$.[5] For a hollow superconducting cylinder $\tilde{t} < 1$, and the pair-breaking parameter at zero winding (i.e. in the first Little-Parks lobe) $\alpha(0, \Phi)$ depends weekly on $\tilde{t}$ but rather on the ratio $\xi(0)/R$. For $n > 0$, however, $\alpha(n, \Phi)$ strongly depends on $\tilde{t}$ and the pair-breaking can be large even at integer $\tilde{\Phi}$ [19]. The larger the pair-breaking parameter the lower the temperature is required to fulfil Eq. (2.3). Apart from the periodic term

[5] Similar considerations on finite thickness effects were actually considered by Groff and Parks already in 1968 [15].

$(n-\tilde{\Phi})^2$ in $\alpha(n,\Phi)$ there is also the thickness-dependent term

$$\tilde{t}^2\tilde{\Phi}^2 + 4n^2\left[\frac{1}{\tilde{t}}\ln\left(\frac{2+\tilde{t}}{2-\tilde{t}}\right)-1\right] \approx \tilde{t}^2\left(\tilde{\Phi}^2+\frac{n^2}{3}\right). \tag{2.4}$$

This term is not periodic in flux and instead leads to an overall decrease of superconductivity which will eventually be destroyed above a certain field B_c. This is shown in Fig. 2.4 which is taken from [21]. We see that with increasing thickness the maximum in $T_\mathrm{c}(\Phi)$ at finite flux is reduced compared to T_c^0 and the parabolic lobes are shifted towards $\Phi = 0$. Hence a cylinder that from the ratio $R/\xi(0)$ is thought to be in the non-destructive regime might actually belong to the destructive regime due to its wall thickness.

The non-periodic pair-breaking can also explain the temperature broadening of the phase transition at finite magnetic field observed in [18]. With disorder, variations in $\alpha(n,\Phi)$ and therefore also $T_c(\Phi,z)$ become larger with increasing field. In Fig. 2.4 we show the phase transition line as function of flux and temperature from [21]. We see how the difference in local $T_c(\Phi,z)$, and thereby the temperature width of the transition, becomes larger with increasing field, in particular near odd half-integer $\tilde{\Phi}$. With their model Dao et al. were able to reproduce the essential features from [18].

The theory was further expanded by Schwiete and Oreg [22, 23] who suggested that Cooper pair fluctuations in the normal phase close to the transition would give a large contribution to a persistent current. This effect should be largest for superconductors with low effective dimensionality and in the presence of disorder. Together with the theory for inhomogeneity effects in [21], this should provide an explanation for the intermediate resistive phase $0 < R < R_\mathrm{N}$.

Furthermore, from the condition in Eq. (2.3) they obtained another expression for the critical flux where the transition temperature becomes zero, $\Phi_\mathrm{c} = \tilde{\Phi}_\mathrm{c}\Phi_0$, than what was found in [20]:

$$\tilde{\Phi}_\mathrm{c} \approx \frac{\pi R}{\xi(0)\sqrt{8\gamma_E}}\left(1-\frac{\tilde{t}^2}{4}\right), \qquad \gamma_E \approx 1.78. \tag{2.5}$$

This equation includes the finite cylinder wall thickness which reduces the critical flux. For superconductivity to be destroyed between the zeroth and first Little-Parks lobes it is required that $\tilde{\Phi}_\mathrm{c} < 0.5$. For a vanishing wall thickness this yields the condition $R/\xi(0) < \sqrt{2\gamma_E}/\pi \approx 0.6$ whereas the de Gennes result $R/\xi(0) < 0.5$ is only valid for $r \gg 1$. However, this correction and that of finite thickness do not change the predicted regimes of the different cylinders used in [18].

In the experiment on full-shell wires by Vaitiėkenas et al. [10] they have also performed measurements on the superconducting shell of the differential resistance versus axial magnetic field and temperature. Although the nanowires are really hexagonal the superconducting shell is approximated by a cylinder of mean diameter $2R = 160$ nm and thickness $t = 30$ nm. The dirty-limit effective penetration depth is calculated to be $\lambda_\mathrm{eff} = 150\ \mathrm{nm} \gg t$ and the Little-Parks effect is indeed relevant. The result of the resistance measurements is reproduced in Fig. 2.5. It shows a periodic destruction of superconductivity and a decreasing maximum $T_c(\Phi)$ of each Little-Parks lobe with magnetic field. A third superconducting lobe is not observed. This, we know now, is characteristic of the destructive Little-Parks regime for a wire with $R/\xi(0) < 0.6$ and a finite t/R. Between the zeroth and first lobes and the first and second lobes the resistance attains the

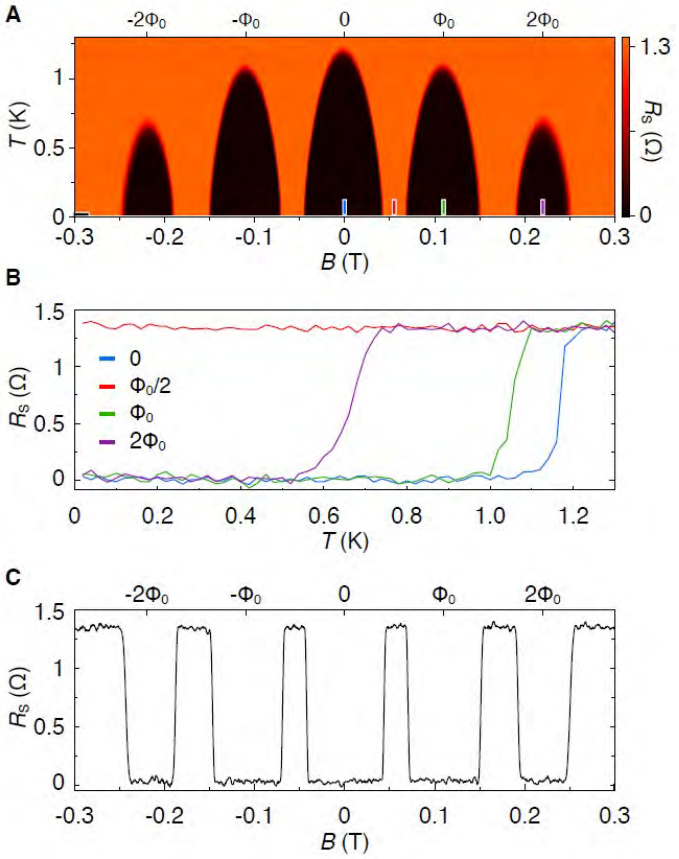

Figure 2.5: Figure S1 from the supplementary material to [10] showing measurements of the destructive Little-Parks effect around zero current bias. **A** shows the differential resistance, R_S, as function of magnetic field, B, and temperature, T. Around $\pm 1/2$ and $\pm 3/2$ flux quanta the resistance remains normal down to the lowest measured temperature 20 K. Line-cuts from this plot at flux $0, \Phi_0/2, \Phi_0$, and $2\Phi_0$ are shown in **B**. In **C** is shown a line-cut at constant temperature $T = 20$ mK.

normal value and is temperature-independent. A normal resistance around one half flux quantum has also been reported by Sternfeld et al. [19] for a thin cylinder fulfilling the destructive regime criterion. In [19], however, no lobes other than the zeroth Little-Parks lobe showed zero resistance. It is difficult to obtain several superconducting lobes because the magnetic field needs to produce a large flux through a small area without destroying superconductivity [23]. By reducing $R/\xi(0)$ such that all cross-sections meet the destructive regime criterion despite inhomogeneities, the normal resistance can be obtained at sufficiently low temperatures.

The dirty-limit coherence length in [10] is estimated to be $\xi(0) = \sqrt{\pi\hbar v_F l_{el}/24 k_B T_c^0} = 180$ nm. According to Eq. (2.5) this yields a critical flux $\tilde{\Phi}_c \approx 0.36$ which fulfils the destructive regime criterion. However, the corresponding critical field $B_c = 0.36\Phi_0/\pi R^2 \approx 37$ mT is below the reported 45 mT. The discrepancy may be due to higher order corrections in $\tilde{t} \approx 0.375$ to the expansion in Eq. (2.4) or to an underestimation of the coherence length.

The resistance as function of temperature shows that the phase transition is broad-

ened with an increasing field (see Fig. 2.5). This suggests that some inhomogeneities are present in the shell but not enough to yield an intermediate resistive phase around odd half-integer flux quanta. The use of expressions in the dirty-limit may then be the reason for a potentially underestimated coherence length. Finally, the absence of a large persistent current near the transition challenges the asserted Cooper pair fluctuations [22,23].

In the next section we shall see that the semiconducting core in the full-shell wires can inherit an electron pairing from the superconducting shell. This is why the differential conductance of the core shows a destructive Little-Parks-like behaviour of the spectral gap (cf. Fig. 1.1).

3 Proximity effect

In the description of semiconductor-superconductor hybrid devices, an essential element is the proximity effect where the superconductor induces electron pairing in the semiconductor when the two are brought into contact. Here we will explain this effect by the tunnelling Hamiltonian approach, based on the methods presented in Refs. [3, 6, 24]. The result will be a self-energy term in the Green's function of the semiconductor which introduces pairing of electrons (and of holes), after we have integrated out the superconductor electron degrees of freedom. Since the proximity effect will be used later to describe full-shell nanowires we will use such a system for illustration. The total Hamiltonian thus consists of a semiconducting core term, an s-wave superconducting shell term and a tunnelling Hamiltonian

$$\mathcal{H} = \mathcal{H}_{\text{semi}} + \mathcal{H}_{\text{s}} + \mathcal{H}_{\text{t}}.$$

We reserve annihilation operators $c_{p_z\sigma}$ for electrons in the core and $f_{\boldsymbol{p}\sigma}$ for electrons in the shell:

$$\boldsymbol{c}_{p_z} = \begin{pmatrix} c_{p_z\uparrow} \\ c^\dagger_{-p_z\downarrow} \end{pmatrix}, \quad \boldsymbol{f}_{\boldsymbol{p}} = \begin{pmatrix} f_{\boldsymbol{p}\uparrow} \\ f^\dagger_{-\boldsymbol{p}\downarrow} \end{pmatrix}.$$

These Nambu spinors consist of two components although 4-Nambu spinors will be used in subsequent sections in order to describe spin terms in the Hamiltonian. Since the spin dependence of the electron pairing is build into the Nambu structure and can be straightforwardly translated from 2-Nambu to 4-Nambu, we work here with spin-less Hamiltonians for simplicity.[6] Furthermore, it is assumed for now that the semiconductor has only one longitudinal channel, i.e. is 1-dimensional. In terms of 2-Nambu spinors, the Hamiltonians read

$$\mathcal{H}_{\text{semi}} = \sum_{p_z} \boldsymbol{c}^\dagger_{p_z} \begin{pmatrix} \varepsilon_{p_z} - \mu & 0 \\ 0 & -\varepsilon_{p_z} + \mu \end{pmatrix} \boldsymbol{c}_{p_z}, \quad \varepsilon_{p_z} = \frac{p_z^2}{2m^*},$$

$$\mathcal{H}_{\text{s}} = \sum_{\boldsymbol{p}} \boldsymbol{f}^\dagger_{\boldsymbol{p}} \begin{pmatrix} \xi_{\boldsymbol{p}} & -\Delta \\ -\Delta^* & -\xi_{\boldsymbol{p}} \end{pmatrix} \boldsymbol{f}_{\boldsymbol{p}}, \quad \xi_{\boldsymbol{p}} = \frac{\boldsymbol{p}^2}{2m} - \mu_{\text{s}},$$

$$\mathcal{H}_{\text{t}} = \sum_{\boldsymbol{p}} \left[\boldsymbol{c}^\dagger_{p_z} \underline{V} \boldsymbol{f}_{\boldsymbol{p}} + \boldsymbol{f}^\dagger_{\boldsymbol{p}} \underline{V}^\dagger \boldsymbol{c}_{p_z} \right], \quad \underline{V} = \begin{pmatrix} V & 0 \\ 0 & -V^* \end{pmatrix}.$$

Here m^* and μ are the effective electron mass and chemical potential in the semiconducting core while m and μ_{s} are those of the superconducting shell. The pairing potential Δ is assumed to be momentum independent. $V = |V|e^{i\theta}$ is the coupling strength between the two materials. The tunnelling Hamiltonian is constructed such that momentum is conserved along the wire (p_z) but not along the transverse directions ($p_r, p_\varphi = \boldsymbol{p}_\perp$). In order to examine the effect of the coupling we define here the imaginary time Nambu

[6] Extending to 4-Nambu, $(c_{p_z\uparrow}, c_{p_z\downarrow}, c^\dagger_{-p_z\downarrow}, -c^\dagger_{-p_z\uparrow})$, the induced gap becomes $\Delta \to \Delta\sigma_0$ where σ_0 is the identity in spin space.

Green's function of the semiconducting core

$$\begin{aligned}\mathcal{G}_{\text{semi}}(p_z,\tau) &= -\left\langle T_\tau\left(\boldsymbol{c}_{p_z}(\tau)\otimes\boldsymbol{c}^\dagger_{p_z}(0)\right)\right\rangle \\ &= \begin{pmatrix} -\left\langle T_\tau\left(c_{p_z\uparrow}(\tau)c^\dagger_{p_z\uparrow}(0)\right)\right\rangle & -\left\langle T_\tau\left(c_{p_z\uparrow}(\tau)c_{-p_z\downarrow}(0)\right)\right\rangle \\ -\left\langle T_\tau\left(c^\dagger_{-p_z\downarrow}(\tau)c^\dagger_{p_z\uparrow}(0)\right)\right\rangle & -\left\langle T_\tau\left(c^\dagger_{-p_z\downarrow}(\tau)c_{-p_z\downarrow}(0)\right)\right\rangle \end{pmatrix} \\ &= \begin{pmatrix} \mathcal{G}^{\text{ee}}_{\text{semi}}(p_z,\tau) & \mathcal{G}^{\text{eh}}_{\text{semi}}(p_z,\tau) \\ \mathcal{G}^{\text{he}}_{\text{semi}}(p_z,\tau) & \mathcal{G}^{\text{hh}}_{\text{semi}}(p_z,\tau)\end{pmatrix}. \end{aligned} \tag{3.1}$$

The anomalous off-diagonal terms $\mathcal{G}^{\text{eh(he)}}_{\text{semi}}(p_z,\tau)$ are non-zero as a result of the coupling with the superconducting shell. They correspond to a process called Andreev reflection or branch conversion scattering, where an electron (hole) from the semiconductor, incoming on the boundary of the superconductor, is retro-reflected as a hole (electron) [25, 26]. Charge is conserved through creation (annihilation) of a Cooper pair of charge $-2e$ at the superconductor Fermi level. Since the Cooper pair in the superconductor is composed of electrons of opposite spin, the reflected hole (electron) must have opposite spin of the incoming electron (hole) as is the case for the off-diagonal elements of Eq. (3.1).[7] Writing the semiconductor and superconductor Nambu Green's functions in absence of coupling as $\mathcal{G}^0_{\text{semi}}$ and $\mathcal{G}^0_{\text{s}}$, respectively, the Dyson equation for the full $\mathcal{G}_{\text{semi}}$ becomes

$$\mathcal{G}_{\text{semi}}(p_z,\tau) = \mathcal{G}^0_{\text{semi}}(p_z,\tau) + \int_0^\beta\int_0^\beta d\tau_1 d\tau_2\; \mathcal{G}^0_{\text{semi}}(p_z,\tau-\tau_1)\sum_{\boldsymbol{p}_\perp}\underline{V}\mathcal{G}^0_{\text{s}}(\boldsymbol{p},\tau_1-\tau_2)\underline{V}^\dagger\mathcal{G}_{\text{semi}}(p_z,\tau_2).$$

To solve the equation we Fourier transform to Matsubara frequencies

$$\mathcal{G}_{\text{semi}}(p_z,ik_n) = \mathcal{G}^0_{\text{semi}}(p_z,ik_n) + \mathcal{G}^0_{\text{semi}}(p_z,ik_n)\sum_{\boldsymbol{p}_\perp}\underline{V}\mathcal{G}^0_{\text{s}}(\boldsymbol{p},ik_n)\underline{V}^\dagger\mathcal{G}_{\text{semi}}(p_z,ik_n),$$

which implies

$$\mathcal{G}_{\text{semi}}(p_z,ik_n) = \left[\left(\mathcal{G}^0_{\text{semi}}(p_z,ik_n)\right)^{-1} - \Sigma_{\text{ss}}(p_z,ik_n)\right]^{-1}. \tag{3.2}$$

Here we have introduced the self-energy of the semiconductor due to coupling to the superconductor,

$$\Sigma_{\text{ss}}(p_z,ik_n) = \sum_{\boldsymbol{p}_\perp}\underline{V}\mathcal{G}^0_{\text{s}}(\boldsymbol{p},ik_n)\underline{V}^\dagger.$$

The self-energy contains the Green's function of the isolated superconductor which can be found from its equation of motion [27, p. 336],

$$\partial_\tau\mathcal{G}^0_{\text{s}}(\boldsymbol{p},\tau) = -\delta(\tau)\begin{pmatrix}1&0\\0&1\end{pmatrix} - \begin{pmatrix}\xi_{\boldsymbol{p}} & -\Delta\\ -\Delta^* & -\xi_{\boldsymbol{p}}\end{pmatrix}\mathcal{G}^0_{\text{s}}(\boldsymbol{p},\tau).$$

By Fourier transformation we obtain

$$\begin{pmatrix} ik_n-\xi_{\boldsymbol{p}} & \Delta \\ \Delta^* & ik_n+\xi_{\boldsymbol{p}}\end{pmatrix}\mathcal{G}^0_{\text{s}}(\boldsymbol{p},ik_n) = \begin{pmatrix}1&0\\0&1\end{pmatrix},$$

[7] An electron from the semiconductor with energy smaller than Δ is forbidden to propagate into the superconducting region and hence only Andreev reflection is possible [25].

whereby

$$\mathcal{G}_{\mathrm{s}}^{0}(\boldsymbol{p}, ik_n) = \frac{1}{(ik_n)^2 - E_{\boldsymbol{p}}^2} \begin{pmatrix} ik_n + \xi_{\boldsymbol{p}} & -\Delta^* \\ -\Delta & ik_n - \xi_{\boldsymbol{p}} \end{pmatrix},$$

where $E_{\boldsymbol{p}} = \sqrt{\xi_{\boldsymbol{p}}^2 + |\Delta|^2}$ is the excitation energy. With this it is possible to calculate the self-energy of the semiconductor due to tunnelling in and out of the superconductor.

$$\begin{aligned}
\Sigma_{\mathrm{ss}}(p_z, ik_n) &= \sum_{\boldsymbol{p}_\perp} \frac{1}{(ik_n)^2 - E_{\boldsymbol{p}}^2} \begin{pmatrix} V & 0 \\ 0 & -V^* \end{pmatrix} \begin{pmatrix} ik_n + \xi_{\boldsymbol{p}} & -\Delta^* \\ -\Delta & ik_n - \xi_{\boldsymbol{p}} \end{pmatrix} \begin{pmatrix} V^* & 0 \\ 0 & -V \end{pmatrix} \\
&= \sum_{\boldsymbol{p}_\perp} \frac{|V|^2}{(ik_n)^2 - E_{\boldsymbol{p}}^2} \begin{pmatrix} ik_n + \xi_{\boldsymbol{p}} & \Delta^* e^{2i\theta} \\ \Delta e^{-2i\theta} & ik_n - \xi_{\boldsymbol{p}} \end{pmatrix} \\
&= -|V|^2 \int_{-\infty}^{\infty} d\xi_{\boldsymbol{p}_\perp} \, \frac{1}{k_n^2 + \xi_{\boldsymbol{p}}^2 + |\Delta|^2} d(\xi_{\boldsymbol{p}_\perp}) \begin{pmatrix} ik_n + \xi_{\boldsymbol{p}} & \tilde{\Delta}^* \\ \tilde{\Delta} & ik_n - \xi_{\boldsymbol{p}} \end{pmatrix}, \qquad \tilde{\Delta} = \Delta e^{-2i\theta}.
\end{aligned}$$

Here $d(\xi_{\boldsymbol{p}_\perp}) = d_2(0)$ is the density of states of free electrons in two dimensions which is constant. We have let the sum over $\xi_{\boldsymbol{p}_\perp}$ run unrestricted instead of using the true upper and lower cut-offs. This introduces a constant correction, $\delta\mu$, to the chemical potential of the semiconductor that depends on the superconductor material properties and that we will disregard. Assuming the Fermi energy in the superconductor to be much larger than the relevant energy scale in the semiconductor, we change the integration variable $\xi_{\boldsymbol{p}_\perp} \to \xi_{\boldsymbol{p}_\perp} + p_z^2/2m = \xi_{\boldsymbol{p}}$

$$\Sigma_{\mathrm{ss}}(p_z, ik_n) = -|V|^2 d_2(0) \int_{-\infty}^{\infty} d\xi_{\boldsymbol{p}} \frac{1}{k_n^2 + \xi_{\boldsymbol{p}}^2 + |\Delta|^2} \begin{pmatrix} ik_n & \tilde{\Delta}^* \\ \tilde{\Delta} & ik_n \end{pmatrix},$$

where we have employed that the function of $\xi_{\boldsymbol{p}}$ on the diagonal is odd. The integral is solved by expanding the line integral on the real axis to a curve in the upper half of the complex plane where $\xi_{\boldsymbol{p}}^{-2} \to 0^-$

$$\int_{-\infty}^{\infty} d\xi_{\boldsymbol{p}} \, \frac{1}{\xi_{\boldsymbol{p}}^2 + k_n^2 + |\Delta|^2} = \oint_C d\xi_{\boldsymbol{p}} \, \frac{1}{\xi_{\boldsymbol{p}} + i\sqrt{k_n^2 + |\Delta|^2}} \frac{1}{\xi_{\boldsymbol{p}} - i\sqrt{k_n^2 + |\Delta|^2}} = \frac{2\pi i}{2i\sqrt{k_n^2 + |\Delta|^2}}.$$

Thus the self-energy is

$$\Sigma_{\mathrm{ss}}(p_z, ik_n) = \frac{-\Gamma}{\sqrt{k_n^2 + |\Delta|^2}} \begin{pmatrix} ik_n & \tilde{\Delta}^* \\ \tilde{\Delta} & ik_n \end{pmatrix}, \qquad \Gamma = |V|^2 d_2(0)\pi,$$

where we have introduced the tunnelling strength Γ. We see on the off-diagonal the induced pairing in the semiconductor which we set to be real since any phase could be removed by a gauge transformation. Inserting the self-energy into Eq. (3.2) and performing analytic continuation $ik_n \to \omega + i\eta$, we obtain the retarded Green's function of the core

$$\mathcal{G}_{\mathrm{semi}}^{\mathrm{R}}(p_z, \omega) = \left[\omega \left(1 + \frac{\Gamma}{\sqrt{|\Delta|^2 - \omega^2}} \right) - H_{\mathrm{semi}} + \frac{\Gamma|\Delta|}{\sqrt{|\Delta|^2 - \omega^2}} \tau_x \right]^{-1}, \tag{3.3}$$

where τ_x is the first Pauli matrix in 2-Nambu space, H_{semi} is the matrix in $\mathcal{H}_{\mathrm{semi}}$, and we have omitted writing the positive infinitesimal $\eta = 0^+$ explicitly. Considering energies

in the semiconductor much smaller than the shell gap, $\omega \ll |\Delta|$, in the weak tunnelling limit, $\Gamma \ll |\Delta|$, we obtain the effective low-energy Green's function

$$\tilde{\mathcal{G}}^{\mathrm{R}}_{\mathrm{semi}}(p_z,\omega) = \left[\omega - H^{\mathrm{eff}}_{\mathrm{semi}}\right]^{-1}, \qquad H^{\mathrm{eff}}_{\mathrm{semi}} = \begin{pmatrix} \varepsilon_{p_z} - \mu & -\Gamma \\ -\Gamma & -\varepsilon_{p_z} + \mu \end{pmatrix},$$

which describes a superconductor with a frequency independent electron pairing Γ, thus the semiconductor has effectively become a superconductor. In the strong tunnelling case, $\Gamma \gg |\Delta|$, one needs to identify the poles of the Green's function in Eq. (3.3) by the determinant equation

$$\left|\omega - Z\left(H_{\mathrm{semi}} - \frac{\Gamma|\Delta|}{\sqrt{|\Delta|^2-\omega^2}}\tau_x\right)\right| = 0, \qquad Z^{-1} = 1 + \frac{\Gamma}{\sqrt{|\Delta|^2-\omega^2}}. \tag{3.4}$$

Both the Hamiltonian H_{semi} and the self-energy are thus renormalised by Z and both frequency dependent. The lowest excitation energy in the proximitized semiconductor is found when $\varepsilon_{p_z} = \mu$ and we can regard this as the induced gap:

$$\Delta_{\mathrm{ind}} - \left(1 + \frac{\Gamma}{\sqrt{|\Delta|^2-\Delta^2_{\mathrm{ind}}}}\right)^{-1} \frac{\Gamma|\Delta|}{\sqrt{|\Delta|^2-\Delta^2_{\mathrm{ind}}}} = 0$$

and for $\Gamma \gg \left(|\Delta|, \sqrt{|\Delta|^2-\Delta^2_{\mathrm{ind}}}\right)$ the effective gap of the semiconductor approaches that of the superconductor [24]:

$$\Delta_{\mathrm{ind}} - \frac{\Gamma|\Delta|}{\sqrt{|\Delta|^2-\Delta^2_{\mathrm{ind}}}+\Gamma} \approx \Delta_{\mathrm{ind}} - |\Delta| = 0.$$

This concludes our introduction to the proximity effect and we will next present a model which incorporates the results of this section in order to describe full-shell nanowires.

4 Model Hamiltonian for full-shell nanowires

In this section we introduce a model Hamiltonian for a nanowire consisting of a semiconducting core covered by a full superconducting shell. It is the model presented by Lutchyn et al. [11] with minor modifications and is aimed at describing full-shell wires like the ones used in experiments by Vaitiėnas et al. [10] where an InAs core is covered by a thin Al shell. For a start, the wire is approximated to be perfectly cylindrical with a radius R_2 of the semiconductor and an outer radius R_3 of the superconductor (see Fig. 4.1). A magnetic field $\boldsymbol{B} = B\hat{\boldsymbol{z}}$ is applied along the wire and a gauge is chosen such that the vector potential is $\boldsymbol{A} = \frac{1}{2}(\boldsymbol{B} \times \boldsymbol{r}) = \frac{1}{2}Br\hat{\boldsymbol{\varphi}} = A\hat{\boldsymbol{\varphi}}$, using cylindrical coordinates (z, r, φ). The flux through a cross-section of radius r is $\Phi(r) = \pi r^2 B$, thus the vector potential can be written as $\boldsymbol{A} = \frac{\Phi(r)}{2\pi r}\hat{\boldsymbol{\varphi}}$. The thickness of the superconducting shell is assumed to be much smaller than the London penetration depth of the superconductor, $R_3 - R_2 = t \ll \lambda_{\mathrm{L}}$ and $R_2 \gg \lambda_{\mathrm{L}}$. As explained in Sec. 2 this leads to a winding of the superconducting order parameter that depends on the flux (which is not quantised), and we therefore take it to be on the form $\tilde{\Delta}(\boldsymbol{r}) = |\tilde{\Delta}|e^{-in\varphi}$. Here the integer n is the winding number and we have assumed the norm to be constant along the wire and ignored radial variations on the length scale t. A field-dependent $|\tilde{\Delta}|(B)$ will not be included explicitly in this model but will instead be considered as a type of boundary condition which can be superimposed on our findings which are for temperatures below the critical value. A Rashba spin-orbit interaction in the semiconductor is included in the model with a coupling strength α, due to an intrinsic, outpointing radial electric field at the semiconductor-superconductor interface [28]. In cylindrical coordinates the Hamiltonian for the semiconducting core in the magnetic field $B = \nabla \times \boldsymbol{A}$ reads

$$H_0 = \frac{(\boldsymbol{p} + eA\hat{\boldsymbol{\varphi}})^2}{2m^*} - \mu_r + \alpha_r \hat{\boldsymbol{r}} \cdot (\boldsymbol{\sigma} \times (\boldsymbol{p} + eA\hat{\boldsymbol{\varphi}})) + B_{\mathrm{Z}}\sigma_z, \tag{4.1}$$

where $\hbar = h/2\pi = 1$, m^* is the effective electron mass in the semiconductor, $-e < 0$ the electron charge, μ the chemical potential of the semiconductor, $\boldsymbol{p}$ the electron momentum operator, and $\boldsymbol{\sigma}$ is a vector of the Pauli spin matrices. Both the chemical potential and the spin-orbit coupling strength are assumed to only depend on r corresponding to using z and φ-averaged values of $\mu(\boldsymbol{r})$ and $\alpha(\boldsymbol{r})$ [11]. $B_{\mathrm{Z}} = g\mu_{\mathrm{B}}B/2$ is the Zeeman energy, g being the effective g-factor in the wire and μ_{B} the Bohr magneton [29].

As described in Sec. 3, a proximity-induced s-wave pairing of electrons in the semiconductor, $\Delta(\boldsymbol{r})$, is inherited from the superconductor, $|\tilde{\Delta}(\boldsymbol{r})| > |\Delta(\boldsymbol{r})|$. In the calculations of Sec. 3, the semiconducting core was assumed to be effectively 1-dimensional whereas here it is 3-dimensional. We adopt the proximity effect result in the strong coupling limit $\Gamma \gg |\tilde{\Delta}|$ for energies in the semiconductor smaller than or at the order of[8] $|\tilde{\Delta}|$ with the assumption that the induced pairing possesses the same φ dependence as in the superconductor while decaying in magnitude towards the centre of the core, corresponding to a decaying coupling $\Gamma(r)$. This way, the pairing potential in the semiconductor inherits the phase winding and an amplitude which, at $r = R_2$ is approximately that of the superconductor; $\Delta(\boldsymbol{r}) = \Delta(r)e^{-in\varphi}$. The reason we assume strong coupling is that the full-shell wires are made with an oxide-free interface between the Al and InAs and that the tunnelling spectrum of the core shows a zero-field gap that is almost that of Al [10]. With the proximity effect the Hamiltonian H_0 in Eq. (4.1) is renormalised to give an

[8] i.e. energies ω such that $\Gamma \gg \sqrt{|\tilde{\Delta}|^2 - \omega^2}$.

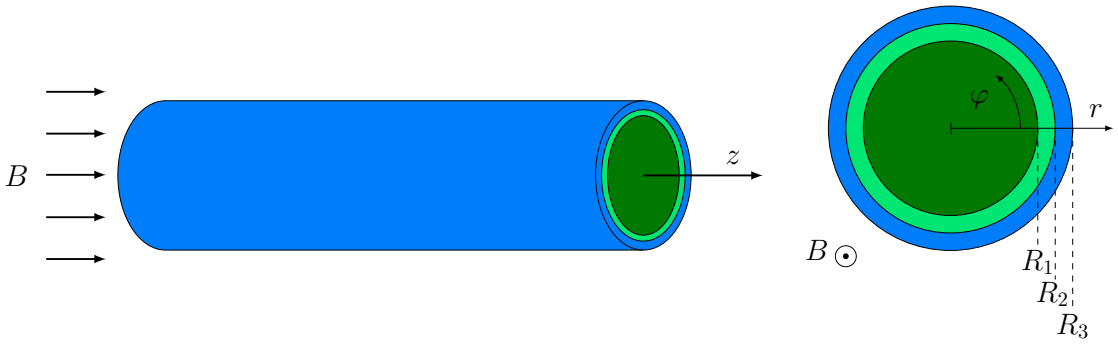

Figure 4.1: Illustration, similar to Fig. 1 in [11], of the full-shell nanowire and its orientation with respect to the magnetic field. The superconducting shell is coloured blue and the semiconducting core is green. Dark green, which is bounded by R_1, indicate a region of the semiconductor that might be effectively insulating for reasons presented in Sec. 4.1.

effective Hamiltonian. In the regime we have chosen to consider, this renormalisation can be approximated to be constant (see Eq. (3.4)) and from here on we will take all the parameters in H_0 to represent instead the renormalised values. In the Nambu basis, $\Psi(\boldsymbol{r}) = (\psi_\uparrow(\boldsymbol{r}), \psi_\downarrow(\boldsymbol{r}), \psi_\downarrow^\dagger(\boldsymbol{r}), -\psi_\uparrow^\dagger(\boldsymbol{r}))$ where $\psi_\uparrow(\boldsymbol{r})$ annihilates a spin-up electron at position $\boldsymbol{r}$ etc., the Bogoliubov-de Gennes (BdG) Hamiltonian [9] for the semiconductor thus reads

$$H_{\text{BdG}} = \begin{pmatrix} H_0(\boldsymbol{A}) & \Delta(\boldsymbol{r}) \\ \Delta^*(\boldsymbol{r}) & -\sigma_y H_0^*(\boldsymbol{A})\sigma_y \end{pmatrix}. \tag{4.2}$$

This is a four dimensional block matrix with spin as the inner structure and electron-hole space as the outer one, i.e. each of the elements in Eq. (4.2) is a matrix in spin space. In the hole-hole element, the time-reversed Hamiltonian is used since the hole part of Nambu space, $(\psi_\downarrow^\dagger(\boldsymbol{r}), -\psi_\uparrow^\dagger(\boldsymbol{r}))$, is the time-reversed vector of the electron part, $(\psi_\uparrow(\boldsymbol{r}), \psi_\downarrow(\boldsymbol{r}))$.[9] We note that time-reversal symmetry is broken by the external magnetic field $\nabla \times \boldsymbol{A}$ which together with the phase winding creates a helical system along z. The BdG Hamiltonian can be diagonalised by the Bogoliubov transformation U_{B} relating the electron and hole operators in the Nambu basis to eigenstate quasiparticle operators which also obey fermionic anti-commutation relations [27].

We write the BdG Hamiltonian from Eq. (4.2) in terms of Pauli matrices for spin σ_i and electron-hole space τ_i

$$\begin{aligned} H_{\text{BdG}} = &\left(\frac{p_z^2}{2m^*} + \frac{p_r^2}{2m^*} + \frac{(p_\varphi + eA\tau_z)^2}{2m^*} - \mu_r - \alpha_r(p_\varphi + eA\tau_z)\sigma_z + \alpha_r p_z \sigma_\varphi + B_{\text{Z}}\sigma_z\tau_z \right)\tau_z \\ &+ \Delta(r)(\cos(n\varphi)\tau_x + \sin(n\varphi)\tau_y). \end{aligned} \tag{4.3}$$

Here $p_z = \frac{-i\partial}{\partial z}$, $p_r^2 = \frac{-1}{r}\frac{\partial}{\partial r}\left(r\frac{\partial}{\partial r}\right)$, and $p_\varphi = \frac{-i}{r}\frac{\partial}{\partial \varphi}$. The notation $\sigma_\varphi = \boldsymbol{\sigma}\cdot\hat{\boldsymbol{\varphi}} = \sigma_y\cos(\varphi) - \sigma_x\sin(\varphi)$ has been introduced as well. As mentioned, the applied magnetic field breaks time reversal symmetry which is why both A and B_{Z} terms appear with an extra τ_z. We now introduce the following operator which commutes with the Hamiltonian:

$$J_z = L_z + \frac{1}{2}\sigma_z + \frac{1}{2}n\tau_z, \tag{4.4}$$

[9] In second quantization the Hamiltonian is $\mathcal{H} = \frac{1}{2}\int\int d\boldsymbol{r}d\boldsymbol{r}'\,\Psi^\dagger(\boldsymbol{r})H_{\text{BdG}}\delta(\boldsymbol{r}-\boldsymbol{r}')\Psi(\boldsymbol{r}') - \text{const.}$

where $L_z = -i\partial_\varphi$ is the angular momentum operator and n is still the winding of the order parameter. The commutator $[H_{\mathrm{BdG}}, J_z] = 0$ is calculated explicitly in App. A.1. The eigenvalues of J_z are thus conserved (angular) quantum numbers and we label the eigenstates of J_z and H_{BdG} with these:

$$\begin{aligned} J_z\Psi_{m_J}(\boldsymbol{r}) &= m_J\Psi_{m_J}(\boldsymbol{r}), \\ \Psi_{m_J}(\boldsymbol{r}) &= \exp\left[i\left(m_J - \frac{1}{2}\sigma_z - \frac{1}{2}n\tau_z\right)\varphi\right]\Psi_{m_J}(r,z). \end{aligned} \tag{4.5}$$

The states $\Psi_{m_J}(\boldsymbol{r})$ are the vector solutions in Nambu space to the Bogoliubov-de Gennes equation [25] with the Hamiltonian in Eq. (4.2). They describe quasiparticle excitations with energy E_{m_J}; $H_{\mathrm{BdG}}\Psi_{m_J}(\boldsymbol{r}) = E_{m_J}\Psi_{m_J}(\boldsymbol{r})$. From the requirement that the wave function must be single-valued, we see that m_J must be an integer if n is odd and a half-integer if n is even. We want to investigate the possibility for existence of MZMs in the nanowire system which are solutions to the equation $H_{\mathrm{BdG}}\Psi_{m_J}(\boldsymbol{r}) = 0$. These are known to be invariant under particle-hole transformation $\mathcal{P}\Psi_{\mathrm{M}} = \Psi_{\mathrm{M}}$ [9], where $\mathcal{P}$ is the particle-hole symmetry operator $\mathcal{P} = \sigma_y\tau_y\mathcal{K}$ with $\mathcal{K}$ representing complex conjugation. We therefore consider how the eigenstate in Eq. (4.5) transforms with $\mathcal{P}$:

$$\begin{aligned} \mathcal{P}\Psi_{m_J}(\boldsymbol{r}) &= \sigma_y\tau_y\mathcal{K}\exp\left[i\left(m_J - \frac{1}{2}\sigma_z - \frac{1}{2}n\tau_z\right)\varphi\right]\Psi_{m_J}(r,z) \\ &= \exp\left[i\left(-m_J - \frac{1}{2}\sigma_z - \frac{1}{2}n\tau_z\right)\varphi\right]\mathcal{P}\Psi_{m_J}(r,z). \end{aligned} \tag{4.6}$$

Furthermore, $\mathcal{P}H_{\mathrm{BdG}}\mathcal{P}^{-1} = -H_{\mathrm{BdG}}$. This means that $\mathcal{P}$ relates eigenstates with opposite energy and angular quantum number[10]: $\mathcal{P}\Psi_{E_{m_J},m_J} = \Psi_{-E_{m_J},-m_J}$. From Eq. (4.6) we see that only states with $m_J = 0$ can be invariant under particle-hole transformation, and thus only the $m_J = 0$ sector, which requires an odd winding number, supports MZMs.

To eliminate the φ dependence of H_{BdG} (Eq. (4.3)) we can make the following unitary transformation[11]:

$$\tilde{H}_{\mathrm{BdG}} = UH_{\mathrm{BdG}}U^\dagger, \qquad U = \exp\left[-i\left(m_J - \frac{1}{2}\sigma_z - \frac{1}{2}n\tau_z\right)\varphi\right]. \tag{4.7}$$

$$\begin{aligned} \tilde{H}_{\mathrm{BdG}} = &\left[\frac{p_z^2}{2m^*} + \frac{p_r^2}{2m^*} + \frac{\left(m_J - \frac{1}{2}\sigma_z - \frac{1}{2}n\tau_z + eAr\tau_z\right)^2}{2m^*r^2} - \mu_r + B_{\mathrm{Z}}\sigma_z\tau_z\right]\tau_z \\ &- \frac{\alpha_r}{r}\left(m_J - \frac{1}{2}\sigma_z - \frac{1}{2}n\tau_z\right)\sigma_z\tau_z - \alpha_r eA\sigma_z + \alpha_r p_z\sigma_y\tau_z + \Delta(r)\tau_x. \end{aligned} \tag{4.8}$$

In writing Eq. (4.8) we have used that $U\sigma_\varphi U^\dagger = \sigma_y$ and $U(\cos(n\varphi)\tau_x + \sin(n\varphi)\tau_y)U^\dagger = \tau_x$, see App. A.2 for a detailed calculation. The transformation, which can be regarded as a rotation around the z axis in a combined electron-hole and real space, has brought angular symmetry to the system. Eigenstates of the $\alpha p_z\sigma_\varphi$ term in the non-rotated H_{BdG} have spins that depend on the φ coordinate and thus rotate around the wire. By the spin part

[10] More explicitly: $\mathcal{P}H_{\mathrm{BdG}}\mathcal{P}^{-1}\mathcal{P}\Psi_{m_J} = -H_{\mathrm{BdG}}\mathcal{P}\Psi_{m_J} = E_{m_J}\mathcal{P}\Psi_{m_J}$. The eigenstate $\mathcal{P}\Psi_{m_J} = \Psi_{-m_J}$ of H_{BdG} thus has the corresponding eigenenergy $E_{-m_J} = -E_{m_J}$.

[11] Schematically: $H_{\mathrm{BdG}}(z,r,\varphi)\Psi_{m_J}(z,r,\varphi) = E_{m_J}\Psi_{m_J}(z,r,\varphi)$,
$UH_{\mathrm{BdG}}(z,r,\varphi)U^\dagger U\Psi_{m_J}(z,r,\varphi) = E_{m_J}U\Psi_{m_J}(z,r,\varphi) \implies \tilde{H}_{\mathrm{BdG}}(z,r)\Psi_{m_J}(z,r) = E_{m_J}\Psi_{m_J}(z,r)$

of the transformation, $e^{-i\varphi\sigma_z/2}$, the eigenstate spins of the αp_z term have been rotated around the z axis with an angle equal to their φ coordinate and eigenstates to that part of the Hamiltonian now have all spins pointing in the same direction, parallel to the y axis. Similarly, the phase of the pairing potential is unwounded by the part $e^{-i\varphi n\tau_z/2}$ such that $\Delta(\boldsymbol{r}) = \Delta(r) \in \mathbb{R}$.

4.1 Hollow-cylinder model

The rotated Hamiltonian in Eq. (4.8) can be further simplified with a restriction of the radial part of the wave functions. This is done by describing the semiconducting core as an effective thin-wall hollow cylinder, corresponding to the conduction electrons in the semiconductor accumulating within the order of 10nm from the super-semi interface, i.e. $R_1 \to R_2$ [11, 28]. The motivation for this assumption is the intrinsic outpointing electric field which also led to the spin-orbit term in Eq. (4.1). The field corresponds to a quantum well potential term $V(r)\tau_z$ in the Hamiltonian[12] $\tilde{H}_{\text{BdG}}$ in Eq. (4.8) where $V(r)$ has a triangular shape with a minimum at $r = R_2$ as found in [28]. We assume this bending of the conduction band to be strong enough that the different radial modes are so well separated in energy compared to the relevant energy scale set by Δ that only the lowest-energy radial mode with energy ε_0 is occupied. In $\tilde{H}_{\text{BdG}}$ of Eq. (4.8) this is implemented by letting $\frac{p_r^2}{2m^*} + V(r) \to \varepsilon_0$ and $r \to R_2$ in the other terms containing r. That way we obtain the one-dimensional Hamiltonian

$$\tilde{H}_{m_J} = \left(\frac{p_z^2}{2m^*} - \mu_{m_J}\right)\tau_z + V_Z\sigma_z + A_{m_J} + C_{m_J}\sigma_z\tau_z + \alpha p_z\sigma_y\tau_z + \Delta(R_2)\tau_x. \tag{4.9}$$

Here we have introduced an effective chemical potential μ_{m_J}, an effective Zeeman field V_Z, A_{m_J}, and C_{m_J} defined as:

$$\begin{aligned}
\mu_{m_J} &= \mu - \frac{1}{8m^*R_2^2}(4m_J^2 + 1 + \phi^2) - \frac{\alpha}{2R_2}, \\
V_{\text{Z}} &= \phi\left(\frac{1}{4m^*R_2^2} + \frac{\alpha}{2R_2}\right) + B_{\text{Z}}, \\
A_{m_J} &= -\phi\frac{m_J}{2m^*R_2^2}, \\
C_{m_J} &= -m_J\left(\frac{1}{2m^*R_2^2} + \frac{\alpha}{R_2}\right),
\end{aligned}$$

where we have introduced the reduced flux $\phi = n - \Phi(R_2)/\Phi_0 = n - \tilde{\Phi}$ and $\mu = \mu(r = R_2), \alpha = \alpha(r = R_2)$. Furthermore, the unknown constant ε_0 is absorbed in the (renormalised) chemical potential: $\mu - \varepsilon_0 \to \mu$. The parameters μ_{m_J}, V_{Z}, and A_{m_J} can be tuned by varying the flux through the wire. We observe that V_{Z} contains a term proportional to n, meaning that a winding of the superconducting order parameter produces a Zeeman-like term that is non-zero even with a $g = 0$. The eigenstates of $\tilde{H}_{m_J}$ are still labelled by the angular quantum number, $\Psi_{m_J}(z)$. For now we will assume the nanowire to be of infinite length such that the spatial part of $\Psi_{m_J}(z)$ is the wave function for a free particle with momentum p_z. Thus the Hamiltonian is more conveniently written in momentum

[12] Actually in H_{BdG} Eq. (4.3), but the term is unaffected by the transformation with U in Eq. (4.7).

basis where $p_z = \frac{-i\partial}{\partial z}$ operators in Eq. (4.9) are replaced by the corresponding eigenvalues p_z, and $\tilde{H}_{m_J,p_z}$ is a matrix of scalars with four eigenvectors on the form

$$\tilde{\Psi}_{m_J,p_z} = \begin{pmatrix} u_{\uparrow,m_J,p_z} \\ u_{\downarrow,m_J,p_z} \\ v_{\downarrow,m_J,p_z} \\ v_{\uparrow,m_J,p_z} \end{pmatrix},$$

where u and v are the electron and hole amplitudes respectively, defining the quasiparticle excitations, and the momentum basis is

$$c_{m_J,p_z} = \begin{pmatrix} c_{\uparrow,m_J,p_z} \\ c_{\downarrow,m_J,p_z} \\ c^\dagger_{\downarrow,-m_J,-p_z} \\ -c^\dagger_{\uparrow,-m_J,-p_z} \end{pmatrix}. \tag{4.10}$$

We notice the following symmetry of the spectrum: $\mathcal{P}\tilde{H}_{m_J,p_z}\mathcal{P}^{-1} = -\tilde{H}_{-m_J,-p_z}$.[13] In Sec. 8 we will consider the finite full-shell nanowire. We remark the important aspect of the system geometry that the electron density and the chemical potential of the core are fixed by the materials and cannot be changed by applying a gate voltage since the semiconductor is completely screened by the superconductor.

As was found in Eq. (4.6), the $m_J = 0$ sector is special as it is the only one that supports MZMs. We therefore consider this special sector and choose $n = 1$, corresponding to $\tilde{\Phi} \in [0.5, 1]$ i.e. the first Little-Parks lobe. With $m_J = 0$, $A_0 = C_0 = 0$ and Eq. (4.9) reduces to the usual Majorana nanowire model created by Oreg et al. [1] and by Lutchyn et al. [2] (the Oreg-Lutchyn model). A system described by that model undergoes a transition between a trivial and a non-trivial topological quantum phase when the gap between zero energy and the nearest excitation energy level vanishes and reopens at zero momentum $p_z = 0$ [1, 2, 9]. The MZMs are quasiparticle excitations associated with the non-trivial phase [8, 9] and thus we are interested in an expression for the gap at $p_z = 0$, which can be found by squaring the Hamiltonian twice:

$$\tilde{H}^2_{m_J=0,p_z} - \left(\xi^2_{p_z} + V_{\mathrm{Z}}^2 + \alpha^2 p_z^2 + \Delta^2\right) = 2\xi_{p_z} V_{\mathrm{Z}} \sigma_z \tau_z + 2\xi_{p_z} \alpha p_z \sigma_y + 2V_{\mathrm{Z}} \Delta \sigma_z \tau_x,$$
$$\left(\tilde{H}^2_{m_J=0,p_z} - \left(\xi^2_{p_z} + V_{\mathrm{Z}}^2 + \alpha^2 p_z^2 + \Delta^2\right)\right)^2 = 4\xi^2_{p_z} V_{\mathrm{Z}}^2 + 4\xi^2_{p_z} \alpha^2 p_z^2 + 4V_{\mathrm{Z}}^2 \Delta^2,$$

$$E^2_{p_z} = \xi^2_{p_z} + V_{\mathrm{Z}}^2 + \alpha^2 p_z^2 + \Delta^2 \pm 2\sqrt{\xi^2_{p_z} V_{\mathrm{Z}}^2 + \xi^2_{p_z} \alpha^2 p_z^2 + V_{\mathrm{Z}}^2 \Delta^2},$$
$$E^2_{p_z=0} = \mu^2_{m_J=0} + V_{\mathrm{Z}}^2 + \Delta^2 \pm 2V_{\mathrm{Z}}\sqrt{\mu^2_{m_J=0} + \Delta^2} = \left(V_{\mathrm{Z}} \pm \sqrt{\mu^2_{m_J=0} + \Delta^2}\right)^2.$$

Here $\xi_{p_z} = \left(\frac{p_z^2}{2m^*} - \mu_{m_J=0}\right)$, $\Delta = \Delta(R_2) \approx |\tilde{\Delta}|$, and E_{p_z} is an eigenvalue of $\tilde{H}_{m_J=0,p_z}$. The solutions $E_{p_z=0} = V_{\mathrm{Z}} - \sqrt{\mu^2_{m_J=0} + \Delta^2}$ and $E_{p_z=0} = -V_{\mathrm{Z}} + \sqrt{\mu^2_{m_J=0} + \Delta^2}$ are the excitation levels closest to zero[14] and define the energy gap at $p_z = 0$; $|V_{\mathrm{Z}} - \sqrt{\mu^2_{m_J=0} + \Delta^2}|$.

[13] i.e. $\mathcal{P}$ relates eigenstates with opposite energy, momentum and angular quantum number: $\mathcal{P}\tilde{H}_{m_J,p_z}\mathcal{P}^{-1}\mathcal{P}\Psi_{m_J,p_z} = -\tilde{H}_{-m_J,-p_z}\mathcal{P}\Psi_{m_J,p_z} = E_{m_J,p_z}\mathcal{P}\Psi_{m_J,p_z}$. The eigenstates of $\tilde{H}_{-m_J,-p_z}$ are thus $\Psi_{-m_J,-p_z} = \mathcal{P}\Psi_{m_J,p_z}$ with eigenenergies $E_{-m_J,-p_z} = -E_{m_J,p_z}$.

[14] Here we are taking $V_{\mathrm{Z}} > 0$ for the sake of argument. For $V_{\mathrm{Z}} < 0$ the lowest excitation states would be the other two solutions to $E_{p_z=0}$.

Hence the transition between the trivial and non-trivial topological phase takes place when $V_{\mathrm{Z}}^2 = \mu_{m_J=0}^2 + \Delta^2$ and by tuning the magnetic flux through the cylinder such that $|V_{\mathrm{Z}}| > \sqrt{\mu_{m_J=0}^2 + \Delta^2}$, the system is in the non-trivial phase. That an Oreg-Lutchyn model with $|V_{\mathrm{Z}}| > \sqrt{\mu_{m_J=0}^2 + \Delta^2}$ does indeed describe a system in the non-trivial topological phase can be seen by calculating the topological invariant (or Majorana number). For a 1-dimensional system described by the Hamiltonian $H(p_z)$ this is [8]

$$\mathcal{Q} = \mathrm{sgn}\left(\mathrm{Pf}(B(p_z = 0))\,\mathrm{Pf}(B(p_z = \infty))\right). \tag{4.11}$$

Here $B(p_z)$ is $H(p_z)$ transformed into Majorana basis; $H(p_z) \to iB(p_z)$, fulfilling $B^\dagger(p_z) = -B(p_z) = B^T(-p_z)$ where T denotes transpose. Pf is the Pfaffian operator:

$$\mathrm{Pf}(B) = \frac{1}{2^N N!} \sum_{\sigma \in S_{2N}} \mathrm{sgn}(\sigma) B_{\sigma(1)\sigma(2)} \dots B_{\sigma(2N-1)\sigma(2N)}, \tag{4.12}$$

where $2N$ is the dimensionality of B and S_{2N} is the set of all permutations of $2N$ elements [8]. The invariant $\mathcal{Q} = \pm 1$ distinguishes between the trivial and the non-trivial phase. Which sign is associated with e.g. the trivial phase is determined by taking $\mathcal{Q}$ in a limit which is known to be trivial. Writing the fermion operator as $c_\uparrow = (\gamma_{\uparrow,a} + i\gamma_{\uparrow,b})/2$, the transformation of $\tilde{H}_{m_J=0,p_z}$ from the fermion basis in Eq. (4.10) to the Majorana basis $(\gamma_{\uparrow,p_z,a}, \gamma_{\uparrow,p_z,b}, \gamma_{\downarrow,p_z,a}, \gamma_{\downarrow,p_z,b})$ is

$$iB_{p_z} = D^{-1}\tilde{H}_{m_J=0,p_z}D = \frac{1}{2}\begin{pmatrix} 1 & 0 & 0 & -1 \\ -i & 0 & 0 & -i \\ 0 & 1 & 1 & 0 \\ 0 & -i & i & 0 \end{pmatrix} \tilde{H}_{m_J=0,p_z} \begin{pmatrix} 1 & i & 0 & \\ 0 & 0 & 1 & i \\ 0 & 0 & 1 & -i \\ -1 & i & 0 & 0 \end{pmatrix}.$$

It is most convenient to transform the different terms separately:

$$\begin{aligned} D^{-1}\tau_z D &= -\sigma_y\tau_0, \\ D^{-1}\sigma_z D &= -\sigma_y\tau_z, \\ D^{-1}\sigma_y\tau_z D &= -\sigma_y\tau_y, \\ D^{-1}\tau_x D &= \sigma_x\tau_y, \end{aligned}$$

whereby the Majorana basis Hamiltonian is

$$B_{p_z} = \begin{pmatrix} 0 & \xi_{p_z} + V_{\mathrm{Z}} & 0 & -i\alpha p_z - \Delta \\ -\xi_{p_z} - V_{\mathrm{Z}} & 0 & i\alpha p_z - \Delta & 0 \\ 0 & i\alpha p_z + \Delta & 0 & \xi_{p_z} - V_{\mathrm{Z}} \\ -i\alpha p_z + \Delta & 0 & -\xi_{p_z} + V_{\mathrm{Z}} & 0 \end{pmatrix}.$$

We see that this indeed fulfils the antihermitian conditions $B_{p_z}^\dagger = -B_{p_z} = B_{-p_z}^T$. From the prescription in Eq. (4.12) we can calculate

$$\mathrm{Pf}\left(B_{p_z}\right) = \frac{1}{8}\sum_{\sigma \in S_4} \mathrm{sgn}(\sigma) B_{p_z;\sigma(1),\sigma(2)} B_{p_z;\sigma(3),\sigma(4)} = \xi_{p_z}^2 - V_{\mathrm{Z}}^2 + \Delta^2.$$

As $p_z \to \infty$, $\mathrm{sgn}\left(\mathrm{Pf}\left(B_{p_z}\right)\right) = +1$. This means that the topological index is alone determined by

$$\mathcal{Q} = \mathrm{sgn}\left(\mu_{m_J=0}^2 - V_{\mathrm{Z}}^2 + \Delta^2\right),$$

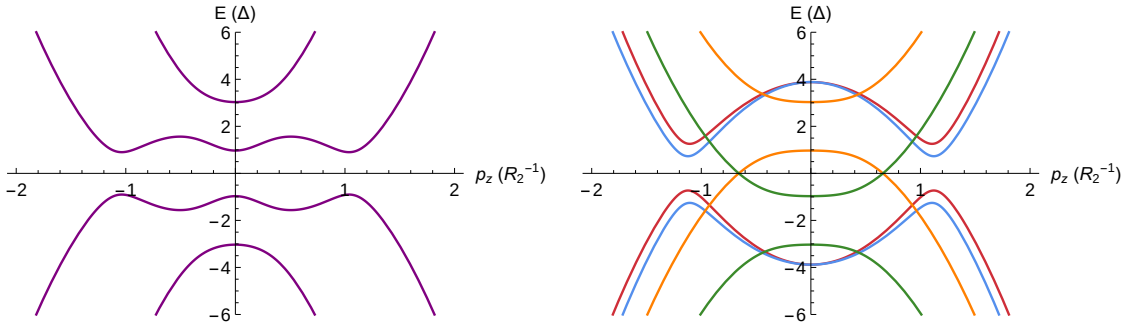

(a) All four excitation energy bands in the $m_J = 0$ sector for parameter values that ensure $|V_Z| > \sqrt{\mu_0^2 + \Delta^2}$. Colours indicate different quasiparticle excitations in $\tilde{H}_{m_J=0}$.

(b) Excitation energy bands close to zero for $m_J = 1$ (blue), $m_J = -1$ (red), $m_J = 2$ (green), and $m_J = -2$ (orange). The gap is open at $p_z = 0$ but closes at finite momentum in the $m_J = \pm 2$ sectors.

Figure 4.1: Excitation energy bands for quasiparticles in different m_J sectors, given in units of the induced gap Δ. The plots are made with parameter values $(\mu = 3\Delta, \alpha = 2\alpha_0)$, $\tilde{\Phi} = 1/2$, $n = 1$, and $R_2 = 0.5R_0$. Even though this is in the non-trivial topological phase for the $m_J = 0$ sector, the total system is gapless and therefore trivial due to the $m_J = \pm 2$ sectors. From these plots we also see that $E_{m_J,p_z} = -E_{-m_J,-p_z} = E_{m_J,-p_z}$.

and indeed we see that the index changes when $V_Z^2 = \mu_{m_J=0}^2 + \Delta^2$. We can find the index of the trivial phase by letting $\Delta \to \infty$ corresponding to an s-wave superconductor. Hence when $\mathcal{Q} = +1$ the system is in the trivial phase with no MZMs and when $|V_Z| > \sqrt{\mu_{m_J=0}^2 + \Delta^2}$ the index changes to $\mathcal{Q} = -1$ and the system is in the non-trivial phase.

Examples of the excitation energy bands for an Oreg-Lutchyn system are given in Fig. 4.1a which indeed shows a gapped spectrum. For notational convenience and in order to be able to compare results with the 2018 article by Lutchyn et al. [11], we use in this thesis the same values for the effective electron mass $m^* = 0.026m_e$ and for the induced gap $\Delta = 0.2$meV (which is close to that of the Al-shell) as in the article and introduce as well the radial unit $R_0 = 1/\sqrt{2m^*\Delta} \approx 85$nm and the spin-orbit coupling unit $\alpha_0 = \sqrt{\Delta/2m^*} \approx 17\text{meV} \cdot \text{nm}$. Throughout the thesis, calculations will be made for a wire of radius $R_2 \sim 0.5R_0 \approx 40$nm.

Including also the other sectors, $m_J \neq 0$, the problem becomes more complicated, partly because the eigenenergies of $\tilde{H}_{m_J \neq 0, p_z}$ are not possible to find analytically and therefore numerical methods have to be employed. Another complication is that, for parameters where the $m_J = 0$ sector is otherwise in the non-trivial topological phase, the excitation bands of the other sectors may be crossing zero energy and thereby close the gap of the total system. This is the case at $(\mu, \alpha) = (3\Delta, 2\alpha_0)$ where a band from the $m_J = 2$ sector and one from $m_J = -2$ both cross zero energy as shown in Fig. 4.1b. A requirement for the non-trivial phase is that the total excitation spectrum is gapped at all momenta and hence the higher sectors bring the system into the trivial phase if they cross zero energy. Therefore $|V_Z| > \sqrt{\mu_{m_J=0}^2 + \Delta^2}$ is no longer a condition that ensures non-trivial topology. Because the different m_J sectors are not mixed in $\tilde{H}_{m_J,p_z}$, each sector can be assigned a topological index $\mathcal{Q}_{m_J}$ like the one in Eq. (4.11) with a B_{m_J,p_z} that is

the Majorana basis transform of $\tilde{H}_{m_J,p_z}$. The total topological index is then $\Pi_{m_J}\mathcal{Q}_{m_J}$. However, since the spectrum possesses the symmetry $E_{m_J,p_z} = -E_{-m_J,-p_z} = -E_{-m_J,p_z}$, i.e. the spectrum has an an equal number of positive and negative energies for any p_z, we choose to instead combine the sectors m_J and $-m_J$ in one $B_{|m_J|,p_z}$ which can be rotated into the block matrix

$$B_{|m_J|,p_z} = \begin{pmatrix} 0_4 & E_{p_z} \\ -E_{p_z} & 0_4 \end{pmatrix}.$$

Here 0_4 is a 4-dimensional matrix of zeroes and E_{p_z} is a 4-dimensional matrix with the positive eigenenergies of sectors $m_J, -m_J$ on the diagonal and zeroes everywhere else. With $B_{|m_J|,p_z}$ written on this form, we have found that the Pfaffian is equal to the determinant of E_{p_z}. At $p_z = 0$, a change in parameters can cause one band from $E_{m_J,p_z=0} > 0$ to cross zero energy while a mirror band from $E_{-m_J,p_z=0} < 0$ will do the same (see e.g. Fig. 4.1b). As a consequence one of the elements in the matrix E_{p_z} changes sign and so will the Pfaffian of $B_{|m_J|,p_z=0}$. At $p_z = \infty$ the bands never cross zero energy since the energies in $B_{|m_J|,p_z}$ are dominated by the term p_z^2 and therefore do not change signs for any relevant variation in parameters and hence $\mathrm{sgn}\left(\mathrm{Pf}(B_{|m_J|,p_z=\infty})\right)$ remains the same. We therefore expect that the topological phase changes when the gap closes and reopens at $p_z = 0$ and that this can be used to define the phase transition instead of $\mathcal{Q}$. However, the spectrum should also be gapped at finite p_z for a well-defined non-trivial phase, so we should compare the gap closing at $p_z = 0$ to calculations of the overall gap E_{gap}. The eigenenergies of $\tilde{H}_{m_J,p_z=0}$ can be found analytically since spin is then a conserved quantum number:

$$E_{m_J,p_z=0,\sigma_z} = V_{\mathrm{Z}}\sigma_z + A_{m_J} \pm \sqrt{(\mu_{m_J} - C_{m_J}\sigma_z)^2 + \Delta^2}.$$

The m_J, σ_z band crosses zero energy at $p_z = 0$ when

$$\Lambda_{m_J,\sigma_z} = \Delta^2 + (\mu_{m_J} - C_{m_J}\sigma_z)^2 - (A_{m_J} + V_{\mathrm{Z}}\sigma_z)^2 = 0.$$

Hence the sign of Λ_{m_J,σ_z} should be the topological invariant $\mathcal{Q}_{m_J,\sigma_z}$. As before, we find out which sign belongs to which phase by taking a limit we know to be trivial e.g. $\phi = 0$ and find that $\mathrm{sgn}\left(\Lambda_{m_J,\sigma_z}\right) = 1$. We are to include gap closings of all the different m_J sectors while still avoid double counting crossings of mirrored bands. Since $\Lambda_{m_J,\sigma_z} = \Lambda_{-m_J,-\sigma_z}$ the zero-energy crossing of $m_J, -\sigma_z$ is already captured by $-m_J, \sigma_z$. Therefore, we cover all gap closings by only including one spin direction and the topological invariant for this system can therefore be expressed as

$$\mathcal{Q} = \mathrm{sgn} \prod_{m_J \in \mathbb{Z}} \left[\Delta^2 + (C_{m_J} - \mu_{m_J})^2 - (A_{m_J} + V_{\mathrm{Z}})^2\right] = \mathrm{sgn} \prod_{m_J \in \mathbb{Z}} \mathcal{Q}_{m_J}, \tag{4.13}$$

which is also what was found in Ref. [11]. In Fig. 4.2 the topological invariant is plotted as function of μ and α together with numerically calculated lines of $E_{\mathrm{gap}}(p_z = 0) = 0$. The purpose of that figure is both to show which areas of (μ, α) space, we predict to be non-trivial, but also that the numerically calculated phase transition lines agree well with the $\mathcal{Q}$ plot. This we will use later in cases where m_J is no longer a well defined quantum number and we cannot find an analytic expression for $\mathcal{Q}$. Note that according to Fig. 4.2 non-trivial domains can also exist outside the parabola defined by $|V_{\mathrm{Z}}| = \sqrt{\mu_{m_J=0}^2 + \Delta^2}$ where the isolated $m_J = 0$ sector is otherwise trivial.

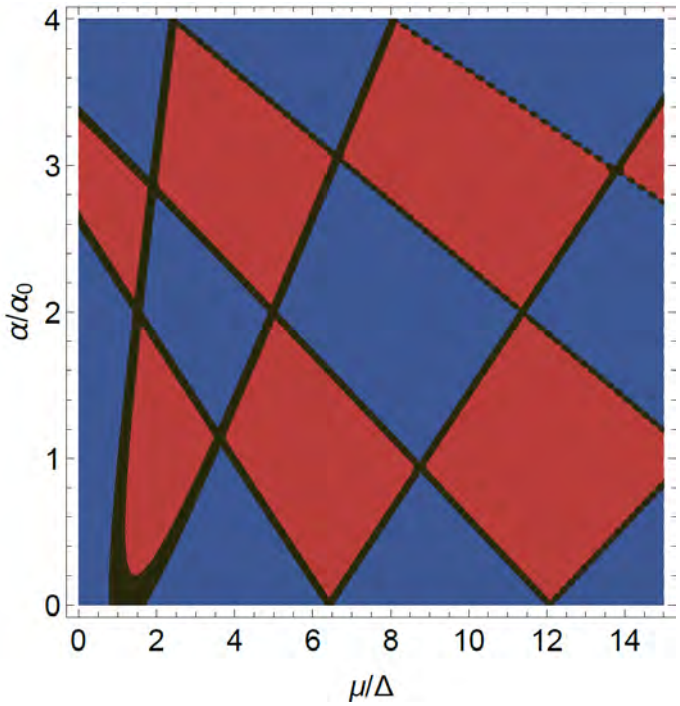

Figure 4.2: Red domains are where $\mathcal{Q} = -1$ and in blue domains $\mathcal{Q} = 1$. Black lines denote where the gap is closed at $p_z = 0$ according to numerical calculations. The plot is for parameter values $\tilde{\Phi} = 1/2$, $n = 1$, $R_2 = 0.5R_0$, and $B_{\mathrm{Z}} = 0$.

In Fig. 4.3 is shown a contour plot of the overall spectral gap E_{gap} in (μ, α) space. The blue to yellow colour scale shows the size of E_{gap} while the black lines are the same as in Fig. 4.2 indicating where $E_{\mathrm{gap}}(p_z = 0) = 0$. Taking these to be the transition lines, Fig. 4.3 can then be regarded as a topological phase diagram of the full-shell nanowire system described by $\tilde{H}_{m_J, p_z}$. Comparing with Fig. 4.2 we find that the gapped region including the point $(\mu = 2\Delta, \alpha = 1\alpha_0)$ is non-trivial and from there we can count our way to other non-trivial domains in a chessboard-like manner. However, as seen from Fig. 4.3, none of the other zones, which could be non-trivial, are gapped due to $m_J \neq 0$ states. As long as all $m_J \neq 0$ states are gapped, the topology of the system is controlled by the $m_J = 0$ sector like in the lower left corner of Fig. 4.3 with small μ and α. But when the higher m_J bands have crossed zero energy the spectrum remains gapless and therefore trivial for higher values of μ, α.

To see if it is possible to open a gap in some of the regions that according to the black phase transition lines should be non-trivial, we will try next to mix the bands that cross at zero energy and thereby open a gap.

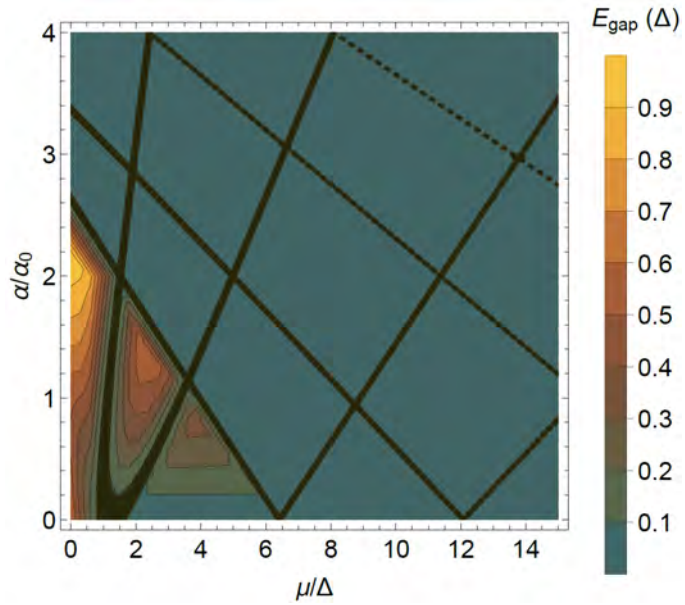

Figure 4.3: Contour plot of the gap in the spectrum of $\sum_{m_J} \tilde{H}_{m_J,p_z}$ in units of the induced pairing strength Δ as a function of the chemical potential μ and spin-orbit interaction strength α. The black lines indicate where the gap is closed at $p_z = 0$. For example, the parabola-shaped line starting in $(2.5\Delta, 4\alpha_0)$ and ending in $(8\Delta, 4\alpha_0)$ is where $|V_{\text{Z}}| = \sqrt{\mu_0^2 + \Delta^2}$ and separates the trivial phase from the non-trivial phase in the $m_J = 0$ sector. Inside the parabola $Q_{m_J=0} = -1$. The line from $(0\Delta, 2.6\alpha_0)$ to $(6.2\Delta, 0\alpha_0)$ is where bands from $m_J = \pm 2$ cross zero energy at $p_z = 0$. The line from $(0\Delta, 3.4\alpha_0)$ to $(12\Delta, 0\alpha_0)$ is where two other bands from $m_J = \pm 2$ cause $E_{\text{gap}}(p_z = 0) = 0$. At the line from $(2.5\Delta, 4\alpha_0)$ to $(15\Delta, 1.2\alpha_0)$ bands from $m_J = \pm 3$ cross zero energy at $p_z = 0$ and the line from $(8\Delta, 4\alpha_0)$ to $(15\Delta, 2.8\alpha_0)$ marks the gap closing due to two other bands from $m_J = \pm 3$. The numerical calculations include the bands $m_J = 0, \pm 1, \ldots, \pm 4$ since these are the ones that lie within a distance $\sim \Delta$ from zero energy for the selected range of μ and α. This we denote by $m_J^{\max} = 4$. The maximum value of α is $\alpha = 4\alpha_0 \approx 68.5$ meV nm. This order of magnitude is in accordance with measurements [7] although α is really the renormalised spin-orbit coupling strength. In this plot, the flux is $\tilde{\Phi} = \frac{1}{2}$, the winding is $n = 1$, and the radius of the semiconductor is $R_2 = 0.5R_0$. The Zeeman effect is not included here ($g = 0$) but for $g \sim -2$ the effect on the phase diagram is negligible (see App. B, Fig. B.10). This, together with larger values of g, will be discussed in Sec. 5.1.

5 Breaking rotational symmetry

Motivated by the results in [11] on breaking the angular symmetry with an anisotropic Rashba spin-orbit coupling, we now introduce deformations of the hollow-cylinder approximated nanowire core described by $\tilde{H}_{m_J,p_z}$ (Eq. (4.9)). When breaking the angular symmetry, different m_J sectors are coupled. This mixing might open a gap in the spectrum around zero energy at momenta where two bands of different m_J would otherwise cross. For example, by coupling the bands from $m_J = \pm 2$ shown in Fig. 4.1b, the non-trivially gapped domain in (μ, α) space (see Fig. 4.3) might be expanded. In general, new non-trivial domains may emerge in areas which are trivial in the cylindrical approximation due to a closed gap at finite p_z but with a $\mathcal{Q} = -1$ (Eq. (4.13)). Hence we set out to examine if deformations can be an advantage for reaching a stable non-trivial topological phase.

With deformations, the eigenstates no longer have a well-defined angular quantum number m_J and we cannot use the topological index in Eq. (4.13). Instead we distinguish the different phases by the numerically calculated lines of $E_{\text{gap}}(p_z = 0) = 0$ as argued in Sec. 4.1.

5.1 Altering the topological phase space with shape deformations

A deformation of the wire from a perfect cylinder will change the electric potential inside the semiconducting core. We include here periodic angular deformations causing an electric potential $V(\varphi) = V_0 \cos(l\varphi)\tau_z$ with a strength V_0 and where l is an integer.[15] Note that as intended, H_{BdG} and $V(\varphi)$ do not share eigenstates since $[J_z, V(\varphi)] \neq 0$. In the momentum basis c_{m_J,p_z} defined in Eq. (4.10) the potential reads $\pi V_0 \tau_z \delta_{(m_J - m'_J \pm l)}$ and we see that a deformation of the form $\cos(l\varphi)$ couples states with a difference in angular quantum number $|m_J - m'_J| = l$. In a combined basis of all m_J sectors $(\ldots, c_{m_J=-1,p_z}, c_{m_J=0,p_z}, c_{m_J=1,p_z}, \ldots)$ the case of $l = 1$ would correspond to the matrix

$$\begin{pmatrix} \ddots & & & & \\ & \tilde{H}_{-1,p_z} & \pi V_0 \tau_z & 0 & \\ & \pi V_0 \tau_z & \tilde{H}_{0,p_z} & \pi V_0 \tau_z & \\ & 0 & \pi V_0 \tau_z & \tilde{H}_{1,p_z} & \\ & & & & \ddots \end{pmatrix}. \tag{5.1}$$

Hence, if we want to use deformations to couple for example the bands from the $m_J = \pm 2$ sectors that cross each other at zero energy, we are to induce a $\cos(4\varphi)$ potential. Alternatively, a $\cos(2\varphi)$ deformation could also do the job by coupling the two states indirectly through the $m_J = 0$ sector.

Fig. 5.1 shows six contour plots of the spectral gap in the deformed nanowire in the parameter space (μ, α) for a "d-like" $\cos(2\varphi)$ potential, each plot corresponding to a different strength V_0. As in Fig. 4.3 the black lines indicate where the gap at $p_z = 0$ is closed and therefore separates trivial from non-trivial domains. From this series of gap plots, we see that the area in (μ, α) space of the initial non-trivial domain in the lobe containing the point $(\mu = 2.3\Delta, \alpha = 1.3\alpha_0)$ shrinks with increasing strength of the potential. Counting the number of transition lines crossed when moving from this lobe

[15] Here we do not include the effects of deformations on the spin-orbit coupling similar to what was done in Ref. [11].

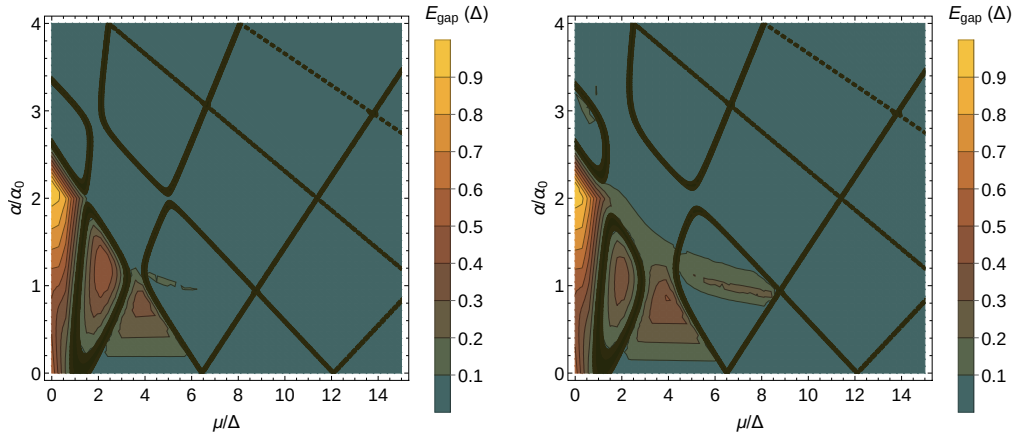

(a) $V_0 = 0.1\Delta$ **(b)** $V_0 = 0.2\Delta$

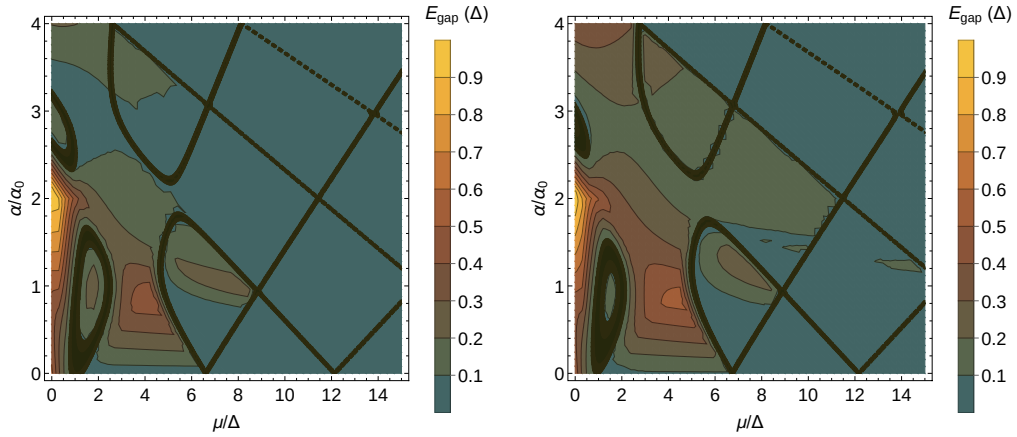

(c) $V_0 = 0.3\Delta$ **(d)** $V_0 = 0.4\Delta$

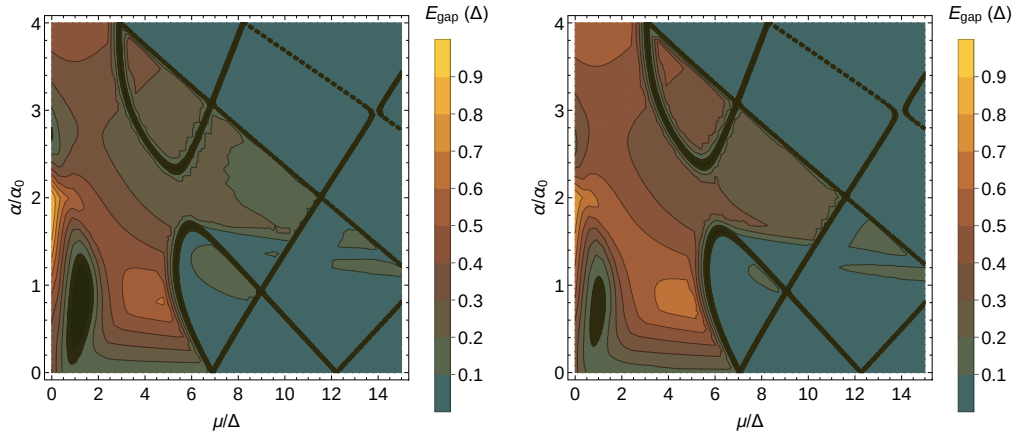

(e) $V_0 = 0.5\Delta$ **(f)** $V_0 = 0.6\Delta$

Figure 5.1: Contour plots of the spectral gap in units of Δ like the one in Fig. 4.3 but now including a d-like symmetry breaking potential $V_0 \cos(2\varphi)\tau_z$ with strengths from 0.1Δ to 0.6Δ through Figs. **(a)** to **(f)**. All other system parameters, used for this calculation, are the same as in Fig. 4.3.

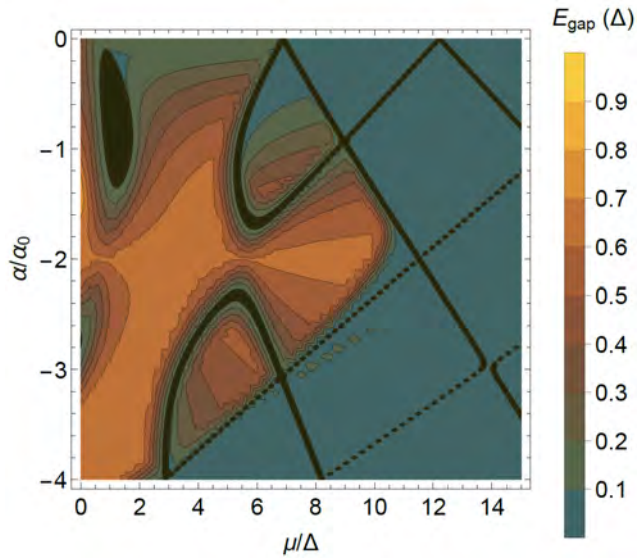

Figure 5.2: Gap contour plot in units of Δ with same system parameters and potential as in Fig. 5.1 with a strength $V_0 = 0.5\Delta$, but for negative values of the spin-orbit coupling parameter.

to another, we find that the gap opened in the area around $(\mu = 7\Delta, \alpha = 1.2\alpha_0)$ when $V_0 = 0.2\Delta$ is also non-trivial and reaches a maximum width and (μ, α) space area when $V_0 \approx 0.35\Delta$. However the gap is closed again when the strength is further increased. Finally, there is an interesting domain containing the point $(\mu = 5\Delta, \alpha = 3\alpha_0)$ where a non-trivial gap opens at $V_0 \approx 0.2\Delta$ and becomes increasingly wide, even though the area in (μ, α) space shrinks with larger V_0 (see Fig. B.2 in App. B for plots with $V_0 > 0.6\Delta$). We are thus lead to conclude that deforming the wire in a π-periodic shape does not lead to an enlarged range of values for the chemical potential and the spin-orbit coupling strength, for which the system is in the non-trivial topological phase. Furthermore, these domains are not very stable in the strength of the deformation. However, with deformations it is possible to move the domains in parameter space which could be useful since μ and α are fixed for a given wire.[16] Topological phase diagrams with a d-like potential have also been made for negative values of the spin-orbit coupling strength, $\alpha < 0$, and can be found in App. B, Fig. B.3. In these plots the black transition lines mirror the behaviour for $\alpha > 0$ although the gap contours do not. For instance, there is no non-trivial domain without perturbations whereas some are emerging as the geometry is changed, which also appears to be the case in [11]. At $V_0 = 0.5\Delta$ the induced non-trivial gap is as large as 0.5Δ (see Fig. 5.2). Therefore, if the interface properties cause an $\alpha < 0$, a $\cos(2\varphi)$ deformation can be beneficial if a full-shell nanowire with values of (μ, α) within the non-trivial domains exists.

From this point forward, a domain which e.g. includes the point $(\mu = 7\Delta, \alpha = 1.2\alpha_0)$ will be referred to as the $(7, 1.2)$ domain.

Introducing instead a "g-like" $\pi/2$-periodic deformation $V_0 \cos(4\varphi)$, the crossing $m_J = 2$ and $m_J = -2$ bands are coupled directly, the result of which is shown in Fig. 5.3. Comparing with Fig. 5.1 we observe that this is more efficient than the $\cos(2\varphi)$ potential

[16] Remember that the core cannot be gated due to superconducting shell.

for enlarging the non-trivial phase space. For example, even though the non-trivial gap in the $(7, 1.2)$ domain does not appear until $V_0 = 0.4\Delta$ and is more narrow than with the d-like potential, it is stable in the sense that it does not close with larger V_0 (see Fig. B.4 for phase diagrams with $V_0 > 0.6\Delta$). Regarding the non-trivial gap emerging at $V_0 = 0.2\Delta$ in the $(5, 3)$ domain, it covers a larger area in the non-trivial part of (μ, α) space than with the d-like deformation since it is stable to an increase in V_0 and does not shrink. Another advantage of the g-like potential is that the initial non-trivial $(2.3, 1.3)$ domain remains the same as the wire geometry changes. Hence, with a $\cos(4\varphi)$ deformation, one can expand the range of chemical potentials and spin-orbit coupling strengths that enable a non-trivial topological phase of the system. Unlike the d-like deformation, it has not been possible to open gaps for $\alpha < 0$ with this potential (see App. B, Fig. B.5).

Other $\cos(l\varphi)$ deformations have also been tested to determine if they would open non-trivial domains elsewhere in the (μ, α) space where other sectors than $m_J = \pm 2$ close the gap. With a "p-like" $\cos(\varphi)$ potential one essentially couples all the m_J sectors. As demonstrated in Fig. B.6, the only effect of such a "dent" in the wire is that the initial $(2, 1)$ domain is closed and it is no longer possible to be in the non-trivial phase. An "f-like" $\cos(3\varphi)$ potential has also been examined to see if it would open crossings between $m_J = \pm 3$ bands which happens at larger μ and α than for $m_J = \pm 2$ bands. According to the phase diagrams in Fig. B.7 this has no effect on the non-trivial domains in (μ, α) space. Nor has a combined "d+f-like" deformation $V_0(\cos(2\varphi) + \cos(3\varphi))$ shown be more favourable than a plain d-like potential in terms of enlarging the non-trivial phase space (see Fig. B.8).

In the experiments on full-shell nanowires by Vaitiekėnas et al. [10] the wires are in fact not cylindrical but hexagonal. To model this geometry we have also examined how a $\pi/3$-periodic deformation $V_0 \cos(6\varphi)$ affects the phase diagram. This couples m_J and m'_J sectors that differ by 6 and from Fig. B.9 we see that the energy correction is small since deformations as large as $1.5\Delta \cos(6\varphi)$ only minimally affects the phase diagram. We can therefore conclude that within this range of V_0, μ, and α, the hexagonal wires are well modelled by a cylindrical geometry.

We note that when including deformations in the model, higher m_J sectors become more relevant for the phase diagram with increasing strength V_0. For example is the phase diagram in Fig. 4.3 for the unperturbed system the same for $m_J^{\max} = 3$ and $m_J^{\max} = 4$ whereas the $m_J = \pm 4$ sectors have a significant effect for large (μ, α) when deformations are included.

5.1.1 Effects of Zeeman splitting on the phase diagram

Including the Zeeman energy in the numerical calculations of the topological phase diagram causes no substantial changes when the g-factor is of the order 1, neither in the unperturbed case nor with a d- or g-like deformation. This is demonstrated in Figs. B.10 and B.13 where $g = -2$. When g is of the order 10 the Zeeman effect has a more pronounced influence on the spectrum. In Fig. 5.4 are shown two phase diagrams which include the Zeeman energy with a g-factor of -12. In Fig. 5.4a the wire is cylindrical and in Fig. 5.4b the deformation is $0.4\Delta \cos(4\varphi)$. Comparing with Fig. 5.3 we see that the initial non-trivial domain is considerably smaller than without the Zeeman effect. In addition, the generation of the non-trivial $(5, 3)$ domain is impeded by the larger g-factor. For results with a d-like deformation and other values of the potential strength up to $V_0 = 0.5\Delta$ see Figs. B.11 and B.14. From this it appears that a g-factor larger than of

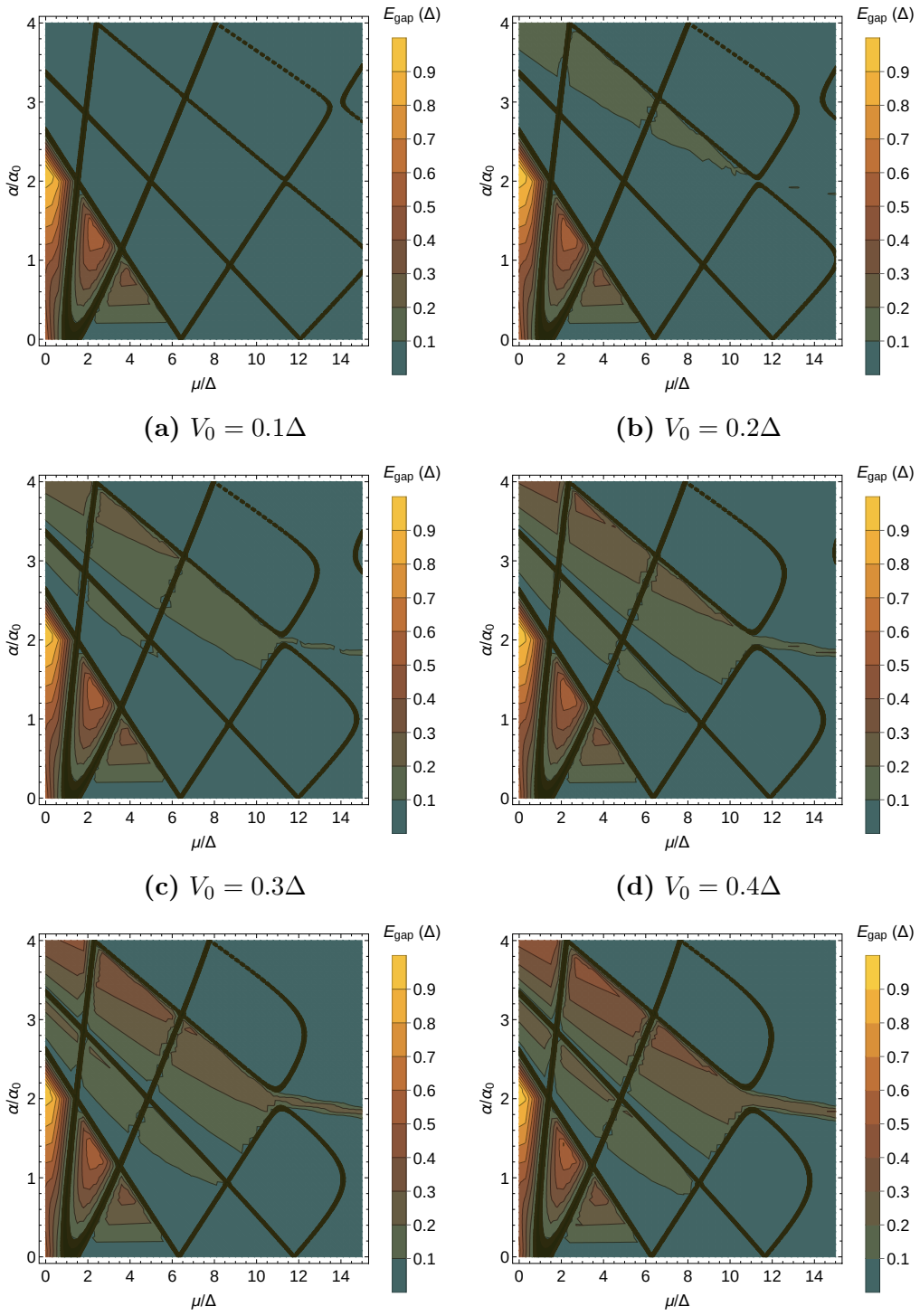

(a) $V_0 = 0.1\Delta$ **(b)** $V_0 = 0.2\Delta$

(c) $V_0 = 0.3\Delta$ **(d)** $V_0 = 0.4\Delta$

(e) $V_0 = 0.5\Delta$ **(f)** $V_0 = 0.6\Delta$

Figure 5.3: Gap contour plots in units of Δ for the full-shell nanowire system described by $\tilde{H}_{m_J,p_z}$ with an applied "g-like" symmetry breaking potential $V(\varphi) = V_0 \cos(4\varphi)$. System parameters used for the calculations are: $\tilde{\Phi} = \frac{1}{2}$, $n = 1$, $R_2 = 0.5R_0$, $B_{\text{Z}} = 0$, and $m_J^{\max} = 4$.

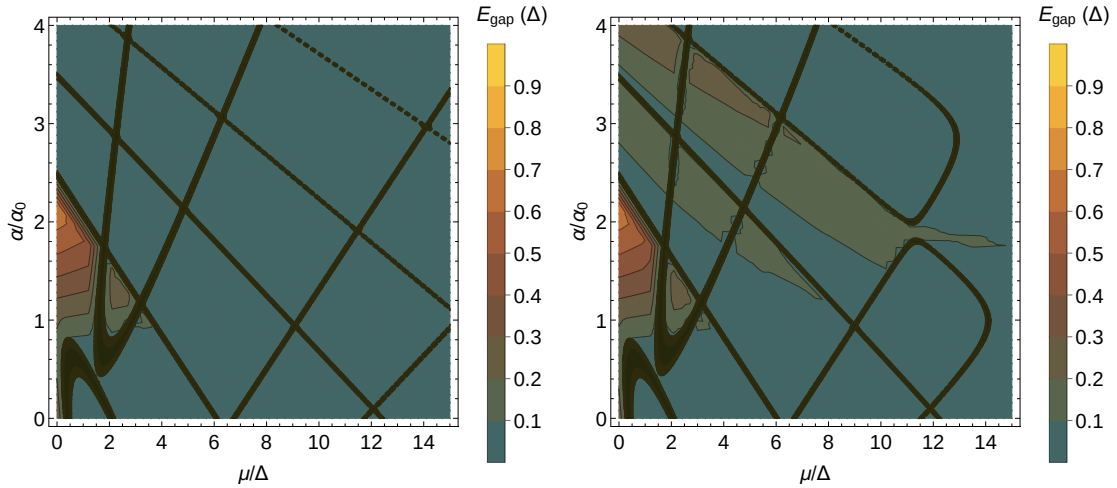

(a) $V_0 = 0\Delta$ **(b)** $V_0 = 0.4\Delta$

Figure 5.4: Gap contour plots in units of Δ with same system parameters and g-like potential as in Fig. 5.3, but with a non-zero Zeeman field $B_Z = g\mu_B B/2 \propto g = -12$.

the order 1 damages the chances of being in the non-trivial phase. This is unlike the traditional Oreg-Lutchyn scheme [1] where a large Zeeman energy caused by a large g drives the transition to the non-trivial topological phase $|V_Z| > \sqrt{\mu_0^2 + \Delta^2}$ as described in Sec. 4.1. Here we see that an increased Zeeman energy "pulls up" the black parabola which was the transition line of the $m_J = 0$ sector in the unperturbed system with $B_Z = 0$. Since the other transition lines do not move correspondingly, the non-trivial phase inside the parabola is diminished. With an even larger Zeeman energy the phase diagram is completely changed as seen in Fig. B.12 where $g = -60$. For InAs, which is the material used for the full-shell wires in [10], a bulk g-factor around -8 to -15 has been measured [7] and two-facet nanowires have shown g factors ranging from -2 up to -50 [5]. Therefore we conclude that the Zeeman energy should be included in the description of full-shell wires in a finite field unless the g factor is of the order 1. However, since we do not know the specific value of the wires on [10], we will carry out the analysis without the Zeeman energy.

5.2 Stability of the non-trivial topological phase

App. B contains a series of phase diagrams where the wire radius R_2, the flux $\tilde{\Phi}$, and the wire geometry are varied to test the stability of the non-trivial phase. For simplicity all these plots are made with a Zeeman energy $B_Z = 0$. Here we present the salient characteristics which demonstrate a phase diagram that is very sensitive to changes in R_2 and $\tilde{\Phi}$ and appears not to be stabilised by deformations.

Keeping the winding number $n = 1$ and the flux $\tilde{\Phi} = \frac{1}{2}$ as in the previous plots while increasing the radius by 4%, $R_2 = 0.5R_0 \to 0.52R_0$ changes both the position of the black phase transition lines and the gap contours. In Figs. B.15 and B.16 two such phase diagrams are made with potentials $V_0\cos(2\varphi)$ and $V_0\cos(4\varphi)$ respectively. Comparing with Figs. 4.3, 5.1, and 5.3 it is seen that the transition lines from "north-west" to "south-east" are pulled slightly down towards the origin for both deformations

while the $|V_Z| = \sqrt{\mu^2_{m_J=0} + \Delta^2}$ parabola is pulled upwards. This results in a non-trivial $(2.3, 1.3)$ domain that is smaller in both energy and area in (μ, α) space. For a d-like deformation the gap is closed at lower values of V_0 than with $R_2 = 0.5R_0$ while it is stable to g-like deformations. Regarding the other generated non-trivial domains, the only significant change is that with increasing $V_0 \cos(2\varphi)$, the $(5, 3)$ domain gap evolves faster with $R_2 = 0.52R_0$.

With a 4% decrease in radius $R_2 = 0.5R_0 \to 0.48R_0$ the change in phase diagrams is not surprisingly the exact opposite of what has just been described (see Figs. B.17 and B.18 for reference).

To test the stability of the non-trivial phase to changes in the magnetic field, the wire radius is now fixed at $R_2 = 0.5R_0$ while $\tilde{\Phi}$ is varied. We start by considering $\tilde{\Phi} = 0$, which implies $n = 0$ and the Hamiltonian is

$$\tilde{H}_{m_J}(\tilde{\Phi} = 0) = (\xi_{p_z,m_J} + C_{m_J}\sigma_z + \alpha p_z \sigma_y)\,\tau_z + \Delta\tau_x,$$

where $\xi_{p_z,m_J} = \left(p_z^2/2m^* - \mu_{m_J}\right)$ and $m_J \in \mathbb{Z} + \frac{1}{2}$. The eigenenergies are

$$E_{m_J} = \pm\sqrt{\left(\xi_{p_z,m_J} \pm \sqrt{C^2_{m_J} + \alpha^2 p_z^2}\right)^2 + \Delta^2},$$

and the energies closest to zero are $\pm\Delta$. Indeed numerical calculations confirm that the gap is trivial and Δ throughout the considered part of (μ, α) space (see Fig. B.1). This is in agreement with the full-shell experiments [10]. Phase diagrams for the cylindrical wire with different $\tilde{\Phi} \in [0, 2.1]$ are presented in Figs. B.19 and B.20. Several important points can be inferred from these results: **1)** The plots confirm that phase diagrams are the same for $\Phi(R_2)$ and $\Phi(R_2) + 2\Phi_0$. For example, the spectrum evolves identically when "scanning" through the first Little-Parks lobe as through the third lobe. This was expected as $\tilde{H}_{m_J,p_z}$ (Eq. (4.9)) only depends on flux through $\phi = n - \tilde{\Phi}$ (which runs from $\frac{1}{2}$ to $\frac{-1}{2}$ in every lobe) and through the parity of the lobe which determines if m_J is half-integer (even parity) or integer (odd parity). **2)** We observe that the phase diagrams are symmetric around the middle of each lobe i.e. around integer $\tilde{\Phi}$. This can also be inferred from the Hamiltonian since odd powers of ϕ only appear together with a factor m_J and we include both $\pm m_J$ in the calculations. **3)** According to the theory presented in Sec. 4, Eq. (4.6), there should be no non-trivial gaps in even Little-Parks lobes, where $m_J = \mathbb{Z} + 1/2$, for the unperturbed system. Fig. B.19 confirm this. **4)** At the boundary between Little-Parks lobes where $\tilde{\Phi} = \frac{\mathbb{Z}}{2}$ the topology phase diagram changes dramatically when switching $n \to n+1$ due to the different allowed values of m_J. **5)** The hollow-cylinder model predicts that within the examined parameters, a potential MZM cannot exist throughout the entire first Little-Parks lobe since only a trivial phase was observed from $\tilde{\Phi} = 0.8$ to $\tilde{\Phi} = 1.2$. This is not surprising as $V_Z \to 0$ at integer flux which in the Oreg-Lutchyn model [1, 2] corresponds to a trivial topological phase. If the model should have been able to explain the findings of [10], there should have been a point in the investigated parameter space that was trivially gapped in zeroth Little-Parks lobe, non-trivially gapped throughout the entire first lobe[17], and again trivially gapped in the second lobe. This was not found and hence the hollow-cylinder model does not describe

[17]The closing of the gap near odd half-integer flux quanta is not reproduced since we have not included pair-breaking effects in our calculations.

the zero-bias peak measured in [10] as a MZM.

However, it might be that deformations of the wire geometry could stabilise the diagrams such that a non-trivial gap would exist throughout the entire first Little-Parks lobe and possibly also in even lobes. We start examining this in the zeroth Little-Parks lobe at $\tilde{\Phi} = 0.4$ where $m_J = \mathbb{Z} + 1/2$. With deformations, m_J is no longer a conserved quantum number and the argument from the symmetrical case imposing no non-trivial states in even lobes no longer apply. Figs. B.21, B.22, and B.23 present phase diagrams for a wire deformed by $V_0\cos(\varphi)$, $V_0\cos(2\varphi)$, and $V_0\left(\cos(\varphi)+\cos(2\varphi)\right)$ respectively. The pure p-like deformation generates non-trivial gaps in a range of μ and α where, at $V_0 = 0$, $m_J = \pm 1/2$ and $m_J = \pm 3/2$ bands cross each other at zero energy. A potential $V_0\cos(\varphi)$ couples $m_J \pm 1/2$ directly and $m_J = \pm 3/2$ indirectly through higher order "scatterings". A pure d-like potential on the other hand, couples for example $m_J = 1/2$ to $m_J = 5/2$ and $m_J = -3/5$ which do not cross each other at zero energy and therefore does not open any non-trivial gaps. A combination of the two types of potentials only reduces the effect of the p-like deformation. We conclude that a non-trivial phase can be reached in the zeroth Little-Parks lobe with a p-like deformation.

Changing the flux to be well within the first lobe, $\tilde{\Phi} = 0.6$, and deforming the wire by $\cos(2\varphi)$ or $\cos(4\varphi)$, we obtain the phase diagrams in Figs. B.24 and B.25, respectively. Compared to the half-flux diagrams in Figs. 5.1 and 5.3, the initial non-trivial domain is smaller and for the d-like deformation it closes at a lower V_0. The generated non-trivial $(5, 3)$ gap, however, is larger at a given V_0 with $\tilde{\Phi} = 0.6$ although changing shape and size in (μ, α) space for both types of deformations. We recall that these effects are similar to those of increasing the radius at half flux. Hence with $V_0 > 0.3\Delta$ we can generate a non-trivial gap that is strong for both $\tilde{\Phi} = 0.5$ and $\tilde{\Phi} = 0.6$ as opposed to the initial gap which shrinks in the unperturbed case. For the unperturbed system we found that the phase diagram is symmetric around integer flux. Results for $\tilde{\Phi} = 1.4$ confirms that this is also true with deformations.

Nevertheless, between $\tilde{\Phi} = 0.8$ and $\tilde{\Phi} = 1.2$ neither a d- nor g-like deformation can keep the non-trivial domains from collapsing and hence the model predicts that no MZMs should exist around $\tilde{\Phi} = 1$.

Finally we try to combine all three types of variations and consider a $\cos(2\varphi)$-deformed wire of radius $R_2 = 0.52R_0$ penetrated by a flux $\tilde{\Phi} = 0.6$ (for the phase diagrams see Fig. B.28). Compared to the case $R_2 = 0.5R_0, \tilde{\Phi} = \frac{1}{2}$ in Fig. 5.1, the initial non-trivial domain and the generated $(7, 1.2)$ domain are smaller in energy and area for all V_0, whereas the gap generated in the $(5, 3)$ domain is larger although with a decreased (μ, α) area. This is not surprising since the shift in radius and flux separately caused these changes which are now enhanced. Put differently the effect of increasing the radius at half flux is the same as at $\tilde{\Phi} = 0.6$ just as a system with radius $R_2 = 0.52R_0$ evolves in the same way from $\tilde{\Phi} = \frac{1}{2}$ to $\tilde{\Phi} = 0.6$ as a system with $R_2 = 0.5R_0$. The same is true with a deformation $\cos(4\varphi)$ as displayed in a similar series of phase diagrams in Fig. B.29 which also combine the influences of increasing the radius or flux separately.

5.3 Conclusions on the effects of angular-symmetry-breaking deformations and on the stability of phase diagrams

In this section we have found that deformations of a full-shell nanowire of the form $\cos(4\varphi)$ can expand the range of μ and α, for which the wire is non-trivial, given that the reduced flux through the wire is $\phi \in [0.5, 0.2]$ or $\phi \in [-0.2, -0.5]$ and the radius $R_2 \sim 0.5R_0$. Such a deformation could therefore be an advantage since the chemical potential cannot be controlled by gating and the spin-orbit coupling strength is fixed by the materials. With a $\cos(2\varphi)$-deformation, it was also possible to generate new non-trivial domains although these were sensitive to the strength V_0 and the original $(2.3, 1.3)$ domain was closed. Deformation could also open non-trivial gaps in even Little-Parks lobes.

We have also found that the topological phase diagram in (μ, α) space is not symmetric around $\alpha = 0$ and that for a negative spin-orbit coupling strength there will be no non-trivial gap at $\tilde{\Phi} = 2\mathbb{Z} + 1/2$. A π-periodic deformation of the wire could however induce such a gap, in agreement with Lutchyn et al. [11]. Furthermore, the hexagonal geometry of the wire was found to be well modelled by a cylinder within the examined parameters, according to our calculations.

The Zeeman splitting energy was seen to have a significant effect on the phase diagram when the g-factor is larger than of the order 1 and should in that case be included in the model.

The topological phase diagrams have been found to be very sensitive to changes in the radius, the flux, and to some types of deformations. Hence according to the hollow-cylinder model, a MZM in a full-shell nanowire would be very fine-tuned in R_2 and (μ, α), which was not reported in [10]. Furthermore, the model predicts that a non-trivial phase should not exist throughout the first Little-Parks lobe since $V_\mathrm{Z} \to 0$ for $\phi \to 0$ and hence it does not explain the zero-bias peak measured in [10] as a MZM. This is true regardless of any difference in parameters between the simulations and the real experiment. In [11] they examined also a full-cylinder model where $R_1 \to 0$ (see Fig. 4.1). With that they were able to find parameters for which the density of states at the end of the wire was predicted to resemble the differential conductance in [10]. We conclude that the hollow-cylinder model, even including deformations, does not describe the experimental findings on full-shell wires as MZMs. But could it be that the model is still valid and provides another explanation of the measured zero-bias peak in the differential conductance? In the next section we will investigate this possibility and check if a trivial peak in the spectral function at zero energy exists in areas of the phase space where the gap is closed. This will be done for both the unperturbed system and in the case where a symmetry-breaking potential $V_0 \cos(n\varphi)$ is present.

6 A search for trivial zero-energy states

As we found in the previous section, the hollow-cylinder model in Eq. (4.9) predicts that a non-trivial phase should not exist throughout the first Little-Parks lobe. Hence, even with deformations the model does not interpret the measured zero-bias peak in differential conductance in [10] as signature of a MZM. Rather than just discarding the hollow-cylinder model, we try if it could instead explain the experimental findings as trivial effects, for example due to the symmetry of the spectrum around zero energy. Perhaps this gives a spectral function that is peaked at zero energy either in the unperturbed case or perhaps even with a deformation $\cos(n\varphi)$. That should lead to a zero-bias tunnelling signal since differential conductance measurements probe the spectral function of the system [27]. A trivial zero-energy peak in the spectral function could be "hiding" in the blue areas of the topology phase diagrams of the previous sections and we will check this possibility here.

6.1 Spectral functions

As mentioned, the eigenstates of the Hamiltonian $\tilde{H}_{m_J,p_z}$, labelled by the quantum numbers p_z and m_J, are not electrons but fermionic quasiparticle excitations. Examples of the energy bands were shown in Fig. 4.1. From the spectral functions of the different quasiparticles one can find the electron spectral function, which we will show in the following.

In Nambu space the spectral function is defined as $A(\omega) = -2\mathrm{Im}\left[G^{\mathrm{R}}(\omega)\right]$ where $G^{\mathrm{R}}(\omega)$ is the retarded Green's function matrix with the (i,j) component in the time domain being

$$G^{\mathrm{R}}_{ij}(m_J p_z t, m'_J p'_z t') = -i\Theta(t-t')\left\langle\left\{c_{m_J,p_z;i}(t), c^{\dagger}_{m'_J,p'_z;j}(t')\right\}\right\rangle. \tag{6.1}$$

Here $\Theta(t)$ is the Heaviside step function, $\{A,B\}$ denotes the anticommutator of the operators A and B, $\langle\cdot\rangle$ denotes thermal average, and $c_{m_J,p_z;i}$ is the i^{th} component of the Nambu spinor in Eq. (4.10). In order to calculate the retarded Green's function matrix we need to relate the Nambu spinor to the eigenspinors of $\tilde{H}_{m_J,p_z}$,

$$\chi_{m_J,p_z}(t) = \begin{pmatrix} \gamma_{\uparrow,m_J,p_z} e^{-iE_{m_J,p_z;1}t} \\ \gamma_{\downarrow,m_J,p_z} e^{-iE_{m_J,p_z;2}t} \\ \gamma^{\dagger}_{\downarrow,-m_J,-p_z} e^{iE_{m_J,p_z;3}t} \\ -\gamma^{\dagger}_{\uparrow,-m_J,-p_z} e^{iE_{m_J,p_z;4}t} \end{pmatrix}.$$

Here γ should not be confused with a MZM operator. The time dependence is simple as the Hamiltonian is diagonal in this basis. The eigenspinor χ_{m_J,p_z} is related to the electron operators in momentum space by the Bogoliubov transformation $U_{\mathrm{B}}(m_J,p_z)$

$$\begin{pmatrix} c_{\uparrow,m_J,p_z} \\ c_{\downarrow,m_J,p_z} \\ c^{\dagger}_{\downarrow,-m_J,-p_z} \\ -c^{\dagger}_{\uparrow,-m_J,-p_z} \end{pmatrix} = U_{\mathrm{B}}(m_J,p_z)\chi_{m_J,p_z}.$$

Hence Eq. (6.1) can be written as

$$G^{\mathrm{R}}_{ij}(m_J p_z t, m'_J p'_z t') = -i\Theta(t-t')\sum_{l,l'}\left\langle U_{\mathrm{B};i,l}(m_J,p_z)U^*_{\mathrm{B};j,l'}(m'_J,p'_z)\{\chi_{m_J,p_z;l}(t),\chi^\dagger_{m'_J,p'_z;l'}(t')\}\right\rangle$$
$$= -i\Theta(t-t')\sum_{l} U_{\mathrm{B};i,l}(m_J,p_z)U^*_{\mathrm{B};j,l}(m_J,p_z)e^{-s(l)iE_{m_J,p_z;l}(t-t')}.$$

Here i,j,l,l' are indices in Nambu basis. In the time exponential, we have introduced the sign function

$$s(l) = \begin{cases} +1, & \text{for } l = 1,2 \\ -1, & \text{for } l = 3,4. \end{cases} \tag{6.2}$$

Fourier transforming to frequency space we obtain

$$G^R_{ij}(m_J,p_z,\omega) = -i\int_{-\infty}^{\infty} dt\ \Theta(t)e^{i(\omega+i\eta)t}\sum_l U_{\mathrm{B};i,l}(m_J,p_z)U^*_{\mathrm{B};j,l}(m_J,p_z)e^{-s(l)iE_{m_J,p_z;l}(t-t')}$$
$$= \sum_l \frac{U_{\mathrm{B};i,l}(m_J,p_z)U^*_{\mathrm{B};j,l}(m_J,p_z)}{\omega - s(l)E_{m_J,p_z;l} + i\eta},$$

where we have introduced the positive infinitesimal $\eta = 0^+$. The (i,j) component of the spectral function for the state $|m_J,p_z\rangle$ is $A_{ij}(m_J,p_z,\omega) = -2\mathrm{Im}\left[G^R_{ij}(m_J,p_z,\omega)\right]$ and the sum of all these is the total spectral function:

$$A_{ij}(\omega) = -2\sum_{m_J,p_z}\mathrm{Im}\left[G^R_{ij}(m_J,p_z,\omega)\right]$$
$$= 2\pi\sum_{p_z,m_J,l} U_{\mathrm{B};i,l}(m_J,p_z)U^*_{\mathrm{B};j,l}(m_J,p_z)\delta(\omega - s(l)E_{m_J,p_z;l}). \tag{6.3}$$

Here we see that the spectral function is a weighted sum of delta functions in the eigenenergies, which are the spectral functions of the quasiparticles. For later use we mention that the trace of $A(\omega)$ is

$$\mathrm{Tr}[A(\omega)] = 2\pi\sum_{p_z,m_J,l}\sum_i U^\dagger_{\mathrm{B};l,i}(m_J,p_z)U_{\mathrm{B};i,l}(m_J,p_z)\delta(\omega - s(l)E_{m_J,p_z;l})$$
$$= 2\pi\sum_{p_z,m_J,l}\mathbb{I}_{l,l}\delta(\omega - s(l)E_{m_J,p_z;l}), \tag{6.4}$$

which is the total spectral function of all the quasiparticle states and only states the basis invariance of the trace.

The density of states at a given energy ω, $D(\omega)$, which is associated with the spectral function [27], is related to the flatness of the band at that particular energy; the flatter the band, the more momentum states can "fit in". This can be expressed as $D(\omega) = dN(\omega)/d\omega \propto \left(\frac{\partial\omega}{\partial p_z}\right)^{-1}$ where $N(\omega)$ is the number of states with energy ω. Hence if the dispersion is flat around some energy ω_0 for a range of p_z and bounded by steep bands on both sides, there will be a peak in the density of states at ω_0. Indeed we see from Eq. (6.3) that the spectral function depends on the slope of the bands via

$$\delta(\omega - E_{m_J,p_z;l}) = \sum_i \frac{\delta(p_z - p_{z,i})}{\mathrm{Abs}\left[\left(\frac{\partial E_{m_J,p_z;l}}{\partial p_z}\right)\Big|_{p_z=p_{z,i}}\right]}, \tag{6.5}$$

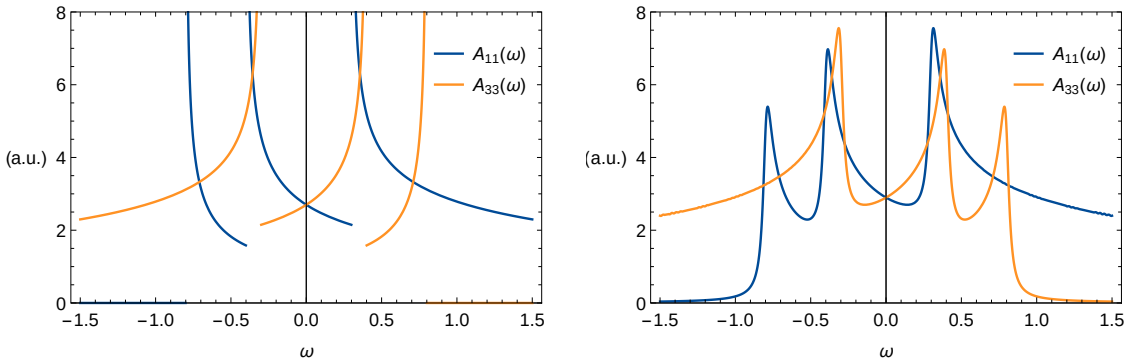

(a) Exact calculation. **(b)** Normalised sum of Lorentzians.

Figure 6.1: Diagonal elements of the spectral function for the system in Eq. (6.6) with $\mu_1 = -0.3, \mu_2 = 0.4$, and $\mu_3 = 0.8$, demonstrating the applicability of the approximation of a delta function by a Lorentzian with $\Gamma = 0.05$.

where $p_{z,i}$ are the roots of $\omega = E_{m_J,p_z;l}$.

In order to calculate the spectral function in Eq. (6.3) numerically, the delta function is replaced by a Lorentzian of full width at half maximum Γ:

$$\delta(\omega - s(l)E_{m_J,p_z;l}) \to \frac{\Gamma/2\pi}{(\omega - s(l)E_{m_J,p_z;l})^2 + (\Gamma/2)^2}.$$

To illustrate the accuracy of the numerical method we compare the exact solution to the spectral function for a simple set of energy bands with one calculated as a sum of Lorentzians over a discretised set of the same energies. The Hamiltonian of the example system has the diagonal form

$$H_n(k) = \xi_n(k)\sigma_0\tau_z = \left(\frac{k^2}{2m} - \mu_n\right)\sigma_0\tau_z, \qquad n \in \mathbb{N}, \tag{6.6}$$

in the basis $\Psi_{n,k} = (c_{\uparrow,n,k}, c_{\downarrow,n,k}, c^\dagger_{\downarrow,n,-k}, -c^\dagger_{\uparrow,n,-k})$. The retarded Green's function is that of a free particle

$$G^0_{ij}(n,k,\omega) = \frac{\delta_{ij}}{\omega - \xi_{n;i}(k) + i\eta},$$

where $\xi_{n;i}(k) = s(i)\xi_n(k)$ with $s(i)$ defined in Eq. (6.2). For clarity, we just work in units where $m = 1/2$ and $[\omega] = [\mu_n] = [k^2] = 1$ in this example. With $L = 1$ being the length of the system and $\omega = \xi_{n;i}(k_l)$, the total spectral function is

$$\begin{aligned} A_{ij}(\omega) &= -2\mathrm{Im}\left[\sum_{n,k} G^0_{ij}(n,k,\omega)\right] = -2\frac{L}{2\pi}\mathrm{Im}\left[\sum_n \int_{-\infty}^{\infty} dk \frac{\delta_{ij}}{\omega - \xi_{n;i}(k) + i\eta}\right] \\ &= \delta_{ij}\sum_n \int_{-\infty}^{\infty} dk\ \delta(\omega - \xi_{n;i}(k)) = \delta_{ij}\sum_n \int_{-\infty}^{\infty} dk\ \sum_l \frac{\delta(k-k_l)}{\left|\frac{\partial \xi_{n;i}(k)}{\partial k}\right|_{k_l}} \\ &= \delta_{ij}\sum_n\sum_l \frac{m}{|k_l|} = \delta_{ij} m \sum_n \frac{2}{\sqrt{2m\,(s(i)\omega + \mu_n)}} = \delta_{ij}\sum_n \frac{\Theta(s(i)\omega + \mu_n)}{\sqrt{s(i)\omega + \mu_n}}. \end{aligned}$$

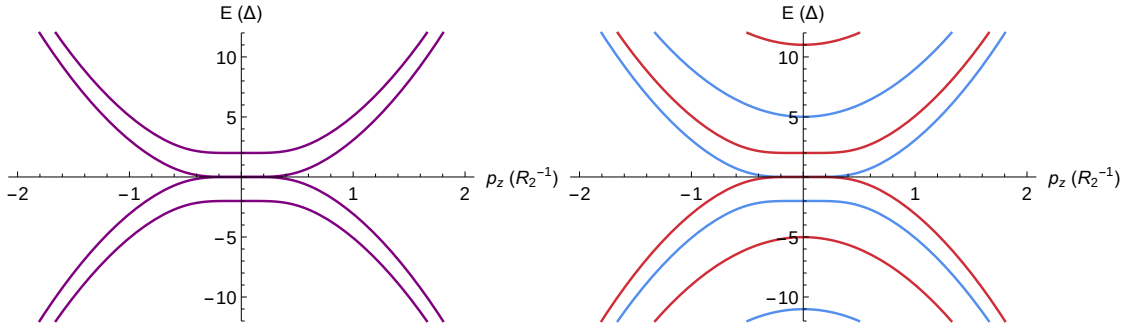

(a) All four bands in the $m_J = 0$ sector.

(b) All four bands for $m_J = 1$ (blue) and $m_J = -1$ (red).

Figure 6.2: Energy bands for quasiparticles in the $m_J = 0, \pm 1$ sectors. For $m_J = 0$ two bands are flattened at $E = 0$ around $p_z = 0$, and for $m_J = \pm 1$ it is only one of the bands. The plots are for $\tilde{\Phi} = 0.5$, $n = 1$, $R_2 = 0.5R_0$, and $(\mu = 1.3\Delta, \alpha = 0)$. For larger values of μ the bands remain at zero energy although at non-zero values of p_z. Notice that the $m_J = 0$ bands coincide with the two bands closest to zero energy from both $m_J = \pm 1$, which is in fact the case for all μ.

The electron components, $A_{11} = A_{22}$, and the hole components, $A_{33} = A_{44}$, are plotted in Fig. 6.1 together with the approximated solution which is a normalised sum of Lorentzians with eigenenergies $\xi_{n;i}(k)$ as roots over a discrete set of k's. The limits on the k-sum are determined by the considered range of ω. We see from Fig. 6.1 that the spectral function is well represented by the approximation.

6.2 Spectral functions for $\alpha = 0$

Considering the energy bands of $\tilde{H}_{m_J,p_z}$, the sectors $m_J = 0, \pm 1$ seem to "stick" to zero energy when $\tilde{\Phi} = 1/2$, $R_2 = 0.5R_0$, and $\alpha = 0$ for all values of μ beyond some critical value μ_c (see Fig. 6.2). As explained in Sec. 6.1, flattening of the bands at zero energy leads to electron and hole spectral functions A_{ii} that are peaked at zero energy with a hight that depends on the weight $U_{\mathrm{B};i,l}(m_J, p_z)U^*_{\mathrm{B};i,l}(m_J, p_z)$. We examine now the stability of this trivial peak to see if it could present an alternative explanation of a zero-bias peak in the differential conductance.

We have chosen to show the symmetric $\mathrm{Tr}[A(\omega)]$ instead of just the separate components. Information about these is lost in the more simple plots of $\mathrm{Tr}[A(\omega)]$. However, since tunnelling into a superconductor,[18] which is used to probe the spectral function, is symmetric in electrons and holes, it still makes sense to consider the trace.

In Fig. 6.3 $\mathrm{Tr}[A(\omega)]$ is plotted for a nanowire system without spin-orbit coupling, $\tilde{H}_{m_J,p_z}(\alpha = 0)$, for varying radii and flux at two values of μ. When $\tilde{\Phi} = 0.5$ and $R_2 = 0.5R_0$, the spectral function has a sharp peak at zero energy for all $\mu > \mu_c$, shown here in the examples $\mu = 2.1\Delta$ and $\mu = 4.1\Delta$ (for other values of μ, see App. B, Figs. C.1 and C.2). Since the peak is there for all $\mu > \mu_c$ one could think that this is a stable peak that can be used to interpret the measured zero-bias signal as a trivial effect of the spectrum, given that the spin-orbit coupling is insignificant in the wire. However, when inspecting

[18] The core at $r = R_2$ is essentially a superconductor due to the proximity effect.

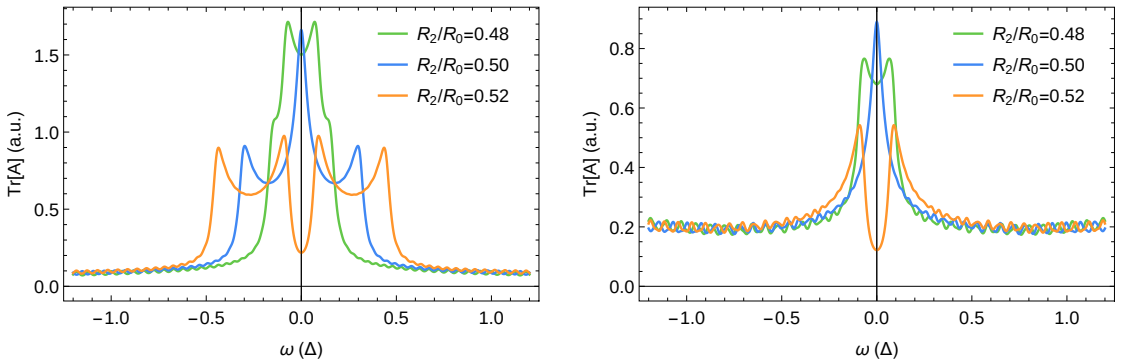

(a) $\mu = 2.1\Delta$, $\tilde{\Phi} = 1/2$ **(b)** $\mu = 4.1\Delta$, $\tilde{\Phi} = 1/2$

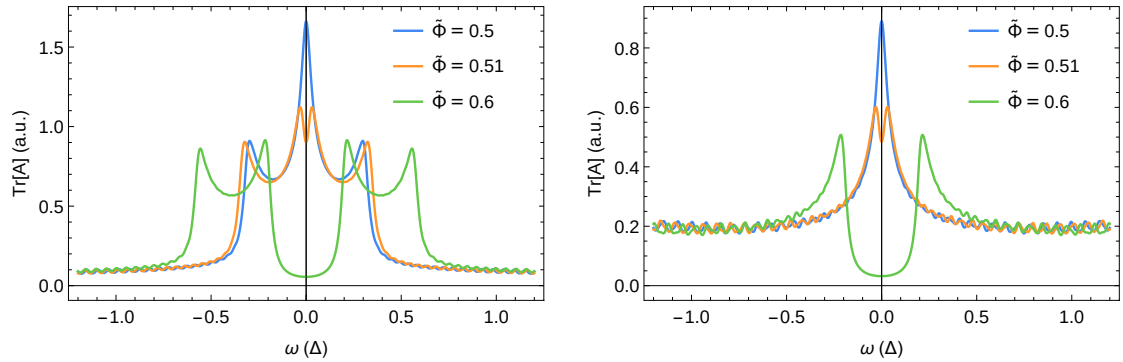

(c) $\mu = 2.1\Delta$, $R_2 = 0.5R_0$ **(d)** $\mu = 4.1\Delta$, $R_2 = 0.5R_0$

Figure 6.3: Tr$[A(\omega)]$ for varying radii (Figs. **(a)** and **(b)**) and varying flux (Figs. **(c)** and **(d)**). Shared parameters are: $\alpha = 0$, $\Gamma = 0.05$, and $m_J^{\max} = 4$. No Zeeman energy or deformation is included. The orange curves in Figs. (a) and (b) and the green curves in Figs. (c) and (d) do in fact all represent a gapped system even though they do not come all the way down to Tr $[A(\omega = 0)] = 0$. This discrepancy is due to the finite width Γ which has been chosen as to ensure smoothness of the spectral functions. Lower values of Γ show that the functions do represent a gapped system.

the curves in Figs. 6.3a and 6.3b for $R_2 = 0.52R_0$ and $R_2 = 0.48R_0$ we find that this peak is at least not stable to minor changes in the radius of just $0.02R_0 \sim 2\text{nm} \sim 4\%$. With a slight increase of the radius, the peak turns into a dip whereas a small decrease in the radius splits the peak into two. Likewise, changing the flux to $\tilde{\Phi} = 0.51$ or $\tilde{\Phi} = 0.6$ while keeping the radius at $R_2 = 0.5R_0$ also turns the peak into a dip as seen from Figs. 6.3c and 6.3d. Hence the trivial peak at zero energy is unstable when moving into the first Little-Parks lobe, and so does not provide an explanation for the measurements in [10].

To see if deformations could make the trivial peak stable we use the relation from Eq. (6.4) which shows that Tr$[A(\omega)]$ is equal to the total spectral function for all the quasiparticle states. If we assume that this also holds with mixing of m_J sectors we will not have to calculate complicated correlation functions where m_J is not a conserved quantum number. Instead we can obtain Tr $[A]$ by summing delta functions with eigenenergies of the $(4(2m_J^{\max}+1)) \times (4(2m_J^{\max}+1))$-dimensional type of matrices shown in Eq. (5.1) as poles. By that method we find that the trivial blue peak is not stable to d-like deformations, $\cos(2\varphi)$, as can be seen from Figs. 6.4a and 6.4c. A g-like deformation, $\cos(4\varphi)$, do

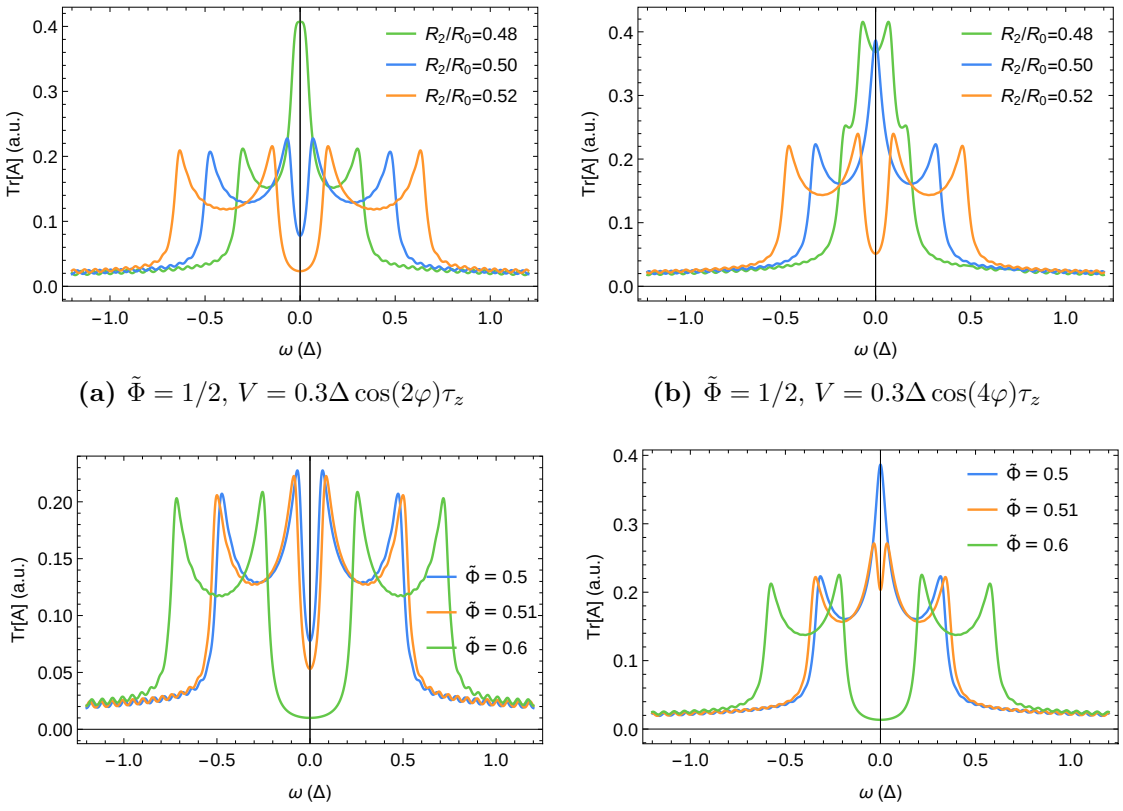

(a) $\tilde{\Phi} = 1/2$, $V = 0.3\Delta\cos(2\varphi)\tau_z$ **(b)** $\tilde{\Phi} = 1/2$, $V = 0.3\Delta\cos(4\varphi)\tau_z$

(c) $R_2 = 0.5R_0$, $V(\varphi) = 0.3\Delta\cos(2\varphi)\tau_z$ **(d)** $R_2 = 0.5R_0$, $V(\varphi) = 0.3\Delta\cos(4\varphi)\tau_z$

Figure 6.4: $\mathrm{Tr}[A(\omega)]$ for varying radii (Figs. **(a)** and **(b)**) and varying flux (Figs. **(c)** and **(d)**). Shared parameters are: $(\mu = 2.1\Delta, \alpha = 0)$, $\Gamma = 0.05$, $B_\mathrm{Z} = 0$, and $m_J^{\max} = 4$. As in Fig. 6.3 the orange curves in Figs. (a) and (b) and the green curves in Figs. (c) and (d) all represent a gapped system. Two different types of deformations are applied. For other μ and V_0 see Figs. C.3, C.4, and C.5 in App. B.

not lead to any significant changes in the spectral function for small potential strengths $V_0 \ll \Delta$. For $V_0 \sim \Delta$, the blue zero-energy peak for $\tilde{\Phi} = 1/2$ and $R_2 = 0.5R_0$ splits up.

In conclusion, the trivial peak is fairly stable under g-like deformations but this cannot prevent the instability to changes in the radius and flux. The chance that the performed experiment has exactly hit one such delicate point in parameter space is very small. In addition, this would also require the spin-orbit coupling parameter in InAs to be negligible. For these reasons we discard the idea that this trivial peak could explain the measured zero-bias conductance peak.

The reason for this unstable trivial peak is commensurable values of the reduced flux $\phi = 1/2$ and the cylinder radius $R_2 = 0.5R_0$. We see this by considering $\tilde{H}_{m_J=0,p_z}$ since $m_J = 0$ was one of the three sectors "sticking" to zero energy. Without any Zeeman effect or spin-orbit coupling the Hamiltonian reads

$$\tilde{H}_{m_J=0,p_z}(\alpha = B_\mathrm{Z} = 0) = \underbrace{\left(\frac{p_z^2}{2m^*} - \mu + \frac{1+\phi^2}{8m^*R_2^2}\right)}_{\xi_{p_z}}\tau_z + \underbrace{\frac{\phi}{4m^*R_2^2}}_{V}\sigma_z + \Delta\tau_x,$$

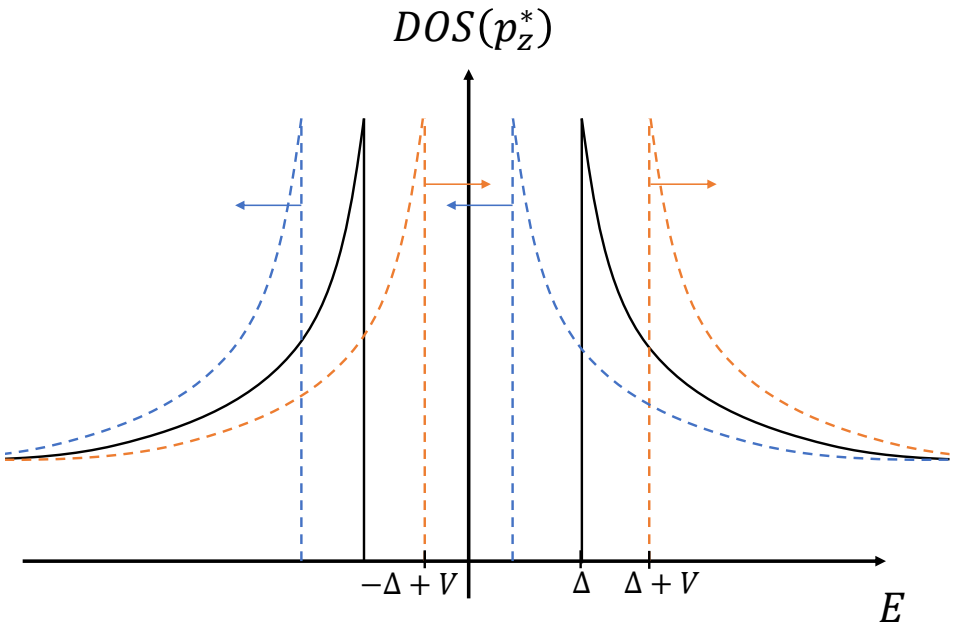

Figure 6.5: The effect of the flux-winding energy, V, on the density of states at p_z^*. Orange (blue) curves correspond to spin up (down). The two energy levels with $\Delta - V$ and $-\Delta + V$ approach zero as V is increased and when $\Delta = V$, there is a peak in the density of states at zero energy.

and the four eigenenergies are $E_{\sigma_z}(p_z) = \sigma_z V \pm \sqrt{\xi_{p_z}^2 + \Delta^2}$. When $\mu \geq \mu_c = \frac{1+\phi^2}{8m^* R_2^2}$ there will always be a p_z^* for which $\xi_{p_z^*} = 0$ and the energy is $E_{\sigma_z}(p_z^*) = \sigma_z V \pm \Delta$. The winding energy, V, diminishes the gap, and when $|V| \geq \Delta$ the gap is closed. For $\phi = 1/2$ and $R_2 = 0.5R_0 = 0.5\sqrt{2m^*\Delta}$, $V = \frac{1}{2m^* R_0^2} = \Delta$ and the gap is just closed at $p_z = p_z^*$ which means that there is a signal in the density of states at zero energy (see Fig. 6.5). For $R_2 = xR_0 < 0.5R_0$, $|V| = \frac{|\phi|}{4m^* x^2 R_0^2} > \Delta$ at the edges of the Little-Parks lobes where $|\phi| = \frac{1}{2}$, and the gap is closed from the edges until a flux where $|n - \tilde{\Phi}| = |\phi| < 4m^* x^2 R_0^2 \Delta = 2x^2$. The zero-energy peak in the density of states is then at $\phi = \pm 2x^2$ and in-between the spectrum is trivially gapped. When $R_2 > 0.5R_0$ there is a trivial gap in the $m_J = 0$ sector throughout the entire first lobe.

We have now seen why the trivial zero-energy peak in $\mathrm{Tr}[A]$ for $m_J = 0$ is not stable to changes in flux or radius, which in this case are equivalent. From Fig. 6.2 it is seen that the energy bands sticking to zero are the same for $m_J = \pm 1$ and $m_J = 0$. Hence the explanation for the "adhesive" behaviour in $m_J = \pm 1$ should be related to the one for $m_J = 0$. For different parameter values, the feature might also appear in other m_J sectors, although this has not been observed.

Instead of examining this part of (μ, α) space, where only an unstable trivial peak was found, we will now search for trivial peaks with a finite spin-orbit coupling.

6.3 Spectral functions for finite spin-orbit coupling

We now investigate whether there are domains in (μ, α) space with a closed gap that contain a stable and trivial zero-energy peak in the spectral function. The search for this

has here been restricted to $\tilde{\Phi} = 0.5$, $\tilde{\Phi} = 0.6$ and $R_2 = 0.5R_0$, $R_2 = 0.52R_0$. The gap contour plots from Secs. 4.1 and 5.1 have been used to choose points in (μ, α) space where such peaks could be concealed. The points are listed and plotted in App. C, Fig. C.6. To examine if there is a zero-energy peak in the density of states, the spectral function has been calculated for each of the points by summing weighted Lorentzian functions as explained in Sec. 6.1. As can be seen from Figs. C.7 to C.13, no zero-energy peak in the spectral function of the unperturbed system has been found for finite spin-orbit coupling in any combination of $R_2 = 0.5R_0$, $R_2 = 0.52R_0$ and $\tilde{\Phi} = 0.5$, $\tilde{\Phi} = 0.6$.

To see if they induce zero-energy peaks, we have included d- and g-like deformations, $V_0 \cos(2\varphi)$ and $V_0 \cos(4\varphi)$, to both commensurable values of radius and flux ($\tilde{\Phi} = 0.5, R_2 = 0.5R_0$) and non-commensurable values ($\tilde{\Phi} = 0.5, R_2 = 0.52R_0$), ($\tilde{\Phi} = 0.6, R_2 = 0.5R_0$). As we saw in Sec. 5, such deformations can close the gap in domains of the phase diagram that were initially gapped. We also examine if a zero energy peak in the density of states follows with this closure. That is why points in Fig. C.6 that are in a gapped domain in the unperturbed case have also been included in the list. The two values of the radius are to check if the peak is stable to changes in this, as was seen not to be the case with $\alpha = 0$. Like before, these spectral functions with deformations are made by summing delta functions as sketched in Eq. (6.4).

In Figs. C.14 to C.18 in App. C, where a d- or g-like deformation is applied, we observe trivial zero-energy peaks in the spectral functions for several of the points in Fig. C.6. These are, however, not stable to a small change in the cylinder radius R_2 and are also very sensitive to changes in the potential strength and the flux. Fig. 6.6 shows some examples of spectral functions with a peak at $\omega = 0$ that vanishes when changing R_2, $\tilde{\Phi}$, or V_0. For instance, with a deformation $0.31\Delta \cos(2\varphi)$ the spectral function in point $(\mu = 0.317\Delta, \alpha = 2.81\alpha_0)$ has a zero-energy peak for non-commensurable values of $\tilde{\Phi} = 1/2, R_2 = 0.52R_0$, but two peaks at finite energy for the commensurable values $\tilde{\Phi} = 1/2, R_2 = 0.5R_0$ (see Fig. 6.6a). A small change of the potential strength to $V_0 = 0.394\Delta$ merges the two finite-energy peaks in the spectral function for $\tilde{\Phi} = 1/2, R_2 = 0.5R_0$ into one zero-energy peak, but not one that lasts when moving into the first Little-Parks lobe (see Fig. 6.6c).

All of the trivial zero-energy peaks in Figs. C.14 to C.18 are just results of phase transition lines moving across the selected point in (μ, α) space as the deformation is increased, which we saw in Sec. 5. Since the energy bands are symmetric and smooth around $p_z = 0$, a gap closing at $p_z = 0$ always involves a flat band, meaning a zero-energy signal in the density of states as argued in Eq. (6.5). This is why none of the observed peaks are stable to changes in deformation potential, radius, or flux. As with $\alpha = 0$, this excludes such a trivial peak as a plausible explanation for the experimental results [10], also for finite spin-orbit coupling.

We make a final remark on this examination: In Figs. 5.3 and B.4, where a g-like deformation is included, the gapped $(2.3, 1.3)$ domain is stable under variation of V_0, which is an advantage for expanding the total non-trivial area in (μ, α) space. However, the spectral function in $(\mu = 2.3\Delta, \alpha = 1.3\alpha_0)$ with $V(\varphi) = V_0 \cos(4\varphi)$ shows that this only applies for $R_2 = 0.5R_0$ and not for $R_2 = 0.52R_0$ (see Figs. C.14e to C.14h). The initial gap, which is conserved under a g-like deformation for commensurable values of R_2 and $\tilde{\Phi}$, is in fact shrinking when the cylinder radius is increased by only 4%.

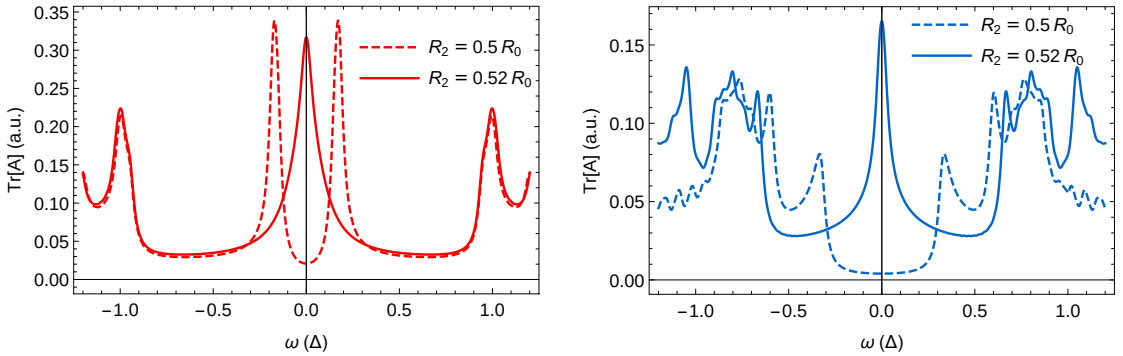

(a) $(\mu = 0.317\Delta, \alpha = 2.81\alpha_0)$, $\tilde{\Phi} = 1/2$ **(b)** $(\mu = 6.62\Delta, \alpha = 0.357\alpha_0)$, $\tilde{\Phi} = 1/2$

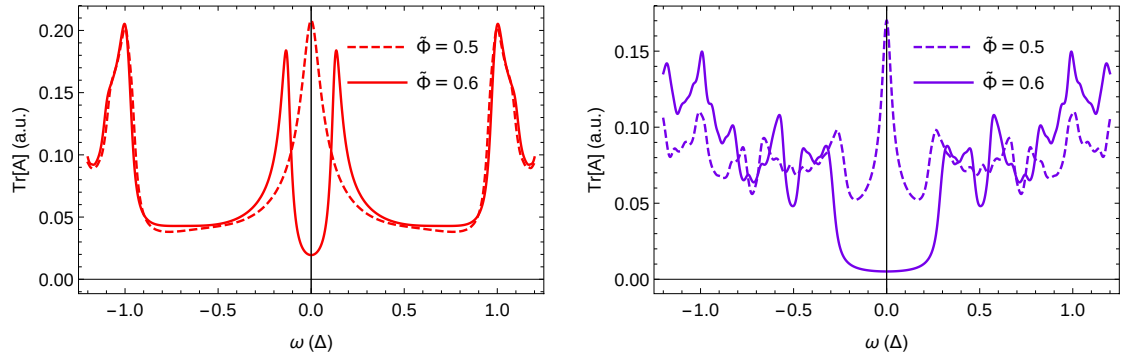

(c) $(\mu = 0.317\Delta, \alpha = 2.81\alpha_0)$, $R_2 = 0.5R_0$ **(d)** $(\mu = 5.16\Delta, \alpha = 3.38\alpha_0)$, $R_2 = 0.5R_0$

Figure 6.6: $\mathrm{Tr}[A(\omega)]$ in different points of (μ, α) space for a deformed wire. In **(a)** the resulting potential is $V(\varphi) = 0.31\Delta\cos(2\varphi)\tau_z$. **(b)** shows the spectral function with a potential $V(\varphi) = 0.84\Delta\cos(2\varphi)\tau_z$. For commensurable parameter values the spectrum is gapped with $\approx 0.3\Delta$, whereas the spectral function for $R_2 = 0.52R_0$ has a sharp peak at $\omega = 0$. **(c)** shows the spectral function at the same point as in (a) but with a potential $V(\varphi) = 0.394\Delta\cos(2\varphi)\tau_z$ and fixed radius. In **(d)** the potential is $V(\varphi) = 0.3\Delta\cos(4\varphi)\tau_z$.

6.4 Conclusions on the search for trivial peaks

To conclude, no stable trivial peaks that could explain the measured zero-bias signal in the differential conductance have been found. For some values of (μ, α), the spectral function has shown a peak at zero energy, but in all the cases this has been unstable to variations in the radius, flux, and deformation strength. Without spin-orbit coupling, the trivial zero-energy peak was an effect of commensurable values of the wire radius and the reduced flux. With finite spin-orbit coupling, zero-energy peaks were only observed on phase transition lines where the gap closes at $p_z = 0$ with flat bands. Hence this type of trivial zero-energy state is an unlikely explanation of the observed zero-bias conductance peak. We continue the investigation of the full-shell nanowire by considering next what effect impurities have on the spectrum.

7 Impurities in full-shell nanowires

In the nanowire fabrication process, defects could occur for example during the growth of the semiconducting core or in the corners of the hexagonal where the crystal structure of the superconductor layers on the different facets is broken. The disorder introduced by impurities becomes relevant at temperatures below a few Kelvin where most of the phonon degrees of freedom are frozen out [27]. In [11] they found that disorder in the superconducting shell could expand the non-trivial phase by coupling different m_J sectors like we tried in Sec. 5. Furthermore, impurities would lower the coherence length in the superconductor and could thereby bring the system out of the destructive regime. However, in [11] they used the full-cylinder model for their numerical calculations whereas here, we will continue to work with the hollow-cylinder model. In this section we will calculate the impact of impurities in the core on the spectral function by the use of Green's functions and the first-order Born approximation. We begin with a brief introduction to the theory of impurity scattering, based on Chapter 12 in Bruus and Flensberg [27], which will then be applied to the full-shell nanowire model.

We work with a model in which a number, N_{imp}, of identical impurities are randomly distributed in the material. We require that the density of impurities, $n_{\text{imp}} = N_{\text{imp}}/\mathcal{V}$, is small compared to the density of conduction electrons, $n_{\text{el}} = N_{\text{el}}/\mathcal{V}$, i.e. $n_{\text{imp}}/n_{\text{el}} \ll 1$, where $\mathcal{V}$ is the volume of the system. The electron-impurity scattering is elastic and the potential from an impurity at position $\boldsymbol{P}_j$ is on the form $u(\boldsymbol{r}-\boldsymbol{P}_j)$. It is assumed that this potential is zero outside some screening length from the impurity and has a characteristic finite strength, $\tilde{u}$, within the screening region. We require that $\tilde{u}$ is small compared to a characteristic energy E_0 of the system, $\tilde{u}/E_0 \ll 1$ [27]. A process with n scattering events of an electron on impurities can be expressed in the diagram

$\mathcal{G}^{(n)}_{\boldsymbol{k}'\boldsymbol{k}} =$ 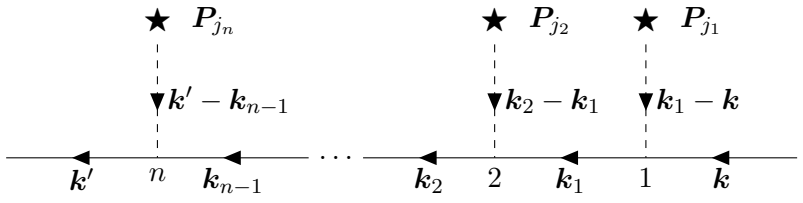

(7.1)

Here a full line  is the propagator $\mathcal{G}^0_{\boldsymbol{k}_i} = (ik_n - \xi_{\boldsymbol{k}_i})^{-1}$ of a free electron with momentum $\boldsymbol{k}_i$ and energy $\xi_{\boldsymbol{k}_i}$, and the dashed line with a star 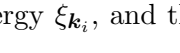 denotes the i^{th} scattering event on an impurity positioned at $\boldsymbol{P}_{j_i}$, in which momentum $\boldsymbol{q}_i = \boldsymbol{k}_i - \boldsymbol{k}_{i-1}$ is transferred. Notice that momentum is conserved at every vertex. j_i is an impurity index $\in \{1, 2, \ldots, N_{\text{imp}}\}$. The Matsubara Green's function in momentum space $\mathcal{G}_{\boldsymbol{k}'\boldsymbol{k}}$ is the full electron propagator and is the sum of all order contributions $\mathcal{G}^{(n)}_{\boldsymbol{k}'\boldsymbol{k}}, n = \{0, 1, \ldots\}$. For simplicity, the frequency argument is not written explicitly, but analytic continuation $ik_n \to \omega + i\eta$ will be performed at the end to obtain the retarded Green's function $\mathcal{G}^R(\omega)$. Furthermore, we do not include spin in this introduction. We can also

write Eq. (7.1) as

$$\mathcal{G}^{(n)}_{\boldsymbol{k}'\boldsymbol{k}} = \sum_{j_1\ldots j_n}^{N_{\rm imp}} \frac{1}{\mathcal{V}^{n-1}} \sum_{\boldsymbol{k}_1\ldots\boldsymbol{k}_{n-1}} e^{-i\left[(\boldsymbol{k}-\boldsymbol{k}_{n-1})\cdot\boldsymbol{P}_{j_n}+\ldots+(\boldsymbol{k}_1-\boldsymbol{k})\cdot\boldsymbol{P}_{j_1}\right]} \times \mathcal{G}^0_{\boldsymbol{k}'}u_{\boldsymbol{k}'-\boldsymbol{k}_{n-1}}\mathcal{G}^0_{\boldsymbol{k}_{n-1}}\ldots\mathcal{G}^0_{\boldsymbol{k}_2}u_{\boldsymbol{k}_2-\boldsymbol{k}_1}\mathcal{G}^0_{\boldsymbol{k}_1}u_{\boldsymbol{k}_1-\boldsymbol{k}}\mathcal{G}^0_{\boldsymbol{k}}, \tag{7.2}$$

where $u_{\boldsymbol{q}}$ is the Fourier transform of the real-space impurity potential:

$$u_{\boldsymbol{q}} = \int_{\mathcal{V}} d\boldsymbol{r}\; u(\boldsymbol{r}-\boldsymbol{P}_j)e^{-i\boldsymbol{q}\cdot\boldsymbol{r}}.$$

In order to calculate the full electron propagator we need to simplify the problem which we do by averaging over all the random, uncorrelated positions of the impurities - a process known as self-averaging.

$$\langle\mathcal{G}_{\boldsymbol{k}'\boldsymbol{k}}\rangle_{\rm imp} \equiv \delta_{\boldsymbol{k}\boldsymbol{k}'}\overline{\mathcal{G}}_{\boldsymbol{k}} = \delta_{\boldsymbol{k}\boldsymbol{k}'}\frac{1}{\mathcal{V}}\int d\boldsymbol{P}_1\;\frac{1}{\mathcal{V}}\int d\boldsymbol{P}_2\ldots\frac{1}{\mathcal{V}}\int d\boldsymbol{P}_{N_{\rm imp}}\;\mathcal{G}_{\boldsymbol{k}}, \tag{7.3}$$

Here overline is shorthand for impurity-averaged. Upon averaging over impurity positions, the system becomes homogeneous and translational invariance is restored. Therefore the impurity-averaged Green's function $\overline{\mathcal{G}}_{\boldsymbol{k}}$ is diagonal in $\boldsymbol{k}$. The $n^{\rm th}$ order contribution to the full propagator, $\mathcal{G}^{(n)}_{\boldsymbol{k}'\boldsymbol{k}}$, may involve any number of impurities p from 1 to n. A process with p impurities is suppressed by a factor $(n_{\rm imp}/n_{\rm el})^p$ and thus the importance of the different processes depends on how few impurities they involve, the one with all n scatterings on just a single impurity being the most important. Before performing the self-average of $\mathcal{G}^{(n)}_{\boldsymbol{k}'\boldsymbol{k}}$ we therefore rearrange the sum over impurity positions in Eq. (7.2) according to the number of impurities involved:

$$\begin{aligned}\sum_{j_1\ldots j_n}^{N_{\rm imp}} e^{-i\sum_{l=1}^n \boldsymbol{q}_l\cdot\boldsymbol{P}_{j_l}} &= \sum_{p_1}^{N_{\rm imp}} e^{-i(\sum_{\boldsymbol{q}_{l_1}\in Q}\boldsymbol{q}_{l_1})\cdot\boldsymbol{P}_{p_1}} \\ &+ \sum_{Q_1\cup Q_2=Q}\sum_{p_1,p_2}^{N_{\rm imp}} e^{-i(\sum_{\boldsymbol{q}_{l_1}\in Q_1}\boldsymbol{q}_{l_1})\cdot\boldsymbol{P}_{p_1}} e^{-i(\sum_{\boldsymbol{q}_{l_2}\in Q_2}\boldsymbol{q}_{l_2})\cdot\boldsymbol{P}_{p_2}} \\ &+ \sum_{Q_1\cup Q_2\cup Q_3=Q}\sum_{p_1,p_2,p_3}^{N_{\rm imp}} e^{-i(\sum_{\boldsymbol{q}_{l_1}\in Q_1}\boldsymbol{q}_{l_1})\cdot\boldsymbol{P}_{p_1}} e^{-i(\sum_{\boldsymbol{q}_{l_2}\in Q_2}\boldsymbol{q}_{l_2})\cdot\boldsymbol{P}_{p_2}} e^{-i(\sum_{\boldsymbol{q}_{l_3}\in Q_3}\boldsymbol{q}_{l_3})\cdot\boldsymbol{P}_{p_3}} \\ &+ \ldots\end{aligned} \tag{7.4}$$

The first term on the right hand side is the most important process where an electron scatters n times on the same impurity (which may be any of the $N_{\rm imp}$ existing ones) with scattering momenta $Q = \{\boldsymbol{q}_1, \boldsymbol{q}_2, \ldots, \boldsymbol{q}_n\}$. In the second term, two impurities are involved. All the scattering momenta in the subset Q_1 are associated with scattering on the impurity in $\boldsymbol{P}_{p_1}$ while the momenta in Q_2 are related to the impurity in $\boldsymbol{P}_{p_2}$. $Q_1 \cup Q_2 = Q$ denotes all possible unions of the two non-empty disjoint subsets that together span Q. The same argumentation applies for the higher order terms up to $p = n$. We have ignored here an error of the order $p/N_{\rm imp}$ originating from not restricting the position sums to ensure $\boldsymbol{P}_{p_1} \neq \boldsymbol{P}_{p_2} \neq \boldsymbol{P}_{p_3}$ etc. Instead we just establish them to be different since $p/N_{\rm imp} \ll 1$ for

the important terms. This enables us to perform the position average for the exponentials separately:

$$\frac{1}{\mathcal{V}}\int d\boldsymbol{P}_{p_i}\, e^{-i(\sum_{\boldsymbol{q}_{l_i}\in Q_i}\boldsymbol{q}_{l_i})\cdot\boldsymbol{P}_{p_i}} = \delta_{0,\sum_{\boldsymbol{q}_{l_i}\in Q_i}\boldsymbol{q}_{l_i}}.$$

This expresses that the sum of all scattering momenta on the same impurity must add to zero. Thus the self-average of Eq. (7.4) is

$$\left\langle \sum_{j_1\ldots j_n}^{N_\mathrm{imp}} e^{-i\sum_{l=1}^n \boldsymbol{q}_l\cdot\boldsymbol{P}_{j_l}} \right\rangle_\mathrm{imp} = \sum_{p=1}^{n}\left[\sum_{Q_1\cup\ldots\cup Q_p=Q}\prod_{i=1}^{p}\left(N_\mathrm{imp}\delta_{0,\sum_{\boldsymbol{q}_{l_i}\in Q_i}\boldsymbol{q}_{l_i}}\right)\right].$$

The factor N_imp is from the p_i sum. Combining this with Eq. (7.2), we can write the n^th order contribution to the impurity-averaged Green's function as

$$\begin{aligned}\overline{\mathcal{G}}^{(n)}_{\boldsymbol{k}} = \frac{1}{\mathcal{V}^{n-1}}\sum_{\boldsymbol{k}_1\ldots\boldsymbol{k}_{n-1}}\sum_{p=1}^{n}\sum_{Q_1\cup\ldots\cup Q_p=Q}\prod_{i=1}^{p}\left(N_\mathrm{imp}\delta_{0,\sum_{\boldsymbol{q}_{l_i}\in Q_i}\boldsymbol{q}_{l_i}}\right)\\ \times\,\mathcal{G}^0_{\boldsymbol{k}}u_{\boldsymbol{k}-\boldsymbol{k}_{n-1}}\mathcal{G}^0_{\boldsymbol{k}_{n-1}}\ldots\mathcal{G}^0_{\boldsymbol{k}_2}u_{\boldsymbol{k}_2-\boldsymbol{k}_1}\mathcal{G}^0_{\boldsymbol{k}_1}u_{\boldsymbol{k}_1-\boldsymbol{k}}\mathcal{G}^0_{\boldsymbol{k}}.\end{aligned} \tag{7.5}$$

The p constraints from the delta functions reduce the number of independent momentum vectors in the $\boldsymbol{k}$ sum to $(n-1)-p$. The p left-over factors of $\mathcal{V}$ are combined with the p factors of N_imp in $N_\mathrm{imp}/\mathcal{V} = n_\mathrm{imp}$.

The diagrammatic expansion of the impurity-averaged Green's function, with diagrams up to third order in number of scattering events written explicitly, is

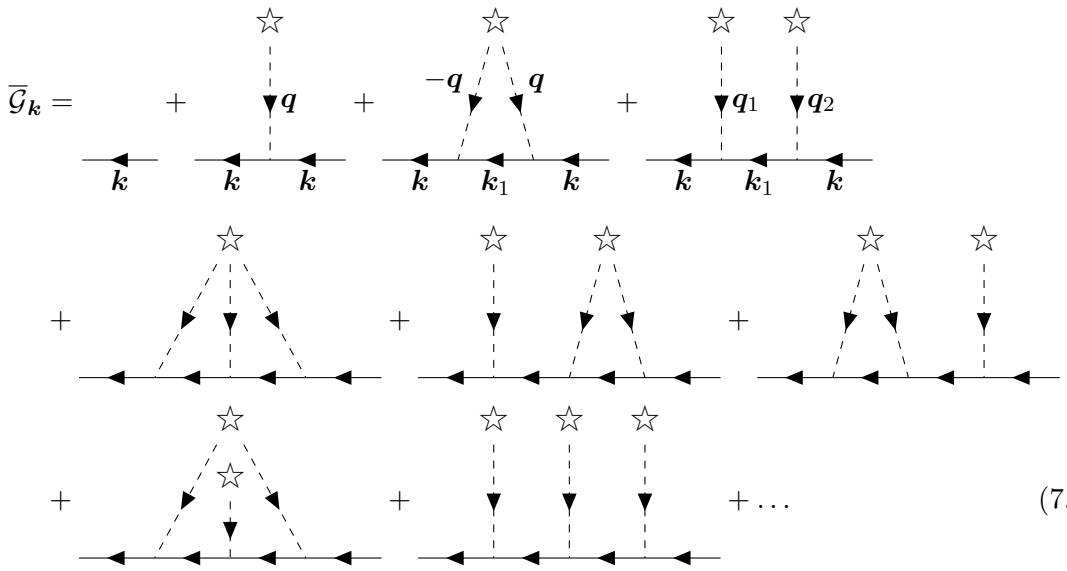

(7.6)

Here we have introduced the symbol ☆ for a position-averaged impurity that conserves the total momentum transfer, corresponding to a factor $n_\mathrm{imp}\delta_{0,\sum\boldsymbol{q}}$ in Eq. (7.5).  denotes a scattering event with momentum transfer $\boldsymbol{q}$ and amplitude $u_{\boldsymbol{q}}$. For clarity, we have not written momentum vectors on the third order terms. Within each order, the diagrams are arranged after the number of impurities involved. Since $\tilde{u}/E_0 \ll 1$, the importance of different diagrams is also controlled by how few scattering processes

they involve, e.g. the third diagram in Eq. (7.6) is larger than the fifth diagram. The impurity-averaged Green's function can also be expressed in terms of the self-energy[19] by the Dyson equation:

$$\overline{\mathcal{G}}_{\boldsymbol{k}} = \mathcal{G}^0_{\boldsymbol{k}} + \mathcal{G}^0_{\boldsymbol{k}}\Sigma_{\boldsymbol{k}}\overline{\mathcal{G}}_{\boldsymbol{k}} = \frac{1}{(\mathcal{G}^0_{\boldsymbol{k}})^{-1} - \Sigma_{\boldsymbol{k}}}. \tag{7.7}$$

The lowest-order approximation to the self-energy is in the second term in Eq. (7.6) which contains only one position-averaged impurity and one scattering event:

$\Sigma^{\mathrm{LOA}}_{\boldsymbol{k}} \equiv$ 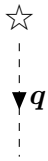 $= n_{\mathrm{imp}} u_{\boldsymbol{q}=0}.$

Inserting this into Eq. (7.7) only gives a constant shift of all the energies which can just be absorbed in the definition of the chemical potential:

$$\mathcal{G}^{R,\mathrm{LOA}}_{\boldsymbol{k}} = \frac{1}{\omega + i\eta - \xi_{\boldsymbol{k}} + n_{\mathrm{imp}} u_0}.$$

The simplest non-trivial diagram in the self-energy is the first-order Born approximation to $\Sigma_{\boldsymbol{k}}$ which is valid in the low-density and small-potential strength limit:

$\Sigma^{\mathrm{1BA}}_{\boldsymbol{k}} =$ 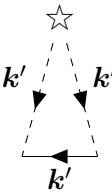 $= \frac{n_{\mathrm{imp}}}{\mathcal{V}} \sum_{\boldsymbol{k}'} u_{\boldsymbol{k}-\boldsymbol{k}'} \mathcal{G}^0_{\boldsymbol{k}'} u_{\boldsymbol{k}'-\boldsymbol{k}} = \frac{n_{\mathrm{imp}}}{\mathcal{V}} \sum_{\boldsymbol{k}'} |u_{\boldsymbol{k}-\boldsymbol{k}'}|^2 \mathcal{G}^0_{\boldsymbol{k}'},$

where it has been employed that $u_{-\boldsymbol{k}} = u^*_{\boldsymbol{k}}$ since the scattering potential in position space is real. If $\Sigma^{\mathrm{1BA}}_{\boldsymbol{k}}$ has an imaginary part, the poles of the corresponding $\mathcal{G}^{\mathrm{1BA}}_{\boldsymbol{k}}$ are in the complex plane and the propagator acquires a finite lifetime. In diagrammatic form it reads

$\mathcal{G}^{\mathrm{1BA}}_{\boldsymbol{k}} = \frac{1}{(\mathcal{G}^0_{\boldsymbol{k}})^{-1} - \Sigma^{\mathrm{1BA}}_{\boldsymbol{k}}} =$ 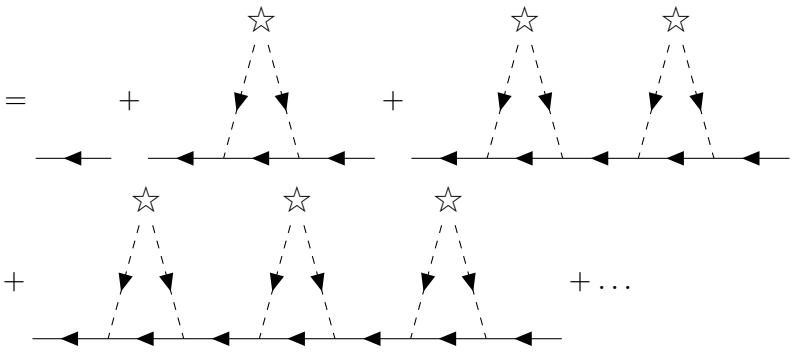

The corresponding spectral function is $A^{\mathrm{1BA}}_{\boldsymbol{k}} = -2\mathrm{Im}\left[\mathcal{G}^{\mathrm{R,1BA}}_{\boldsymbol{k}}(\omega)\right]$.

[19] i.e. the sum of all irreducible diagrams in the full Green's function without the two external legs.

The presented theory of impurity scattering will now be applied to the full-shell nanowire system described by the Hamiltonian $\tilde{H}_{m_J,p_z}$ (Eq. (4.9)). In the clean system, the conserved momentum quantum numbers are p_z and m_J and thus we translate the Dyson equation (7.7) to be in these variables instead:

$$\overline{\mathcal{G}}_{m,p} = \mathcal{G}^0_{m,p} + \mathcal{G}^0_{m,p}\Sigma_{m,p}\overline{\mathcal{G}}_{m,p} = \frac{1}{(\mathcal{G}^0_{m,p})^{-1} - \Sigma_{m,p}}. \tag{7.8}$$

Here $m_J = m$ and $p_z = p$ for notational simplicity. Equations for the electron propagator previously written in $\boldsymbol{k}$ are also translated directly to be in m and p with the same conservation rules. Note for example that the impurity-averaged propagator in Eq. (7.8) is diagonal in m and p. However, as the nanowire problem is formulated in Nambu basis, we want $\mathcal{G}^0_{m,p}$ not only to represent the normal spin-less free electron propagator but in fact to be the 4×4 matrix

$$\mathcal{G}^0_{m,p}(\omega) = \frac{1}{\omega + i\eta - \tilde{H}_{m,p}}.$$

Similarly, we will also interpret $\overline{\mathcal{G}}_{m,p}$ and $\Sigma_{m,p}$ as 4-dimensional matrices. Again we assume that $n_{\mathrm{imp}}/n_{\mathrm{el}} \ll 1$ and $\tilde{u}/E_0 \ll 1$, where E_0 is the induced pairing potential in the semiconducting core Δ. The considered type of scattering is spin- and particle-conserving such that the amplitude is $u_{\boldsymbol{q}}\tau_z$ with time reversal for holes. Also here, the lowest-order approximation to the self-energy is absorbed in the definition of the chemical potential:

$$\mathcal{G}^{R,\mathrm{LOA}}_{m,p} = \frac{1}{\omega + i\eta - \tilde{H}_{m,p} + n_{\mathrm{imp}}u_0\tau_z}.$$

The first-order Born approximation to the self-energy is

$$\Sigma^{1\mathrm{BA}}_{m,p} = \frac{n_{\mathrm{imp}}}{\mathcal{A}} \sum_{m',p'} u_{m-m',p-p'}\tau_z\mathcal{G}^0_{m',p'}u_{m'-m,p'-p}\tau_z,$$

where $\mathcal{A}$ is the surface area of the core cylinder. As an example, we write the (11) and (22) components of $\Sigma^{1\mathrm{BA}}_{m,p}$:

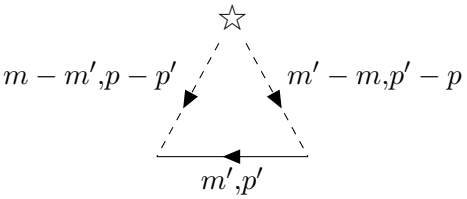

We make the simplification that the scattering amplitude is constant, $u_{m-m',p-p'} = v_0$, and thus independent of the incoming and outgoing m, p. That way, the first-order Born approximation to the self-energy becomes

$$\Sigma^{R,1\mathrm{BA}}(\omega) = \frac{v_0^2 n_{\mathrm{imp}}}{\mathcal{A}} \sum_{m',p'} \tau_z \frac{1}{\omega + i\eta - \tilde{H}_{m',p'}}\tau_z.$$

The inverse of $F = \omega + i\eta - \tilde{H}_{m',p'}$ is calculated by the prescription [30]

$$F^{-1} = \frac{C^T}{|F|}, \quad C_{ij} = (-1)^{i+j}M_{ij}, \quad M_{23} = \begin{vmatrix} F_{11} & F_{12} & F_{14} \\ F_{31} & F_{32} & F_{34} \\ F_{41} & F_{42} & F_{44} \end{vmatrix}. \tag{7.9}$$

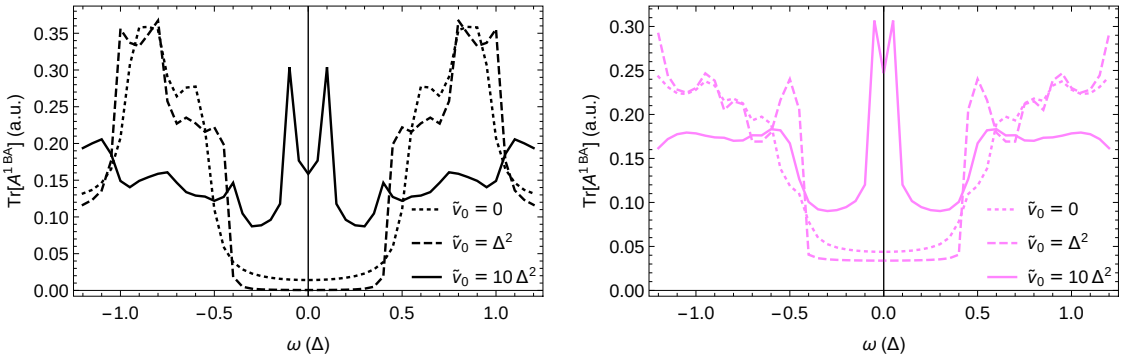

(a) $(\mu = 2.3\Delta, \alpha = 1.3\alpha_0)$ **(b)** $(\mu = 6.62\Delta, \alpha = 1.12\alpha_0)$

Figure 7.1: $\mathrm{Tr}\left[A^{1\mathrm{BA}}\right](\omega)$ for different effective strengths of the impurity scattering potential $\tilde{v}_0 = v_0^2 n_{\mathrm{imp}}/\mathcal{A}$.

Here T denotes transpose and C is the matrix containing the cofactors of the elements of F, given by the minors M_{ij}. The minor M_{ij} is the determinant of F with the ith row and jth column removed. When calculating the determinant $|F|$ one finds that this is even in p. The same is true for the diagonal elements of C as well as $C_{24} = C_{42}$ and $C_{13} = C_{31}$. The rest of the C elements are odd functions of p and thus so are the corresponding elements of F^{-1}. Integrating over all p's these therefore evaluate to zero. See App. D for written-out expressions of the elements. This means that $\Sigma^{R,1\mathrm{BA}}(\omega)$ is on the form

$$\Sigma^{R,1\mathrm{BA}}(\omega) = \frac{v_0^2 n_{\mathrm{imp}}}{\mathcal{A}} \begin{pmatrix} \mathcal{G}^0_{11}(\omega) & 0 & -\mathcal{G}^0_{13}(\omega) & 0 \\ 0 & \mathcal{G}^0_{22}(\omega) & 0 & -\mathcal{G}^0_{24}(\omega) \\ -\mathcal{G}^0_{13}(\omega) & 0 & \mathcal{G}^0_{33}(\omega) & 0 \\ 0 & -\mathcal{G}^0_{24}(\omega) & 0 & \mathcal{G}^0_{44}(\omega) \end{pmatrix},$$

where

$$\mathcal{G}^0_{ij}(\omega) = \sum_{m',p'} \left(\frac{1}{\omega + i\eta - \tilde{H}_{m',p'}} \right)_{ij}.$$

In order to find $A^{1\mathrm{BA}}(\omega) = -2\mathrm{Im}\left[\mathcal{G}^{R,1\mathrm{BA}}(\omega)\right]$ we need to calculate the matrix[20]

$$\mathcal{G}^{R,1\mathrm{BA}}_{m,p}(\omega) = \frac{1}{\omega - \tilde{H}_{m,p} - \Sigma^{R,1\mathrm{BA}}(\omega)}. \tag{7.10}$$

As previously mentioned, a finite imaginary part of the self-energy will lead to a broadening of the peaks in the spectral function, reflecting a finite lifetime of the propagator. The determinant of $\tilde{F} = \omega - \tilde{H}_{m,p} - \Sigma^{R,1\mathrm{BA}}(\omega)$ is even in p as the expression for it in Eq. (D.1) shows. Eight of the elements in $\mathcal{G}^{R,1\mathrm{BA}}_{m,p}(\omega)$ are odd functions of p and therefore integrate to zero. Hence, $\mathcal{G}^{R,1\mathrm{BA}}(\omega)$ is on the same form as $\Sigma^{R,1\mathrm{BA}}(\omega)$ with only the diagonal elements, $\mathcal{G}^{R,1\mathrm{BA}}_{13}(\omega) = \mathcal{G}^{R,1\mathrm{BA}}_{31}(\omega)$, and $\mathcal{G}^{R,1\mathrm{BA}}_{24}(\omega) = \mathcal{G}^{R,1\mathrm{BA}}_{42}(\omega)$ different from zero. The elements of $\Sigma^{R,1\mathrm{BA}}(\omega)$ and $\mathcal{G}^{R,1\mathrm{BA}}(\omega)$ are all found by numerical integration over p and summation over m until convergence of the spectral function. For the calculation of $\mathcal{G}^0_{ij}(\omega)$ we used the broadening $\eta = 0.05\Delta$.

In App. E, $\mathrm{Tr}\left[A^{1\mathrm{BA}}\right](\omega)$ is plotted for various points in (μ, α) space for different strengths of the scattering potential $\tilde{v}_0 = v_0^2 n_{\mathrm{imp}}/\mathcal{A}$ and in Fig. 7.1 we show two of such

[20] It is not necessary to have an η here when the self-energy has a finite imaginary part.

spectral function plots. For the first-order Born approximation to be valid we required that $n_{\mathrm{imp}}/n_{\mathrm{el}} \ll 1$ and $\tilde{u}/\Delta \ll 1$. To understand what restrictions this imposes on $\tilde{v}_0$ we consider the related condition for a moderately clean superconductor $\Delta\tau_r \gg 1$ where the relaxation time τ_r is the inverse of the self-energy. A crude approximation of $\mathcal{G}^0(\omega) \sim \Delta^{-1}$ yields $\tau_r \approx \Delta/\tilde{v}_0$ meaning that we must have $\tilde{v}_0 \ll \Delta^2$ for the higher order diagrams to be negligible. From Figs. 7.1, E.1, and E.2 we see that only when breaking this condition is there a change in the spectral function. This tells us that if the semiconductor is moderately clean, impurities will not be important within the hollow-cylinder model.

7.1 Conclusions on impurities

Within the first-order Born approximation we have found that impurities in the semiconductor do not have a significant effect on the spectrum in the hollow-cylinder model. Only when misusing the approximation did we see a change in the spectral function and for this reason neither a disordered core can provide a plausible explanation for a zero-bias peak in the differential conductance.

From the findings on impurities in [11], it appears that one should not perform the self-average as in Eq. (7.3) but rather numerically simulate a discrete nanowire system with randomly positioned impurities in the core. Alternatively, one could also break the angular symmetry with an impurity scattering potential $u_{m-m',p-p'}$ that couples the different m_J sectors.

8 Finite full-shell nanowire

Up until now we have assumed the nanowire to be of infinite length such that the spatial solutions along the wire would simply be free electron waves. With this, we were able to examine the bulk properties of the full-shell nanowire. However, the MZMs, which we hope exist in the system, are located on the boundaries of topological superconductors and are therefore properties of finite systems. For this reason we will now modify the description by assigning a length L to the wire. This will allow us to calculate the local quasiparticle density of states as well as the differential conductance of the wire core and we will compare our findings with the experimental results from Ref. [10].

With a finite length L of the wire, we have to discretise the BdG Hamiltonian from Eq. (4.3) along z. This we do by dividing it into N slices along the z direction, each of them labelled by an index $j = \{1, 2, \ldots, N\}$. For a discrete version of the operator p_z we use the Leibniz notation symmetrised:

$$\frac{\partial\psi(z)}{\partial z}\Big|_{z=z_j} = \lim_{\delta z\to 0}\left(\frac{1}{2}\frac{\psi(z_{j+1})-\psi(z_j)}{\delta z} + \frac{1}{2}\frac{\psi(z_j)-\psi(z_{j-1})}{\delta z}\right) = \lim_{\delta z\to 0}\frac{\psi(z_{j+1})-\psi(z_{j-1})}{2\delta z},$$

where $\delta z = z_{j+1} - z_j = z_j - z_{j-1} = L/N$. To find the discrete form of the p_z^2 operator we start by a Taylor expansion of $\psi(z)$ around z_j.

$$\psi(z) \approx \psi(z_j) + \frac{\partial\psi(z)}{\partial z}\Big|_{z=z_j}(z-z_j) + \frac{1}{2}\frac{\partial^2\psi(z)}{\partial z^2}\Big|_{z=z_j}(z-z_j)^2 \implies$$

$$\begin{aligned}
\frac{\partial^2\psi(z)}{\partial z^2}\Big|_{z_j} &= \frac{2(\psi(z)-\psi(z_j))}{(z-z_j)^2} - \frac{2}{(z-z_j)}\frac{\partial\psi(z)}{\partial z}\Big|_{z_j} \\
&= \frac{1}{2}\left(\frac{2(\psi(z_{j+1})-\psi(z_j))}{(z_{j+1}-z_j)^2} - \frac{1}{(z_{j+1}-z_j)}\frac{\psi(z_{j+1})-\psi(z_{j-1})}{\delta z}\right) \\
&\quad + \frac{1}{2}\left(\frac{2(\psi(z_{j-1})-\psi(z_j))}{(z_{j-1}-z_j)^2} - \frac{1}{(z_{j-1}-z_j)}\frac{\psi(z_{j+1})-\psi(z_{j-1})}{\delta z}\right) \\
&= \frac{\psi(z_{j+1})+\psi(z_{j-1})-2\psi(z_j)}{(\delta z)^2}.
\end{aligned}$$

The discretised Hamiltonian is now a $4N\times 4N$ dimensional matrix in both Nambu space and z_j space where we take the slice index to be the outer structure, i.e. the basis is $\Big(\psi_\uparrow(z_1), \psi_\downarrow(z_1), \psi_\downarrow^\dagger(z_1), -\psi_\uparrow^\dagger(z_1), \psi_\uparrow(z_2), \psi_\downarrow(z_2), \ldots\Big)$. The kinetic term $\sim p_z^2$ will thus have both diagonal and next to-diagonal terms in the z_j structure as in the usual tight-binding model, whereas the spin-orbit term will only be off-diagonal and couple neighbouring sites. A hopping constant is introduced, $t = 1/2m^*(\delta z)^2$, and with i, j labelling z site the Hamiltonian is

$$\begin{aligned}
H_{ij}^{\mathrm{BdG}} &= \delta_{ij}\left[\left(\frac{p_r^2 + (p_\varphi + eA\tau_z)^2}{2m^*} - \mu - \alpha(p_\varphi + eA\tau_z)\sigma_z + 2t\right)\tau_z + \Delta\left(\cos(n\varphi)\tau_x + \sin(n\varphi)\tau_y\right)\right] \\
&\quad + \delta_{i,j\pm1}\left[\left(-t \mp \frac{i}{2\delta z}\alpha\sigma_\varphi\right)\tau_z\right].
\end{aligned}$$

Since $[\cos(n\varphi)\tau_x + \sin(n\varphi)\tau_y, -i\partial_\varphi + n\tau_z/2] = [\sigma_\varphi, -i\partial_\varphi + \sigma_z/2] = 0$, the discretised Hamiltonian still commutes with the J_z operator from Eq. (4.4): $\left[H^{\mathrm{BdG}}, J_z\otimes\mathbb{I}_N\right]$, where

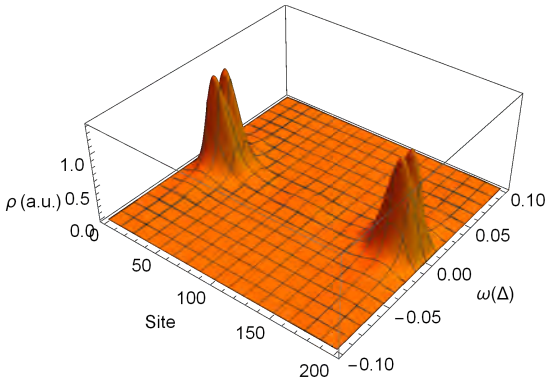

(a) ($\mu = 2.3\Delta, \alpha = 1.3\alpha_0$). Only the $m_J = 0$ sector (orange) has a significant density of states this close to zero energy.

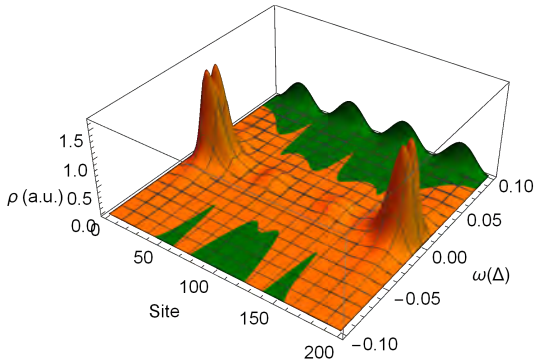

(b) ($\mu = 2.9\Delta, \alpha = 1.8\alpha_0$). Apart from the $m_J = 0$ sector (orange), $m_J = 2$ (green) is also visible.

Figure 8.1: Local quasiparticle density of states for different values of (μ, α) with $\tilde{\Phi} = \frac{1}{2}$, $n = 1$, $R_2 = 0.5R_0$, and $B_Z = 0$. Only $m_J \geq 0$ sectors are included for clarity since the negative sectors mirror the behaviour. However, this close to zero energy only $m_J = 0$ and $m_J = \pm 2$ have non-zero local density of states.

$\mathbb{I}_N$ is the N-dimensional identity matrix. A natural next step is therefore to transform with the unitary matrix U that was given in Eq. (4.7). The result is

$$\Big[(U \otimes \mathbb{I}_N) H^{\mathrm{BdG}} (U^\dagger \otimes \mathbb{I}_N)\Big]_{ij} =$$
$$\delta_{ij} \left[\left(\frac{p_r^2}{2m^*} + \frac{\left(m_J - \frac{1}{2}\sigma_z - \frac{n}{2}\tau_z + erA\tau_z\right)^2}{2m^* r^2} - \mu - \frac{\alpha}{r}\left(m_J - \frac{1}{2}\sigma_z - \frac{n}{2}\tau_z + erA\tau_z\right)\sigma_z + 2t \right)\tau_z + \Delta\tau_x \right]$$
$$+ \delta_{i,j\pm1}\left[-t \mp \frac{i\alpha}{2\delta z}\sigma_y\right]\tau_z.$$

Assuming, as in Sec. 4.1, that the semiconducting core is effectively a hollow cylinder we obtain the discretised version of $\tilde{H}_{m_J}$ from Eq. (4.9):

$$\tilde{H}_{ij}^{m_J} = \delta_{ij}\Big[(2t - \mu_{m_J})\tau_z + V_Z\sigma_z + A_{m_J} + C_{m_J}\sigma_z\tau_z + \Delta\tau_x\Big] - \delta_{i,j\pm1}\left[\left(t \pm \frac{i\alpha}{2\delta z}\sigma_y\right)\tau_z\right]. \quad (8.1)$$

From this it is seen that the different m_J sectors are still not coupled. The eigenenergies in a tight binding model, like the one made for the p_z^2 term, take values between $-2t$ and $+2t$ when including both electron-like and hole-like excitations. From [10] we take the length of the nanowire to be $L = 1\mu$m and divide it into $N = 200$ slices along the z direction, such that the hopping energy becomes $t = \hbar^2 N^2/2m^* L^2 \approx 300\Delta$. This means the kinetic term in the discretised $\tilde{H}^{m_J}$ strongly dominates the energy since the other terms are only of order $\sim \Delta$, and the spectrum depends weakly on the m_J quantum number except at small energies. The approximation of a tight-binding model for the p_z^2 term is therefore valid.

Finding the eigenstates and eigenenergies of the Hamiltonian in Eq. (8.1) numerically, we can calculate the local quasiparticle density of states $\rho_{m_J}(\omega, z) = \sum_{i=1}^{4N} |\Psi_{m_J}^i(z)|^2 \delta(\omega - E_{m_J}^i)$, where the sum runs over the $4N$ eigenstates. Fig. 8.1 shows two examples of the

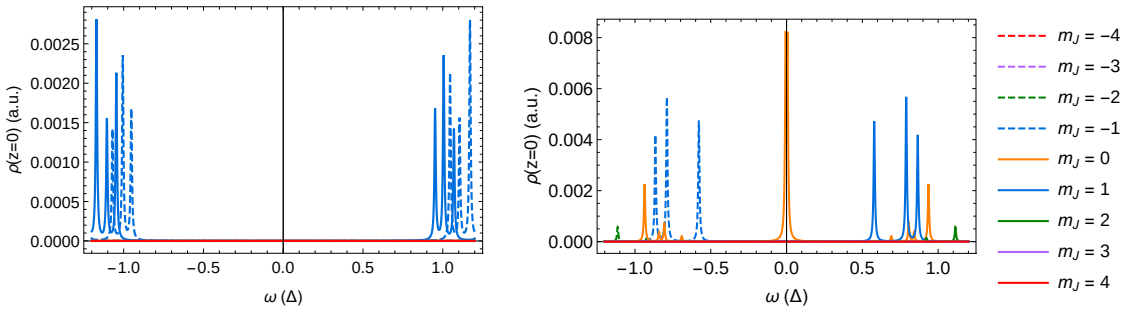

(a) ($\mu = 0.124\Delta, \alpha = 2.04\alpha_0$). The gap is defined by the $m_J = \pm 1$ bands and is between 0.9Δ and 1.0Δ in agreement with the bulk calculations.

(b) ($\mu = 2.3\Delta, \alpha = 1.3\alpha_0$). Apart from the zero-energy peak, the gap is around $0.5\Delta - 0.6\Delta$ and defined by the $m_J = \pm 1$ sector as in the bulk calculations where no zero-energy state was registered.

Figure 8.2: Local quasiparticle density of states at $z = 0$ at two different points in (μ, α) space for $\tilde{\Phi} = 1/2$, $n = 1$, $R_2 = 0.5R_0$, and $B_Z = 0$. We do not pay attention to the units of ρ but only the relative hight and position of the peaks.

local density of states with a Lorentzian of width 0.01Δ replacing the delta function as explained in Sec. 6.1. In both plots we observe peaks in the density of states at the two ends of the wire at energies $\pm\delta\omega$, $|\delta\omega| \ll \Delta$. We know that in a finite 1-dimensional system, MZMs located at each end will have a weak interaction $i\tilde{t}$ between them which decays exponentially with the length of the system [8, 9]. This overlap of the wave functions means that the two MZMs are hybridised and both acquire a small finite energy in the sense that they become superpositions of $\pm\tilde{t}$ energy states. We see this splitting in energy in both of the end-states and hence the two plots of the local quasiparticle density of states in the full-shell nanowire are consistent with the Majorana picture. Furthermore, the end-states are in the $m_J = 0$ sector which was also the one we predicted would allow MZMs, back in Sec. 4. The plot in Fig. 8.1a is for parameter values where the bulk was found to be in the non-trivial phase (see e.g. the phase diagrams in Figs. 4.2 and 4.3) and the finding of a zero-energy state in the calculations for a finite nanowire supports the theory of MZMs in the system. The parameters for which Fig. 8.1b is made was found to describe a bulk system forced into the trivial phase by the gap closing of the $m_J = \pm 2$ bands across the $|V_Z| = \sqrt{\mu^2_{m_J=0} + \Delta^2}$ parabola. We observe also here that the $m_J = 2$ sector has states below 0.1Δ while the isolated $m_J = 0$ sector still shows a local density of states resemblant of a MZM. The two small tops inside the wire demonstrate an oscillatory behaviour of the MZM wave function which is in general controlled by the chemical potential and the Zeeman splitting [31].

An interesting line-cut of the local quasiparticle density of states is that at one of the ends, for example $\rho_{m_J}(\omega, z = 0)$, which, if the system possesses MZMs, should have peaks at $\pm\delta\omega$ inside a well-defined gap. In Fig. 8.2 the end-density of states in sector $m_J = \{-4, \ldots, 4\}$ is plotted for two different points in (μ, α) space which were both gapped in the infinite-wire calculations (Fig. 4.3), one of them trivially (Fig. 8.2a) and the other one with a non-trivial gap (Fig. 8.2b). The plot in Fig. 8.2a shows that the bulk and finite-wire calculations agree on the gap size $E_{\text{gap}} \in [0.9\Delta, 1.0\Delta]$ in this point (compare with Fig. 4.3), and as expected there is no state at zero energy. Similarly, the gap size in the non-trivial point ($\mu = 2.3\Delta, \alpha = 1.3\alpha_0$) is between 0.5Δ and 0.6Δ in both cases except for a zero-energy state in the $m_J = 0$ sector for the finite wire (compare

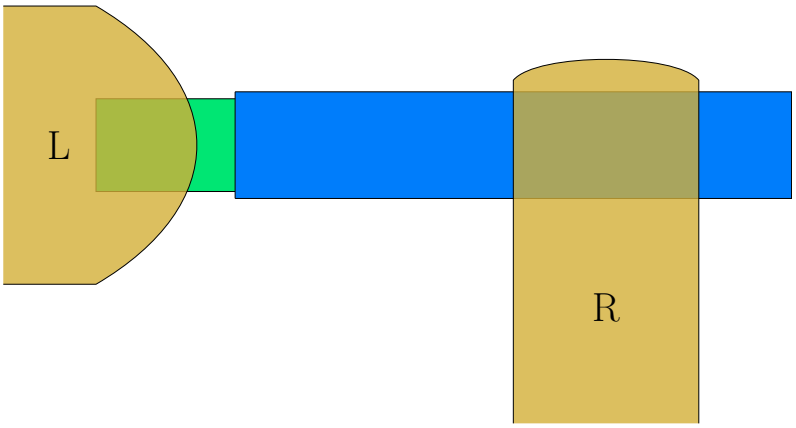

Figure 8.3: Setup for measuring the differential conductance in the nanowire core. The semiconductor is coloured green, the superconducting shell is blue, and gold is used for the metallic leads.

Figs. 8.2b and 4.3). That the zero-energy state is only observed in the finite wire and not in the bulk calculations suggests that it might be a MZM.

Now we turn to calculate instead what one can actually measure, namely the differential conductance of the nanowire. This can be found through electron tunnelling spectroscopy at the end of the wire [24] in a setup like the one sketched in Fig. 8.3, which is was also used in the experiment [10]. Since we are interested in states in the semiconductor it is assumed that one of the normal leads is coupled only to the core. This requires etching off the Al shell in one off the ends. What are then the possible scattering processes for an incoming electron from the left lead? Effectively the lead and the rim of the core constitute a normal-superconductor interface which was described by Blonder, Tinkham, and Klapwijk in 1982 [25]. In their article they used a generalised semiconductor scheme to describe the superconductor and found that the types of scattering processes in this model for an electron incident on the interface from the normal side with energy E were the following: $A(E)$: Andreev reflection as a hole on the other side of the Fermi surface with transfer of a Cooper pair carrying charge $-2e$ across the interface. $B(E)$: Ordinary reflection. $C(E)$: Transmission with a wave vector on the same side of the Fermi surface. $D(E)$: Transmission with crossing through the Fermi surface. Using the Bogoliubov equations to match wave functions at the normal-superconductor boundary they could express the reflection and transmission amplitudes by the energy E, the superconducting order parameter Δ, and the strength of a repulsive potential modelling the interface. Here we will take a slightly different approach by using the scattering matrix formalism instead. In Refs. [24, 27, 32] this formalism is presented using the Landauer-Büttiker approach in order to find the current across a normal-superconductor interface. We will here give a brief summary of the method ending with an expression for the differential conductance of the wire in terms of the reflection coefficients, relating amplitudes of incoming and outgoing electron waves on the boundary.

The nanowire is considered to be a mesoscopic sample connected to two macroscopic electron reservoirs (metal contacts) through leads which we denote left (L) and right (R), see Fig. 8.3. In the mesoscopic regime the electron coherence length is larger than the

length of the wire. The leads are assumed to have a constant, straight cross-section Ω and an impenetrable boundary $\delta\Omega$. The contact between reservoir and lead is assumed to be reflectionless such that all electrons incident on the reservoir will be fully absorbed and thermalised before being re-emitted into the lead. This way, the occupation of electrons in the lead is given by the Fermi-Dirac distribution function of the connected reservoir. Using the coordinate system $(x, y, z) = (\boldsymbol{r}_\perp, z)$, where z is the coordinate along the wire and leads, the Hamiltonians and eigenstates of the leads $\beta = L, R$ are [24]:

$$\begin{aligned}
H_\beta &= -\left(\frac{\partial_\perp^2}{2m} + \frac{\partial_z^2}{2m}\right)\tau_z, && \text{for } \boldsymbol{r}_\perp \in \Omega, \text{else } 0,\\
\phi^\pm_{\beta\zeta nE}(\boldsymbol{r}_\perp, z) &= \frac{1}{\sqrt{k_n(E)}}\boldsymbol{v}_\zeta \chi_n(\boldsymbol{r}_\perp) e^{\pm i k_n(E) z}, && \zeta = \{\text{e,h}\},\\
\frac{-\partial_\perp^2}{2m}\chi_n(\boldsymbol{r}_\perp) &= \varepsilon_n \chi_n(\boldsymbol{r}_\perp), && n = \{1, 2, \ldots, \tilde{N}\},\\
\chi_n(\boldsymbol{r}_\perp) &= 0, && \text{for } \boldsymbol{r}_\perp \in \delta\Omega,\\
E &= s(\zeta)\left(\frac{k_n^2}{2m} + \varepsilon_n\right). && (8.2)
\end{aligned}$$

The Hamiltonian of lead β is expressed in terms of the third Pauli matrix in electron-hole space. The eigenstate in lead β with energy E and transverse mode quantum number n is $\phi^\pm_{\beta\zeta nE}$, where $+/-$ refers to right/left moving waves with wavenumber $k_n(E)$. $\zeta = \{\text{e,h}\}$ denotes whether the particle is an electron or a hole. $\chi_n(\boldsymbol{r}_\perp)$ are the transverse eigenfunctions with eigenenergies ε_n in a basis where $\langle \chi_n | \chi_{n'} \rangle = \delta_{nn'}$. The quantum number $n = \{1, 2, \ldots, \tilde{N}\}$ can therefore be regarded as an independent channel which could for example be spin. Finally, the spinors $\boldsymbol{v}_\text{e} = (1, 0)$, $\boldsymbol{v}_\text{h} = (0, 1)$ are eigenvectors of τ_z with the corresponding eigenvalues $s(\zeta = \text{e}) = 1$, $s(\zeta = \text{h}) = -1$.
An eigenstate $\psi_{\zeta E}(\boldsymbol{r}_\perp, z)$ with energy E of the lead-wire-lead system is

$$\psi_{\zeta E}(\boldsymbol{r}_\perp, z) = \begin{cases} \sum_n a^+_{\zeta n}\phi^+_{L\zeta nE}(\boldsymbol{r}_\perp, z) + \sum_n a^-_{\zeta n}\phi^-_{L\zeta nE}(\boldsymbol{r}_\perp, z), & (\boldsymbol{r}_\perp, z) \in L,\\ \psi_{M,\zeta E}(\boldsymbol{r}_\perp, z), & (\boldsymbol{r}_\perp, z) \in M,\\ \sum_n b^+_{\zeta n}\phi^+_{R\zeta nE}(\boldsymbol{r}_\perp, z) + \sum_n b^-_{\zeta n}\phi^-_{R\zeta nE}(\boldsymbol{r}_\perp, z), & (\boldsymbol{r}_\perp, z) \in R. \end{cases}$$

Here M refers to the nanowire in the middle region between the leads where the wave function $\psi_{M,\zeta E}$ is unspecified. The amplitudes $\boldsymbol{a}^+_\zeta = (a^+_{\zeta 1}, a^+_{\zeta 2}, \ldots, a^+_{\zeta\tilde{N}})$, $\boldsymbol{a}^-_\zeta, \boldsymbol{b}^+_\zeta, \boldsymbol{b}^-_\zeta$ are the coefficients of the linear combination of incoming and outgoing waves on the middle region. These are linearly dependent from the boundary conditions of the problem and can be related by the scattering matrix:

$$\begin{pmatrix} \boldsymbol{a}^-_\text{e} \\ \boldsymbol{a}^-_\text{h} \\ \boldsymbol{b}^+_\text{e} \\ \boldsymbol{b}^+_\text{h} \end{pmatrix} = \begin{pmatrix} R(E) & T'(E) \\ T(E) & R'(E) \end{pmatrix} \begin{pmatrix} \boldsymbol{a}^+_\text{e} \\ \boldsymbol{a}^+_\text{h} \\ \boldsymbol{b}^-_\text{e} \\ \boldsymbol{b}^-_\text{h} \end{pmatrix} = S(E) \begin{pmatrix} \boldsymbol{a}^+_\text{e} \\ \boldsymbol{a}^+_\text{h} \\ \boldsymbol{b}^-_\text{e} \\ \boldsymbol{b}^-_\text{h} \end{pmatrix}.$$

Hence the (unitary) scattering matrix $S(E)$ relates the amplitudes of the incoming waves ϕ^+_L, ϕ^-_R to those of the outgoing waves ϕ^-_L, ϕ^+_R. The submatrices are $2\tilde{N}$-dimensional with particle type as the outer structure and channel as the inner one. For example, $R_{\text{e}n',\text{e}n}(E)$ is the amplitude for normal reflection of an incoming electron in the left lead

in channel n to an outgoing electron in the same lead in channel n'. Similarly, $T_{en',en}(E)$ is the normal transmission amplitude from the left to right lead. The primed matrices are amplitudes for incoming particles from the right lead. Matrix elements such as $R_{\mathrm{hn}',en}$ are non-zero due to the finite electron paring in the wire and denote the amplitude of an incoming electron in channel n being reflected as a hole in channel n', the process of Andreev reflection described previously.[21] In order to calculate the current through the wire we define the scattering states $\psi_{\beta\zeta nE}$ which are (originating from) incoming waves from lead β of a ζ type particle in channel n with energy E. In equilibrium the current is the same in both leads and we therefore only consider the left one and assume the right lead to be far away from the left interface. Scattering states from the left lead are $\psi_{L\zeta nE} = \phi^+_{L\zeta nE}(\boldsymbol{r}_\perp, z) + \sum_{\zeta' n'} R_{\zeta' n',\zeta n}\phi^-_{L\zeta' n' E}(\boldsymbol{r}_\perp, z)$ where $(\boldsymbol{r}_\perp, z) \in L$. The current contribution of scattering state $\psi_{\beta\zeta nE}$ is

$$I_{\beta\zeta nE} = \int_\Omega d\boldsymbol{r}_\perp \left(\psi_{\beta\zeta nE}(\boldsymbol{r}_\perp, z)\right)^\dagger \frac{1}{2mi}\left(\overrightarrow{\partial_z} - \overleftarrow{\partial_z}\right)\tau_z\left(\psi_{\beta\zeta nE}(\boldsymbol{r}_\perp, z)\right)$$

In App. F the current of a scattering state of type ζ from the left reservoir, $I_{L\zeta nE}$ is calculated. From this we find that

$$I_{LenE} = \frac{1}{m}\left[1 - \left[R^\dagger_{\mathrm{ee}}R_{\mathrm{ee}}\right]_{nn} + \left[R^\dagger_{\mathrm{he}}R_{\mathrm{he}}\right]_{nn}\right],$$

where we have introduced the new submatrices

$$R(E) = \begin{pmatrix} R_{\mathrm{ee}}(E) & R_{\mathrm{eh}}(E) \\ R_{\mathrm{he}}(E) & R_{\mathrm{hh}}(E)\end{pmatrix},$$

each of which is $\tilde{N}$ dimensional. The first two terms in I_{LenE} is the contribution from the transmitted electrons while the last term is that from Andreev reflection. As previously explained the occupation of electrons from the left reservoir is $n_F(E-\mu_L)$ where μ_L is the chemical potential of that reservoir. We set the chemical potential of the wire and that of the right reservoir to zero, $\mu = \mu_R = 0$, and apply a bias voltage such that the chemical potential of the left reservoir is $\mu_L = -eV$. That way the total electron current is

$$\begin{aligned} I &= -e\sum_{nE} I_{LenE}(n_F(E+eV) - n_F(E)) \\ &= \frac{-e}{2\pi}\int_0^\infty dE\ \mathrm{Tr}\left[1 - R^\dagger_{\mathrm{ee}}R_{\mathrm{ee}} + R^\dagger_{\mathrm{he}}R_{\mathrm{he}}\right](n_F(E+eV) - n_F(E)) \\ &= \frac{-1}{e}\int_0^\infty dE\ G_s(E,V)(n_F(E+eV) - n_F(E)). \end{aligned}$$

Here we have introduced the *spectral conductance*

$$G_s(E,V) = \frac{e^2}{h}\mathrm{Tr}\left[1 - R^\dagger_{\mathrm{ee}}R_{\mathrm{ee}} + R^\dagger_{\mathrm{he}}R_{\mathrm{he}}\right], \tag{8.3}$$

and used that $\sum_E = \frac{m}{2\pi}\int dE$ from the normalisation of the wave functions in Eq. 8.2 and $2\pi = h$. The differential conductance of the nanowire core is then

$$\left.\frac{dI}{dV}\right|_V = -\int_0^\infty dE\ \left[n'_F(E+eV)G_s(E,V) + \frac{n_F(E+eV) - n_F(E)}{e}\frac{dG_s(E,V)}{dV}\right].$$

[21] If n and n' denote spin, they are opposite in the Andreev reflection.

We make the simplification that the spectral conductance is approximately independent of the bias voltage, $\frac{dG_s(E,V)}{dV} \approx 0$, corresponding to low coupling between the leads and the wire [24]. That way, the differential conductance at low temperatures compared to eV is

$$\left.\frac{dI}{dV}\right|_V = -\int_0^\infty dE\; n_F'(E+eV)G_s(E) \approx G_s(-eV).$$

We see now that it is possible to calculate the differential conductance of the nanowire without ever finding the wave function inside. Instead we need the reflection matrix which can be expressed as [33]

$$R(E) = 1 - 2\pi i W^\dagger \frac{1}{E - H + i\pi W W^\dagger} W. \tag{8.4}$$

Here H is the Hamiltonian of the sample and W is a matrix describing the coupling between the left lead and the sample. The coupling matrix W is of size $M \times \tilde{N}$ where M is the number of modes in the sample. For example, if we work with the channels spin up and spin down, $R(E)$ is 4-dimensional and conveniently represented in the Nambu basis $(\psi_\uparrow, \psi_\downarrow, \psi_\downarrow^\dagger, -\psi_\uparrow^\dagger)$. If the sample Hamiltonian is also written in Nambu and discretised into N coordinates along z, like the Hamiltonian in Eq. (8.1), the coupling matrix is $4N \times 4$-dimensional. Assuming that the left lead only couples to the first site in the sample, W has the form

$$W = \sqrt{\gamma_W}(\mathbb{I}_4 \otimes \underbrace{(1, 0, \ldots, 0)}_{N})^T. \tag{8.5}$$

The site vector $(1, 0, \ldots, 0)$ is of length N and it has been assumed that all channels couple with the same strength.

We now apply this theory to the case where the mesoscopic sample is a full-shell nanowire described by the Hamiltonian $\tilde{H}^{m_J}$ in Eq. (8.1). For a start we make the rather unrealistic assumption that the lead possesses the same symmetry as the wire. This will allow us to perform the calculation of the differential conductance in a very straightforward way. Later we will discuss the modifications from a more realistic model in which the wire possesses no particular symmetry.

For a lead with the same symmetry as the wire, the eigenstates will also be labelled by the angular quantum number m_J which is then conserved in the scattering process and we can therefore treat these as independent channels. Hence, there is a reflection matrix like the one in Eq. (8.4) for each sector:

$$R_{m_J}(E) = 1 - 2\pi i W_{m_J}^\dagger \frac{1}{E - \tilde{H}^{m_J} + i\pi W_{m_J} W_{m_J}^\dagger} W_{m_J},$$

where $R_{m_J}(E)$ is 4-dimensional (Nambu space), $\tilde{H}^{m_J}$ is the $4N$-dimensional matrix from Eq. (8.1), and W_{m_J} as given in Eq. (8.5) with a coupling strength $\sqrt{\gamma_W^{m_J}}$ that we take to be the same for all sectors for simplicity. The symmetry of the reflection matrix under particle-hole inversion is $\mathcal{P} R_{m_J}(E) \mathcal{P}^{-1} = R_{-m_J}(-E)$. The total differential conductance is

$$\left.\frac{dI}{dV}\right|_V \approx G_s(E) = \frac{e^2}{h} \sum_{m_J} \mathrm{Tr}\left[1 - R_{m_J,\mathrm{ee}}^\dagger R_{m_J,\mathrm{ee}} + R_{m_J,\mathrm{he}}^\dagger R_{m_J,\mathrm{he}}\right]. \tag{8.6}$$

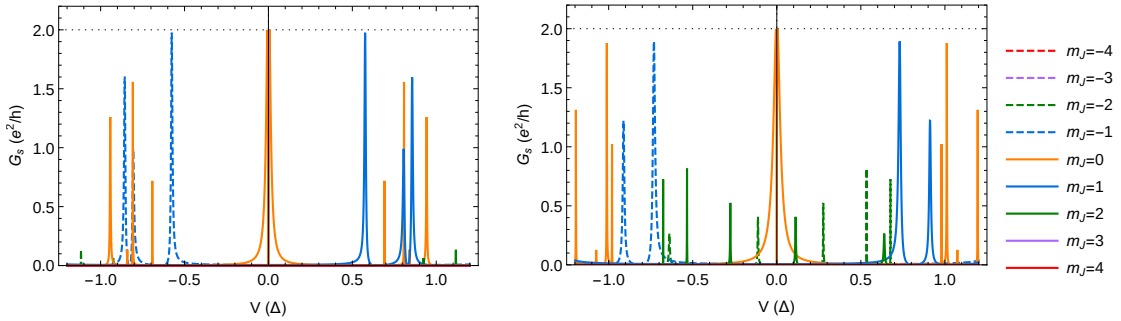

(a) $(\mu = 2.3\Delta, \alpha = 1.3\alpha_0)$ **(b)** $(\mu = 2.9\Delta, \alpha = 1.8\alpha_0)$

Figure 8.4: Differential conductance approximated by $G_s(E)$ in Eq. (8.6) for two different point in (μ, α) space and $\tilde{\Phi} = 0.5$, $R_2 = 0.5R_0$. The two peaks at zero bias voltage are $2e^2/h$ consistent with a MZM.

The differential conductance for two points in (μ, α) space is plotted in Fig. 8.4 where the contributions from the different m_J sectors are made distinct. The parameters used in Fig. 8.4a were found by the calculations in Sec. 4.1 to describe an infinite wire in a non-trivially gapped topological phase, corresponding to the bulk properties of the finite-sized wire. Indeed we see in Fig. 8.4a a zero-bias peak in the $m_J = 0$ sector which we predicted to be the only one that allowed Majorana zero-modes. The height of the peak is $2e^2/h$ which is consistent with a MZM since a tunnelling contact to such a mode induces a resonant Andreev reflection that gives a peak of $2e^2/h$ in the zero-bias conductance [12]. Apart from the zero-bias peak in $m_J = 0$, the spectrum gap is $5\Delta - 6\Delta$ and defined by the $m_J = \pm 1$ sectors in agreement with the bulk calculations (Fig. 4.3) and the local quasiparticle density of states at $z = 0$ (Fig. 8.2b). The differential conductance plot in Fig. 8.4b is for parameters where the (bulk) $m_J = 0$ sector is in the non-trivial phase but the gap is closed by $m_J = \pm 2$ bands as discussed in Sec. 4.1. The conductance plot confirms that a zero-energy state, causing a peak of $2e^2/h$, exists in the $m_J = 0$ sector, and also shows a gap that is closed by $m_J = \pm 2$ bands. In Figs. G.1 and G.2 in App. G differential conductance plots like the ones in Fig. 8.4 are given for many of the points in Fig. C.6, which were also used in Secs. 6 and 7. The summary of those plots is that they agree well with the bulk calculations on the size of the gap[22] and on the values of (μ, α) for which there should be a zero-energy state in the $m_J = 0$ sector, i.e. inside the $|V_Z| = \sqrt{\mu^2_{m_J=0} + \Delta^2}$-parabola, at that the hight of the zero-bias peak is $2e^2/h$. We do, however, observe splitting of the zero-bias conductance peak for some (μ, α) inside the parabola. The splitting could be ascribed to the finite length of the wire leading to a hybridisation of the two theoretical Majorana zero-modes as previously mentioned.

Our calculations show the height of the zero-bias conductance peak to be $2e^2/h$, consistent with the Majorana picture, whereas the peak measured in [10] was $< 0.2e^2/h$. This discrepancy is well-known and different explanations for it have been suggested [24]. These include: interfacial tunnel barriers resulting in low coupling between lead electrons and the MZM, the absence of a hard gap due to other subgap states, finite temperature, and dissipation such as coupling between the MZM and the drain (right) lead causing a finite life time of the MZM that affects the conductance.

[22] There is one point, $(\mu = 6.62\Delta, \alpha = 1.12\alpha_0)$, where the conductance does not appear to agree with the bulk calculations on the gap, see Fig. G.2d.

We can also compare the differential conductance in the different points of (μ, α) space with the bulk spectral functions in App. B, Figs. C.7 to C.13. For example is $\mathrm{Tr}[A]$ in point $(\mu = 2.9\Delta, \alpha = 1.8\alpha_0)$ a smeared out version of the conductance except for the zero-energy peak (compare Figs. 8.4b and C.7e). However, this consistency is not true for all of the points and therefore the bulk spectral function cannot just be taken as a direct representation of the differential conductance. Furthermore, the conductance plots are similar to the local quasiparticle density of states at the end $\rho(z = 0)$ in the sense that the peaks of the distinct sectors are at the same energies for the two functions but with different relative height. Hence neither can the density of states at the end of the wire be directly translated to differential conductance.

In conclusion, the hollow-cylinder model at half a flux quantum agrees with the experiment [10] on a zero-energy state inside a gap which according to the model is non-trivial. However, we keep in mind that this only holds true for some specific parameter values.

Now we examine how the calculated differential conductance develops through the first and zeroth Little-Parks lobes. If the zero-energy state is really a MZM, we expect the zero-energy peak in the differential conductance to vanish at integer flux quanta since the bulk calculations predicted the topological phase to be trivial here. Surely, when "scanning" the conductance in point $(\mu = 2.3\Delta, \alpha = 1.3\alpha_0)$ through the first Little-Parks lobe, we observe that the zero-bias peak splits as the flux increases towards one flux quantum where the spectral gap becomes 1Δ (see Fig. 8.5a). From $\tilde{\Phi} = 1$ to $\tilde{\Phi} = 1.5$ the conductance peaks mirror the behaviour between $\tilde{\Phi} = 0.5$ and $\tilde{\Phi} = 1$ which is exactly what we also found for the bulk phase diagrams in Sec. 5. Line cuts of Fig. 8.5a at different values of the reduced flux ϕ confirm that m_J and $-m_J$ bands are switched when $\phi \to -\phi$ due to terms $\propto \phi m_J$ in $\tilde{H}^{m_J}$. The line cuts are taken for $\tilde{\Phi} = \{0.5, 0.6, \ldots, 1.5\}$ and shown in Figs. G.5 and G.6. A similar behaviour is found for the conductance in $(\mu = 2.9\Delta, \alpha = 1.8\alpha_0)$ although the gap is closed at $\tilde{\Phi} = 0.5$ (see Figs. 8.5b and G.7). More plots of the differential conductance as function of the bias voltage and reduced flux in both the zeroth and first Little-Parks lobes are shown for five different points inside the $|V_Z| = \sqrt{\mu^2_{m_J=0} + \Delta^2}$-parabola in Figs. G.3 and G.4. The results strongly disagree with the experiment [10] where a peak in the differential conductance at zero voltage bias was measured through the entire gapped part of the first Little-Parks lobe (Fig. 1.1). As for the bulk calculations we therefore conclude that the hollow-cylinder model is not sufficient for describing the experiment at all flux values.

We remark that a more realistic model for the conductance measurement would not assign any particular symmetry to the lead. Instead the lead could be gated to only include two spin channels that couple equally well to all m_J sectors in the nanowire and the coupling matrix would be

$$W = \sqrt{\gamma_W} \left(\mathbb{I}_4 \otimes \underbrace{(1, 1, \ldots, 1)}_{2m_J^{\max}+1} \otimes \underbrace{(1, 0, \ldots, 0)}_{N} \right)^T .$$

With such a coupling, the different m_J sectors would be mixed in the scattering process. Nevertheless, as the conductance peaks in e.g. Fig. 8.4 are narrow and fairly separated we do not expect the mixing to have a large effect on the results.

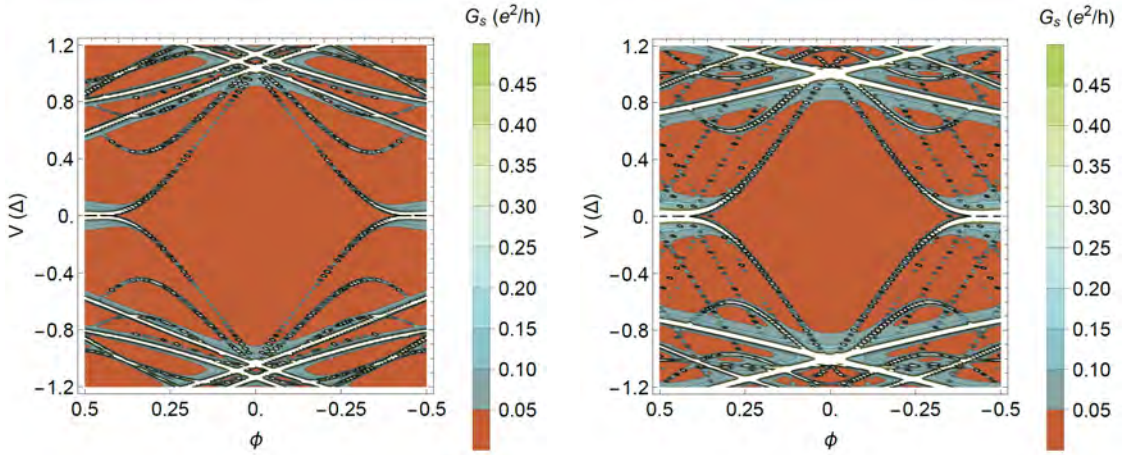

(a) $(\mu = 2.3\Delta, \alpha = 1.3\alpha_0)$ **(b)** $(\mu = 2.9\Delta, \alpha = 1.8\alpha_0)$

Figure 8.5: Differential conductance approximated by $G_s(E)$ in Eq. (8.6) as function of the reduced flux and bias voltage through the first Little-Parks lobe for a cylinder radius $R_2 = 0.5R_0$.

8.1 Conclusions on the analysis of a finite full-shell nanowire

In our analysis of the hollow-cylinder model for a finite wire we have used the scattering matrix formalism to calculate the differential conductance in the core. This has shown $2e^2/h$ peaks at zero bias voltage in sector $m_J = 0$ only for parameters that describe a non-trivial bulk gap. We have also observed a splitting of some of the zero-bias peaks which we assigned to the overlap of MZM wave functions. The local quasiparticle density of states has shown a similar behaviour with states in the $m_J = 0$ sector located at each end of the wire and split around zero energy. However, we have also seen that the differential conductance is not equal to thee bulk spectral function or density of states at the end as they differed in relative signal height. Calculations of the differential conductance as function of flux and bias voltage have confirmed that the hollow-cylinder model is not sufficient for describing the experiment in [10]. Although the measurements agrees with our predictions at $\tilde{\Phi} = 1/2$, the zero-bias peak splits and vanishes as $\tilde{\Phi} \to 1$.

9 Conclusions and outlook

In this thesis we have thoroughly examined to what extent the hollow-cylinder model from [11] can be modified by perturbations to describe the Al-InAs full-shell wires in [10].

With the destructive Little-Parks effect [20, 21, 23], we explained the oscillations in transition temperature that lead to a temperature-flux phase diagram of re-emergent lobes of superconductivity separated by the normal phase. Since the transition between zero and normal resistance was sharp at zero field and slightly broadened with increasing flux (Fig. 2.5), we concluded that the Al shell of the wires used in [10] was only weakly disordered and had a reasonably homogeneous geometry. With the proximity effect in the strong coupling regime we were able to explain the observed gap in the zero-field spectrum of the semiconductor and the destructive Little-Parks-like behaviour of the gap at finite flux (see Fig. 1.1).

The simplified hollow-cylinder model for the full-shell wires assumed the conduction electrons in the semiconductor to be accumulated in the outermost layer. The eigenstates of the Hamiltonian were characterised by angular quantum numbers m_J, whereof the $m_J = 0$ was special as it was the only sector that allowed eigenstates invariant under particle-hole inversion and thereby MZMs. With $m_J = 0$ the Hamiltonian took the form of an Oreg-Lutchyn model [1, 2] and we were able to calculate the topological invariant. When including other m_J sectors the distinction between the trivial and the non-trivial phase became more complicated. We argued that a gap closing at zero momentum along the wire led to a sign change of the topological invariant. By comparing this to numerical calculations of the total spectrum it was possible to tell, when the nanowire system would undergo a phase transition.

In an attempt to expand the parameter range of the non-trivial phase, we introduced periodic deformations of the wire to break the angular symmetry. That way, different m_J states that otherwise caused a closed gap were coupled, and in some cases this led to an avoided crossing at zero energy. Our findings were in agreement with some of the results from [11]. The non-trivial phase was, however, unstable to variations in for example the radius of the semiconductor and the flux through the wire cross-section. This sensitivity could not be stabilised by deformations. Therefore, we concluded that the hollow-cylinder model could not be used to describe the observed zero-bias peak in [10] as a signature of a MZM, even with the introduced perturbations. Nevertheless, we did find, by introducing a $\pi/3$-periodic deformation, that the hexagonal wires used in [10] are well approximated by a cylinder within the model. Furthermore, we also found that the Zeeman energy should be included in the calculations when the g-factor is larger than of the order 1, which can be the case in InAs [5, 7].

We then examined if the hollow-cylinder model predicted a trivial zero-energy peak in the spectral function that could provide an alternative explanation of the observations in [10]. For a system without spin-orbit coupling, we only found a trivial zero-energy peak that was unstable to even small changes in wire radius, flux and deformations, and was only a consequence of commensurable values in the Hamiltonian. No trivial zero-energy peaks were found for finite spin-orbit coupling except at the topological phase transition points. Considering the narrow conditions, we discarded this type of trivial zero-energy state as a possible explanation in the hollow-cylinder model of the observations in [10].

Within the first-order Born approximation, we also investigated what effect a small concentration of impurities inside the semiconductor would have on the spectrum. We calculated the spectral function for different scattering strengths and found that only when

breaking the approximation was there a considerable change to the spectrum. Therefore, we concluded that impurities in the semiconductor are not relevant within the hollow-cylinder model when the inverse of the relaxation time is on the order of or larger than the induced gap.

Lastly, we considered a finite full-shell nanowire and found end states in the local quasiparticle density of states with energies close to zero, compatible with the theory of MZMs. We also used the scattering matrix formalism to calculate the differential conductivity. At one half flux quantum this showed zero-bias peaks in the $m_J = 0$ sector for parameters that were previously found to describe a topologically non-trivial bulk system. However, also the finite-wire results were inconsistent with the experimental findings of a peak at zero voltage bias throughout the entire gapped part of the first Little-Parks lobe.

In summary, we have found that even with deformations or impurities, the hollow-cylinder model is inadequate for describing the experimental findings in [10] since the model is unable to explain the zero-bias peak in conductance near one flux quantum. However, we did see an agreement between the model and the experiment at one half flux quantum and maybe the discrepancies could be corrected by including more radial modes in the semiconductor. That way, the flux would be different in the distinct radial modes and flux-dependent terms in the Hamiltonian that are required to be finite for a non-trivial phase would not become zero for all modes simultaneously. Such a model could then be further extended by also coupling the different radial modes.

In future work, we should also gain a better understanding of the multiple subgap states at finite energy that were also measured in the first Little-Parks lobe [10].

References

[1] Y. Oreg, G. Refael, and F. von Oppen, "Helical liquids and Majorana bound states in quantum wires," *Phys. Rev. Lett.*, vol. 105, p. 177002, 2010.

[2] R. M. Lutchyn, J. D. Sau, and S. Das Sarma, "Majorana Fermions and a Topological Phase Transition in Semiconductor-Superconductor Heterostructures," *Phys. Rev. Lett.*, vol. 105, p. 077001, 2010.

[3] T. D. Stanescu, R. M. Lutchyn, and S. Das Sarma, "Majorana fermions in semiconductor nanowires," *Phys. Rev. B*, vol. 84, no. 14, p. 144522, 2011.

[4] V. Mourik, K. Zuo, S. M. Frolov, S. R. Plissard, E. P. A. M. Bakkers, and L. P. Kouwenhoven, "Signatures of Majorana Fermions in Hybrid Superconductor-Semiconductor Nanowire Devices," *Science*, vol. 336, no. 6084, pp. 1003–1007, 2012.

[5] S. M. Albrecht, A. P. Higginbotham, M. Madsen, F. Kuemmeth, T. S. Jespersen, J. Nygård, P. Krogstrup, and C. M. Marcus, "Exponential Protection of Zero Modes in Majorana Islands," *Nature*, vol. 531, no. 7593, pp. 206–209, 2016.

[6] M. T. Deng, S. Vaitiekenas, E. B. Hansen, J. Danon, M. Leijnse, K. Flensberg, J. Nygård, P. Krogstrup, and C. M. Marcus, "Majorana bound state in a coupled quantum-dot hybrid-nanowire system," *Science*, vol. 354, no. 6319, pp. 1557–1562, 2016.

[7] R. M. Lutchyn, E. P. A. M. Bakkers, L. P. Kouwenhoven, P. Krogstrup, C. M. Marcus, and Y. Oreg, "Majorana zero modes in superconductor-semiconductor heterostructures," *Nature Reviews Materials*, vol. 3, no. 5, pp. 52–68, 2018.

[8] A. Y. Kitaev, "Unpaired Majorana fermions in quantum wires," *Physics-Uspekhi*, vol. 44, no. 10S, p. 131, 2001.

[9] M. Leijnse and K. Flensberg, "Introduction to topological superconductivity and Majorana fermions," *Semiconductor Science and Technology*, vol. 27, no. 12, p. 124003, 2012.

[10] S. Vaitiekėnas, M. T. Deng, P. Krogstrup, and C. M. Marcus, "Flux-induced Majorana modes in full-shell nanowires," *arXiv e-prints*, 2018.

[11] R. M. Lutchyn, G. W. Winkler, B. van Heck, T. Karzig, K. Flensberg, L. I. Glazman, and C. Nayak, "Topological superconductivity in full shell proximitized nanowires," *arXiv e-prints*, 2018.

[12] K. Flensberg, "Tunneling characteristics of a chain of Majorana bound states," *Phys. Rev. B*, vol. 82, p. 180516, 2010.

[13] W. A. Little and R. D. Parks, "Observation of quantum periodicity in the transition temperature of a superconducting cylinder," *Phys. Rev. Lett.*, vol. 9, pp. 9–12, 1962.

[14] A. A. Abrikosov, *Fundamentals of the theory of metals.* North Holland (Elsevier Science Publishers B. V.), 1988.

[15] R. P. Groff and R. D. Parks, "Fluxoid quantization and field-induced depairing in a hollow superconducting microcylinder," *Phys. Rev.*, vol. 176, pp. 567–580, 1968.

[16] M. Tinkham, *Introduction to Superconductivity.* Dover Publications, Inc., 2nd ed., 1996.

[17] H. Smith, *Introduction to Many-particle Physics.* H. C. Ørsted Institute, University of Copenhagen, 1994.

[18] Y. Liu, Y. Zadorozhny, M. M. Rosario, B. Y. Rock, P. T. Carrigan, and H. Wang, "Destruction of the global phase coherence in ultrathin, doubly connected superconducting cylinders," *Science*, vol. 294, no. 5550, pp. 2332–2334, 2001.

[19] I. Sternfeld, E. Levy, M. Eshkol, A. Tsukernik, M. Karpovski, H. Shtrikman, A. Kretinin, and A. Palevski, "Magnetoresistance oscillations of superconducting Al-film cylinders covering InAs nanowires below the quantum critical point," *Phys. Rev. Lett.*, vol. 107, p. 037001, 2011.

[20] P.-G. de Gennes, "Champ critique d'une boucle supraconductrice ramifiée," *C. R. Acad. Sc. Paris*, no. 292, pp. 279–282, 1981.

[21] V. H. Dao and L. F. Chibotaru, "Destruction of global coherence in long superconducting nanocylinders," *Phys. Rev. B*, vol. 79, p. 134524, 2009.

[22] G. Schwiete and Y. Oreg, "Persistent current in small superconducting rings," *Phys. Rev. Lett.*, vol. 103, p. 037001, 2009.

[23] G. Schwiete and Y. Oreg, "Fluctuation persistent current in small superconducting rings," *Phys. Rev. B*, vol. 82, p. 214514, 2010.

[24] E. B. Hansen, *Majorana Bound States in Semiconductor-Superconductor Hybrid Devices.* PhD thesis, Center for Quantum Devices, Niels Bohr Institute, University of Copenhagen, 2018.

[25] G. E. Blonder, M. Tinkham, and T. M. Klapwijk, "Transition from metallic to tunneling regimes in superconducting microconstrictions: Excess current, charge imbalance, and supercurrent conversion," *Phys. Rev. B*, vol. 25, pp. 4515–4532, 1982.

[26] J. A. Sauls, "Andreev bound states and their signatures," *Philosophical Transactions of the Royal Society of London Series A*, vol. 376, p. 20180140, 2018.

[27] H. Bruus and K. Flensberg, *Many-body Quantum Theory in Condensed Matter Physics - an introduction.* United States: Oxford University Press, 2004.

[28] A. E. G. Mikkelsen, P. Kotetes, P. Krogstrup, and K. Flensberg, "Hybridization at superconductor-semiconductor interfaces," *Phys. Rev. X*, vol. 8, p. 031040, 2018.

[29] S. Blundell, *Magnetism in Condensed Matter.* Oxford University Press, 1st ed., 2001.

[30] K. F. Riley and M. P. Hobson, *Essential Mathematical Methods for the Physical Sciences.* Cambrigde University Press, 2011.

[31] S. Das Sarma, J. D. Sau, and T. D. Stanescu, "Splitting of the zero-bias conductance peak as smoking gun evidence for the existence of the Majorana mode in a superconductor-semiconductor nanowire," *Phys. Rev. B*, vol. 86, p. 220506, 2012.

[32] Y. V. Nazarov and Y. M. Blanter, *Quantum Transport*. Cambridge CB2 8RU, UK: Cambridge University Press, 2009.

[33] I. L. Aleiner, P. W. Brouwer, and L. I. Glazman, "Quantum effects in Coulomb blockade," *Physics Reports*, vol. 358, no. 5, pp. 309 – 440, 2002.

Appendices

A Detailed calculations for section 4

A.1 The commutator $[J_z, H_{\mathbf{BdG}}]$

$$\begin{aligned}[J_z, H_{BdG}] &= \left[-i\partial_\varphi + \frac{1}{2}\sigma_z + \frac{1}{2}n\tau_z \ , \ \alpha_r p_z \sigma_\varphi \tau_z + \Delta(r)\left(\cos(n\varphi)\tau_x + \sin(n\varphi)\tau_y\right)\right] \\ &= \alpha_r p_z \tau_z \underbrace{\left[-i\partial_\varphi + \frac{1}{2}\sigma_z \ , \ \sigma_\varphi\right]}_{①} + \Delta(r) \underbrace{\left[-i\partial_\varphi + \frac{1}{2}n\tau_z \ , \ \cos(n\varphi)\tau_x + \sin(n\varphi)\tau_y\right]}_{②}.\end{aligned}$$

$$① = \underbrace{[-i\partial_\varphi \ , \ \sigma_y\cos(\varphi) - \sigma_x\sin(\varphi)]}_{1a} + \frac{1}{2}\underbrace{[\sigma_z \ , \ \sigma_y\cos(\varphi) - \sigma_x\sin(\varphi)]}_{1b}.$$

We calculate (1a) by use of a test function $f(\varphi)$.

$$\begin{aligned}(1a)f(\varphi) &= -i\partial_\varphi\left\{(\sigma_y\cos(\varphi) - \sigma_x\sin(\varphi))f(\varphi)\right\} + i(\sigma_y\cos(\varphi) - \sigma_x\sin(\varphi))\partial_\varphi f(\varphi) \\ &= -i\left\{(-\sigma_y\sin(\varphi) - \sigma_x\cos(\varphi))f(\varphi) + (\sigma_y\cos(\varphi) - \sigma_x\sin(\varphi))f'(\varphi)\right\} \\ &+ i(\sigma_y\cos(\varphi) - \sigma_x\sin(\varphi))f'(\varphi) \\ &= i(\sigma_y\sin(\varphi) + \sigma_x\cos(\varphi))f(\varphi).\end{aligned}$$

Using that the Pauli matrices anticommute we write (1b) as

$$(1b) = 2\sigma_z\left(\sigma_y\cos(\varphi) - \sigma_x\sin(\varphi)\right) = -2i\sigma_x\cos(\varphi) - 2i\sigma_y\sin(\varphi).$$

$$① = (1a) + \frac{1}{2}(1b) = 0.$$

For ② the procedure is the same

$$② = \underbrace{[-i\partial_\varphi \ , \ \tau_x\cos(n\varphi) + \tau_y\sin(n\varphi)]}_{2a} + \frac{1}{2}n\underbrace{[\tau_z \ , \ \tau_x\cos(n\varphi) + \tau_y\sin(n\varphi)]}_{2b}.$$

$$\begin{aligned}(2a)f(\varphi) &= -i\left\{(-n\tau_x\sin(n\varphi) + n\tau_y\cos(n\varphi))f(\phi) + (\tau_x\cos(n\varphi) + \tau_y\sin(n\varphi))f'(\varphi)\right\} \\ &+ i(\tau_x\cos(n\varphi) + \tau_y\sin(n\varphi))f'(\varphi) \\ &= in(\tau_x\sin(n\varphi) - \tau_y\cos(n\varphi))f(\phi).\end{aligned}$$

$$(2b) = 2\tau_z(\tau_x\cos(n\varphi) + \tau_y\sin(n\varphi)) = 2i\tau_y\cos(n\varphi) - 2i\tau_x\sin(n\varphi).$$

$$② = (2a) + \frac{1}{2}n(2b) = 0.$$

A.2 Transformation from $H_{\mathbf{BdG}}$ to $\tilde{H}_{\mathbf{BdG}}$

In the transformation of the Hamiltonian H_{BdG} in Eq. (4.3) by

$$U = \exp\left[-i\left(m_J - \frac{1}{2}\sigma_z - \frac{n}{2}\tau_z\right)\varphi\right],$$

we have made the following calculations.

$$U\sigma_\varphi U^\dagger = e^{i\varphi\sigma_z/2}(\sigma_y\cos(\varphi) - \sigma_x\sin(\varphi))e^{-i\varphi\sigma_z/2}.$$

$$\begin{aligned} e^{i\varphi\sigma_z/2}\sigma_y e^{-i\varphi\sigma_z/2} &= \left(\mathbb{1} + \frac{i\varphi}{2}\sigma_z + \frac{1}{2}\left(\frac{i\varphi}{2}\right)^2\mathbb{1} + \frac{1}{3!}\left(\frac{i\varphi}{2}\right)^3\sigma_z + \dots\right)\sigma_y e^{-i\varphi\sigma_z/2} \\ &= \sigma_y\left(\mathbb{1} - \frac{i\varphi}{2}\sigma_z + \frac{1}{2}\left(\frac{i\varphi}{2}\right)^2\mathbb{1} - \frac{1}{3!}\left(\frac{i\varphi}{2}\right)^3\sigma_z + \dots\right)e^{-i\varphi\sigma_z/2} \\ &= \sigma_y e^{-i\varphi\sigma_z}, \end{aligned}$$

A similar calculation is made for the σ_x term where we write $\sigma_x = -i\sigma_y\sigma_z$. In total we thus obtain

$$\begin{aligned} U\sigma_\varphi U^\dagger &= \sigma_y\left(\mathbb{1}\cos(\varphi) + i\sigma_z\sin(\varphi)\right)e^{-i\varphi\sigma_z} \\ &= \sigma_y\left(\mathbb{1} + \varphi i\sigma_z - \frac{1}{2}\varphi^2\mathbb{1} - \frac{1}{3!}\varphi^3 i\sigma_z + \dots\right)e^{-i\varphi\sigma_z} = \sigma_y. \end{aligned}$$

For the pairing term in H_{BdG} we make the same kind of calculations and find

$$U(\cos(n\varphi)\tau_x + \sin(n\varphi)\tau_y)U^\dagger = \tau_x\left(\cos(n\varphi) + i\tau_z\sin(n\varphi)\right)e^{-in\varphi\tau_z} = \tau_x.$$

B Topology phase diagrams

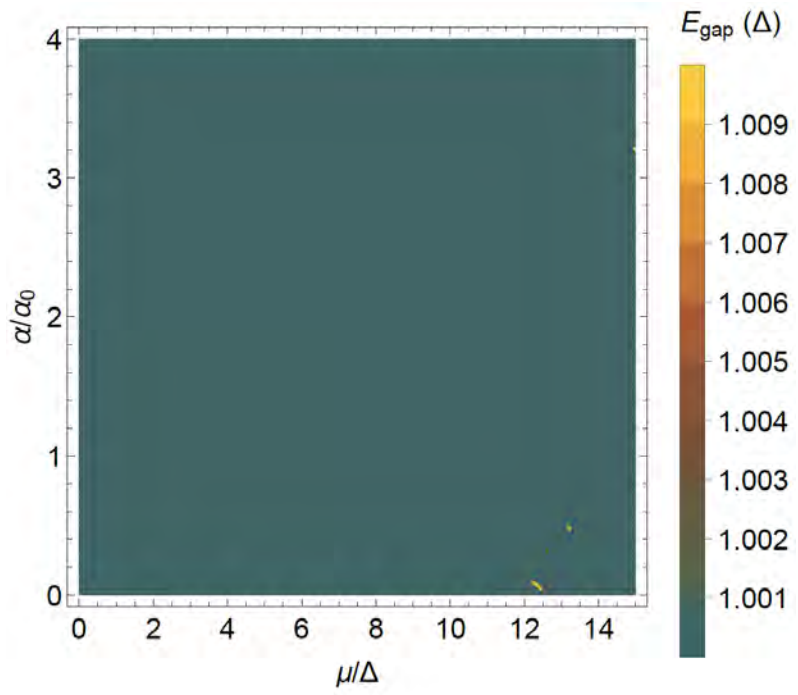

Figure B.1: Contour plot of the energy gap in the spectrum of $\sum_{m_J} \tilde{H}_{m_J,p_z}(\phi = 0)$ with no magnetic flux through the nanowire. Notice that the scale is different from the other phase diagrams and that the gap is 1Δ throughout the shown part of (μ, α) space. Hence there are no phase transition lines and since the gap is known to be trivial for $(\mu = 0, \alpha = 0)$ [1, 2], the entire domain is trivial. Zero flux implies no phase winding of the order parameter $n = 0$, meaning m_J is an odd half-integer. The sum $\sum_{m_J}$ runs over $-2.5, -1.5, \ldots, 2.5$ i.e. $m_J^{\max} = 2.5$. The plot is made for a wire radius $R_2 = 0.5R_0$ and without a Zeeman energy $B_Z = 0$. Adding a $V_0 \cos(2\varphi)\tau_z$ deformation does not change this picture.

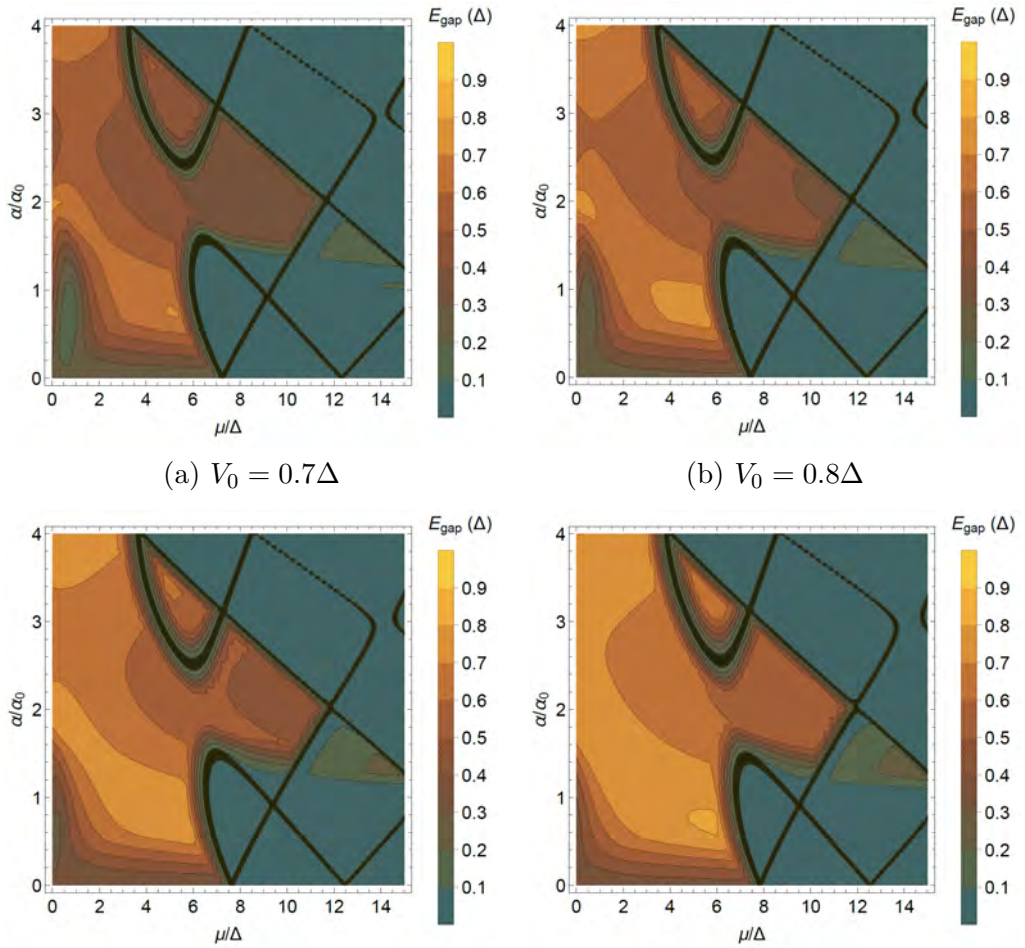

(a) $V_0 = 0.7\Delta$ (b) $V_0 = 0.8\Delta$

(c) $V_0 = 0.9\Delta$ (d) $V_0 = 1.0\Delta$

Figure B.2: Topology phase diagrams for the same parameter values as in Fig. 5.1 in the main text but with stronger symmetry-breaking potential $V_0 \cos(2\varphi)$. The induced non-trivial gap in the $(7, 1.2)$ domain, which was seen to appear for lower values of V_0, is now closed again. Although the induced gap in the non-trivial $(5, 3)$ domain has become larger with growing V_0, its area in (μ, α) space is diminished.

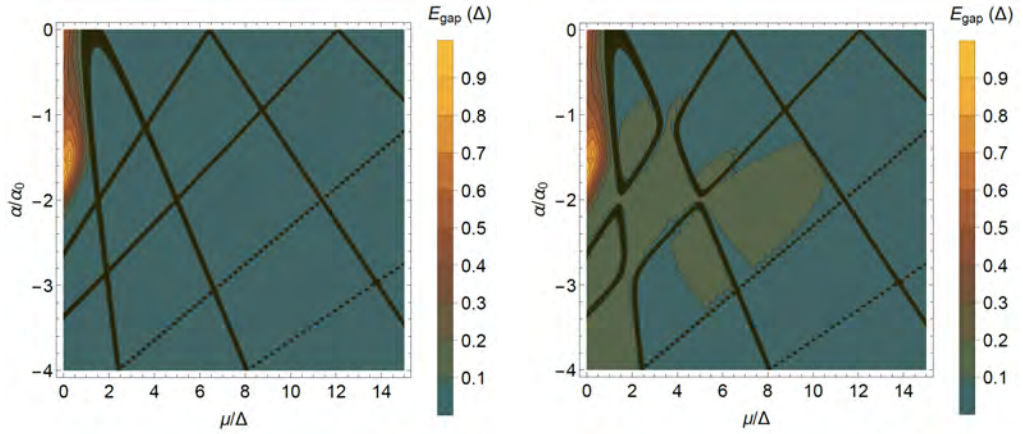

(a) $V_0 = 0\Delta$ (b) $V_0 = 0.1\Delta$

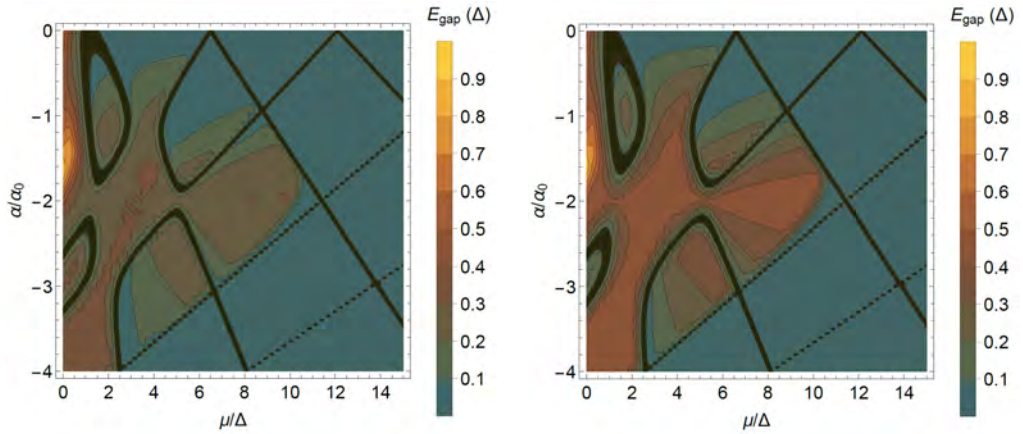

(c) $V_0 = 0.2\Delta$ (d) $V_0 = 0.3\Delta$

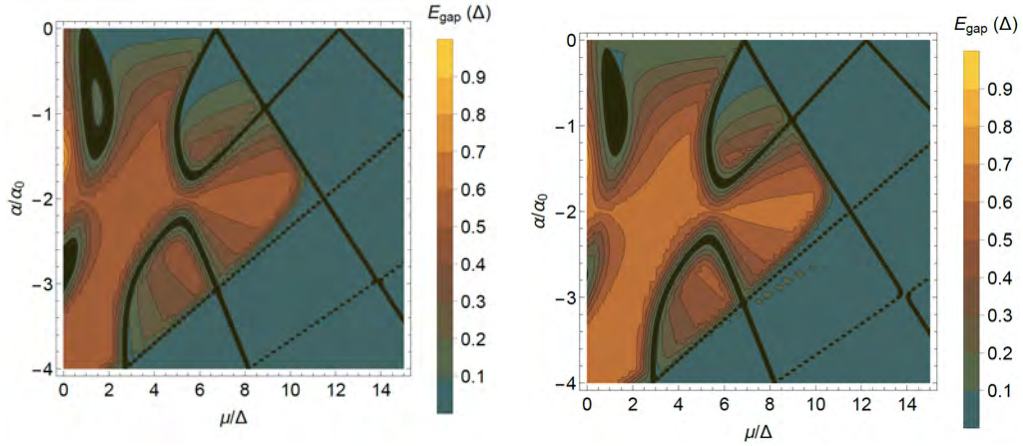

(e) $V_0 = 0.4\Delta$ (f) $V_0 = 0.5\Delta$

Figure B.3: Topology phase diagrams similar to the ones in Fig. 5.1 but for negative values of the spin-orbit coupling strength α. Notice that these do not mirror the behaviour for $\alpha > 0$ except for the phase transition lines. For instance, there is no non-trivial gap without deformation but one is opened in the lobe including point $(5\Delta, -3\alpha_0)$ and another one in $(7\Delta, -1\alpha_0)$ as V_0 is increased. At $V_0 = 0.5\Delta$ the induced gap is as large as 0.5Δ.

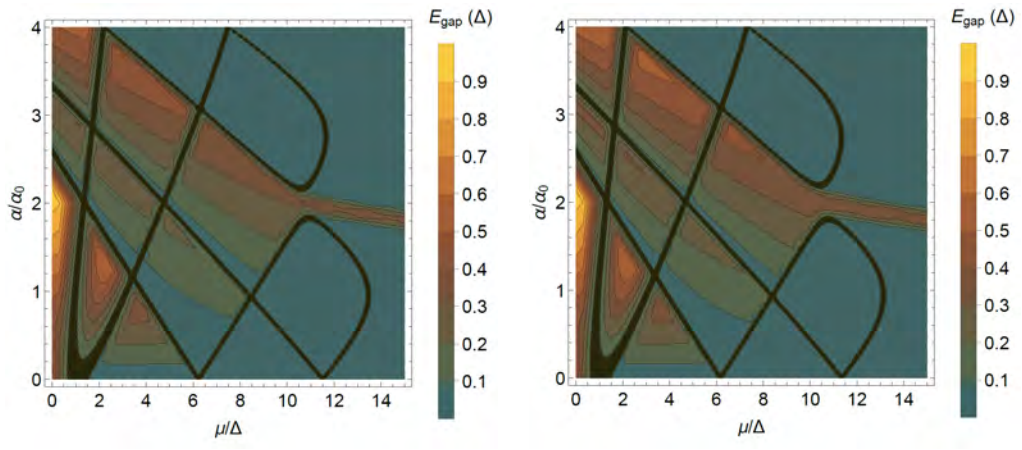

(a) $V_0 = 0.7\Delta$ (b) $V_0 = 0.8\Delta$

(c) $V_0 = 0.9\Delta$ (d) $V_0 = 1.0\Delta$

Figure B.4: Topology phase diagrams for same parameter values as in Fig. 5.3 in the main text but with stronger symmetry-breaking potential $V_0 \cos(4\varphi)$. The $(2.3, 1.3)$ non-trivial domain is still unaffected by the deformation and the non-trivial gaps in the $(7, 1.2)$ and $(5, 3)$ domains continues to increase with stronger V_0.

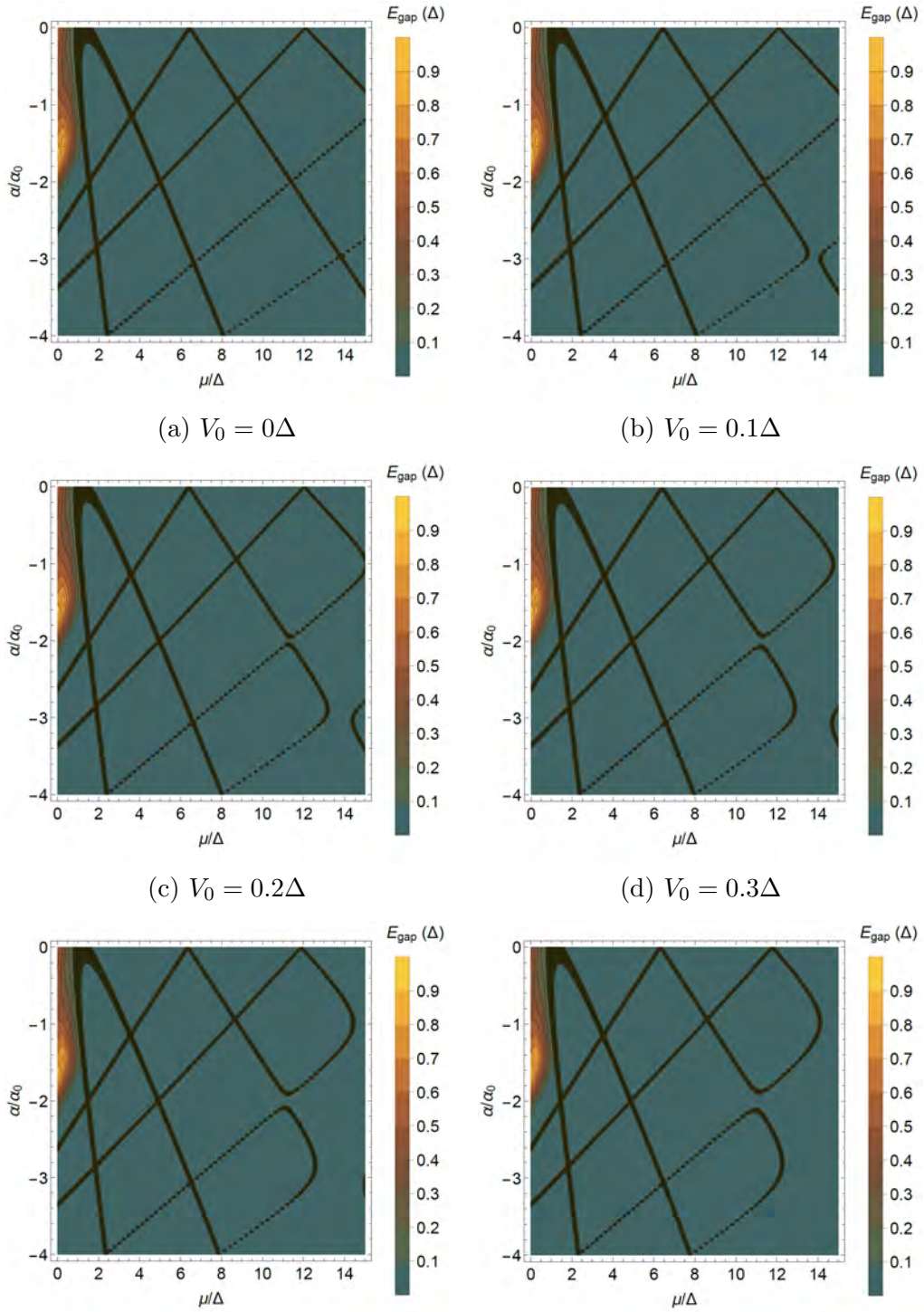

(a) $V_0 = 0\Delta$ (b) $V_0 = 0.1\Delta$

(c) $V_0 = 0.2\Delta$ (d) $V_0 = 0.3\Delta$

(e) $V_0 = 0.4\Delta$ (f) $V_0 = 0.5\Delta$

Figure B.5: Topology phase diagrams similar to the ones in Fig. 5.3 but for negative values of the spin-orbit coupling strength α. Notice that only the black phase transition lines mirror the behaviour for $\alpha > 0$. There are no non-trivial gaps even with a $\cos(4\varphi)$ deformation.

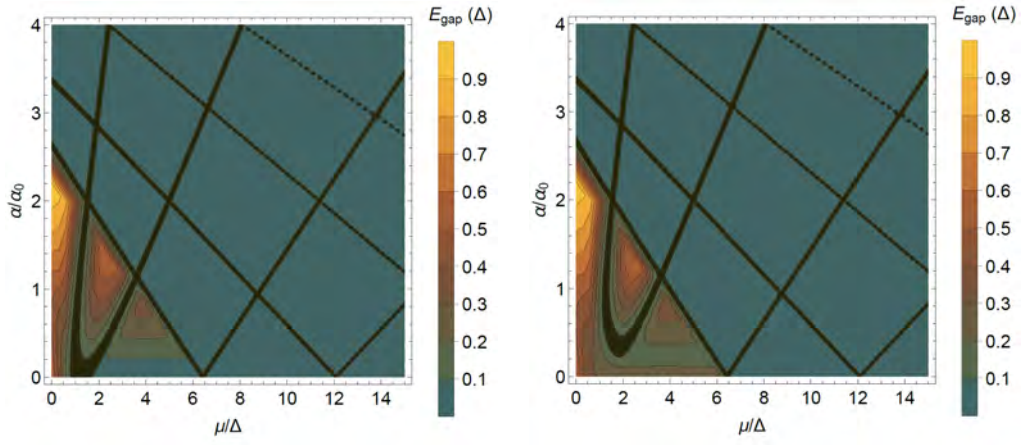

(a) $V_0 = 0\Delta$ (b) $V_0 = 0.1\Delta$

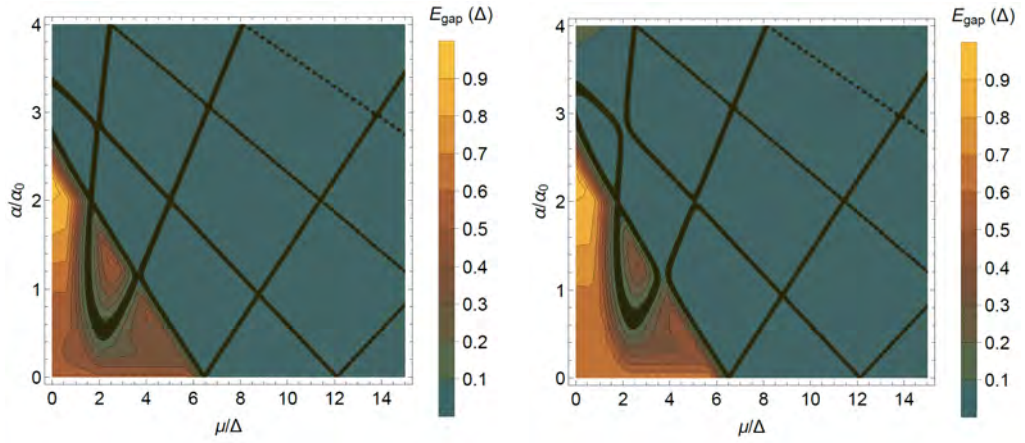

(c) $V_0 = 0.2\Delta$ (d) $V_0 = 0.3\Delta$

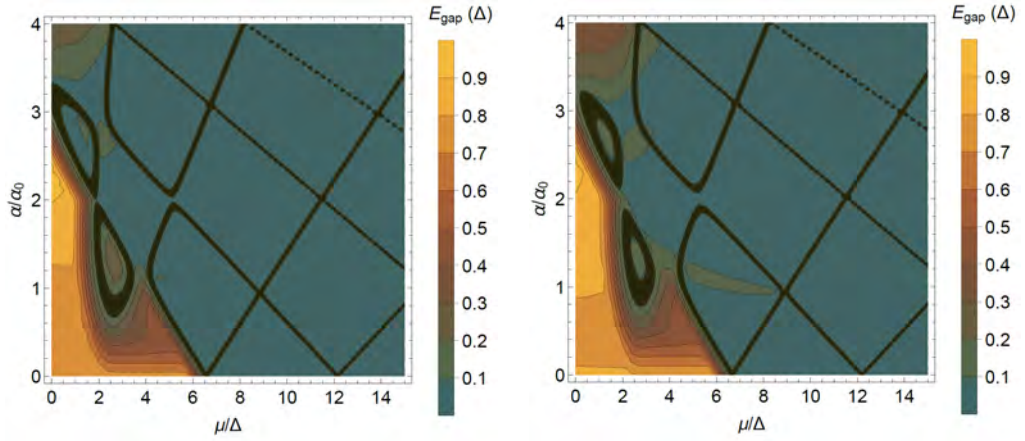

(e) $V_0 = 0.4\Delta$ (f) $V_0 = 0.5\Delta$

Figure B.6: Topology phase diagrams for the full-shell nanowire system described by $\sum_{m_J} \tilde{H}_{m_J,p_z}$ with a "p-like" symmetry-breaking deformation $V(\varphi) = V_0 \cos(\varphi)\tau_z$ effectively coupling all states. As opposed to the d and g-like potentials this does not have any advantages in terms of expanding the non-trivial parameter space. On the contrary, the p-like deformation closes the original non-trivial $(2.3, 1.3)$ domain. Parameters used in the calculation are: $\tilde{\Phi} = \frac{1}{2}$, $n = 1$, $R_2 = 0.5R_0$, $B_Z = 0$, and $m_J^{\max} = 3$.

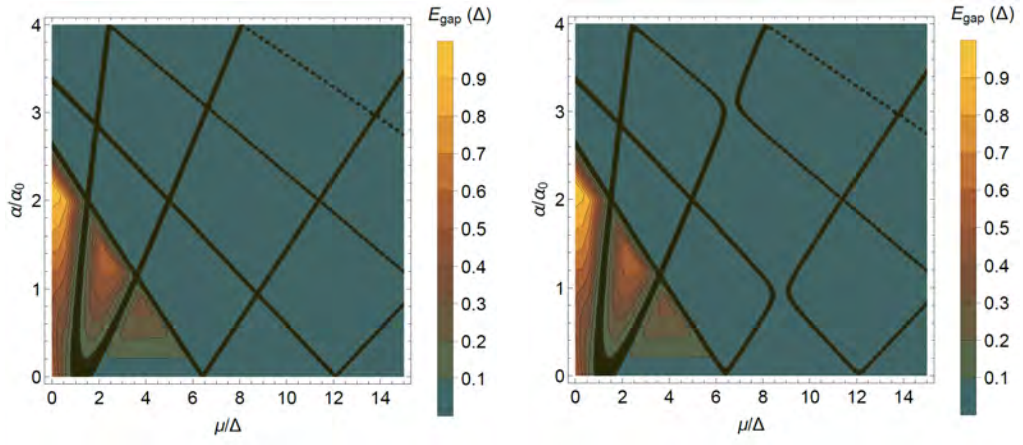

(a) $V_0 = 0\Delta$ (b) $V_0 = 0.1\Delta$

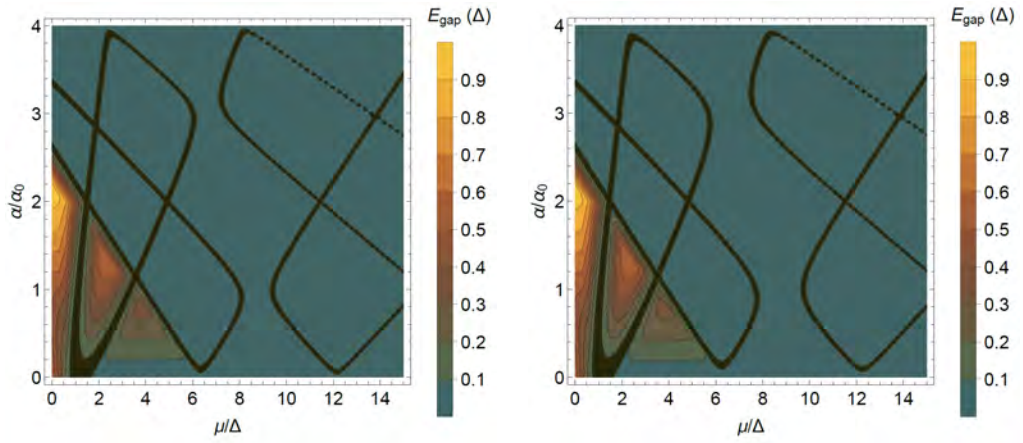

(c) $V_0 = 0.2\Delta$ (d) $V_0 = 0.3\Delta$

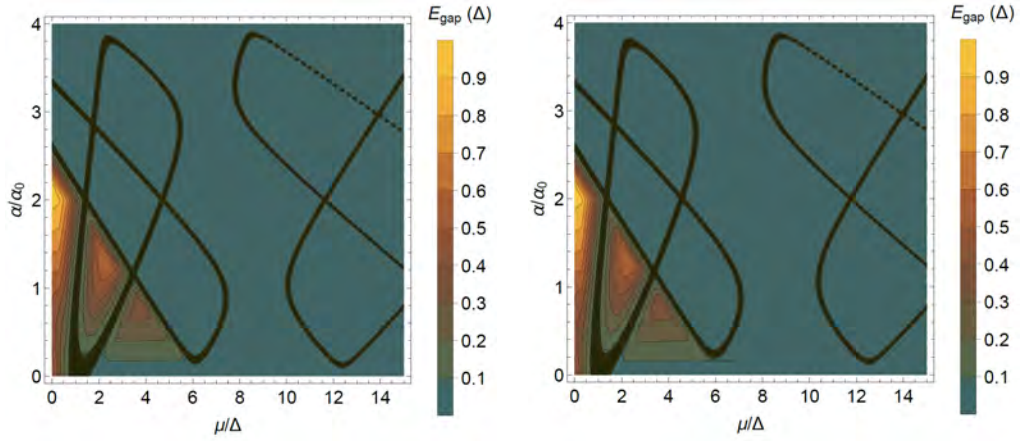

(e) $V_0 = 0.4\Delta$ (f) $V_0 = 0.5\Delta$

Figure B.7: Topology phase diagrams for the full-shell nanowire system described by $\sum_{m_J} \tilde{H}_{m_J,p_z}$ with an "f-like" symmetry-breaking deformation $V(\varphi) = V_0 \cos(3\varphi)\tau_z$ introduced to prevent the crossing of $m_J = 3$ and $m_J = -3$ bands at zero energy. We observe that the area in (μ, α) space containing a non-trivial gap neither changes in size nor position with increasing V_0. Parameters used in the calculation are: $\tilde{\Phi} = \frac{1}{2}$, $n = 1$, $R_2 = 0.5R_0$, $B_{\text{Z}} = 0$, and $m_J^{\text{max}} = 3$.

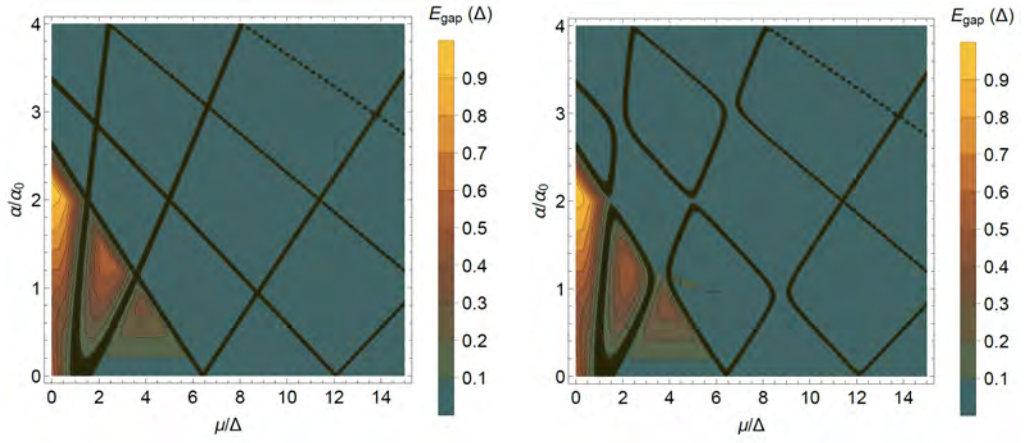

(a) $V_0 = 0\Delta$ (b) $V_0 = 0.1\Delta$

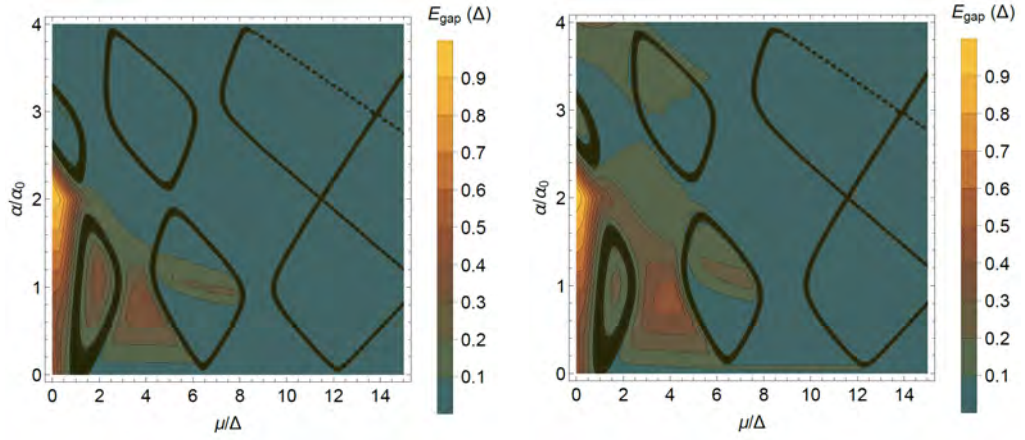

(c) $V_0 = 0.2\Delta$ (d) $V_0 = 0.3\Delta$

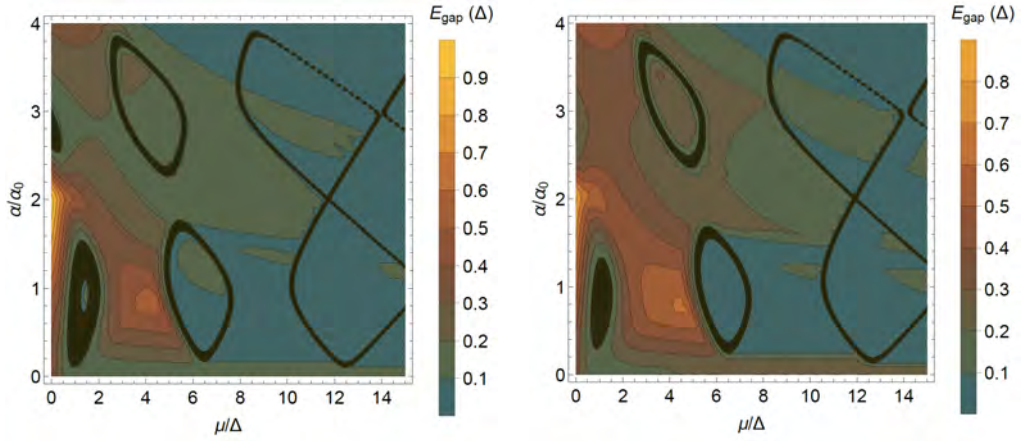

(e) $V_0 = 0.4\Delta$ (f) $V_0 = 0.5\Delta$

Figure B.8: Topology phase diagrams for the full-shell nanowire system described by $\sum_{m_J} \tilde{H}_{m_J,p_z}$ with a symmetry-breaking deformation $V(\varphi) = V_0(\cos(2\varphi) + \cos(3\varphi))\tau_z$. Comparing with Fig. 5.1, we observe that an f-like potential only reduces the beneficial effects of a d-like one. System parameters used for the calculation are: $\tilde{\Phi} = \frac{1}{2}$, $n = 1$, $R_2 = 0.5R_0$, $B_Z = 0$, and $m_J^{\max} = 3$.

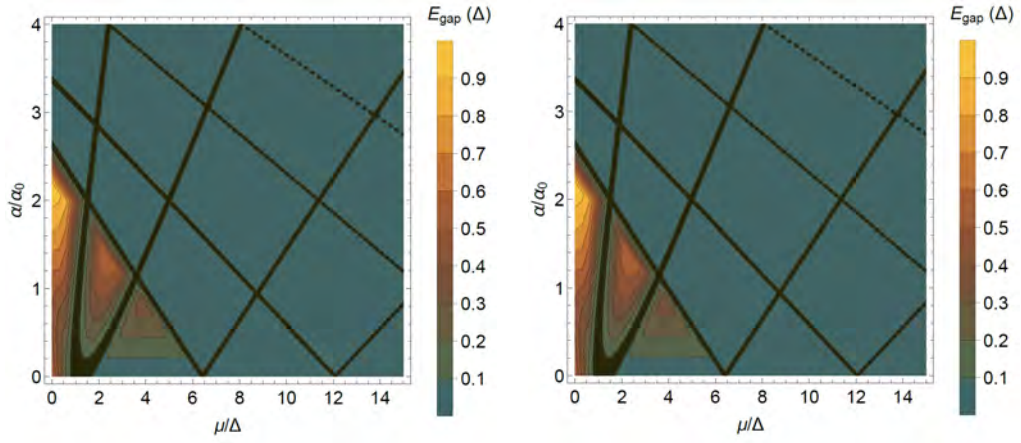

(a) $V_0 = 0\Delta$ (b) $V_0 = 0.3\Delta$

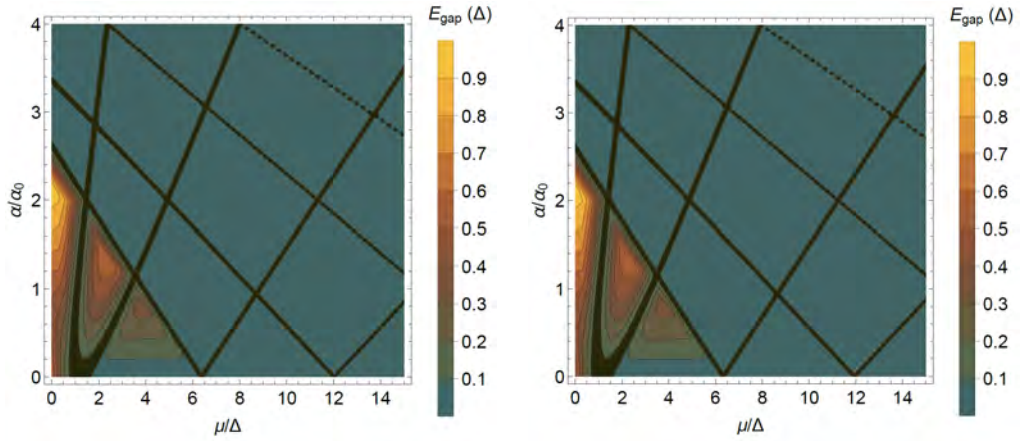

(c) $V_0 = 0.6\Delta$ (d) $V_0 = 0.9\Delta$

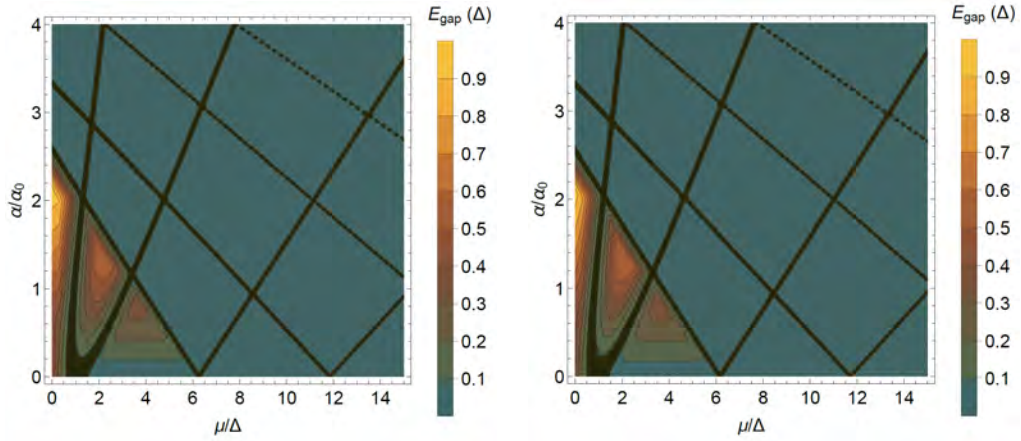

(e) $V_0 = 1.2\Delta$ (f) $V_0 = 1.5\Delta$

Figure B.9: Topology phase diagrams for the full-shell nanowire system described by $\sum_{m_J} \tilde{H}_{m_J,p_z}$ with a symmetry-breaking deformation $V(\varphi) = V_0 \cos(6\varphi)\tau_z$ modelling the hexagonal shape of the wires used in experiments by Vaitiekėnas et al. [10]. We see that even for $V_0 = 1.5\Delta$ the phase diagram is only minimally affected by such a deformation. Parameters used in the calculation are: $\tilde{\Phi} = \frac{1}{2}$, $n = 1$, $R_2 = 0.5R_0$, $B_{\text{Z}} = 0$, and $m_J^{\max} = 6$.

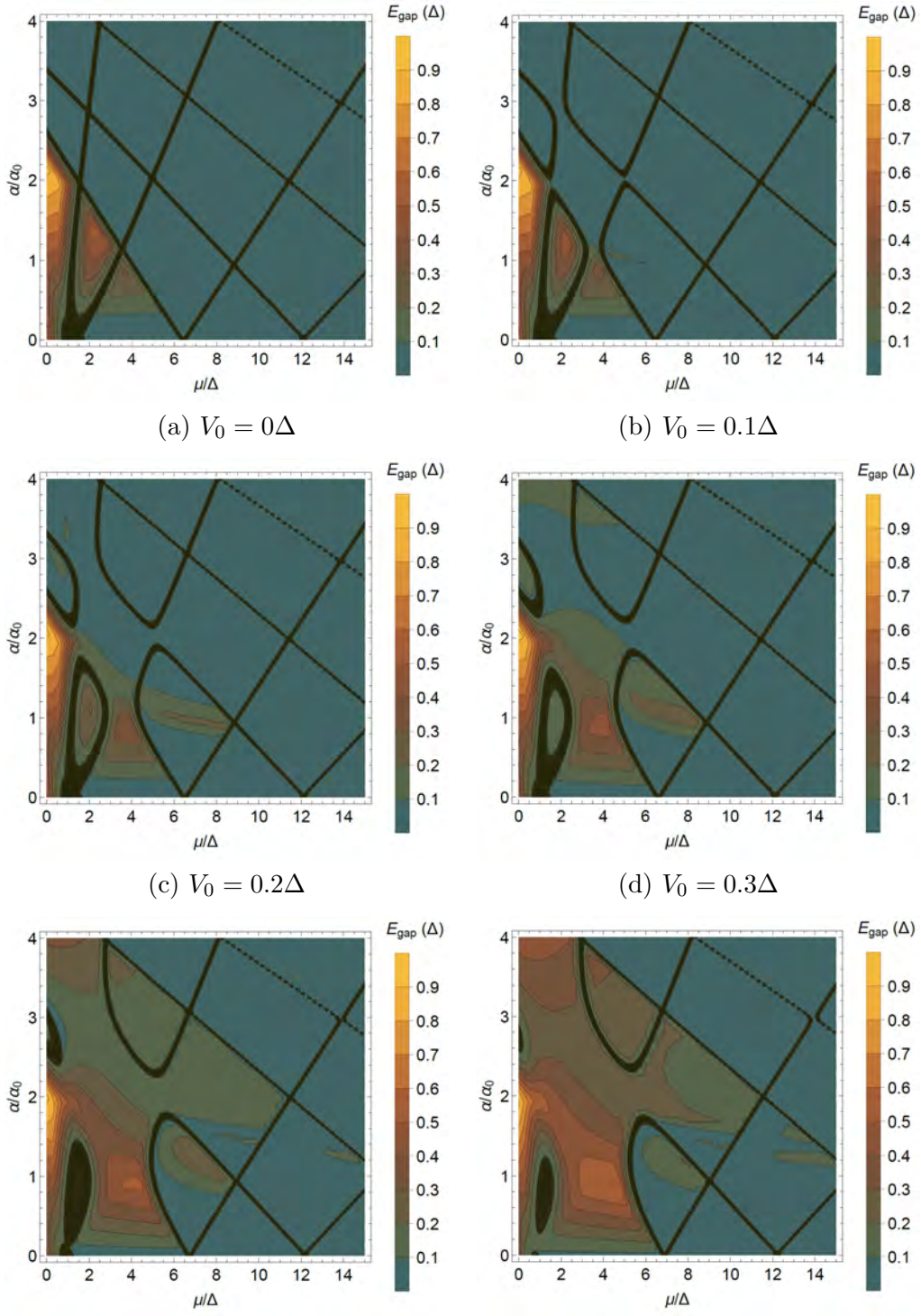

(a) $V_0 = 0\Delta$ (b) $V_0 = 0.1\Delta$

(c) $V_0 = 0.2\Delta$ (d) $V_0 = 0.3\Delta$

(e) $V_0 = 0.4\Delta$ (f) $V_0 = 0.5\Delta$

Figure B.10: Topology phase diagrams like the ones in Figs. 4.3 and 5.1 of the main text which are deformed by $V_0 \cos(2\varphi)$, but with a non-zero Zeeman field, $B_Z = g\mu_B B/2 \propto g = -2$. Comparing with the case $B_Z = 0$ one sees that the Zeeman effect has little influence on the phase diagram when the g-factor is of the order 1.

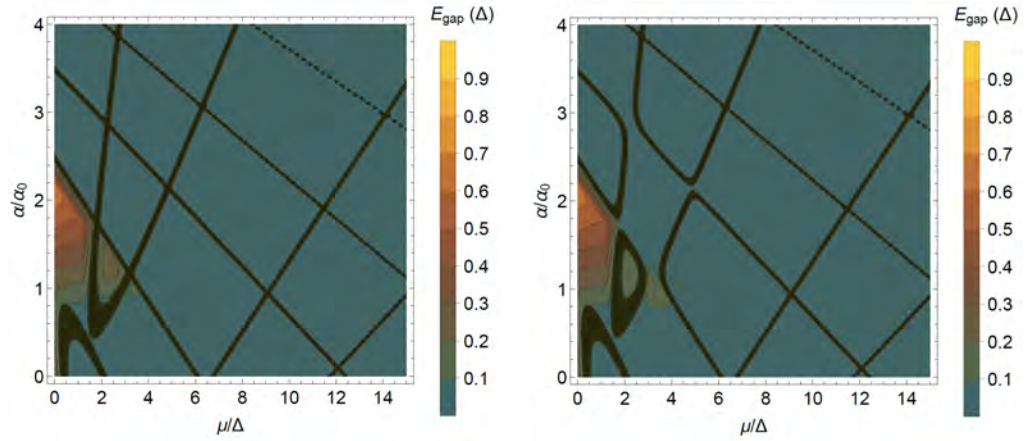

(a) $V_0 = 0\Delta$ (b) $V_0 = 0.1\Delta$

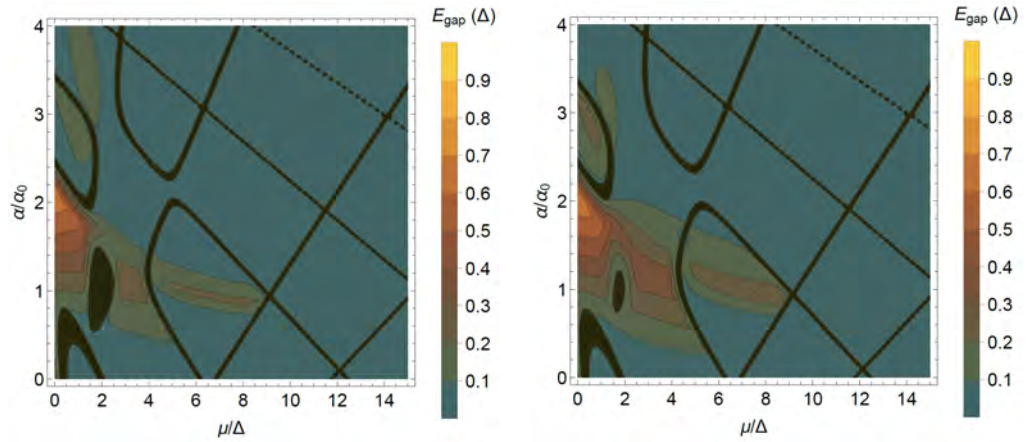

(c) $V_0 = 0.2\Delta$ (d) $V_0 = 0.3\Delta$

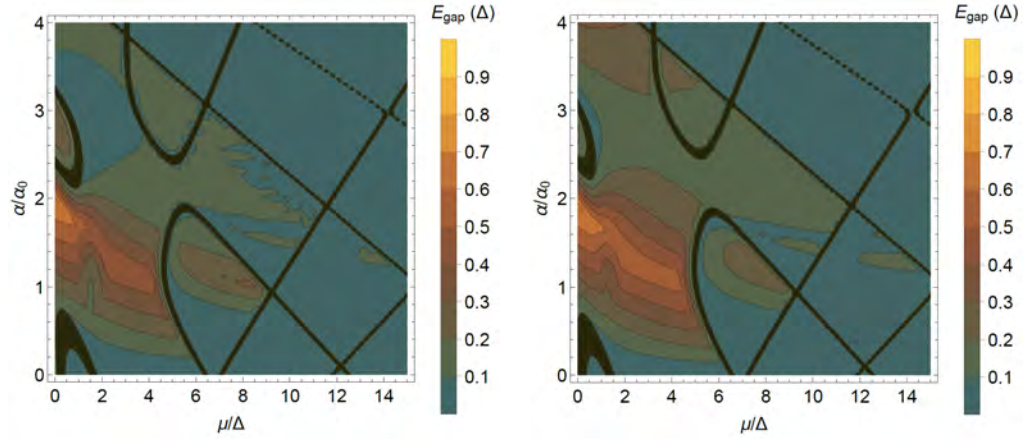

(e) $V_0 = 0.4\Delta$ (f) $V_0 = 0.5\Delta$

Figure B.11: Topology phase diagrams like the ones in Figs. 4.3 and 5.1 of the main text which are deformed by $V_0 \cos(2\varphi)$, but with a non-zero Zeeman field, $B_{\text{Z}} = g\mu_{\text{B}}B/2 \propto g = -12$. All other parameters are the same. The initial non-trivial domain dies out already at $V_0 = 0.2\Delta$ instead of $V_0 = 0.5\Delta$ which is the case with $g = 0$. The induced non-trivial gap in the $(7, 1.2)$ domain could seem to favour slightly from the stronger g-factor, but as in the cases $g = 0$ and $g = -2$ this gap dies out at higher $V_0 \sim 5\Delta$.

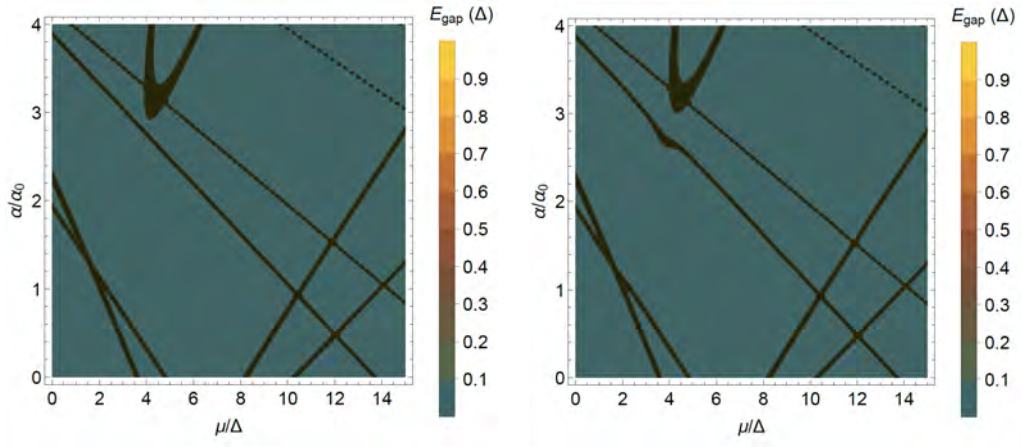

(a) $V_0 = 0\Delta$ (b) $V_0 = 0.1\Delta$

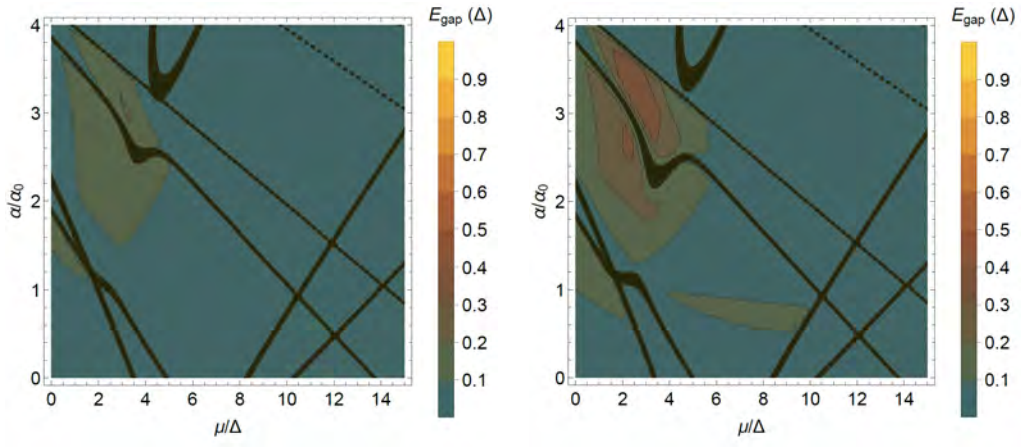

(c) $V_0 = 0.2\Delta$ (d) $V_0 = 0.3\Delta$

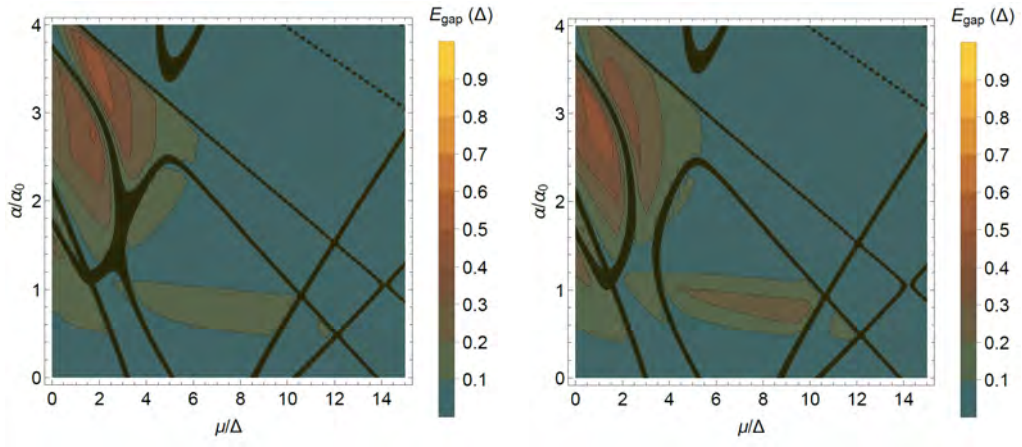

(e) $V_0 = 0.4\Delta$ (f) $V_0 = 0.5\Delta$

Figure B.12: Topology phase diagrams like the ones in Figs. 4.3 and 5.1 of the main text which are deformed by $V_0 \cos(2\varphi)$, but with a large Zeeman energy, $B_Z = g\mu_B B/2 \propto g = -60$. All other parameters are the same. Counting from the trivial origin ($\mu = 0, \alpha = 0$) we see that the emergent gap in the lobe containing the point $(2\Delta, 3.5\alpha_0)$ is non-trivial.

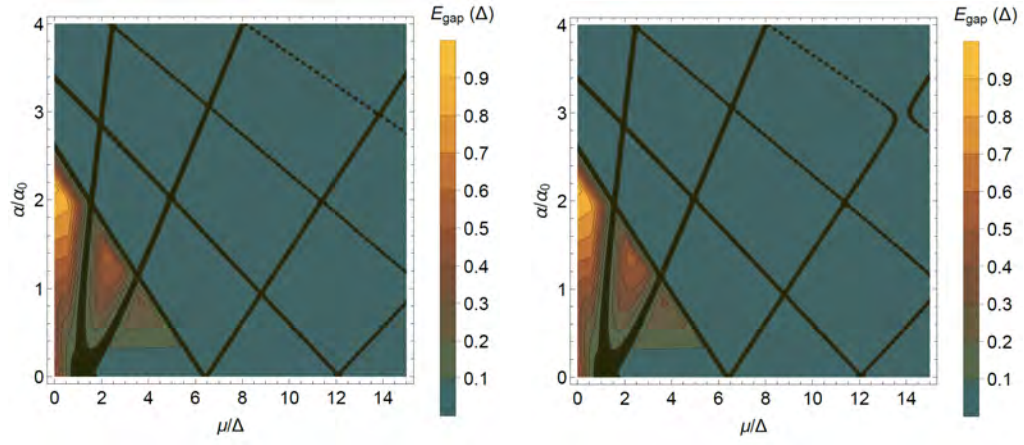

(a) $V_0 = 0\Delta$ (b) $V_0 = 0.1\Delta$

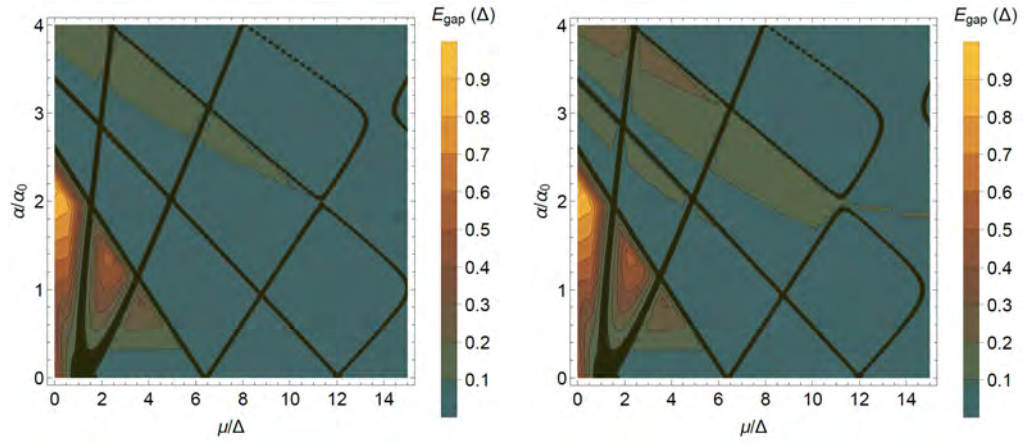

(c) $V_0 = 0.2\Delta$ (d) $V_0 = 0.3\Delta$

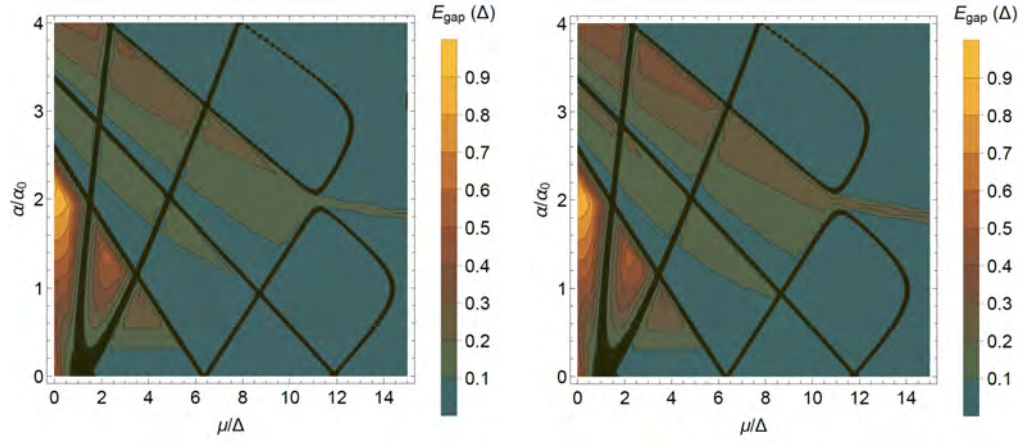

(e) $V_0 = 0.4\Delta$ (f) $V_0 = 0.5\Delta$

Figure B.13: Topology phase diagrams for the full-shell nanowire system described by $\sum_{m_J} \tilde{H}_{m_J,p_z}$ with a g-like deformation and a non-zero Zeeman field, $B_{\text{Z}} = g\mu_{\text{B}}B/2 \propto g = -2$. Comparing with Fig. 5.3 in the main text, we see that a g factor of order one brings no significant changes to the phase diagram. Parameters used in the calculation are: $\tilde{\Phi} = \frac{1}{2}$, $n = 1$, $R_2 = 0.5R_0$, $m_J^{\max} = 4$.

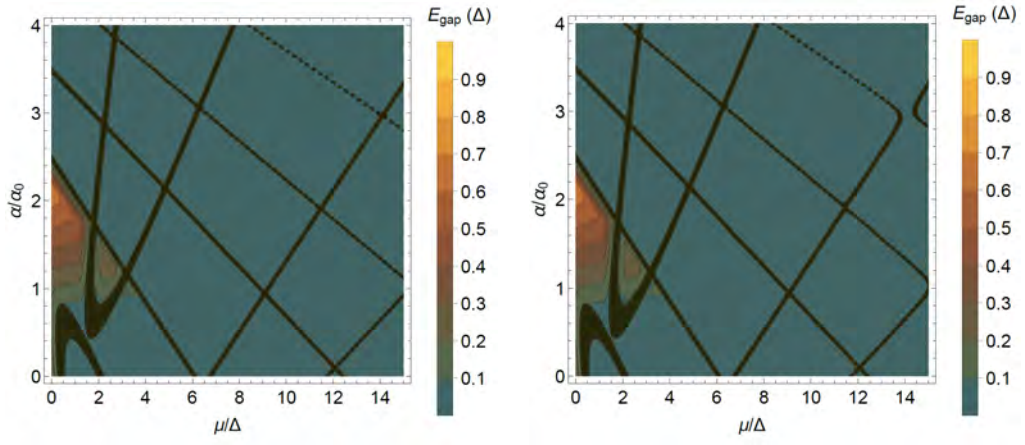

(a) $V_0 = 0\Delta$ (b) $V_0 = 0.1\Delta$

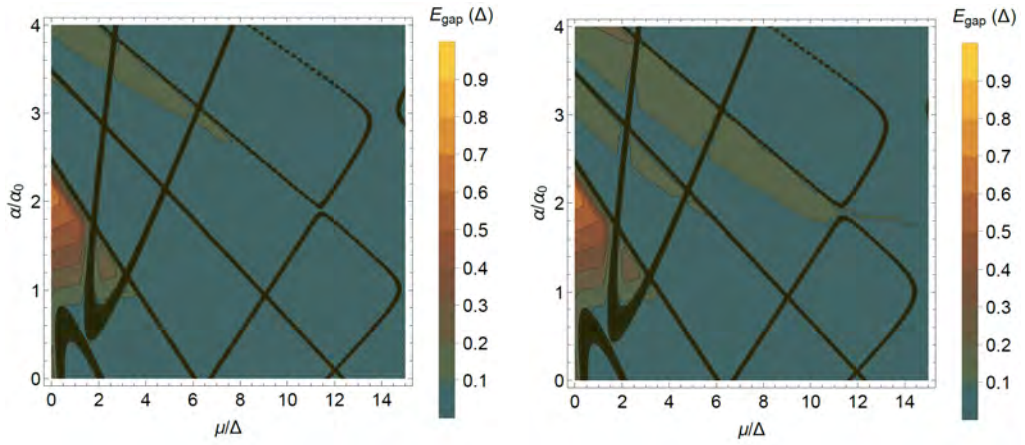

(c) $V_0 = 0.2\Delta$ (d) $V_0 = 0.3\Delta$

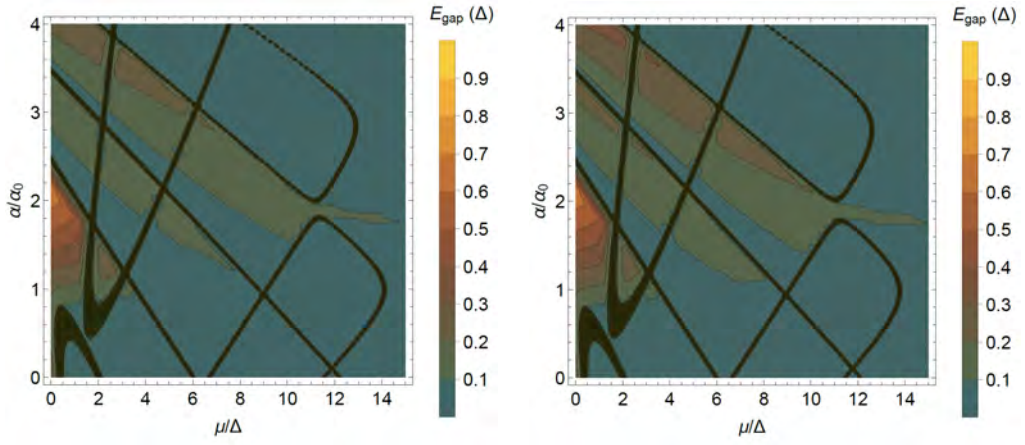

(e) $V_0 = 0.4\Delta$ (f) $V_0 = 0.5\Delta$

Figure B.14: Topology phase diagrams for the full-shell nanowire system described by $\sum_{m_J} \tilde{H}_{m_J,p_z}$ with a g-like deformation and a non-zero Zeeman field, $B_{\text{Z}} = g\mu_{\text{B}}B/2 \propto g = -12$. Comparing with Fig. 5.3 in the main text, we see that a g factor of order 10 has a significant effect on the phase diagram. Parameters used in the calculation are: $\tilde{\Phi} = \frac{1}{2}$, $n = 1$, $R_2 = 0.5R_0$, and $m_J^{\max} = 4$.

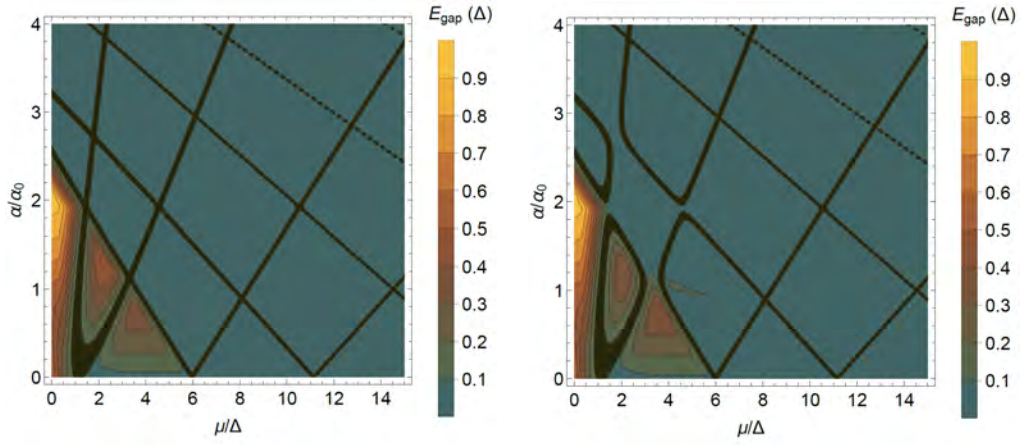

(a) $V_0 = 0\Delta$ (b) $V_0 = 0.1\Delta$

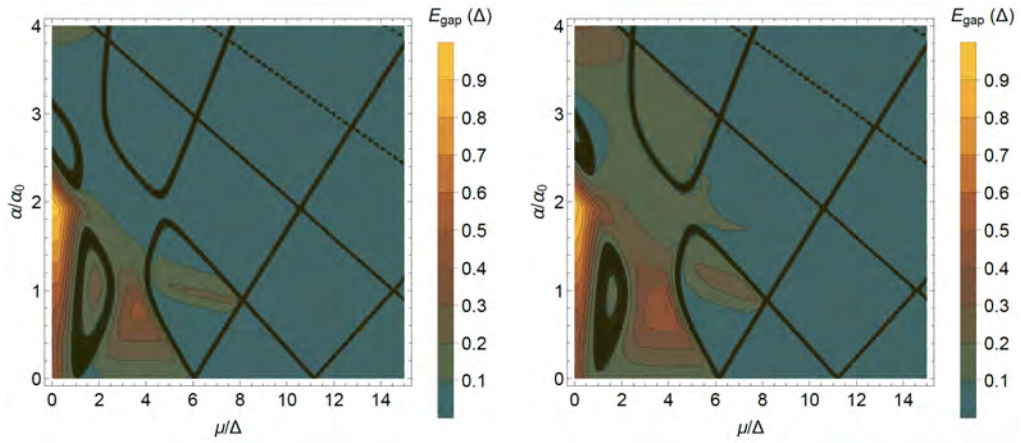

(c) $V_0 = 0.2\Delta$ (d) $V_0 = 0.3\Delta$

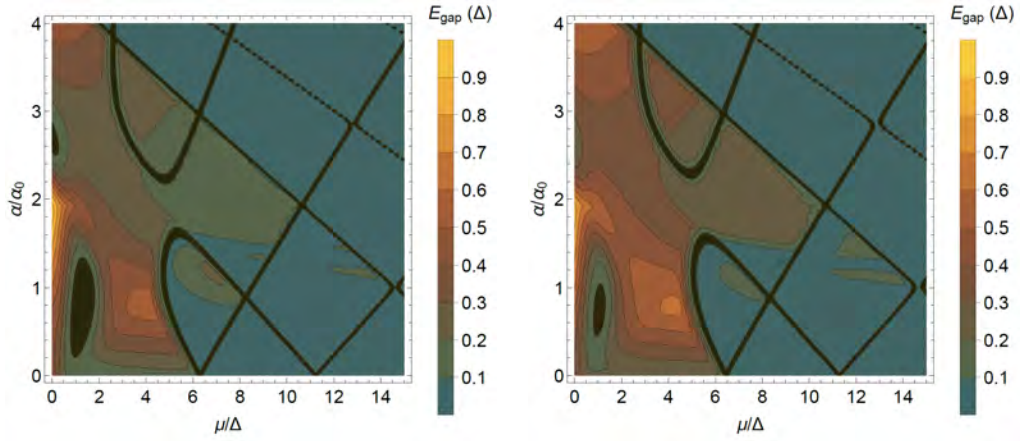

(e) $V_0 = 0.4\Delta$ (f) $V_0 = 0.5\Delta$

Figure B.15: Topology phase diagrams for the full-shell nanowire system described by $\sum_{m_J} \tilde{H}_{m_J,p_z}$ with $B_Z = 0$ and a deformation $V_0 \cos(2\varphi)$. The flux through the cylinder is $\tilde{\Phi} = \frac{1}{2}$, the winding is $n = 1$, and the radius is $R_2 = 0.52R_0$. Bands are included up to and with $m_J^{\max} = 4$. The only changed parameter from Fig. 5.1 is thus a 4% increase in radius.

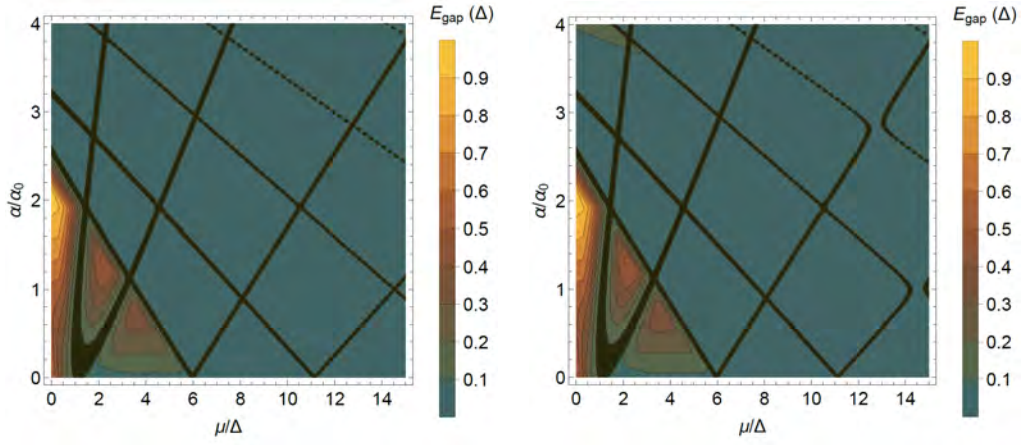

(a) $V_0 = 0\Delta$ (b) $V_0 = 0.1\Delta$

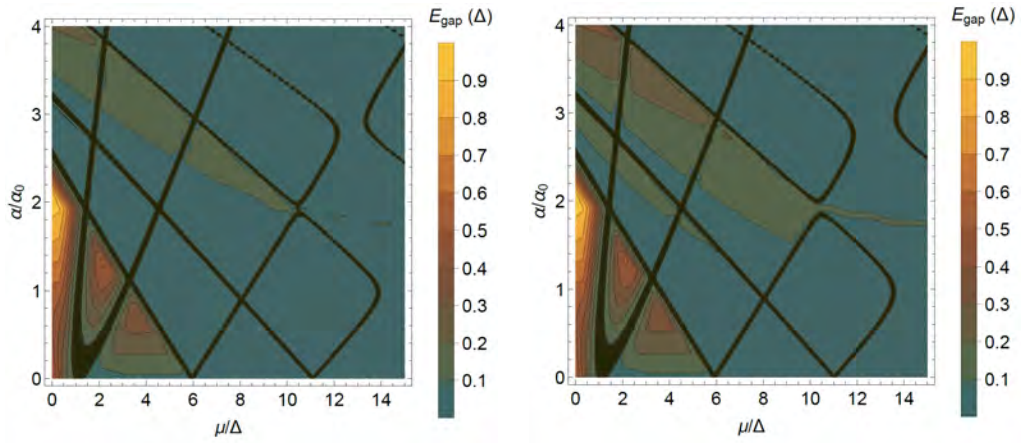

(c) $V_0 = 0.2\Delta$ (d) $V_0 = 0.3\Delta$

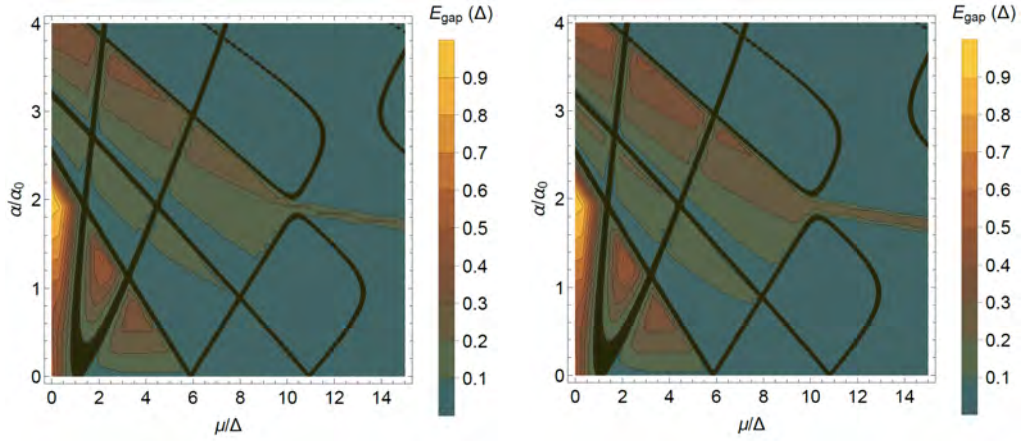

(e) $V_0 = 0.4\Delta$ (f) $V_0 = 0.5\Delta$

Figure B.16: Topology phase diagrams for the full-shell nanowire system described by $\sum_{m_J} \tilde{H}_{m_J,p_z}$ with $B_Z = 0$ and a deformation $V_0 \cos(4\varphi)$. The flux through the cylinder is $\tilde{\Phi} = \frac{1}{2}$, the winding is $n = 1$, and the radius is $R_2 = 0.52R_0$. Bands are included up to and with $m_J^{\max} = 4$. The only changed parameter from Fig. 5.3 is thus a 4% increase in radius.

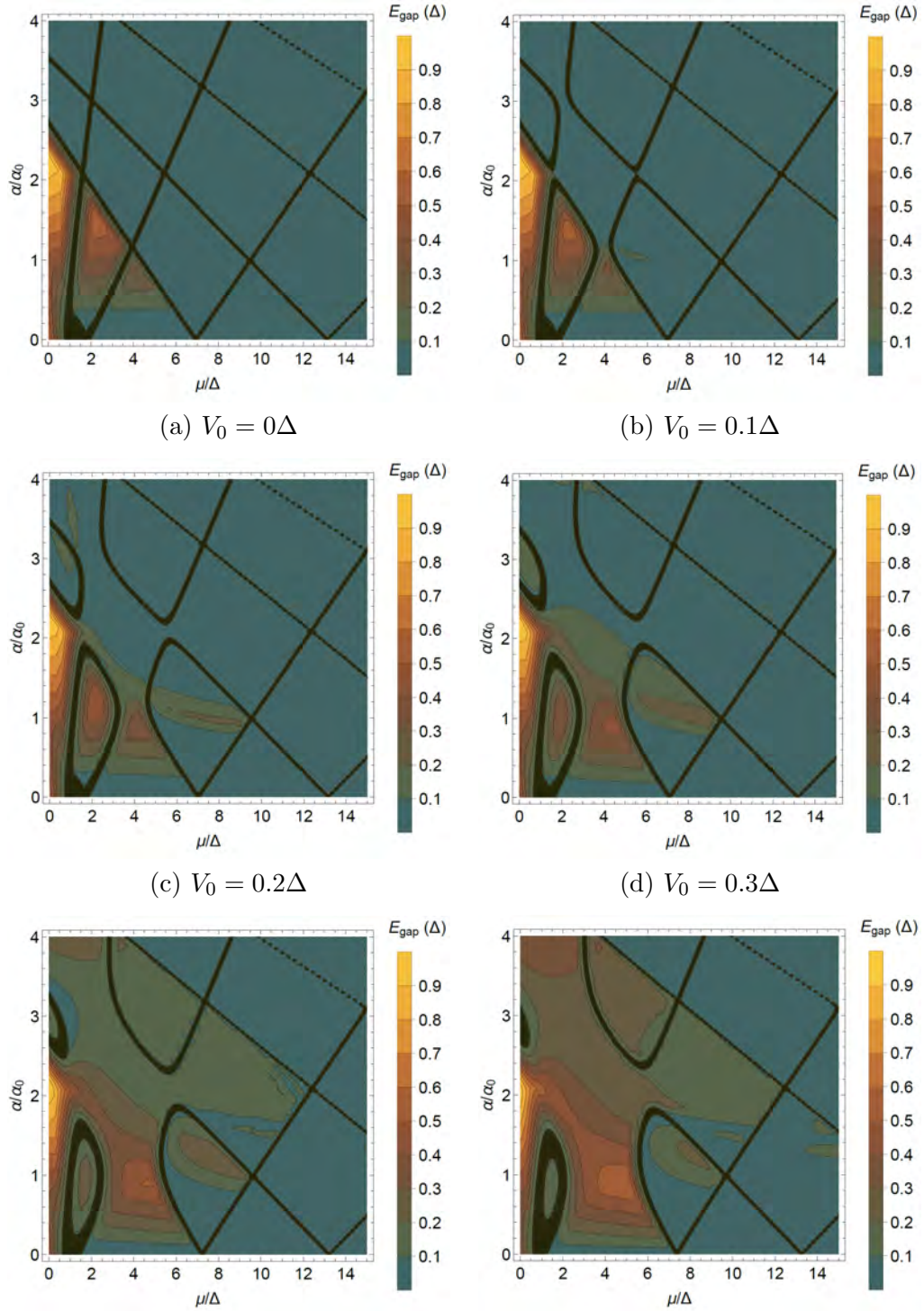

(a) $V_0 = 0\Delta$ (b) $V_0 = 0.1\Delta$

(c) $V_0 = 0.2\Delta$ (d) $V_0 = 0.3\Delta$

(e) $V_0 = 0.4\Delta$ (f) $V_0 = 0.5\Delta$

Figure B.17: Topology phase diagrams for the full-shell nanowire system described by $\sum_{m_J} \tilde{H}_{m_J,p_z}$ with $B_Z = 0$ and a deformation $V_0 \cos(2\varphi)$. The flux through the cylinder is $\tilde{\Phi} = \frac{1}{2}$, the winding is $n = 1$, and the radius is $R_2 = 0.48R_0$. Bands are included up to and with $m_J^{\max} = 4$. The only changed parameter from Fig. 5.1 is thus a 4% decrease in radius.

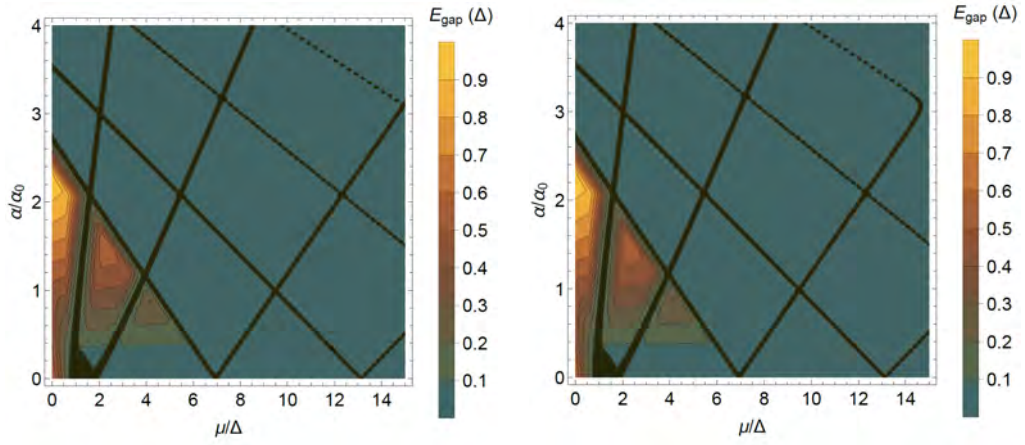

(a) $V_0 = 0\Delta$ (b) $V_0 = 0.1\Delta$

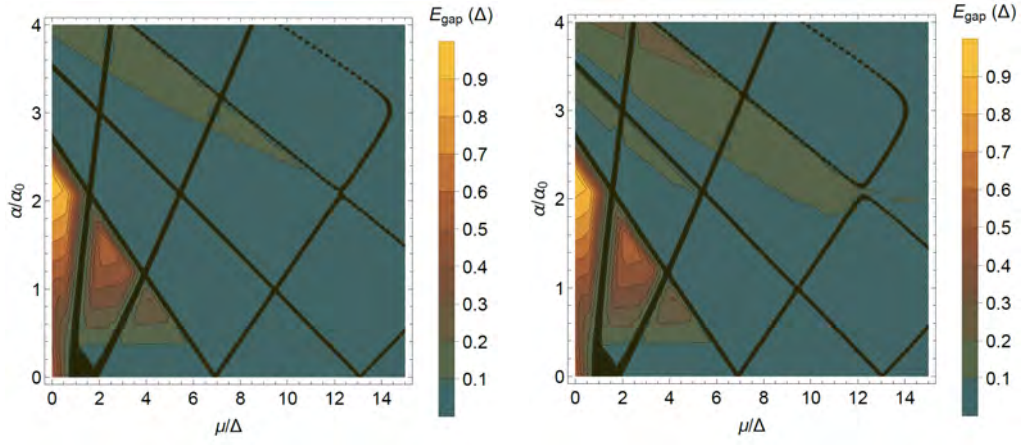

(c) $V_0 = 0.2\Delta$ (d) $V_0 = 0.3\Delta$

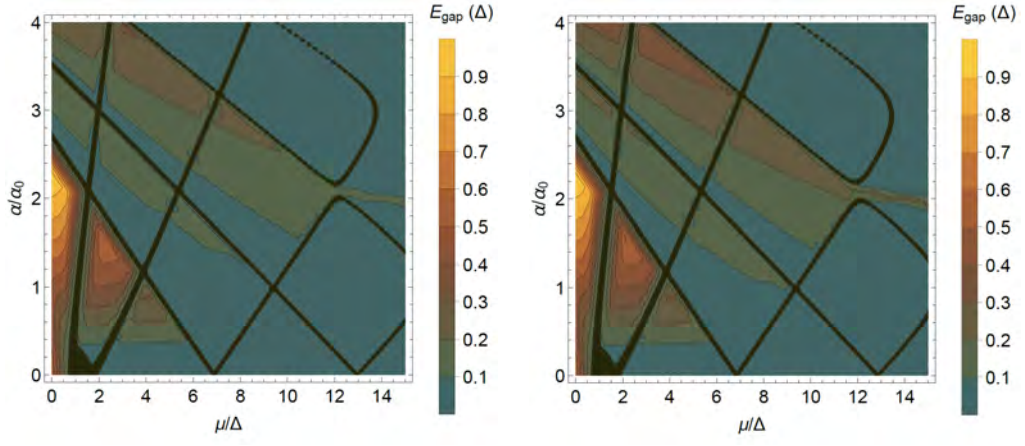

(e) $V_0 = 0.4\Delta$ (f) $V_0 = 0.5\Delta$

Figure B.18: Topology phase diagrams for the full-shell nanowire system described by $\sum_{m_J} \tilde{H}_{m_J,p_z}$ with $B_Z = 0$ and a deformation $V_0 \cos(4\varphi)$. The flux through the cylinder is $\tilde{\Phi} = \frac{1}{2}$, the winding is $n = 1$, and the radius is $R_2 = 0.48R_0$. Bands are included up to and with $m_J^{\max} = 4$. The only changed parameter from Fig. 5.3 is thus a 4% decrease in radius.

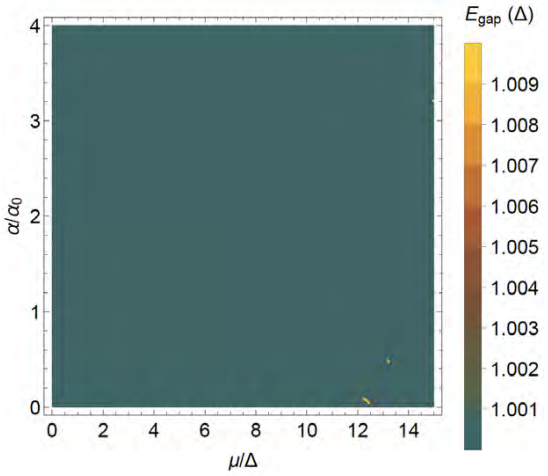

(a) $(\tilde{\Phi} = 0, n = 0)$, $(\tilde{\Phi} = 2, n = 2)$. Notice the different scale.

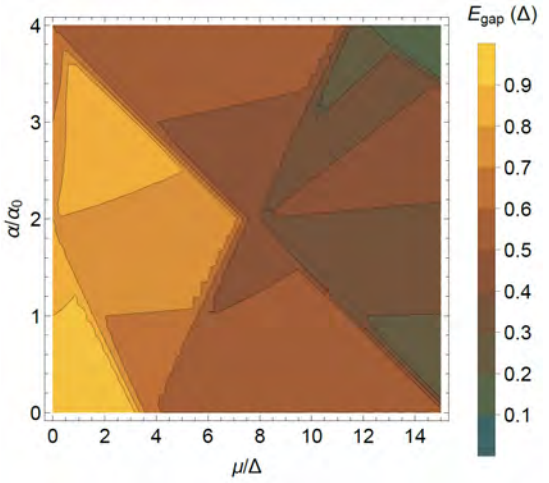

(b) $(\tilde{\Phi} = 0.1, n = 0)$, $(\tilde{\Phi} = 1.9, n = 2)$, $(\Phi/\Phi_0 = 2.1, n = 2)$

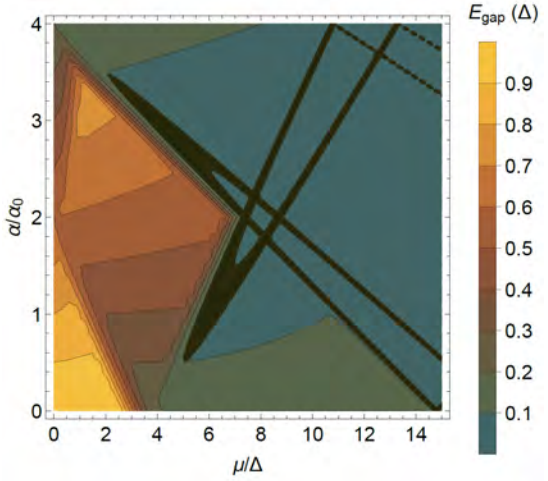

(c) $(\tilde{\Phi} = 0.2, n = 0)$, $(\tilde{\Phi} = 1.8, n = 2)$

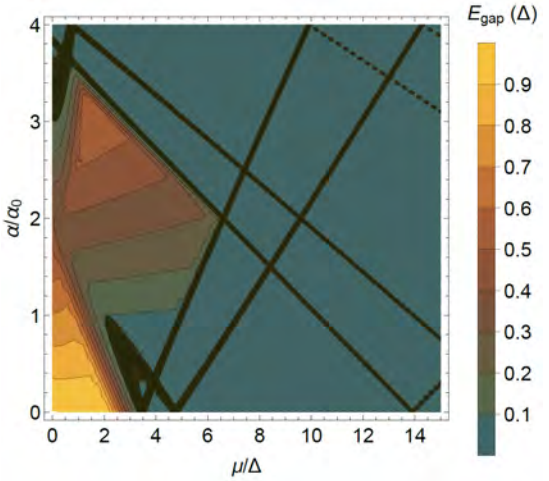

(d) $(\tilde{\Phi} = 0.3, n = 0)$, $(\tilde{\Phi} = 1.7, n = 2)$

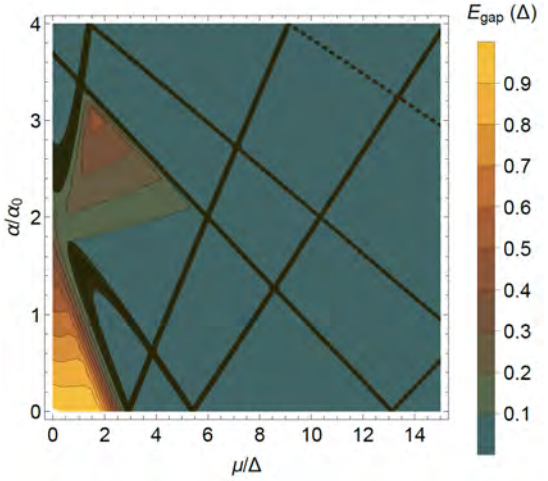

(e) $(\tilde{\Phi} = 0.4, n = 0)$, $(\tilde{\Phi} = 1.6, n = 2)$

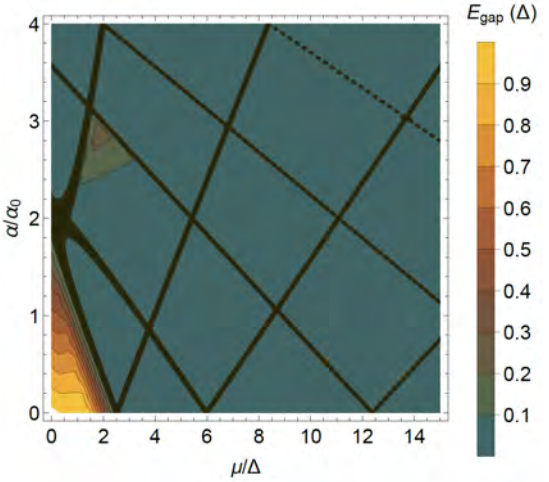

(f) $(\tilde{\Phi} = 0.5, n = 0)$, $(\tilde{\Phi} = 1.5, n = 2)$

Figure B.19: Topology phase diagrams for the full-shell nanowire system described by $\sum_{m_J} \tilde{H}_{m_J,p_z}$ with $B_Z = 0$, $R_2 = 0.5R_0$, and cylindrical geometry.

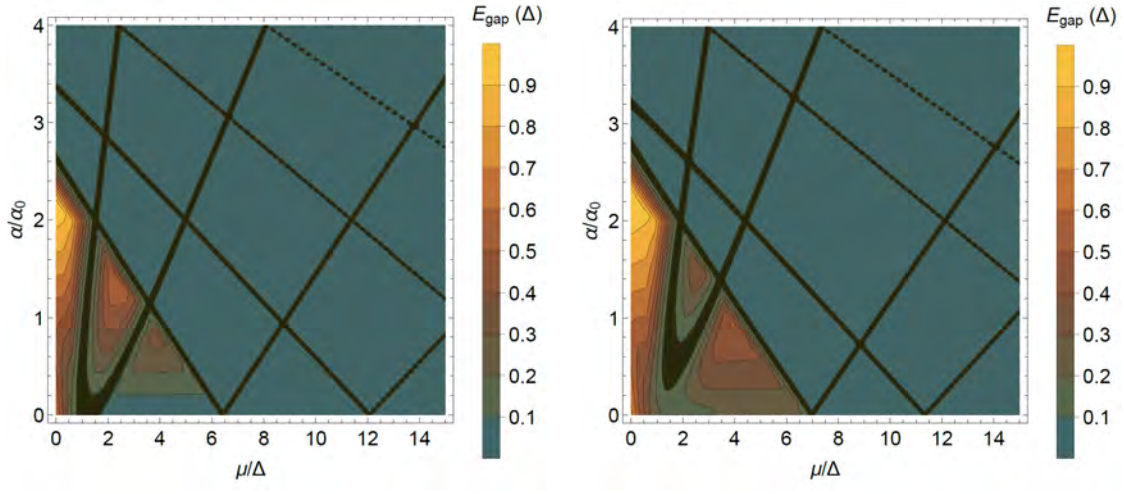

(a) $(\tilde{\Phi} = 0.5, n = 1)$, $(\tilde{\Phi} = 1.5, n = 1)$

(b) $(\tilde{\Phi} = 0.6, n = 1)$, $(\tilde{\Phi} = 1.4, n = 1)$

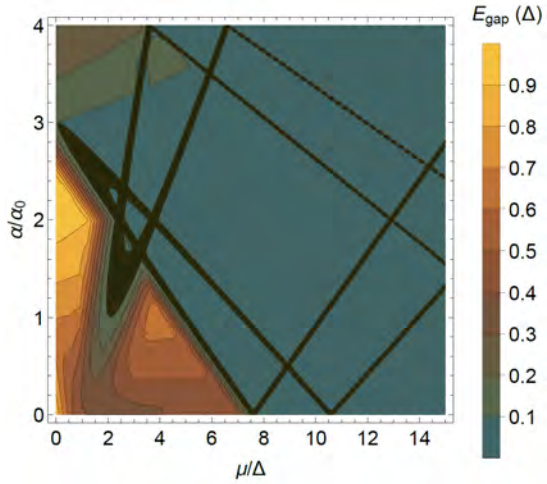

(c) $(\tilde{\Phi} = 0.7, n = 1)$, $(\tilde{\Phi} = 1.3, n = 1)$

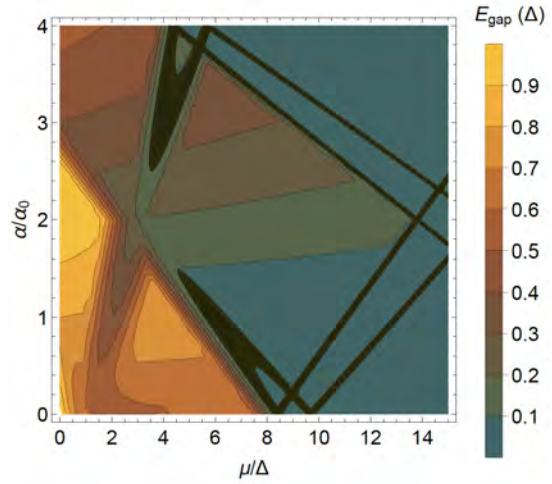

(d) $(\tilde{\Phi} = 0.8, n = 1)$, $(\tilde{\Phi} = 1.2, n = 1)$

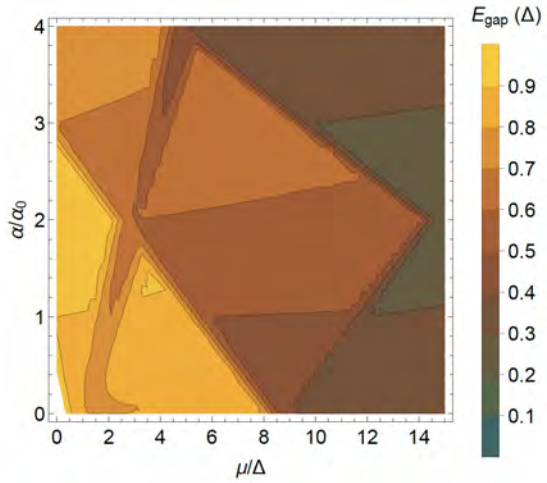

(e) $(\tilde{\Phi} = 0.9, n = 1)$, $(\tilde{\Phi} = 1.1, n = 1)$

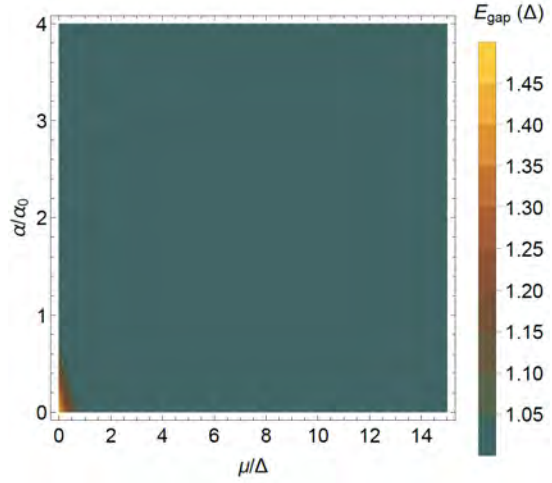

(f) $(\tilde{\Phi} = 1.0, n = 1)$. Notice the different scale.

Figure B.20: Topology phase diagrams for the full-shell nanowire system described by $\sum_{m_J} \tilde{H}_{m_J,p_z}$ with $B_Z = 0$, $R_2 = 0.5R_0$, and cylindrical geometry.

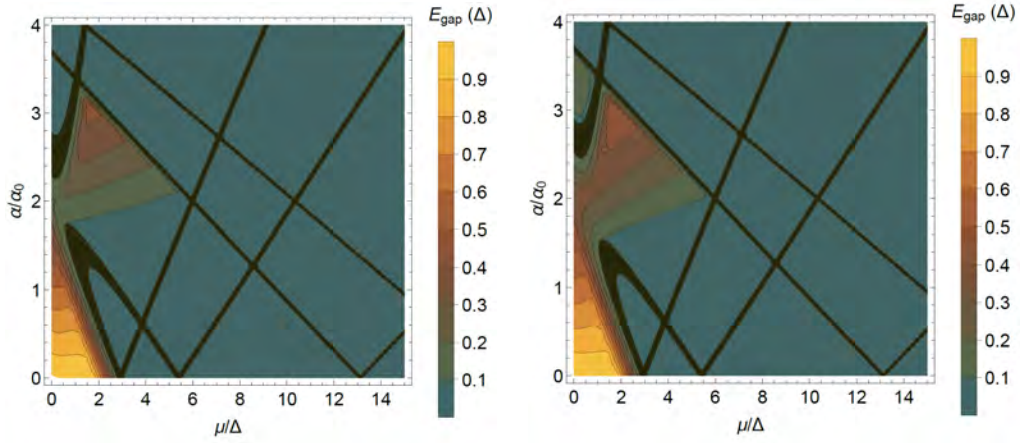

(a) $V_0 = 0\Delta$ (b) $V_0 = 0.1\Delta$

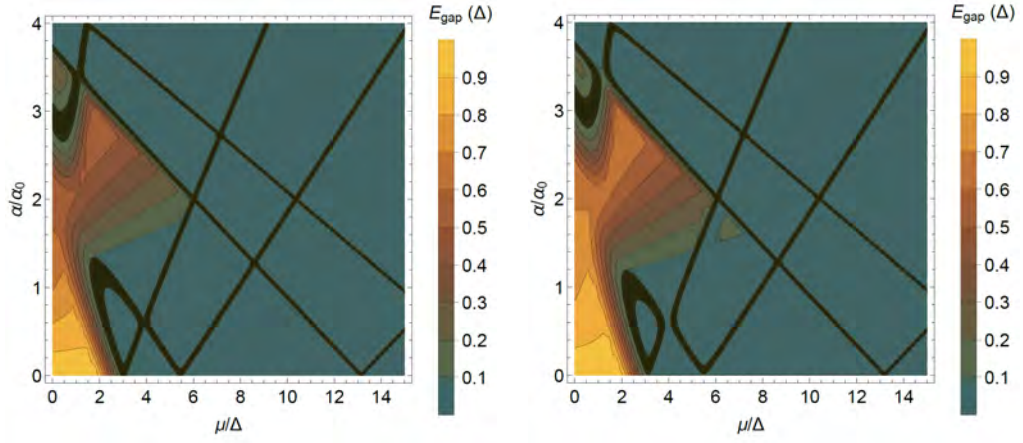

(c) $V_0 = 0.2\Delta$ (d) $V_0 = 0.3\Delta$

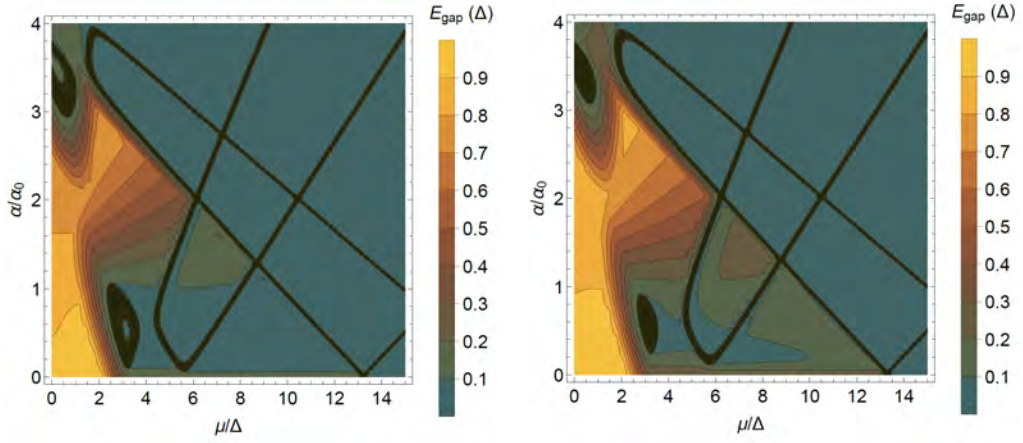

(e) $V_0 = 0.4\Delta$ (f) $V_0 = 0.5\Delta$

Figure B.21: Topology phase diagrams for the full-shell nanowire system described by $\sum_{m_J} \tilde{H}_{m_J,p_z}$ with a p-like deformation $V_0 \cos(\varphi)$, $B_Z = 0$, $R_2 = 0.5R_0$, and $\tilde{\Phi} = \frac{2}{5}$. Since this is in the $n = 0$ lobe there are no non-trivial domains when $V_0 = 0$. For finite V_0 a very small non-trivial domain around $(0.5\Delta, 3.5\alpha_0)$ appears and vanishes again whereas a narrow gap opens in the $(7, 1.2)$ domain for large $V_0 > 0.4\Delta$. In the calculations $m_J^{\max} = 2.5$.

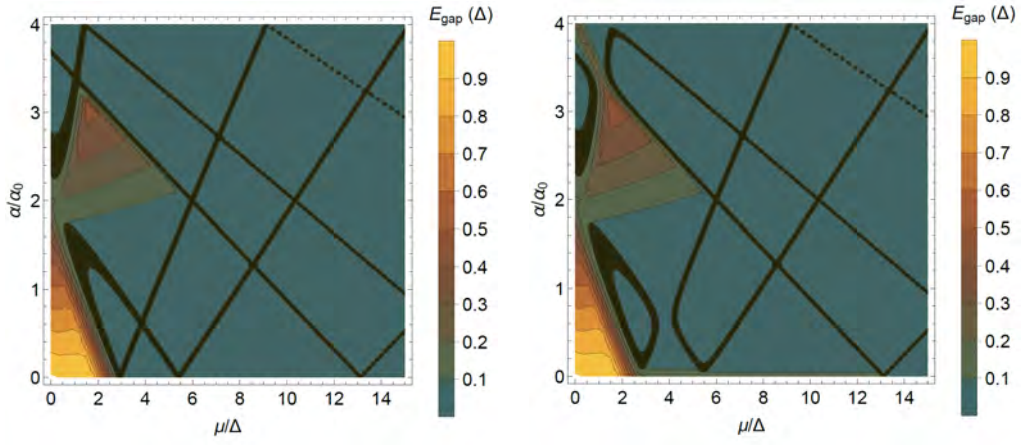

(a) $V_0 = 0\Delta$ (b) $V_0 = 0.1\Delta$

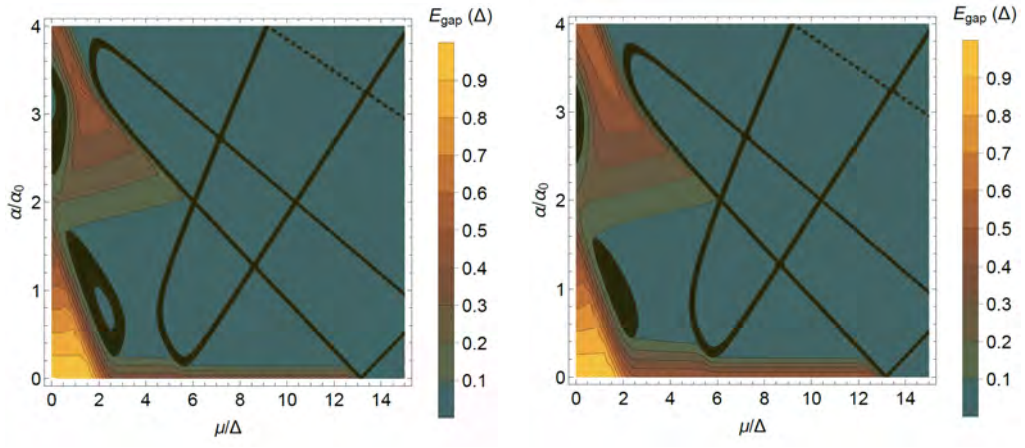

(c) $V_0 = 0.2\Delta$ (d) $V_0 = 0.3\Delta$

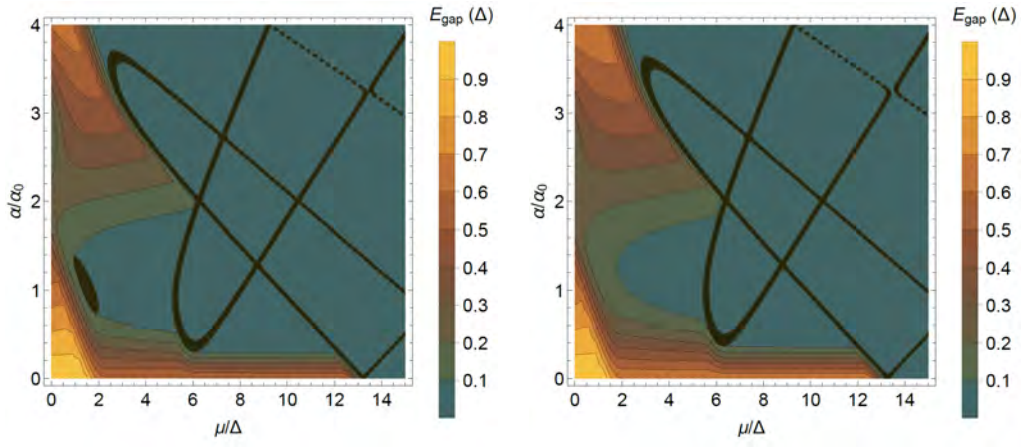

(e) $V_0 = 0.4\Delta$ (f) $V_0 = 0.5\Delta$

Figure B.22: Topology phase diagrams for the full-shell nanowire system described by $\sum_{m_J} \tilde{H}_{m_J,p_z}$ with a d-like deformation $V_0 \cos(2\varphi)$, $B_Z = 0$, $R_2 = 0.5R_0$, and $\tilde{\Phi} = \frac{2}{5}$. Since this is in the $n = 0$ lobe there are no domains of non-trivial phases at $V_0 = 0$. Nor do any non-trivial gaps emerge with finite V_0. In the calculations $m_J^{\max} = 3.5$.

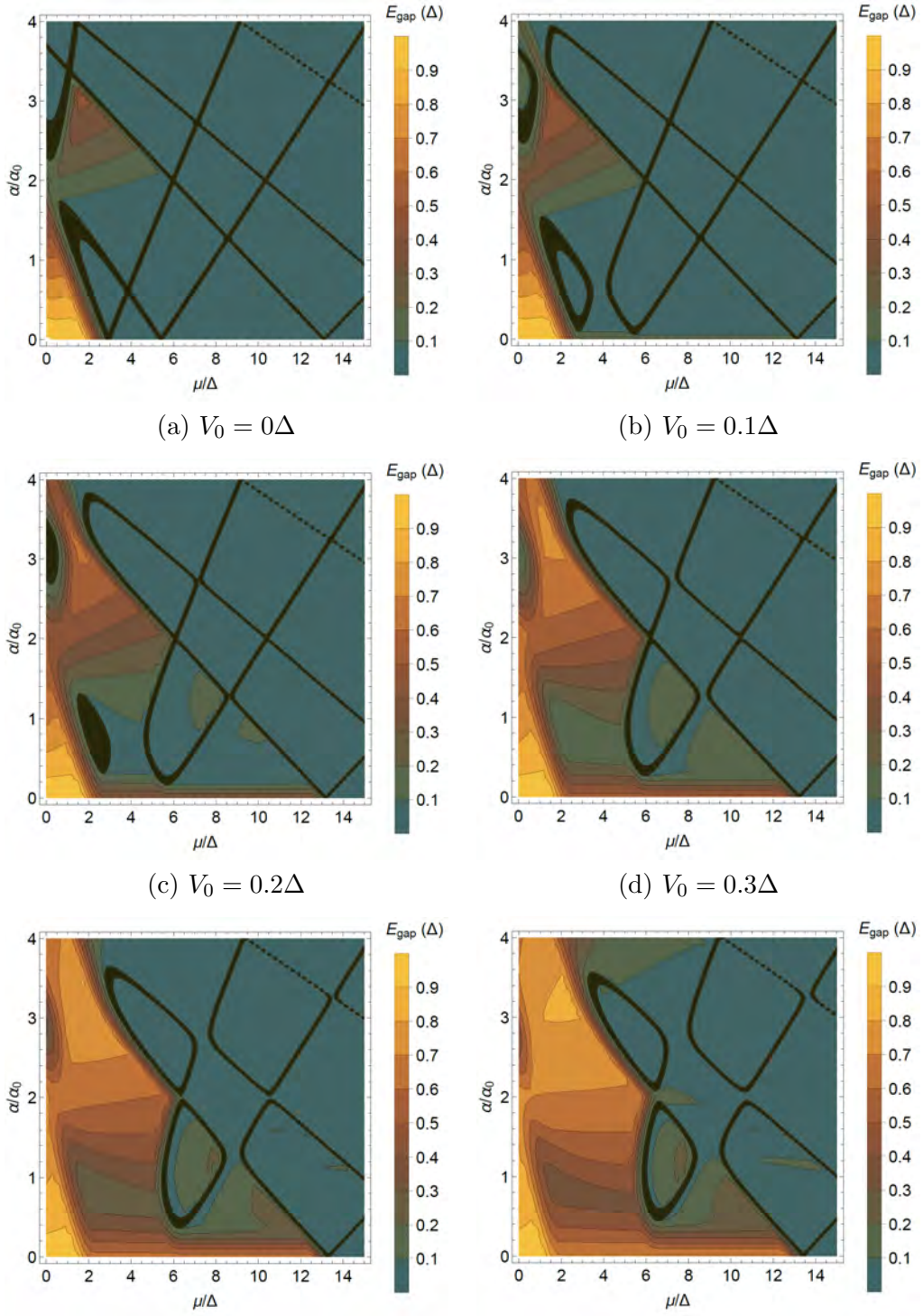

(a) $V_0 = 0\Delta$ (b) $V_0 = 0.1\Delta$

(c) $V_0 = 0.2\Delta$ (d) $V_0 = 0.3\Delta$

(e) $V_0 = 0.4\Delta$ (f) $V_0 = 0.5\Delta$

Figure B.23: Topology phase diagrams for the full-shell nanowire system described by $\sum_{m_J} \tilde{H}_{m_J,p_z}$ with a p+d-like deformation $V_0\left(\cos(\varphi) + \cos(2\varphi)\right)$, $B_Z = 0$, $R_2 = 0.5R_0$, and $\tilde{\Phi} = \frac{2}{5}$. Since this is in the $n = 0$ lobe there are no non-trivial domains at $V_0 = 0$. For finite V_0 a small non-trivial gap emerges. In the calculations $m_J^{\max} = 3.5$.

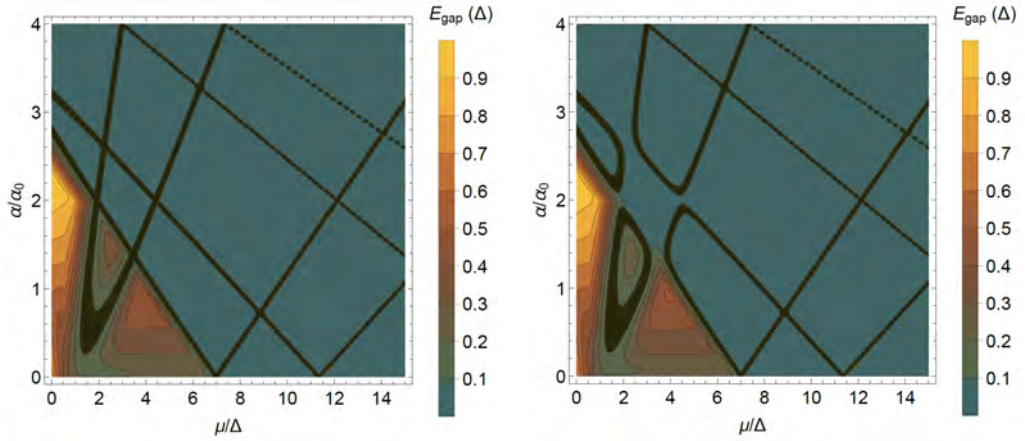

(a) $V_0 = 0\Delta$ (b) $V_0 = 0.1\Delta$

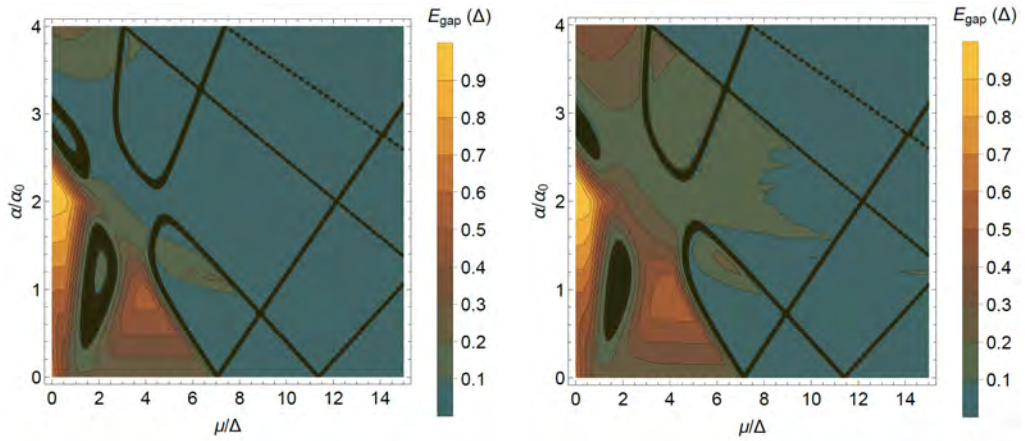

(c) $V_0 = 0.2\Delta$ (d) $V_0 = 0.3\Delta$

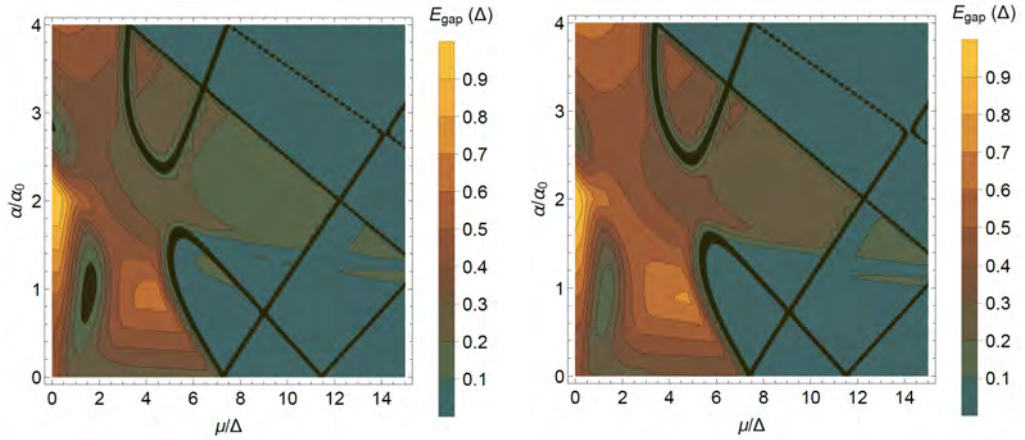

(e) $V_0 = 0.4\Delta$ (f) $V_0 = 0.5\Delta$

Figure B.24: Topology phase diagrams for the full-shell nanowire system described by $\sum_{m_J} \tilde{H}_{m_J,p_z}$ with a symmetry-breaking deformation $V_0 \cos(2\varphi)$. These plots are calculated for a flux well within the first lobe $\tilde{\Phi} = 0.6$ (and $\tilde{\Phi} = 1.4$) for a wire radius $R_2 = 0.5R_0$ without a Zeeman energy. Comparing with the half-flux counterparts in Figs. 4.3 and 5.1 one can see that the initial non-trivial domain is smaller, whereas the non-trivial gap in the $(5, 3)$ domain is larger. The relevant bands for calculating the gap include $m_J^{\max} = 4$.

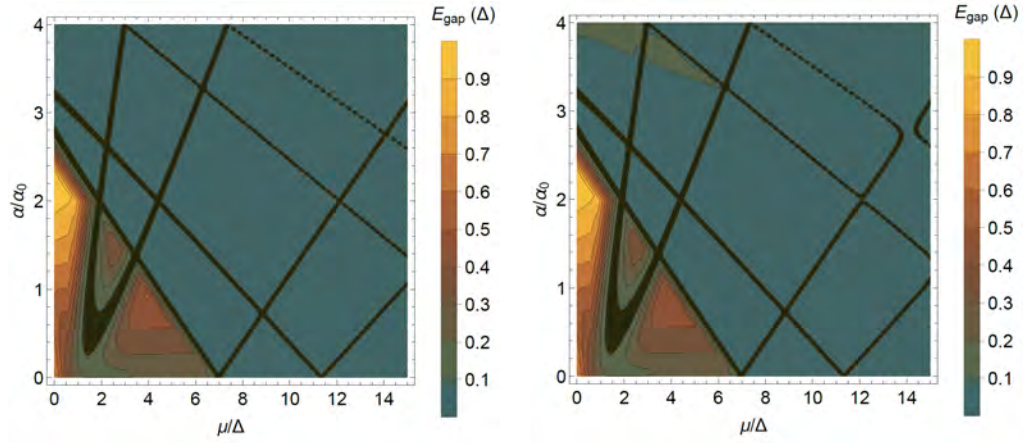

(a) $V_0 = 0\Delta$ (b) $V_0 = 0.1\Delta$

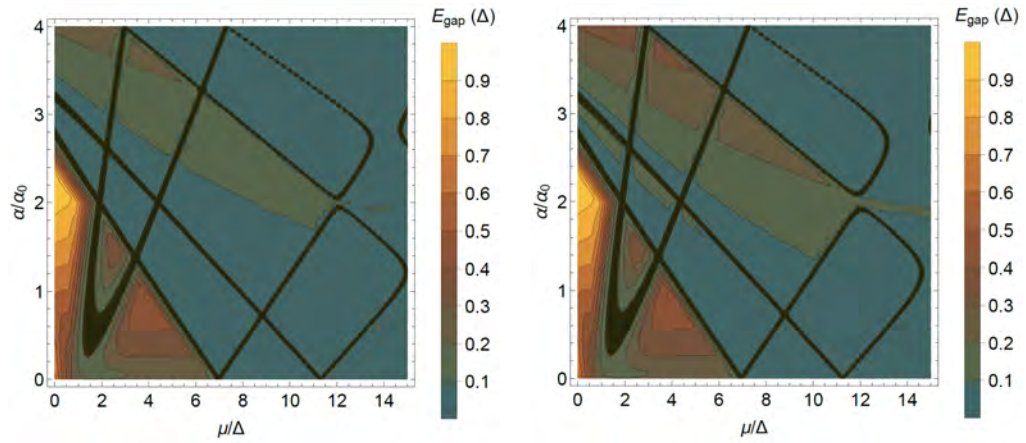

(c) $V_0 = 0.2\Delta$ (d) $V_0 = 0.3\Delta$

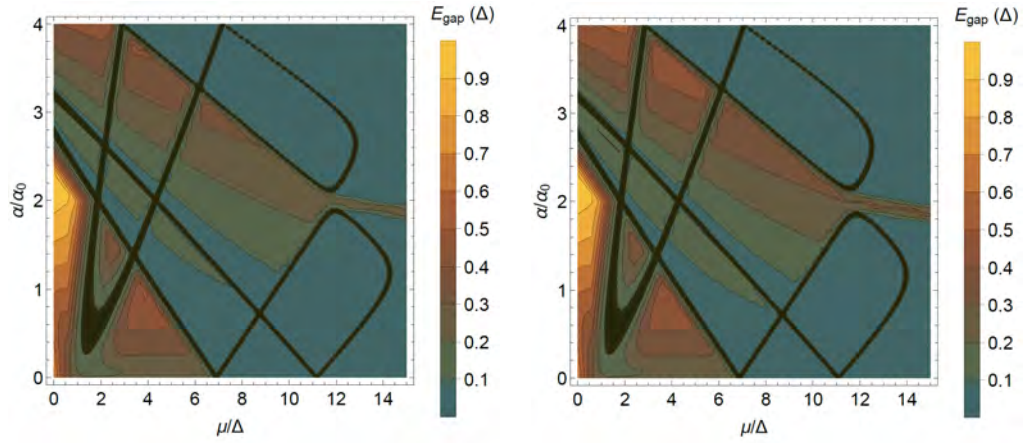

(e) $V_0 = 0.4\Delta$ (f) $V_0 = 0.5\Delta$

Figure B.25: Topology phase diagrams for the full-shell nanowire system described by $\sum_{m_J} \tilde{H}_{m_J,p_z}$ with a symmetry-breaking deformation $V_0 \cos(4\varphi)$. These plots are calculated for a flux well within the first lobe $\tilde{\Phi} = 0.6$ (and $\tilde{\Phi} = 1.4$) for a wire radius $R_2 = 0.5R_0$ without a Zeeman energy. The relevant bands for calculating the gap include $m_J^{\max} = 4$.

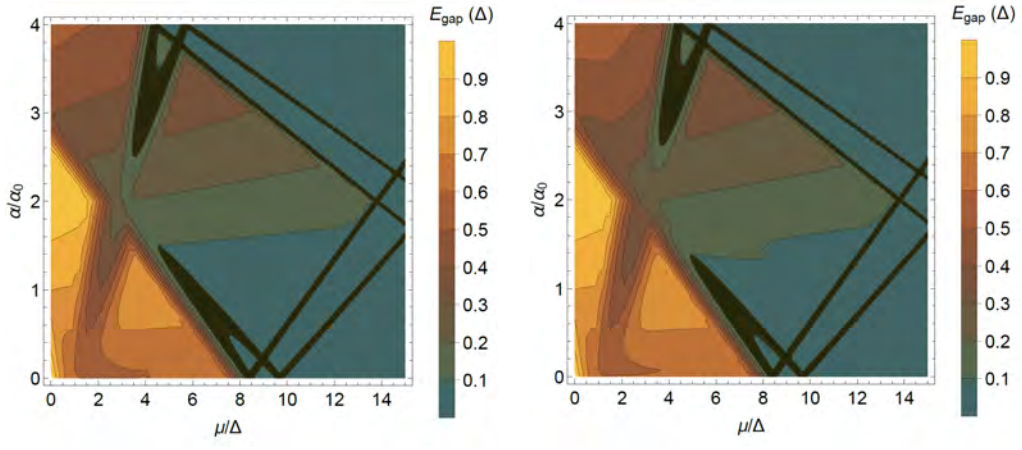

(a) $V_0 = 0\Delta$ (b) $V_0 = 0.1\Delta$

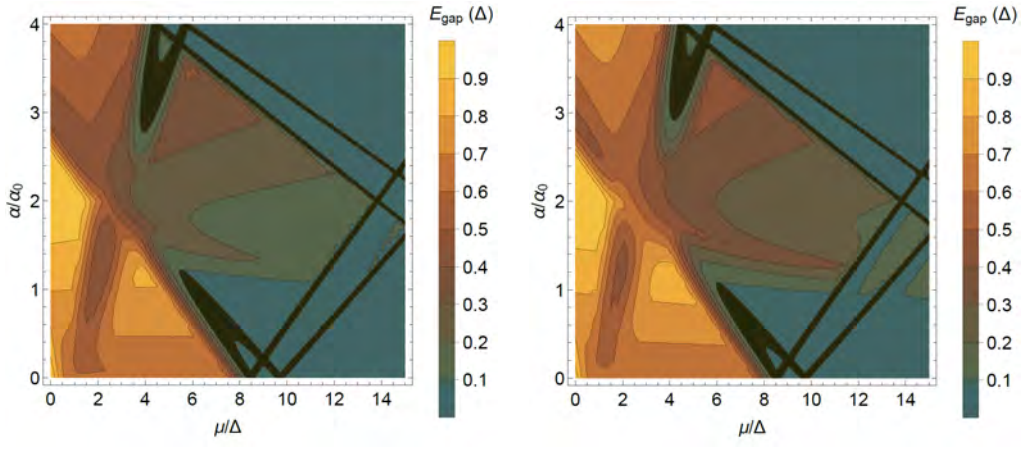

(c) $V_0 = 0.2\Delta$ (d) $V_0 = 0.3\Delta$

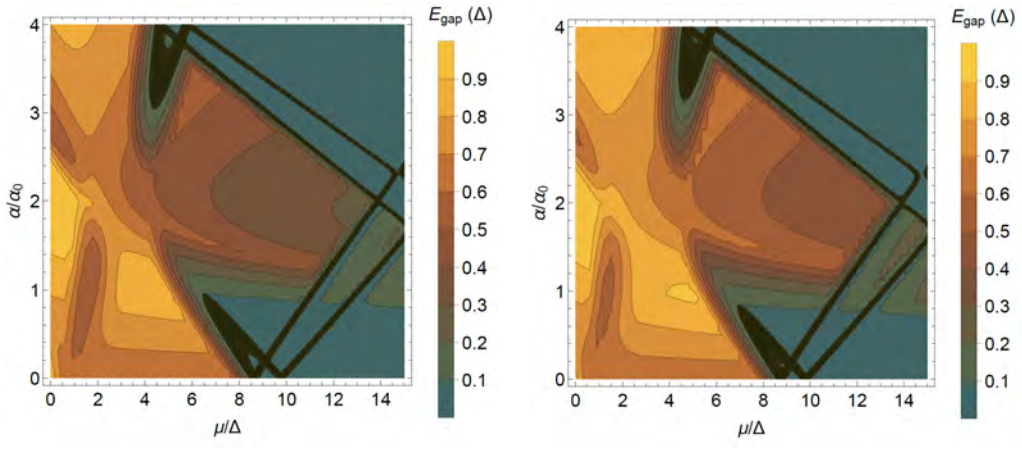

(e) $V_0 = 0.4\Delta$ (f) $V_0 = 0.5\Delta$

Figure B.26: Topology phase diagrams for the full-shell nanowire system described by $\sum_{m_J} \tilde{H}_{m_J,p_z}$ with a symmetry-breaking deformation $V_0 \cos(2\varphi)$ and a flux $\tilde{\Phi} = 0.8$ (and $\tilde{\Phi} = 1.2$) for a wire radius $R_2 = 0.5R_0$ without a Zeeman energy. The relevant bands for calculating the gap include $m_J^{\max} = 4$.

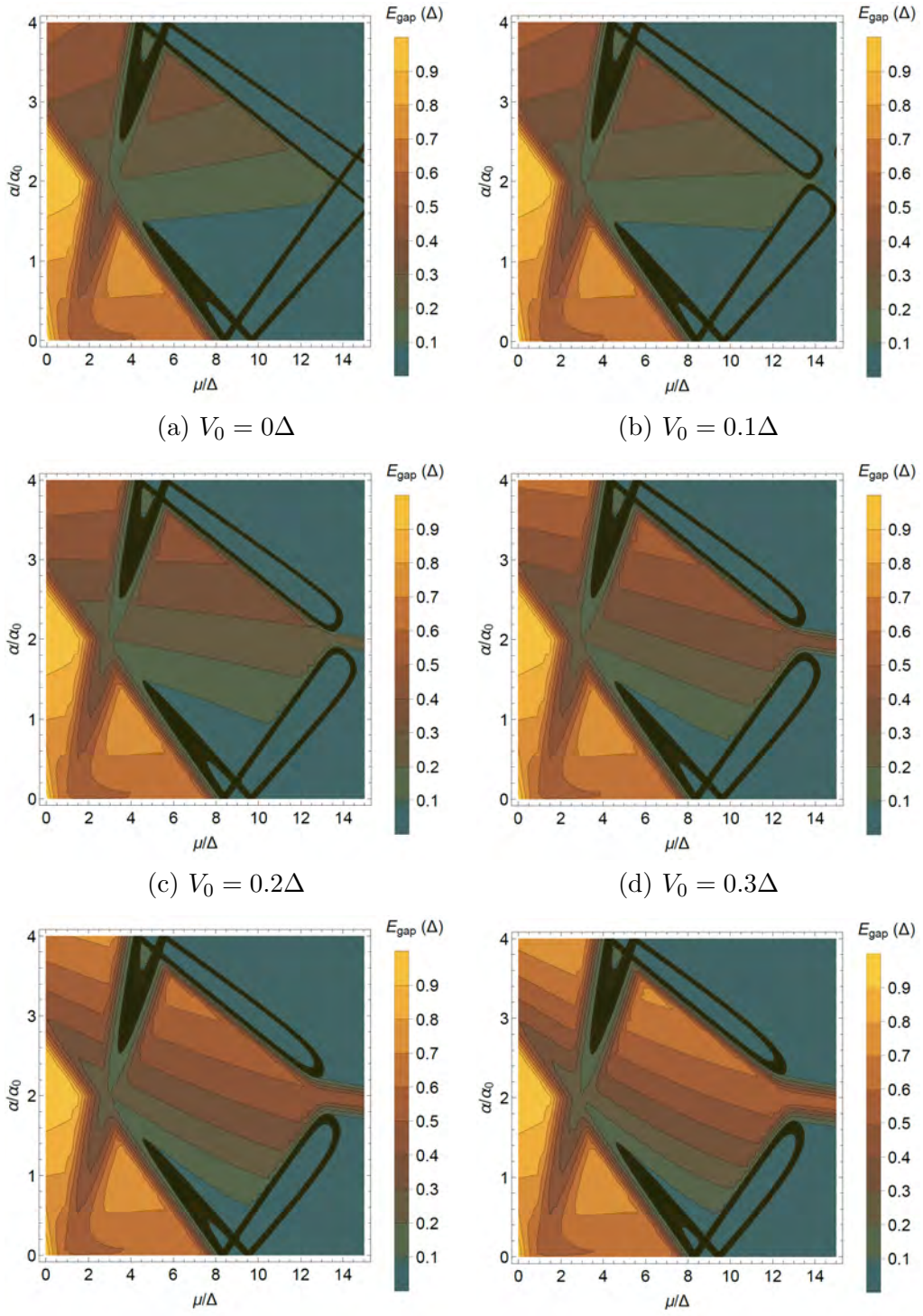

(a) $V_0 = 0\Delta$ (b) $V_0 = 0.1\Delta$

(c) $V_0 = 0.2\Delta$ (d) $V_0 = 0.3\Delta$

(e) $V_0 = 0.4\Delta$ (f) $V_0 = 0.5\Delta$

Figure B.27: Topology phase diagrams for the full-shell nanowire system described by $\sum_{m_J} \tilde{H}_{m_J,p_z}$ with a symmetry-breaking deformation $V_0 \cos(4\varphi)$ and a flux $\tilde{\Phi} = 0.8$ (and $\tilde{\Phi} = 1.2$) for a wire radius $R_2 = 0.5R_0$ without a Zeeman energy. The relevant bands for calculating the gap include $m_J^{\max} = 4$.

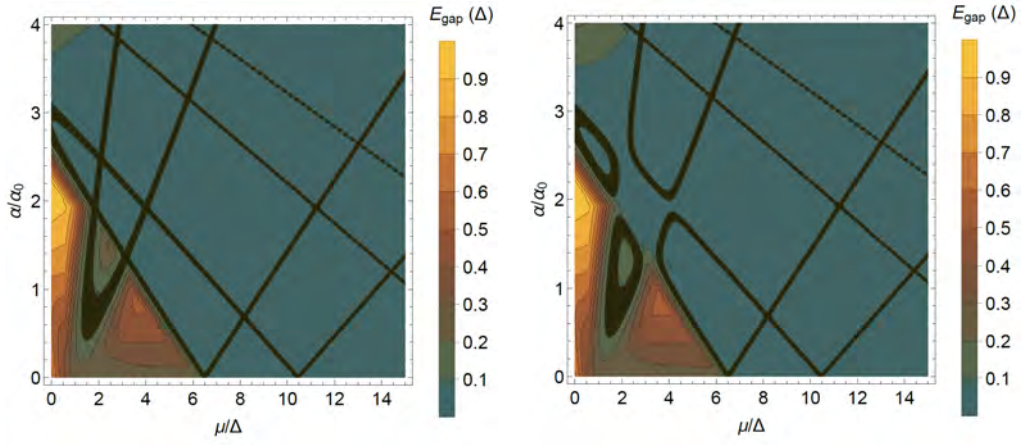

(a) $V_0 = 0\Delta$ (b) $V_0 = 0.1\Delta$

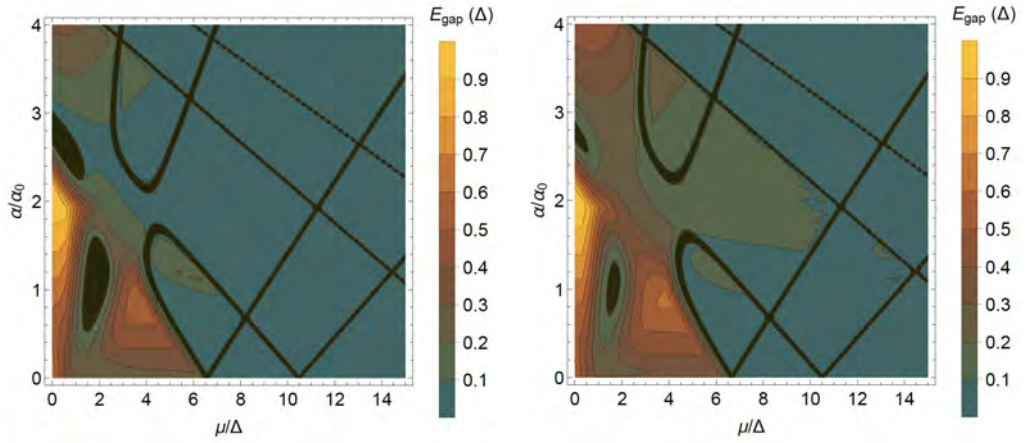

(c) $V_0 = 0.2\Delta$ (d) $V_0 = 0.3\Delta$

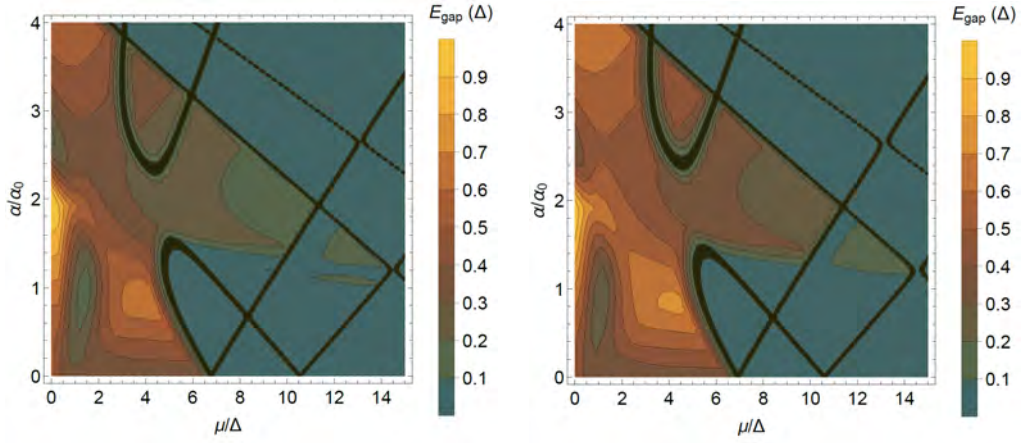

(e) $V_0 = 0.4\Delta$ (f) $V_0 = 0.5\Delta$

Figure B.28: Topology phase diagrams for the full-shell nanowire system described by $\sum_{m_J} \tilde{H}_{m_J,p_z}$ with $B_Z = 0$, $R_2 = 0.52R_0$, $\tilde{\Phi} = 0.6$, and a deformation $V_0 \cos(2\varphi)$. Compared with Fig. B.15 the black phase transition lines going north-west to south-east are squeezed together pairwise and the $V_Z = \sqrt{\mu^2_{m_J=0} + \Delta^2}$ parabola is pulled upwards to the left compared to the half-flux case. Combined, this causes a smaller initial non-trivial domain which already dies out at $V_0 = 0.2\Delta$. Here $m_J^{\max} = 4$.

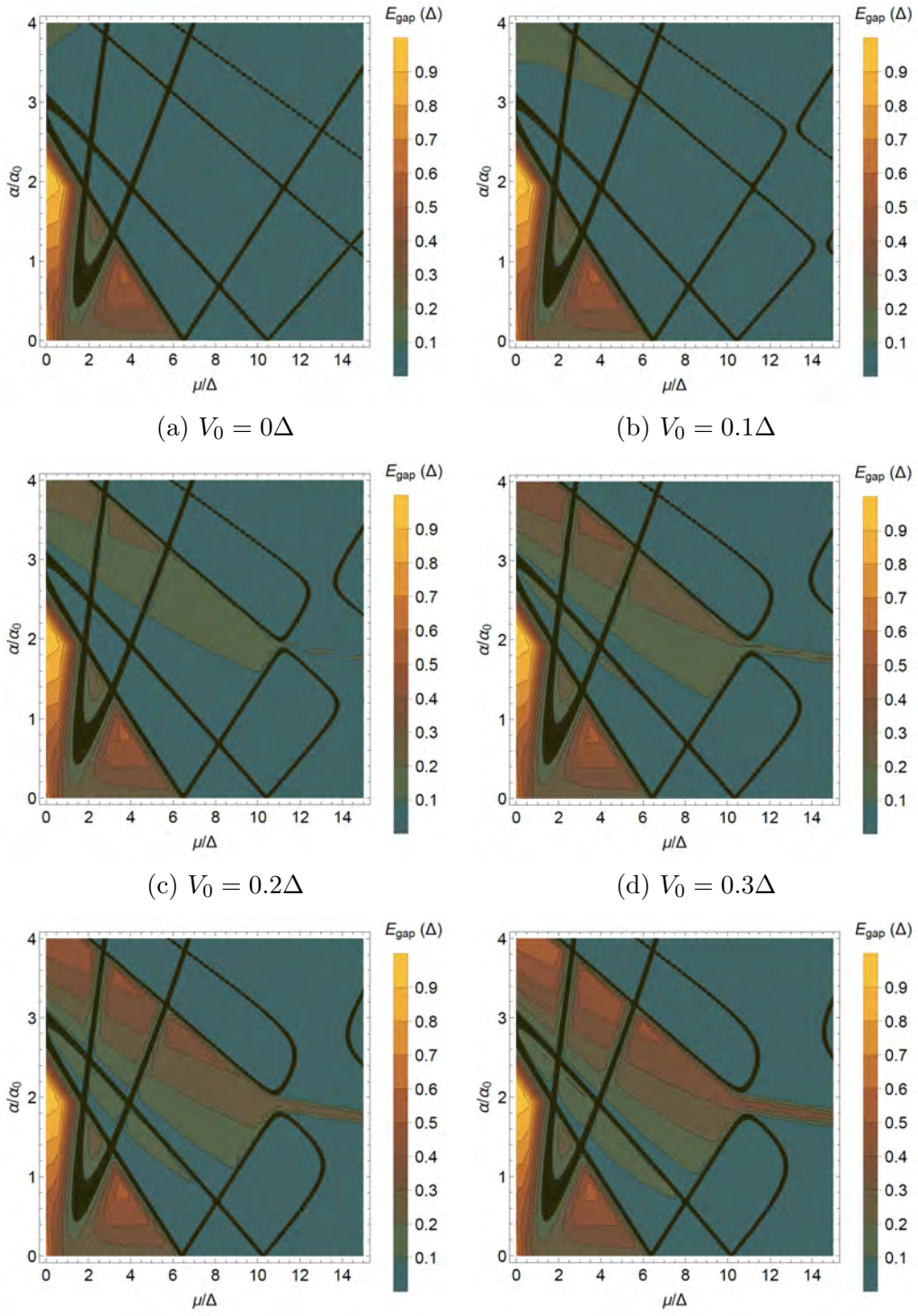

(a) $V_0 = 0\Delta$ (b) $V_0 = 0.1\Delta$

(c) $V_0 = 0.2\Delta$ (d) $V_0 = 0.3\Delta$

(e) $V_0 = 0.4\Delta$ (f) $V_0 = 0.5\Delta$

Figure B.29: Topology phase diagrams for the full-shell nanowire system described by $\sum_{m_J} \tilde{H}_{m_J,p_z}$ with $B_Z = 0$, $R_2 = 0.52R_0$, $\tilde{\Phi} = 0.6$, and a deformation $V_0 \cos(4\varphi)$. Compared with Fig. B.16 the initial non-trivial domain is smaller and the generated gap in the $(5, 3)$ domain is larger although the area is smaller. Here $m_J^{\max} = 4$.

C Spectral function plots

All results in this appendix are made without a Zeeman energy, $B_Z = 0$. The width used for the Lorentzian is $\Gamma = 0.05\Delta$ and $m_J^{\max} = 4$.

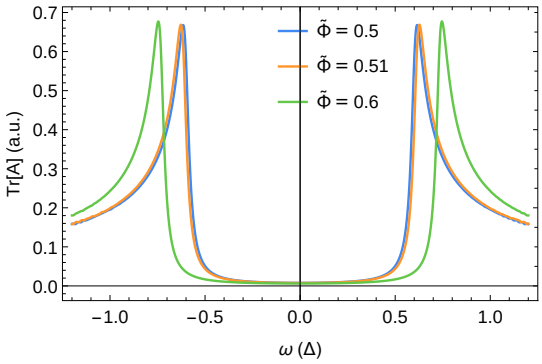

(a) $\mu = 0\Delta$

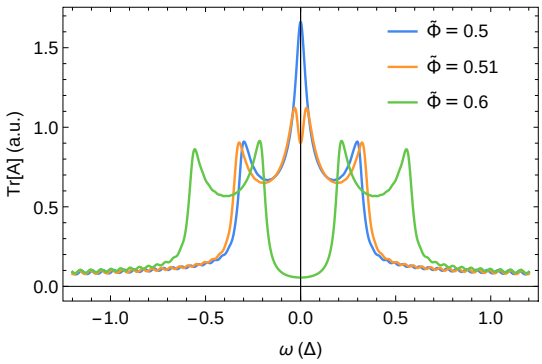

(b) $\mu = 2.1\Delta$

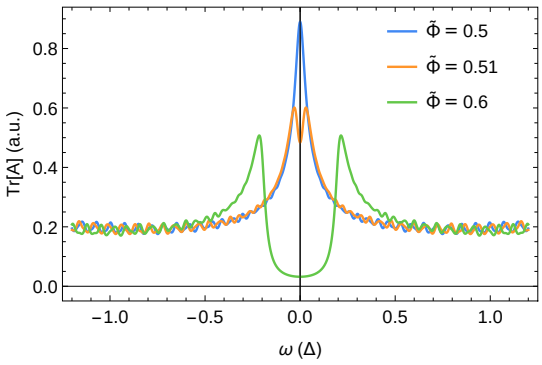

(c) $\mu = 4.1\Delta$

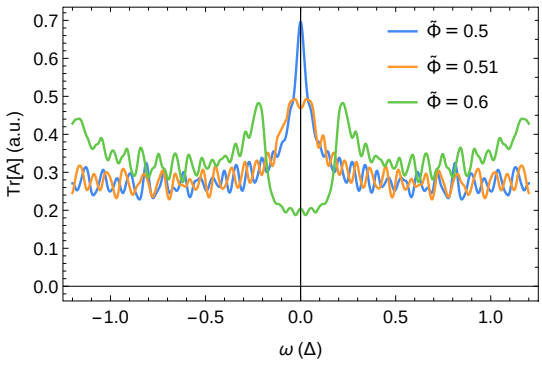

(d) $\mu = 9.1\Delta$

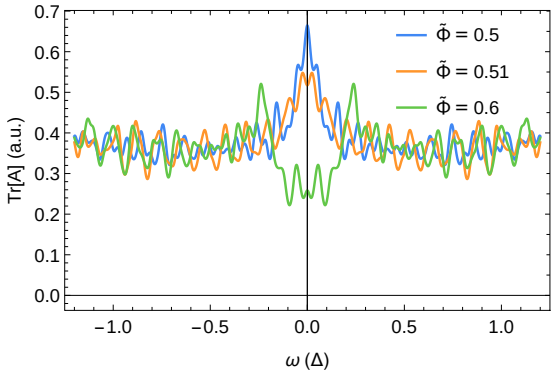

(e) $\mu = 14.1\Delta$.

Figure C.1: $\mathrm{Tr}[A](\omega)$ for different values of the flux, $\tilde{\Phi}$. A persistent peak is observed in the spectral function for $\tilde{\Phi} = 0.5$ through Figs. (b) to (e). Shared parameter values are: $\alpha = 0$, $R_2 = 0.5R_0$, $V(\varphi) = 0$, $\Gamma = 0.05\Delta$, and $m_J^{\max} = 4$. $\mathrm{Tr}[A](\omega)$ for $\tilde{\Phi} = 0.6$ in Figs. (b) and (c) is really gapped which is seen only when lowering the width of the Lorentzian.

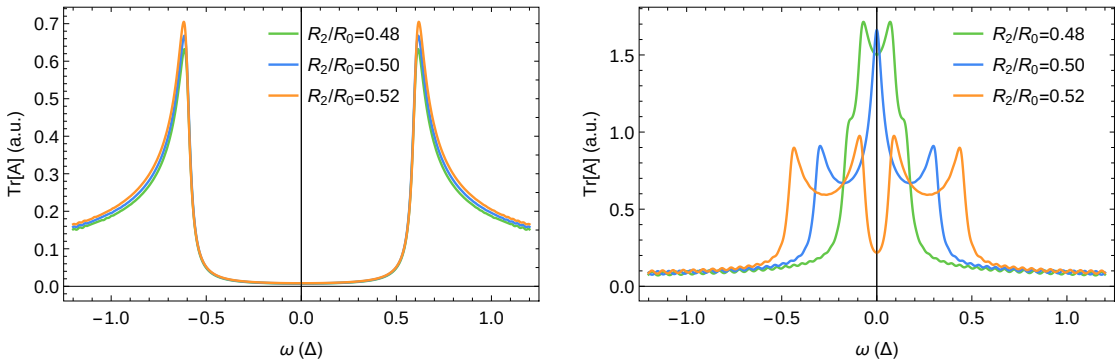

(a) $\mu = 0\Delta$ **(b)** $\mu = 2.1\Delta$

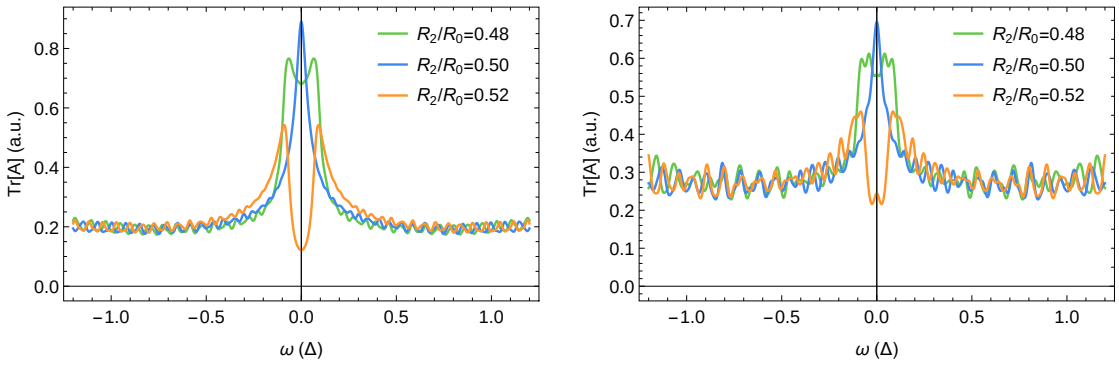

(c) $\mu = 4.1\Delta$ **(d)** $\mu = 9.1\Delta$

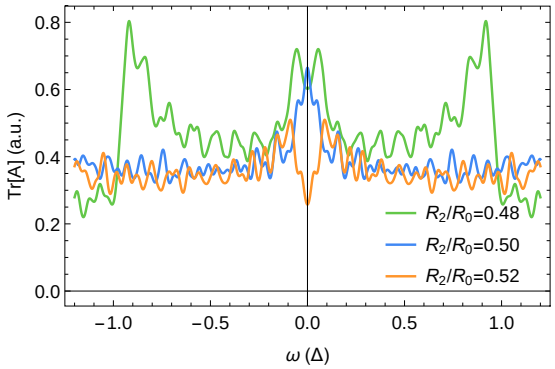

(e) $\mu = 14.1\Delta$. For higher μ more bands are down near zero energy.

Figure C.2: Tr$[A](\omega)$ for different radii. A persistent peak is observed in the spectral function for $R_2 = 0.5R_0$ through Figs. (b) to (e). Shared parameter values are: $\alpha = 0$, $\tilde{\Phi} = \frac{1}{2}$, $V(\varphi) = 0$, $\Gamma = 0.05\Delta$, and $m_J^{\max} = 4$. Tr$[A](\omega)$ for $R_2 = 0.52R_0$ in Figs. (b) and (c) is really gapped which is seen only when lowering the width of the Lorentzian.

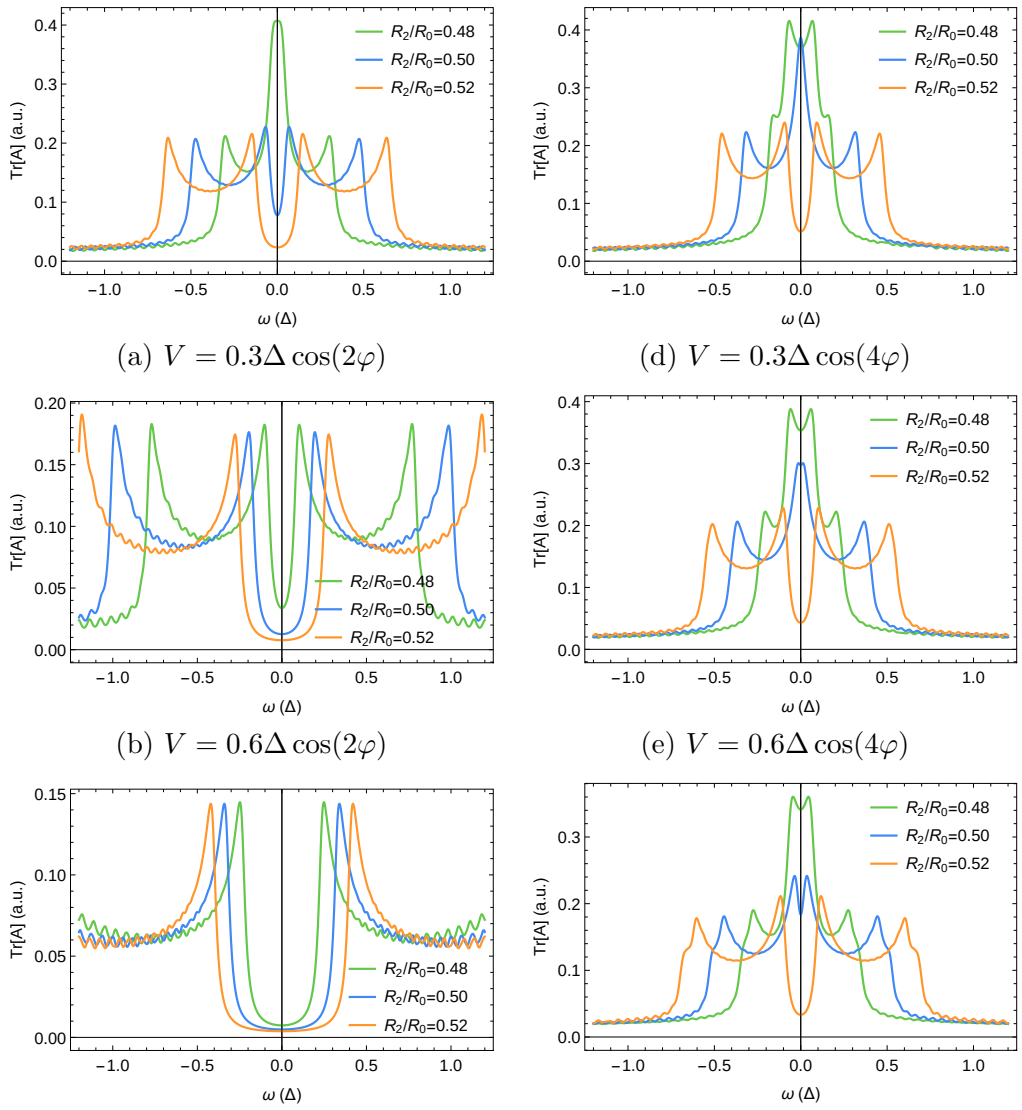

(a) $V = 0.3\Delta\cos(2\varphi)$ (d) $V = 0.3\Delta\cos(4\varphi)$

(b) $V = 0.6\Delta\cos(2\varphi)$ (e) $V = 0.6\Delta\cos(4\varphi)$

(c) $V = 0.9\Delta\cos(2\varphi)$ (f) $V = 0.9\Delta\cos(4\varphi)$

Figure C.3: $\mathrm{Tr}[A](\omega)$ at $(\mu = 2.1\Delta, \alpha = 0)$ for different radii. A d-like deformation $V_0\cos(2\varphi)$, applied in (a)-(c), turns the peaks in the blue and green functions into dips. With increasing strength, the three spectral functions become more alike. A g-like deformation $V_0\cos(4\varphi)$ in (d)-(f) has little effect unless $V_0 \sim \Delta$ where the blue peak splits up. Shared parameters are $\tilde{\Phi} = \frac{1}{2}$ and $n = 1$. As in Figs. C.1 and C.2 gaps in the spectral functions are closed by the finite width of the Lorentzian.

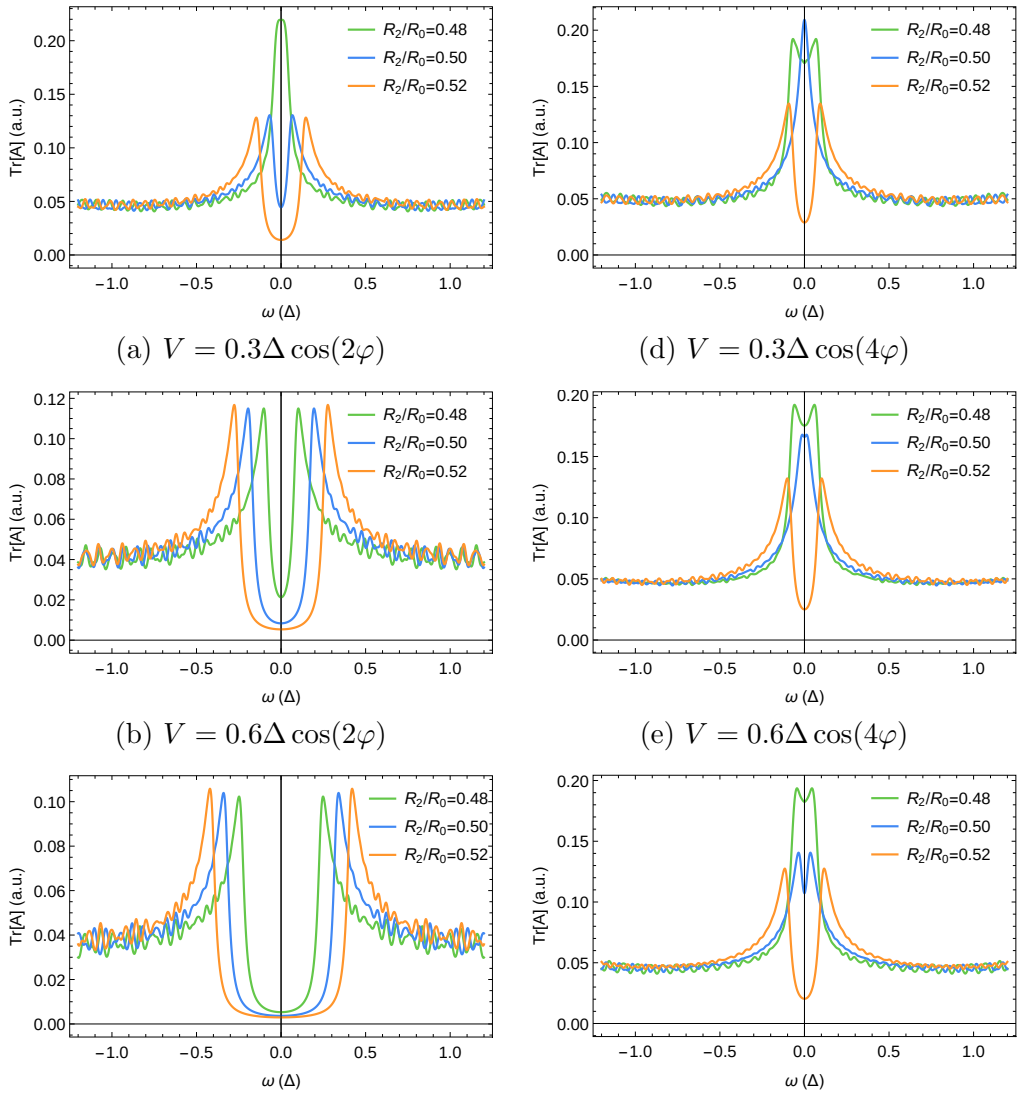

(a) $V = 0.3\Delta\cos(2\varphi)$ (d) $V = 0.3\Delta\cos(4\varphi)$

(b) $V = 0.6\Delta\cos(2\varphi)$ (e) $V = 0.6\Delta\cos(4\varphi)$

(c) $V = 0.9\Delta\cos(2\varphi)$ (f) $V = 0.9\Delta\cos(4\varphi)$

Figure C.4: $\mathrm{Tr}[A](\omega)$ at $(\mu = 4.1\Delta, \alpha = 0)$ for different radii. A d-like deformation $V_0\cos(2\varphi)$, applied in (a)-(c), turns the peaks in the blue and green functions into dips. With increasing strength, the three spectral functions become more alike. A g-like deformation $V_0\cos(4\varphi)$ in (d)-(f) has little effect unless $V_0 \sim \Delta$ where the blue peak splits up. Shared parameters are $\tilde{\Phi} = \frac{1}{2}$ and $n = 1$. As in Figs. C.1 and C.2 gaps in the spectral functions are closed by the finite width of the Lorentzian.

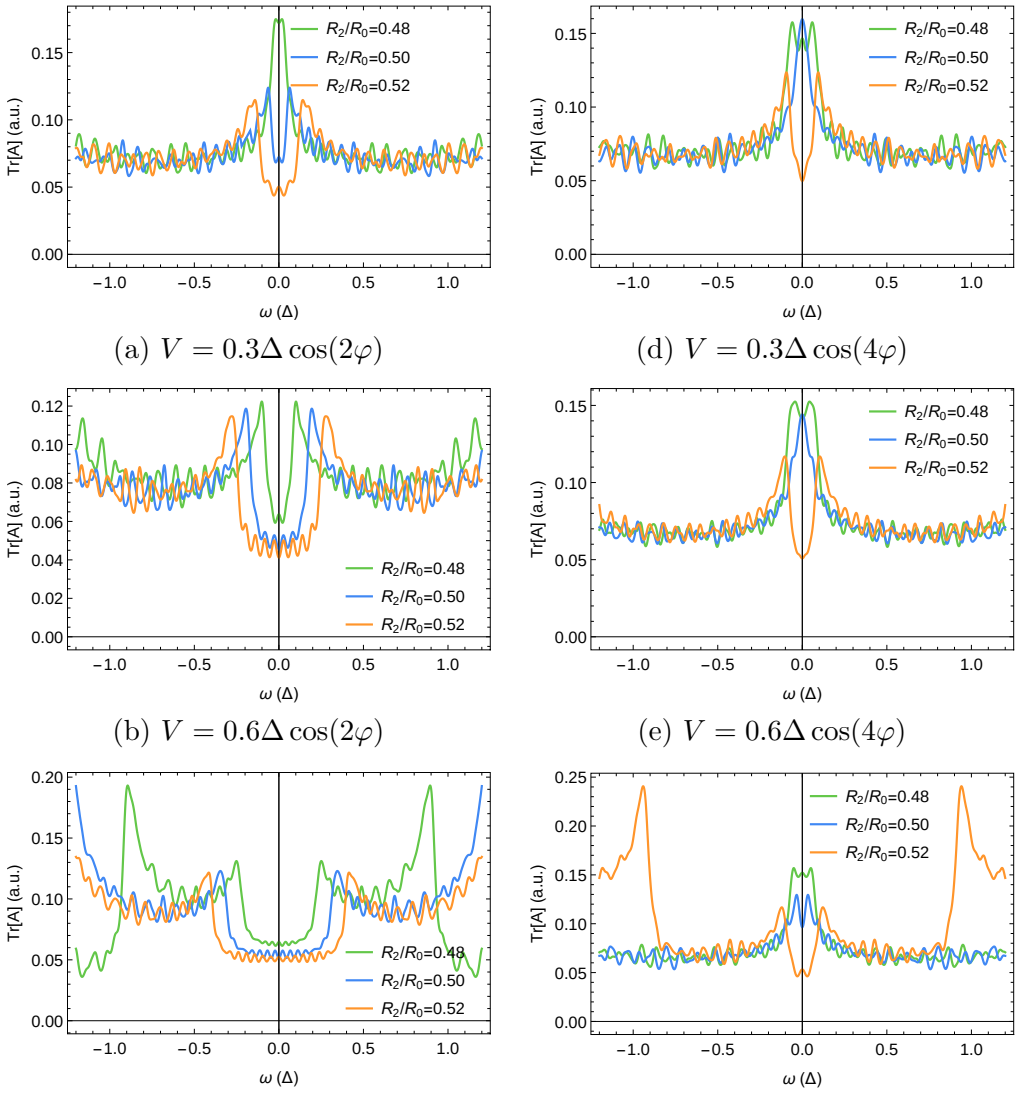

(a) $V = 0.3\Delta\cos(2\varphi)$ (d) $V = 0.3\Delta\cos(4\varphi)$

(b) $V = 0.6\Delta\cos(2\varphi)$ (e) $V = 0.6\Delta\cos(4\varphi)$

(c) $V = 0.9\Delta\cos(2\varphi)$ (f) $V = 0.9\Delta\cos(4\varphi)$

Figure C.5: $\mathrm{Tr}[A](\omega)$ at $(\mu = 9.1\Delta, \alpha = 0)$ for different radii. A d-like deformation $V_0\cos(2\varphi)$, applied in (a)-(c), turns the peaks in the blue and green functions into dips. With increasing strength, the three spectral functions become more alike. A g-like deformation $V_0\cos(4\varphi)$ in (d)-(f) has little effect unless $V_0 \sim \Delta$ where the blue peak splits up. Shared parameters are $\tilde{\Phi} = \frac{1}{2}$ and $n = 1$. As in Figs. C.1 and C.2 gaps in the spectral functions are closed by the finite width of the Lorentzian.

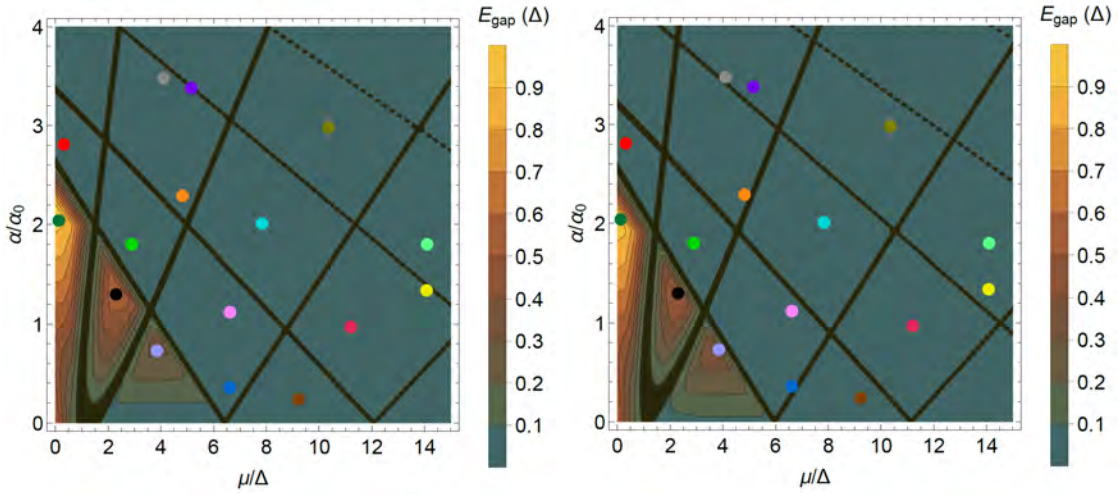

(a) $R_2 = 0.5R_0$ **(b)** $R_2 = 0.52R_0$

(0.124,2.04)
(0.317,2.81)
(2.3,1.3)
(2.9,1.8)
(3.85,0.731)
(4.1,3.48)
(4.82,2.29)
(5.16,3.38)
(6.62,0.357)
(6.62,1.12)
(7.84,2.01)
(9.23,0.24)
(10.35,2.98)
(11.2,0.97)
(14.08,1.34)
(14.1,1.8)

Figure C.6: Points in (μ, α) space chosen for calculations of the spectral functions discussed in Secs. 6.3, 7, and 8. The points are plotted on top of the topological phase diagrams for two different radii with $\tilde{\Phi} = \frac{1}{2}$ and $n = 1$. Electron and hole components of the spectral functions in Figs. C.7 to C.13 are calculated by summing weighted Lorentzian functions (as explained in Sec. 6) including sectors $m_J = -4, \ldots, m_J = 4$. In Figs. C.14 to C.18 only the trace of the spectral function is calculated.

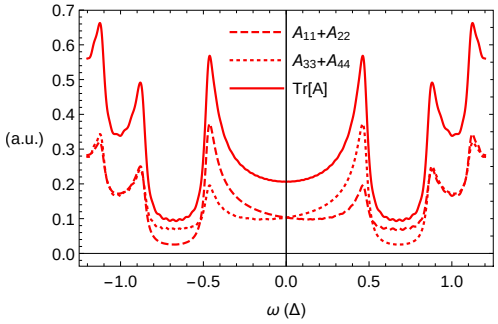

(a) $(\mu = 0.317\Delta, \alpha = 2.81\alpha_0)$, $\tilde{\Phi} = 0.5$

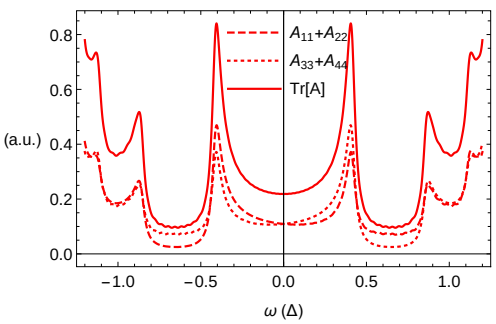

(b) $(\mu = 0.317\Delta, \alpha = 2.81\alpha_0)$, $\tilde{\Phi} = 0.5$

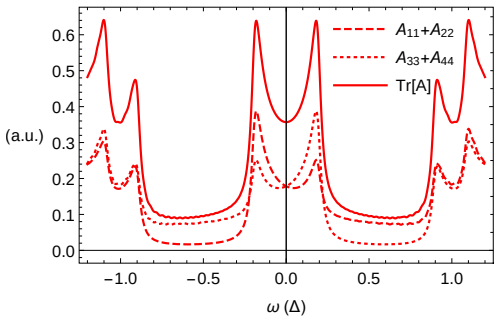

(c) $(\mu = 0.317\Delta, \alpha = 2.81\alpha_0)$, $\tilde{\Phi} = 0.6$

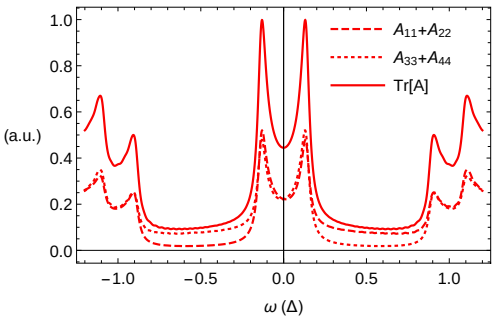

(d) $(\mu = 0.317\Delta, \alpha = 2.81\alpha_0)$, $\tilde{\Phi} = 0.6$

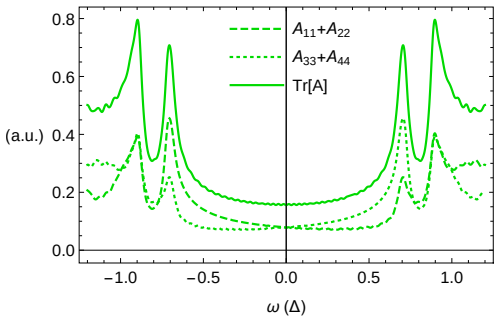

(e) $(\mu = 2.9\Delta, \alpha = 1.8\alpha_0)$, $\tilde{\Phi} = 0.5$

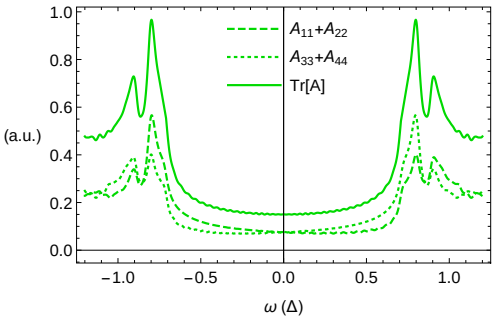

(f) $(\mu = 2.9\Delta, \alpha = 1.8\alpha_0)$, $\tilde{\Phi} = 0.5$

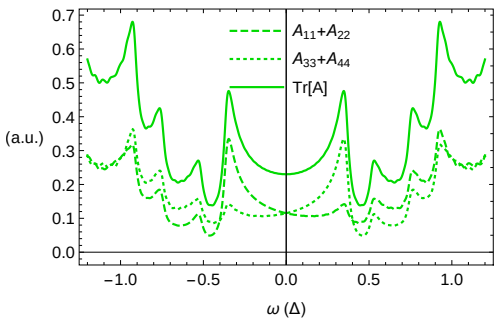

(g) $(\mu = 2.9\Delta, \alpha = 1.8\alpha_0)$, $\tilde{\Phi} = 0.6$

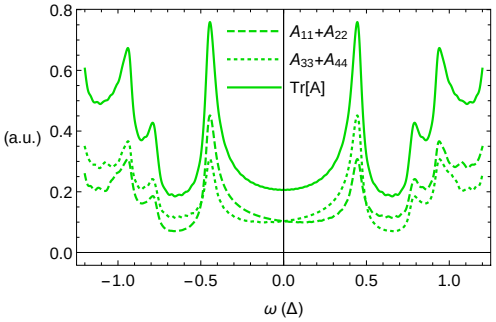

(h) $(\mu = 2.9\Delta, \alpha = 1.8\alpha_0)$, $\tilde{\Phi} = 0.6$

Figure C.7: Spectral functions for the full-shell nanowire system described by $\sum_{m_J} \tilde{H}_{m_J,p_z}$ (Eq. (4.9)) without deformations. Left column is for $R_2 = 0.5R_0$ and right column for $R_2 = 0.52R_0$.

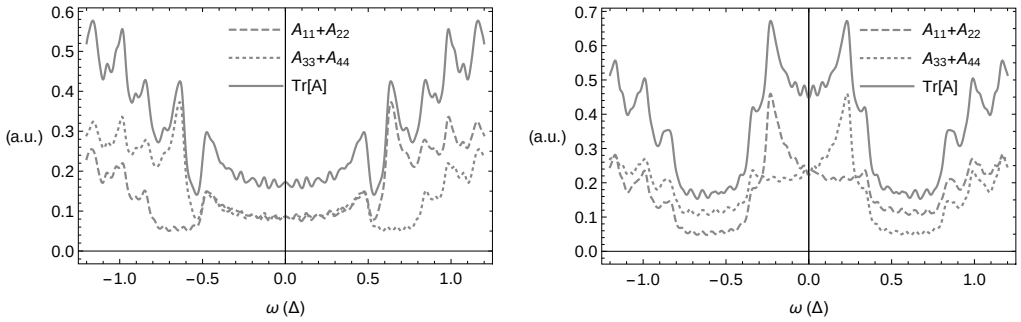

(a) $(\mu = 4.1\Delta, \alpha = 3.48\alpha_0)$, $\tilde{\Phi} = 0.5$

(b) $(\mu = 4.1\Delta, \alpha = 3.48\alpha_0)$, $\tilde{\Phi} = 0.5$

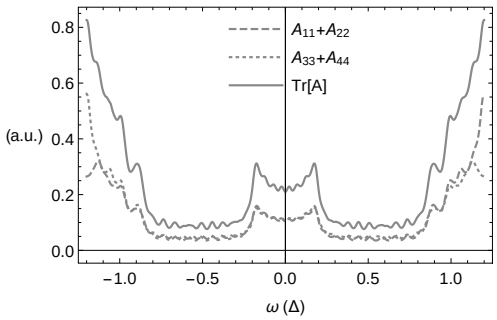

(c) $(\mu = 4.1\Delta, \alpha = 3.48\alpha_0)$, $\tilde{\Phi} = 0.6$

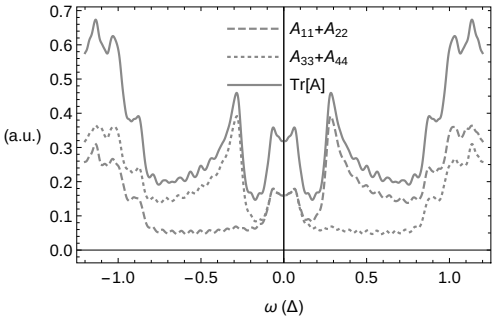

(d)$(\mu = 4.1\Delta, \alpha = 3.48\alpha_0)$, $\tilde{\Phi} = 0.6$

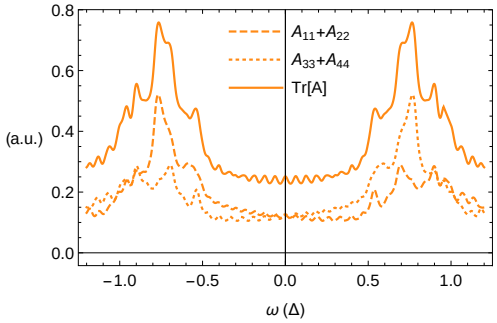

(e) $(\mu = 4.82\Delta, \alpha = 2.29\alpha_0)$, $\tilde{\Phi} = 0.5$

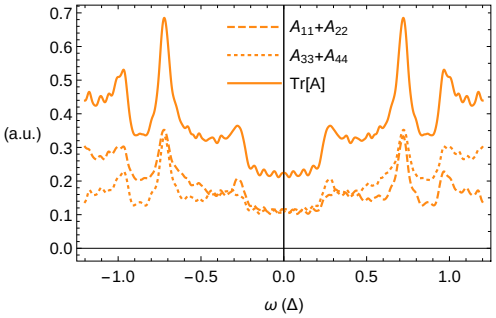

(f) $(\mu = 4.82\Delta, \alpha = 2.29\alpha_0)$, $\tilde{\Phi} = 0.5$

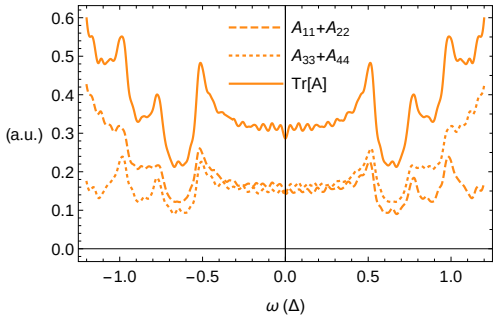

(g) $(\mu = 4.82\Delta, \alpha = 2.29\alpha_0)$, $\tilde{\Phi} = 0.6$

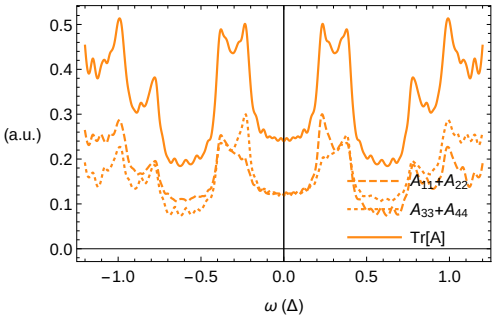

(h) $(\mu = 4.82\Delta, \alpha = 2.29\alpha_0)$, $\tilde{\Phi} = 0.6$

Figure C.8: Spectral functions for the full-shell nanowire system described by $\sum_{m_J} \tilde{H}_{m_J,p_z}$ (Eq. (4.9)) without deformations. Left column is for $R_2 = 0.5R_0$ and right column for $R_2 = 0.52R_0$.

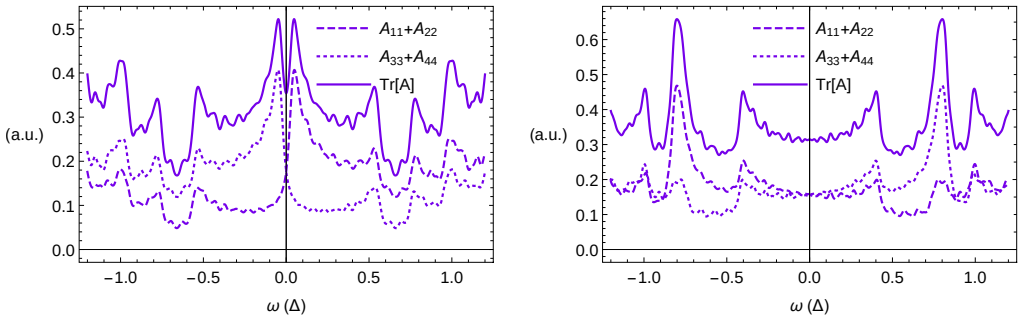

(a) $(\mu = 5.16\Delta, \alpha = 3.38\alpha_0)$, $\tilde{\Phi} = 0.5$

(b) $(\mu = 5.16\Delta, \alpha = 3.38\alpha_0)$, $\tilde{\Phi} = 0.5$

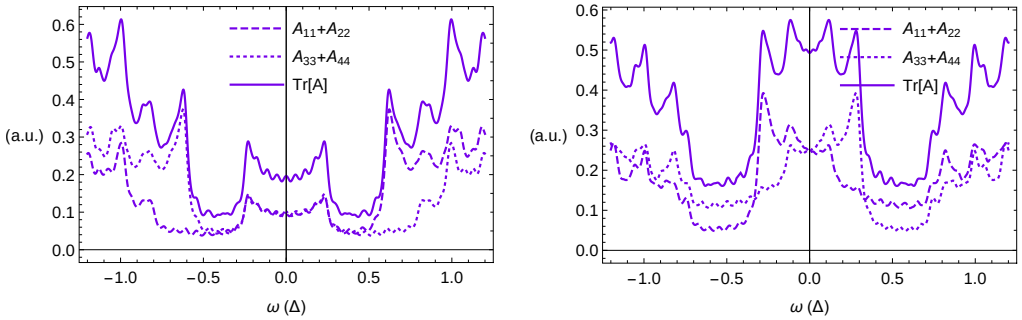

(c) $(\mu = 5.16\Delta, \alpha = 3.38\alpha_0)$, $\tilde{\Phi} = 0.6$

(d)$(\mu = 5.16\Delta, \alpha = 3.38\alpha_0)$, $\tilde{\Phi} = 0.6$

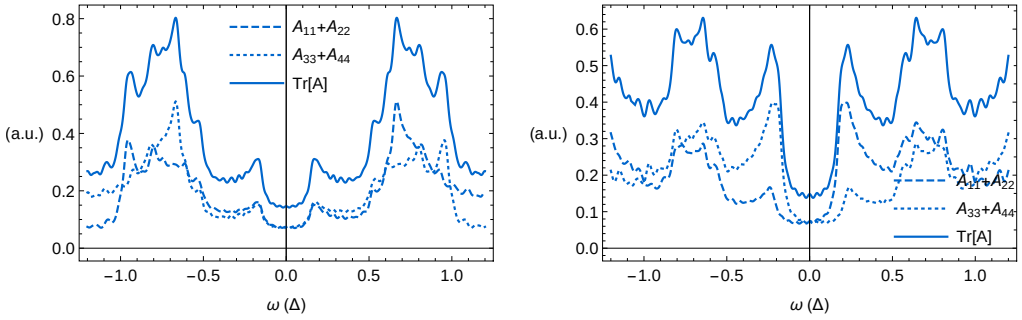

(e) $(\mu = 6.62\Delta, \alpha = 0.357\alpha_0)$, $\tilde{\Phi} = 0.5$

(f) $(\mu = 6.62\Delta, \alpha = 0.357\alpha_0)$, $\tilde{\Phi} = 0.5$

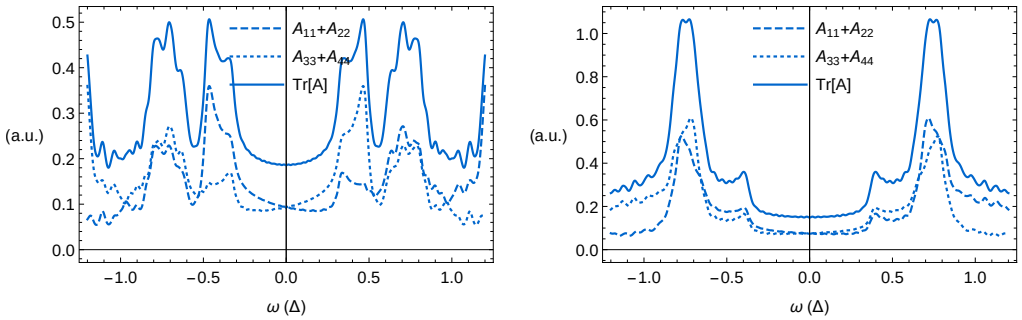

(g) $(\mu = 6.62\Delta, \alpha = 0.357\alpha_0)$, $\tilde{\Phi} = 0.6$

(h) $(\mu = 6.62\Delta, \alpha = 0.357\alpha_0)$, $\tilde{\Phi} = 0.6$

Figure C.9: Spectral functions for the full-shell nanowire system described by $\sum_{m_J} \tilde{H}_{m_J,p_z}$ (Eq. (4.9)) without deformations. Left column is for $R_2 = 0.5R_0$ and right column for $R_2 = 0.52R_0$.

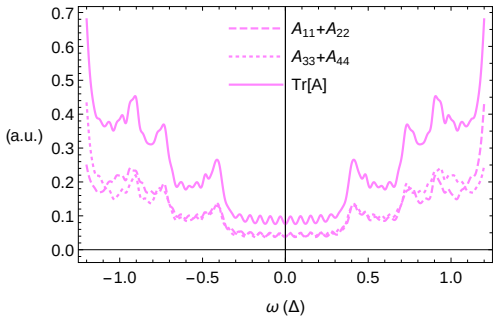

(a) $(\mu = 6.62\Delta, \alpha = 1.12\alpha_0)$, $\tilde{\Phi} = 0.5$

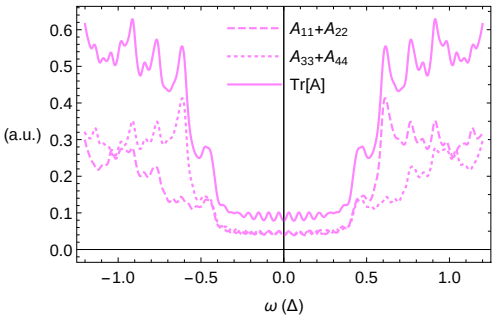

(b) $(\mu = 6.62\Delta, \alpha = 1.12\alpha_0)$, $\tilde{\Phi} = 0.5$

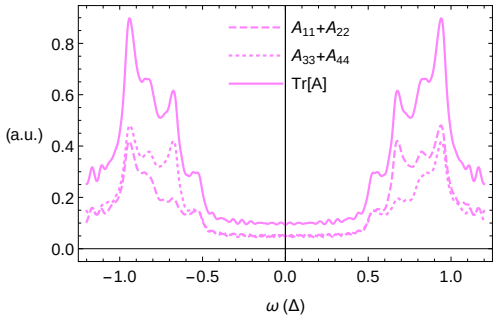

(c) $(\mu = 6.62\Delta, \alpha = 1.12\alpha_0)$, $\tilde{\Phi} = 0.6$

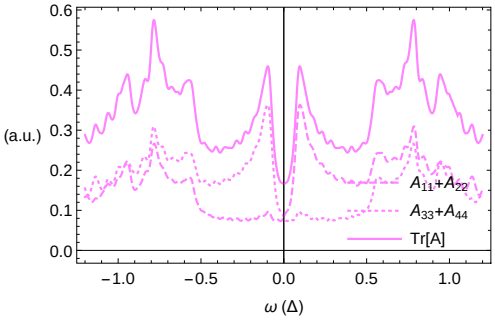

(d)$(\mu = 6.62\Delta, \alpha = 1.12\alpha_0)$, $\tilde{\Phi} = 0.6$

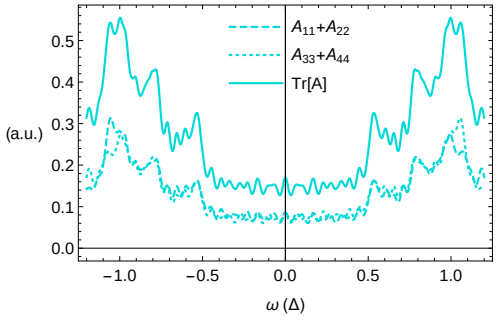

(e) $(\mu = 7.84\Delta, \alpha = 2.01\alpha_0)$, $\tilde{\Phi} = 0.5$

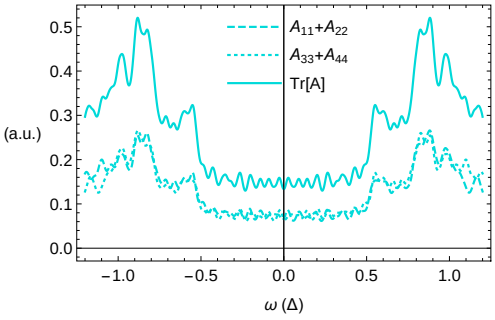

(f) $(\mu = 7.84\Delta, \alpha = 2.01\alpha_0)$, $\tilde{\Phi} = 0.5$

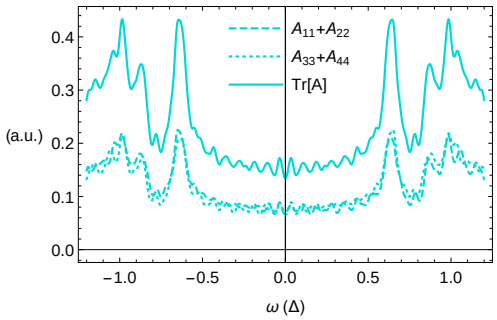

(g)$(\mu = 7.84\Delta, \alpha = 2.01\alpha_0)$, $\tilde{\Phi} = 0.6$

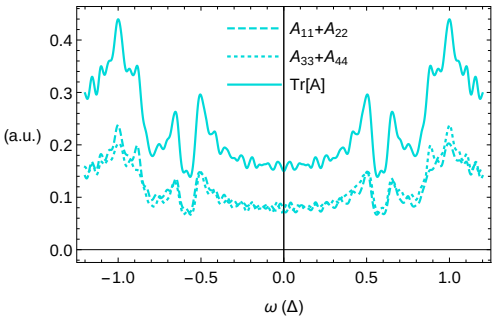

(h) $(\mu = 7.84\Delta, \alpha = 2.01\alpha_0)$, $\tilde{\Phi} = 0.6$

Figure C.10: Spectral functions for the full-shell nanowire system described by $\sum_{m_J} \tilde{H}_{m_J,p_z}$ (Eq. (4.9)) without deformations. Left column is for $R_2 = 0.5R_0$ and right column for $R_2 = 0.52R_0$.

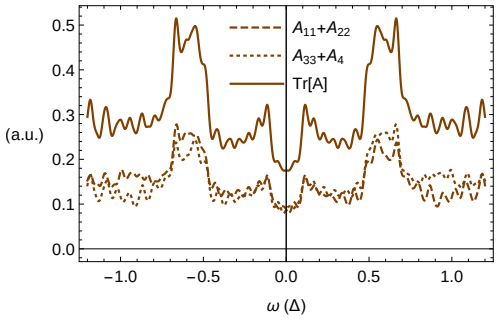

(a) $(\mu = 9.23\Delta, \alpha = 0.24\alpha_0)$, $\tilde{\Phi} = 0.5$

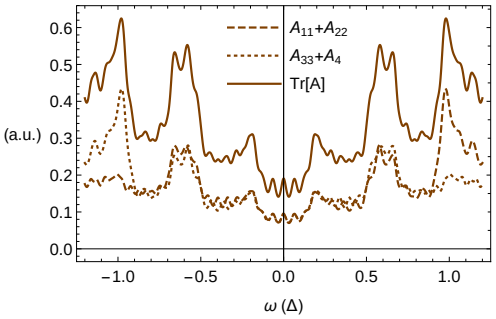

(b) $(\mu = 9.23\Delta, \alpha = 0.24\alpha_0)$, $\tilde{\Phi} = 0.5$

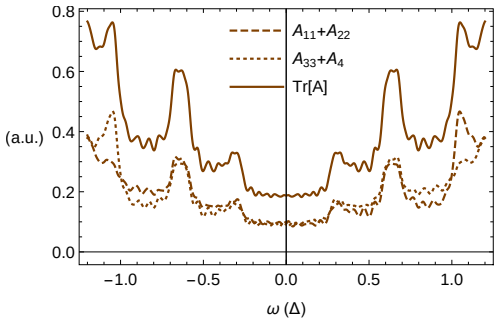

(c) $(\mu = 9.23\Delta, \alpha = 0.24\alpha_0)$, $\tilde{\Phi} = 0.6$

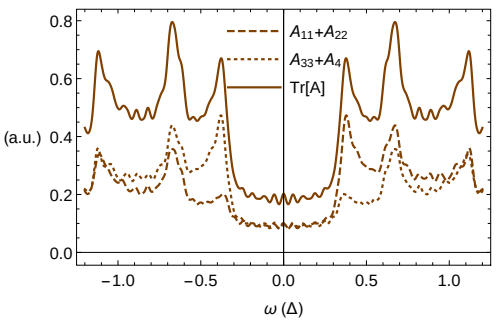

(d)$(\mu = 9.23\Delta, \alpha = 0.24\alpha_0)$, $\tilde{\Phi} = 0.6$

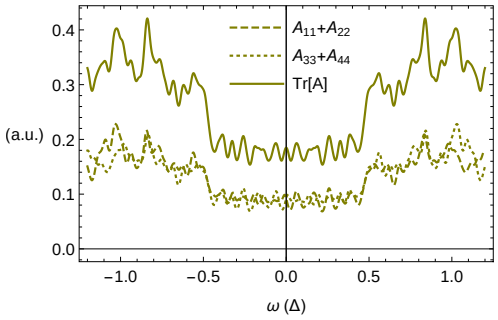

(e) $(\mu = 10.35\Delta, \alpha = 2.98\alpha_0)$, $\tilde{\Phi} = 0.5$

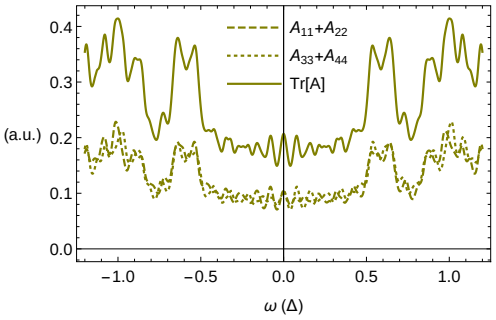

(f) $(\mu = 10.35\Delta, \alpha = 2.98\alpha_0)$, $\tilde{\Phi} = 0.5$

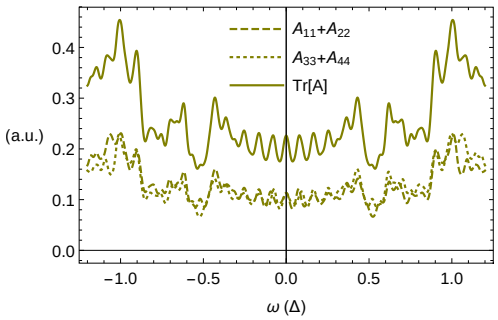

(g)$(\mu = 10.35\Delta, \alpha = 2.98\alpha_0)$, $\tilde{\Phi} = 0.6$

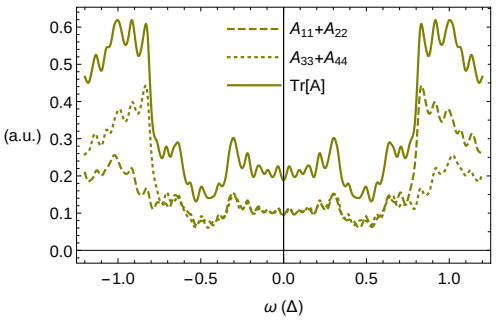

(h) $(\mu = 10.35\Delta, \alpha = 2.98\alpha_0)$, $\tilde{\Phi} = 0.6$

Figure C.11: Spectral functions for the full-shell nanowire system described by $\sum_{m_J} \tilde{H}_{m_J,p_z}$ (Eq. (4.9)) without deformations. Left column is for $R_2 = 0.5R_0$ and right column for $R_2 = 0.52R_0$.

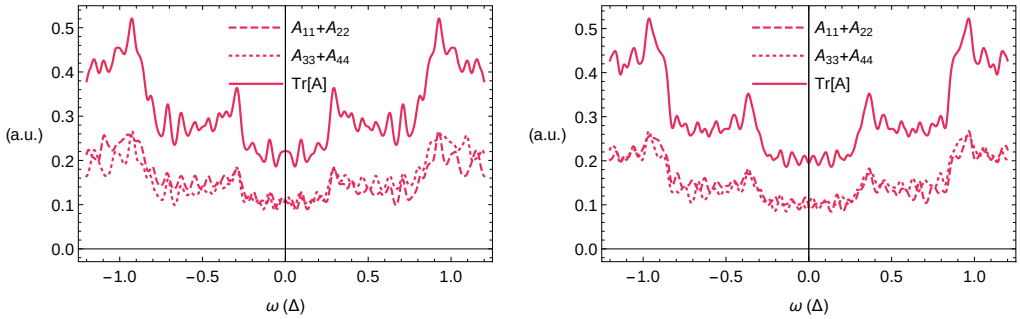

(a) $(\mu = 11.2\Delta, \alpha = 0.97\alpha_0)$, $\tilde{\Phi} = 0.5$

(b) $(\mu = 11.2\Delta, \alpha = 0.97\alpha_0)$, $\tilde{\Phi} = 0.5$

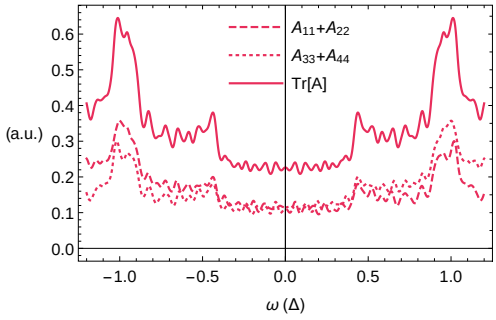

(c) $(\mu = 11.2\Delta, \alpha = 0.97\alpha_0)$, $\tilde{\Phi} = 0.6$

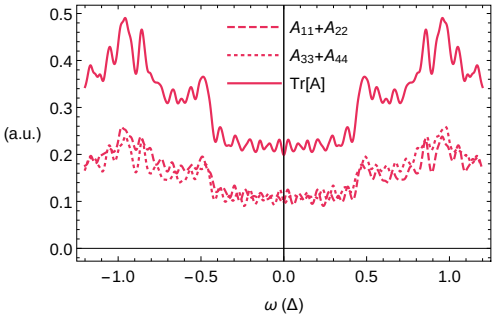

(d)$(\mu = 11.2\Delta, \alpha = 0.97\alpha_0)$, $\tilde{\Phi} = 0.6$

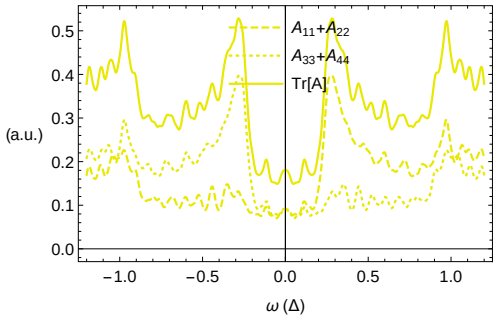

(e) $(\mu = 14.08\Delta, \alpha = 1.34\alpha_0)$, $\tilde{\Phi} = 0.5$

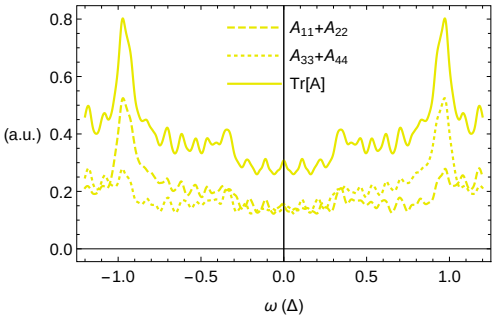

(f) $(\mu = 14.08\Delta, \alpha = 1.34\alpha_0)$, $\tilde{\Phi} = 0.5$

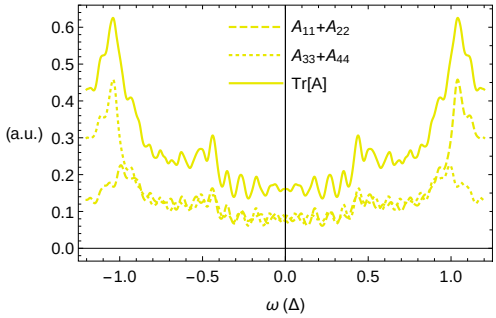

(g)$(\mu = 14.08\Delta, \alpha = 1.34\alpha_0)$, $\tilde{\Phi} = 0.6$

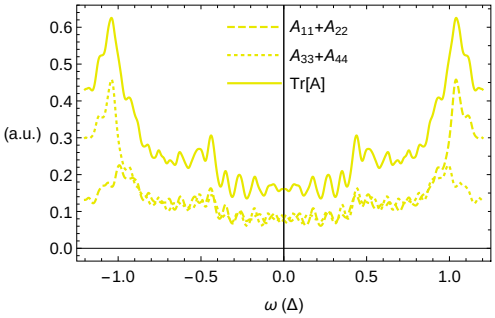

(h) $(\mu = 14.08\Delta, \alpha = 1.34\alpha_0)$, $\tilde{\Phi} = 0.6$

Figure C.12: Spectral functions for the full-shell nanowire system described by $\sum_{m_J} \tilde{H}_{m_J,p_z}$ (Eq. (4.9)) without deformations. Left column is for $R_2 = 0.5R_0$ and right column for $R_2 = 0.52R_0$.

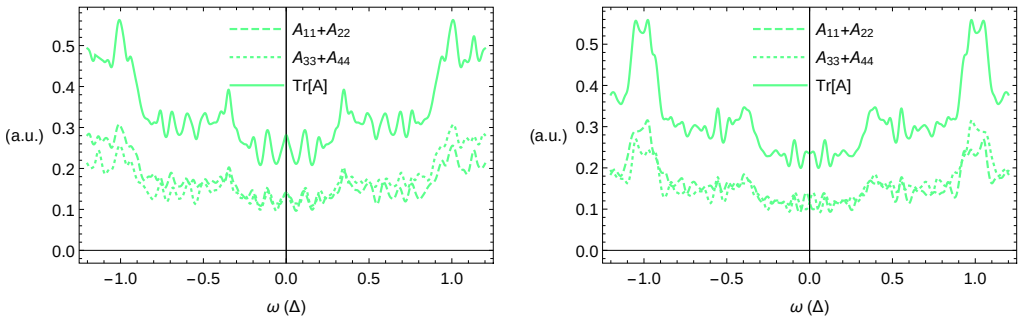

(a) $(\mu = 14.1\Delta, \alpha = 1.8\alpha_0)$, $\tilde{\Phi} = 0.5$ (b) $(\mu = 14.1\Delta, \alpha = 1.8\alpha_0)$, $\tilde{\Phi} = 0.5$

(c) $(\mu = 14.1\Delta, \alpha = 1.8\alpha_0)$, $\tilde{\Phi} = 0.6$ (d)$(\mu = 14.1\Delta, \alpha = 1.8\alpha_0)$, $\tilde{\Phi} = 0.6$

Figure C.13: Spectral functions for the full-shell nanowire system described by $\sum_{m_J} \tilde{H}_{m_J,p_z}$ (Eq. (4.9)) without deformations. Left column is for $R_2 = 0.5R_0$ and right column for $R_2 = 0.52R_0$.

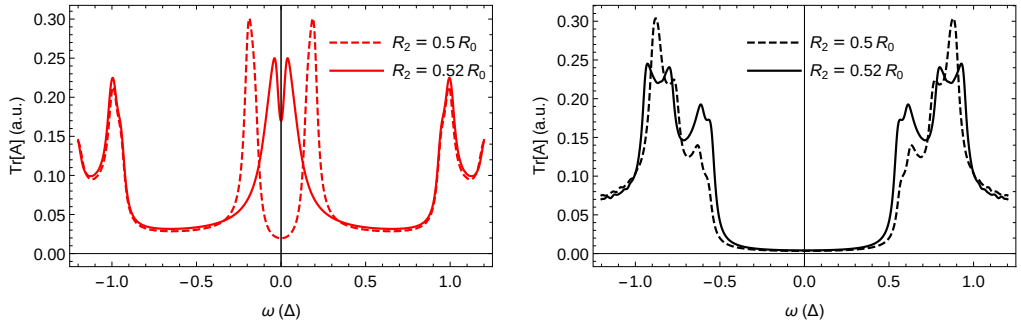

(a) $V_0 = 0.3\Delta$

(e) $V_0 = 0\Delta$

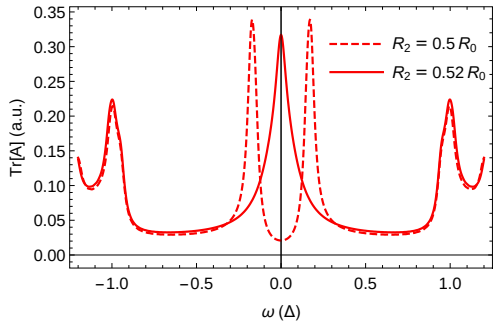

(b) $V_0 = 0.31\Delta$

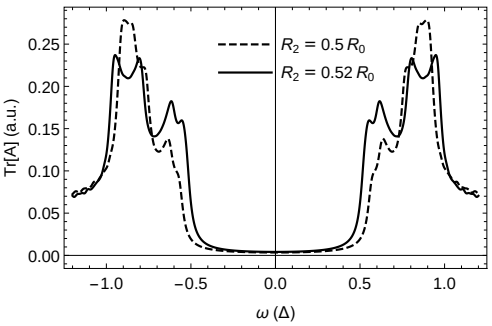

(f) $V_0 = 0.3\Delta$

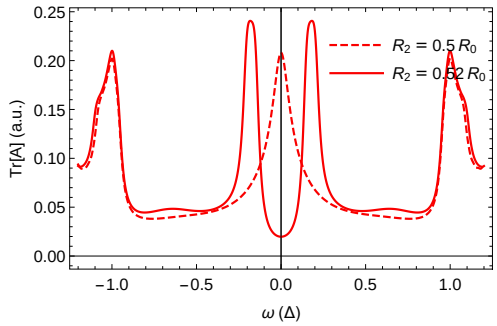

(c) $V_0 = 0.394\Delta$

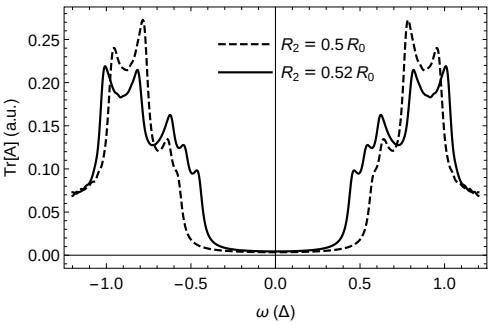

(g) $V_0 = 0.6\Delta$

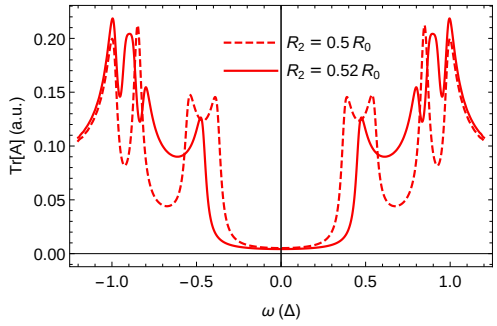

(d) $V_0 = 0.6\Delta$

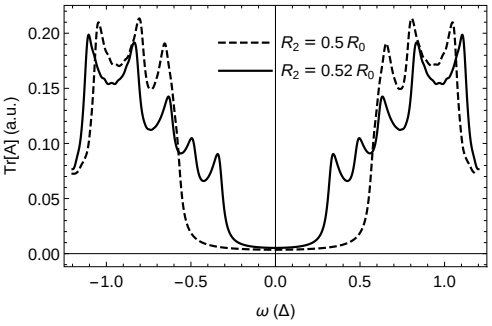

(h) $V_0 = 0.9\Delta$

Figure C.14: Figs. (a)-(d) show $\mathrm{Tr}[A(\omega)]$ at point $(\mu = 0.317\Delta, \alpha = 2.81\alpha_0)$ with a potential $V_0\cos(2\varphi)$. The zero-energy peaks in (b) and (c) are not stable to changes in V_0, R_2 or $\tilde{\Phi}$. Figs. (e)-(h) show $\mathrm{Tr}[A(\omega)]$ at $(\mu = 2.3\Delta, \alpha = 1.3\alpha_0)$ with a potential $V_0\cos(4\varphi)$. The gap is not stable for $R_2 = 0.52R_0$ but it is for $R_2 = 0.5R_0$. Here $\tilde{\Phi} = 0.5$.

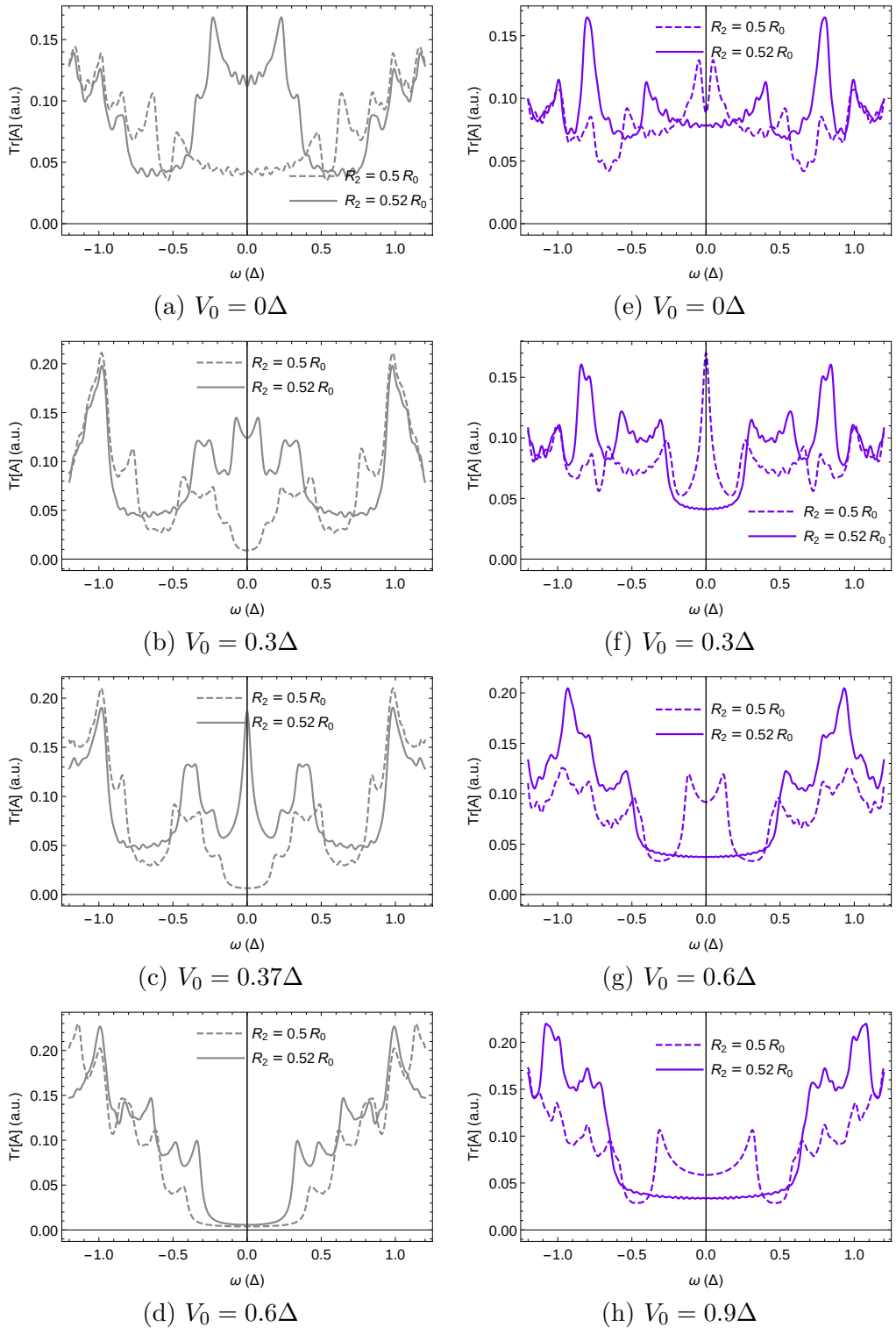

(a) $V_0 = 0\Delta$ (e) $V_0 = 0\Delta$

(b) $V_0 = 0.3\Delta$ (f) $V_0 = 0.3\Delta$

(c) $V_0 = 0.37\Delta$ (g) $V_0 = 0.6\Delta$

(d) $V_0 = 0.6\Delta$ (h) $V_0 = 0.9\Delta$

Figure C.15: Figs. (a)-(d) show $\mathrm{Tr}[A(\omega)]$ at the point $(\mu = 4.1\Delta, \alpha = 3.48\alpha_0)$ with a potential $V_0\cos(2\varphi)$. The peak in (c) at $\omega = 0$ is not stable to small changes in V_0, R_2 or $\tilde{\Phi}$. Figs. (e)-(h) show $\mathrm{Tr}[A(\omega)]$ at $(\mu = 5.16\Delta, \alpha = 3.38\alpha_0)$ with a potential $V_0\cos(4\varphi)$. The zero energy peak in (f) exists over quite a wide range of $V_0 \in [0.226, 0.392]\Delta$ but is not stable to radius and flux changes. Here $\tilde{\Phi} = 0.5$.

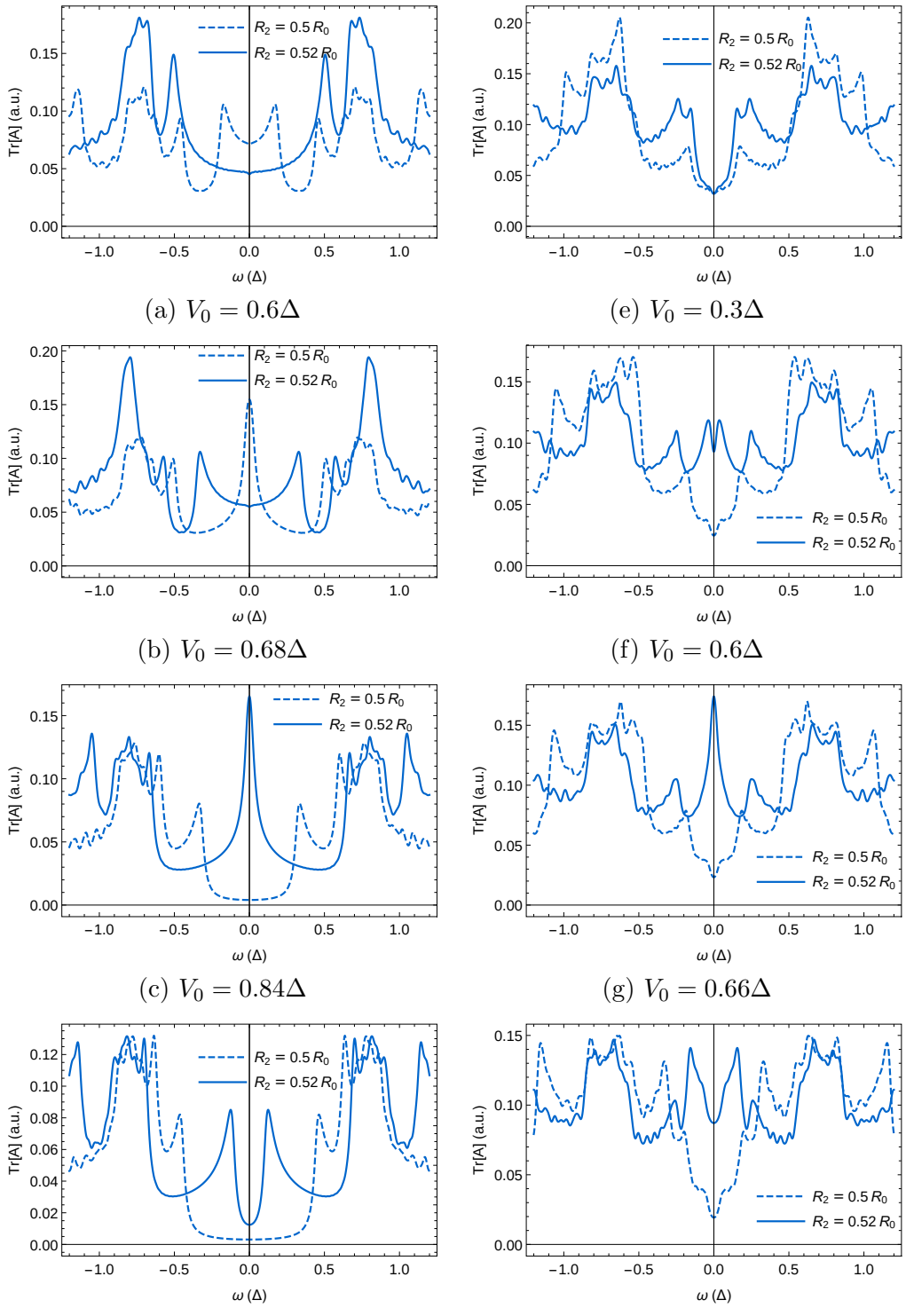

(a) $V_0 = 0.6\Delta$ (e) $V_0 = 0.3\Delta$

(b) $V_0 = 0.68\Delta$ (f) $V_0 = 0.6\Delta$

(c) $V_0 = 0.84\Delta$ (g) $V_0 = 0.66\Delta$

(d) $V_0 = 0.9\Delta$ (h) $V_0 = 0.9\Delta$

Figure C.16: Figs. (a)-(h) show $\mathrm{Tr}[A(\omega)]$ at the point $(\mu = 6.62\Delta, \alpha = 0.357\alpha_0)$ with a potential $V_0\cos(2\varphi)$ in (a)-(d) and $V_0\cos(4\varphi)$ in (e)-(h). All the zero-energy peaks are unstable to changes is V_0, R_2, and $\tilde{\Phi}$. Here $\tilde{\Phi} = 0.5$.

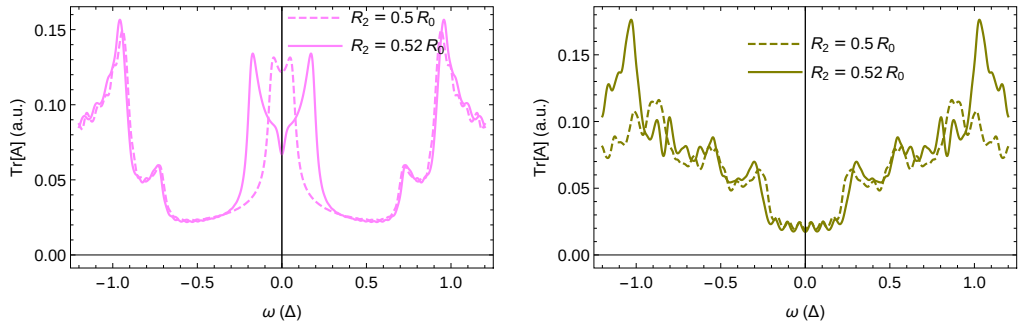

(a) $V_0 = 0.9\Delta$

(e) $V_0 = 0.3\Delta$

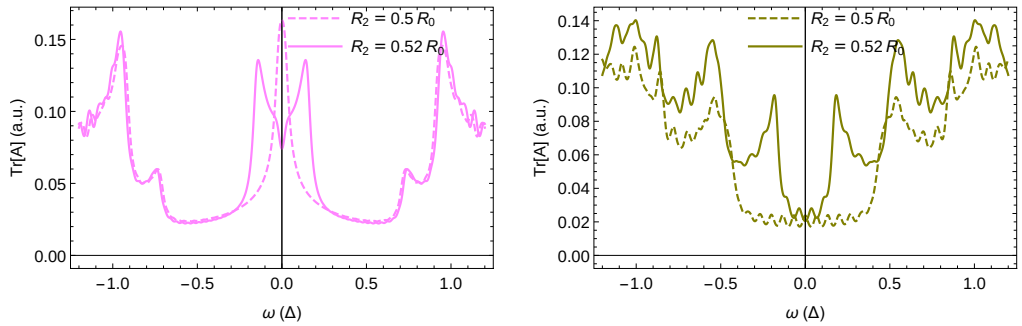

(b) $V_0 = 0.92\Delta$

(f) $V_0 = 0.6\Delta$

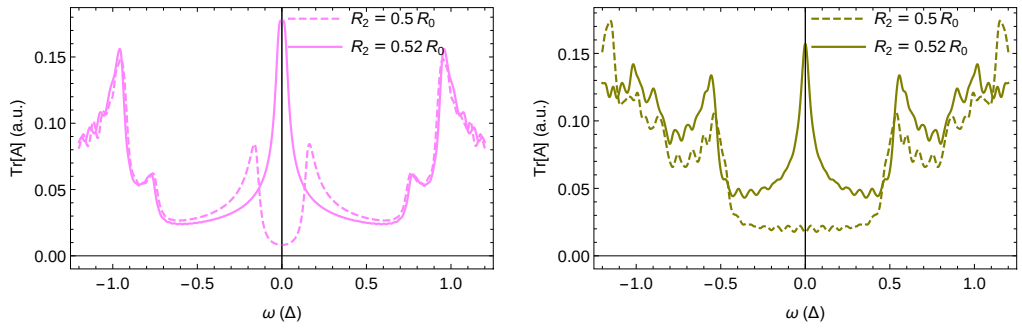

(c) $V_0 = 1.0\Delta$

(g) $V_0 = 0.66\Delta$

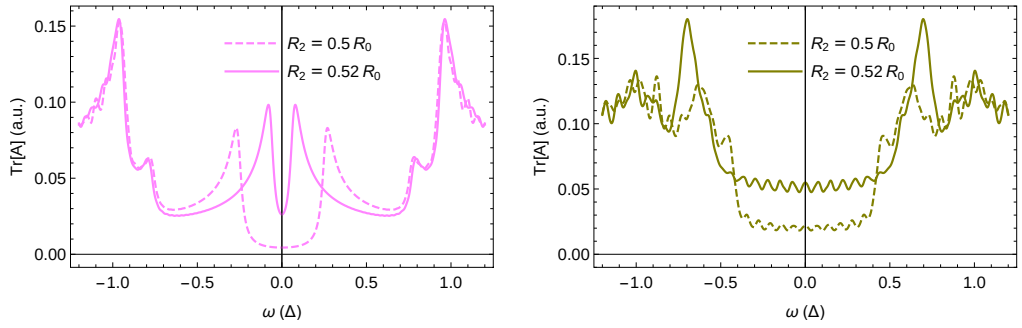

(d) $V_0 = 1.05\Delta$

(h) $V_0 = 0.9\Delta$

Figure C.17: Figs. (a)-(d) show $\mathrm{Tr}[A(\omega)]$ at point $(\mu = 6.62\Delta, \alpha = 1.12\alpha_0)$ with a potential $V_0\cos(2\varphi)$ and Figs. (e)-(h) show $\mathrm{Tr}[A(\omega)]$ at $(\mu = 10.35\Delta, \alpha = 2.98\alpha_0)$ with a potential $V_0\cos(4\varphi)$. None of the zero-energy peaks are stable to small changes in V_0, R_2, or $\tilde{\Phi}$. Here $\tilde{\Phi} = 0.5$.

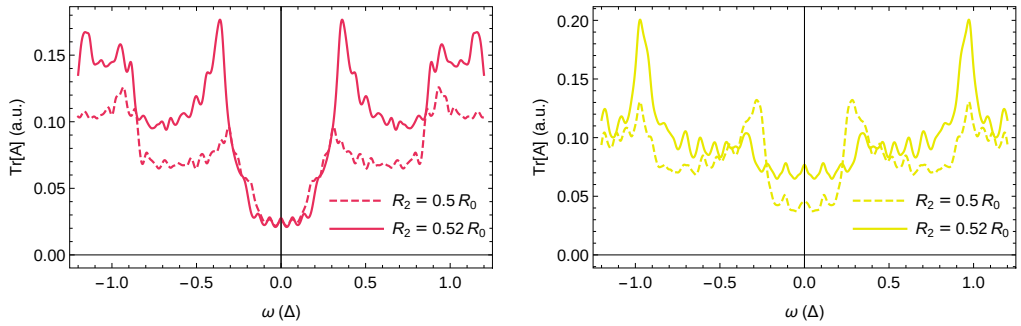

(a) $V_0 = 0.9\Delta$

(e) $V_0 = 0\Delta$

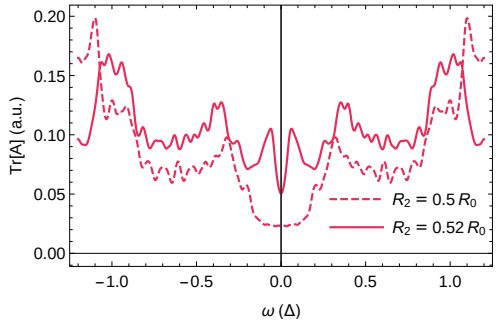

(b) $V_0 = 1.0\Delta$

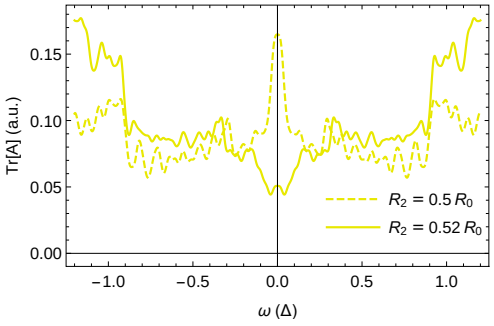

(f) $V_0 = 0.27\Delta$

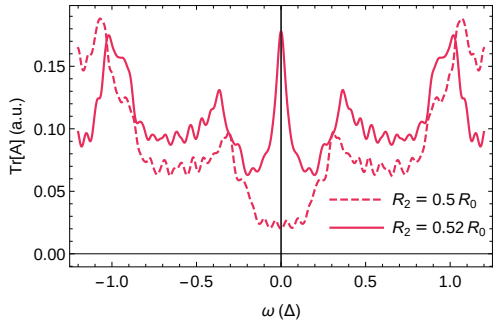

(c) $V_0 = 1.02\Delta$

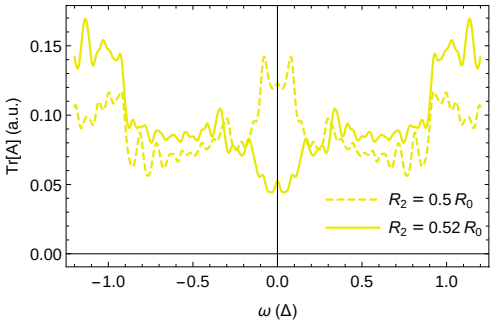

(g) $V_0 = 0.3\Delta$

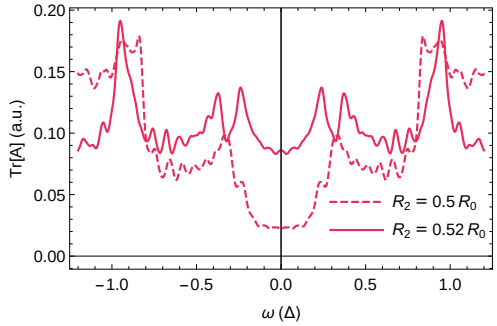

(d) $V_0 = 1.1\Delta$

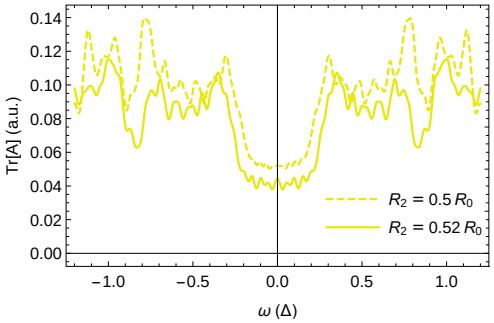

(h) $V_0 = 0.6\Delta$

Figure C.18: Figs. (a)-(d) show $\mathrm{Tr}[A(\omega)]$ at point $(\mu = 11.2\Delta, \alpha = 0.97\alpha_0)$ with a potential $V_0\cos(4\varphi)$ and Figs. (e)-(h) show $\mathrm{Tr}[A(\omega)]$ at $(\mu = 14.08\Delta, \alpha = 1.34\alpha_0)$ with a potential $V_0\cos(4\varphi)$. The zero-energy peaks are not stable to changes in V_0, R_2, or $\tilde{\Phi}$. Here $\tilde{\Phi} = 0.5$.

D Inversion of matrices

For calculating F^{-1} from Sec. 7 we define the matrix elements:

$$\begin{aligned}
\tilde{H}_{11} &= \frac{p^2}{2m^*} - \mu_m + V_z + A_m + C_m, \\
\tilde{H}_{22} &= \frac{p^2}{2m^*} - \mu_m - V_z + A_m - C_m, \\
\tilde{H}_{33} &= -\frac{p^2}{2m^*} + \mu_m + V_z + A_m - C_m, \\
\tilde{H}_{22} &= -\frac{p^2}{2m^*} + \mu_m - V_z + A_m + C_m, \\
\tilde{H}_{12} &= \tilde{H}_{43} = -\tilde{H}_{21} = -\tilde{H}_{34} = -i\alpha p.
\end{aligned}$$

$$F = \begin{pmatrix}
\omega + i\eta - \tilde{H}_{11} & \tilde{H}_{21} & -\Delta & 0 \\
-\tilde{H}_{21} & \omega + i\eta - \tilde{H}_{22} & 0 & -\Delta \\
-\Delta & 0 & \omega + i\eta - \tilde{H}_{33} & -\tilde{H}_{21} \\
0 & -\Delta & \tilde{H}_{21} & \omega + i\eta - \tilde{H}_{44}
\end{pmatrix}.$$

The determinant is found to be an even function of p:

$$\begin{aligned}
|F| = (\omega + i\eta - \tilde{H}_{11})\Big((\omega + i\eta - \tilde{H}_{22})(\omega + i\eta - \tilde{H}_{33})(\omega + i\eta - \tilde{H}_{44}) - \Delta^2(\omega + i\eta - \tilde{H}_{33}) \\
+ (\omega + i\eta - \tilde{H}_{22})\tilde{H}_{21}^2\Big) \\
- \tilde{H}_{21}\left(-\tilde{H}_{21}(\omega + i\eta - \tilde{H}_{33})(\omega + i\eta - \tilde{H}_{44}) + \Delta^2\tilde{H}_{21} - \tilde{H}_{21}^3\right) \\
+ \Delta\left(-\Delta^3 + \Delta\tilde{H}_{21}^2 + \Delta(\omega + i\eta - \tilde{H}_{22})(\omega + i\eta - \tilde{H}_{44})\right).
\end{aligned}$$

The elements of the matrix C that contains the cofactors of the elements in F (see Eq. (7.9)) are

$$\begin{aligned}
C_{11} &= (\omega + i\eta - \tilde{H}_{22})(\omega + i\eta - \tilde{H}_{33})(\omega + i\eta - \tilde{H}_{44}) - \Delta^2(\omega + i\eta - \tilde{H}_{33}) + (\omega + i\eta - \tilde{H}_{22})\tilde{H}_{21}^2, \\
C_{12} &= \tilde{H}_{21}(\omega + i\eta - \tilde{H}_{33})(\omega + i\eta - \tilde{H}_{44}) - \Delta^2\tilde{H}_{21} + \tilde{H}_{21}^3, \\
C_{13} &= -\Delta^3 + \Delta\tilde{H}_{21}^2 + \Delta(\omega + i\eta - \tilde{H}_{22})(\omega + i\eta - \tilde{H}_{44}), \\
C_{14} &= \Delta(\omega + i\eta - \tilde{H}_{33})\tilde{H}_{21} - \Delta(\omega + i\eta - \tilde{H}_{22})\tilde{H}_{21}, \\
C_{21} &= -C_{21}, \\
C_{22} &= (\omega + i\eta - \tilde{H}_{11})(\omega + i\eta - \tilde{H}_{33})(\omega + i\eta - \tilde{H}_{44}) + (\omega + i\eta - \tilde{H}_{11})\tilde{H}_{21}^2 - \Delta^2(\omega + i\eta - \tilde{H}_{44}), \\
C_{23} &= \Delta(\omega + i\eta - \tilde{H}_{11})\tilde{H}_{21} - \Delta(\omega + i\eta - \tilde{H}_{44})\tilde{H}_{21}, \\
C_{24} &= -\Delta^3 + \Delta(\omega + i\eta - \tilde{H}_{11})(\omega + i\eta - \tilde{H}_{33}) + \Delta\tilde{H}_{21}^2, \\
C_{31} &= C_{13}, \\
C_{32} &= -C_{23}, \\
C_{33} &= (\omega + i\eta - \tilde{H}_{11})(\omega + i\eta - \tilde{H}_{22})(\omega + i\eta - \tilde{H}_{44}) + (\omega + i\eta - \tilde{H}_{44})\tilde{H}_{21}^2 - \Delta^2(\omega + i\eta - \tilde{H}_{11}), \\
C_{34} &= -(\omega + i\eta - \tilde{H}_{11})(\omega + i\eta - \tilde{H}_{22})\tilde{H}_{21} + \Delta^2\tilde{H}_{21} - \tilde{H}_{21}^3, \\
C_{41} &= -C_{14}, \\
C_{42} &= C_{24}, \\
C_{43} &= -C_{34}, \\
C_{44} &= (\omega + i\eta - \tilde{H}_{11})(\omega + i\eta - \tilde{H}_{22})(\omega + i\eta - \tilde{H}_{33}) - \Delta^2(\omega + i\eta - \tilde{H}_{22}) + (\omega + i\eta - \tilde{H}_{33})\tilde{H}_{21}^2.
\end{aligned}$$

The elements $C_{12} = -C_{21}$, $C_{14} = -C_{41}$, $C_{23} = -C_{32}$, and $C_{34} = -C_{43}$ are all odd functions of p and thus integrate to zero.

To calculate the matrix $\mathcal{G}^{\mathrm{R,1BA}}_{m,p}(\omega)$ in Eq. (7.10) we need to find the inverse of

$$\tilde{F} = \begin{pmatrix} \omega - \tilde{H}_{11} - \Sigma^{\mathrm{1BA}}_{11}(\omega) & \tilde{H}_{21} & -\Delta - \Sigma^{\mathrm{1BA}}_{13}(\omega) & 0 \\ -\tilde{H}_{21} & \omega - \tilde{H}_{22} - \Sigma^{\mathrm{1BA}}_{22}(\omega) & 0 & -\Delta - \Sigma^{\mathrm{1BA}}_{24}(\omega) \\ -\Delta - \Sigma^{\mathrm{1BA}}_{13}(\omega) & 0 & \omega - \tilde{H}_{33} - \Sigma^{\mathrm{1BA}}_{33}(\omega) & -\tilde{H}_{21} \\ 0 & -\Delta - \Sigma^{\mathrm{1BA}}_{24}(\omega) & \tilde{H}_{21} & \omega - \tilde{H}_{44} - \Sigma^{\mathrm{1BA}}_{44}(\omega) \end{pmatrix}.$$

Again, the determinant is an even function of p

$$\begin{aligned} |\tilde{F}| = (\omega - \tilde{H}_{11} - \Sigma^{\mathrm{1BA}}_{11}(\omega))\Big((\omega - \tilde{H}_{22} - \Sigma^{\mathrm{1BA}}_{22}(\omega))(\omega - \tilde{H}_{33} - \Sigma^{\mathrm{1BA}}_{33}(\omega))(\omega - \tilde{H}_{44} - \Sigma^{\mathrm{1BA}}_{44}(\omega)) \\ - (\omega - \tilde{H}_{33} - \Sigma^{\mathrm{1BA}}_{33}(\omega))(\Delta + \Sigma^{\mathrm{1BA}}_{24}(\omega))^2 + (\omega - \tilde{H}_{22} - \Sigma^{\mathrm{1BA}}_{22}(\omega))\tilde{H}^2_{21}\Big) \\ + \tilde{H}^2_{21}\Big((\omega - \tilde{H}_{33} - \Sigma^{\mathrm{1BA}}_{33}(\omega))(\omega - \tilde{H}_{44} - \Sigma^{\mathrm{1BA}}_{44}(\omega)) - (\Delta + \Sigma^{\mathrm{1BA}}_{13}(\omega))(\Delta + \Sigma^{\mathrm{1BA}}_{24}(\omega)) + \tilde{H}^2_{21}\Big) \\ - (\Delta + \Sigma^{\mathrm{1BA}}_{13}(\omega))\Big((\Delta + \Sigma^{\mathrm{1BA}}_{13}(\omega)(\omega - \tilde{H}_{22} - \Sigma^{\mathrm{1BA}}_{22}(\omega))(\omega - \tilde{H}_{44} - \Sigma^{\mathrm{1BA}}_{44}(\omega)) \\ - (\Delta + \Sigma^{\mathrm{1BA}}_{13}(\omega))(\Delta + \Sigma^{\mathrm{1BA}}_{24}(\omega))^2 + \tilde{H}^2_{21}(\Delta + \Sigma^{\mathrm{1BA}}_{24}(\omega))\Big). \end{aligned} \tag{D.1}$$

We calculate the corresponding new cofactors $\tilde{C}_{ij}$ which are odd functions of p for $ij = 12, 14, 21, 23, 32, 34, 41, 43$. Factors that do not integrate to zero are:

$$\begin{aligned} \tilde{C}_{11} &= (\omega - \tilde{H}_{22} - \Sigma^{\mathrm{1BA}}_{22}(\omega))(\omega - \tilde{H}_{33} - \Sigma^{\mathrm{1BA}}_{33}(\omega))(\omega - \tilde{H}_{44} - \Sigma^{\mathrm{1BA}}_{44}(\omega)) \\ &\quad - (\omega - \tilde{H}_{33} - \Sigma^{\mathrm{1BA}}_{33}(\omega))(\Delta + \Sigma^{\mathrm{1BA}}_{24}(\omega))^2 + (\omega - \tilde{H}_{22} - \Sigma^{\mathrm{1BA}}_{22}(\omega))\tilde{H}^2_{21}, \\ \tilde{C}_{13} &= \tilde{C}_{31} = (\omega - \tilde{H}_{22} - \Sigma^{\mathrm{1BA}}_{22}(\omega))(\omega - \tilde{H}_{44} - \Sigma^{\mathrm{1BA}}_{44}(\omega))(\Delta + \Sigma^{\mathrm{1BA}}_{13}(\omega)) \\ &\quad - (\Delta + \Sigma^{\mathrm{1BA}}_{13}(\omega))(\Delta + \Sigma^{\mathrm{1BA}}_{24}(\omega))^2 + \tilde{H}^2_{21}(\Delta + \Sigma^{\mathrm{1BA}}_{24}(\omega)), \\ \tilde{C}_{22} &= (\omega - \tilde{H}_{11} - \Sigma^{\mathrm{1BA}}_{11}(\omega))(\omega - \tilde{H}_{33} - \Sigma^{\mathrm{1BA}}_{33}(\omega))(\omega - \tilde{H}_{44} - \Sigma^{\mathrm{1BA}}_{44}(\omega)) \\ &\quad - (\omega - \tilde{H}_{44} - \Sigma^{\mathrm{1BA}}_{44}(\omega))(\Delta + \Sigma^{\mathrm{1BA}}_{13}(\omega))^2 + (\omega - \tilde{H}_{11} - \Sigma^{\mathrm{1BA}}_{11}(\omega))\tilde{H}^2_{21}, \\ \tilde{C}_{24} &= \tilde{C}_{42} = (\omega - \tilde{H}_{11} - \Sigma^{\mathrm{1BA}}_{11}(\omega))(\omega - \tilde{H}_{33} - \Sigma^{\mathrm{1BA}}_{33}(\omega))(\Delta + \Sigma^{\mathrm{1BA}}_{24}(\omega)) \\ &\quad - (\Delta + \Sigma^{\mathrm{1BA}}_{13}(\omega))^2(\Delta + \Sigma^{\mathrm{1BA}}_{24}(\omega)) + \tilde{H}^2_{21}(\Delta + \Sigma^{\mathrm{1BA}}_{13}(\omega)), \\ \tilde{C}_{33} &= (\omega - \tilde{H}_{11} - \Sigma^{\mathrm{1BA}}_{11}(\omega))(\omega - \tilde{H}_{22} - \Sigma^{\mathrm{1BA}}_{22}(\omega))(\omega - \tilde{H}_{44} - \Sigma^{\mathrm{1BA}}_{44}(\omega)) \\ &\quad - (\omega - \tilde{H}_{11} - \Sigma^{\mathrm{1BA}}_{11}(\omega))(\Delta + \Sigma^{\mathrm{1BA}}_{24}(\omega))^2 + (\omega - \tilde{H}_{44} - \Sigma^{\mathrm{1BA}}_{44}(\omega))\tilde{H}^2_{21}, \\ \tilde{C}_{44} &= (\omega - \tilde{H}_{11} - \Sigma^{\mathrm{1BA}}_{11}(\omega))(\omega - \tilde{H}_{22} - \Sigma^{\mathrm{1BA}}_{22}(\omega))(\omega - \tilde{H}_{33} - \Sigma^{\mathrm{1BA}}_{33}(\omega)) \\ &\quad - (\omega - \tilde{H}_{22} - \Sigma^{\mathrm{1BA}}_{22}(\omega))(\Delta + \Sigma^{\mathrm{1BA}}_{13}(\omega))^2 + (\omega - \tilde{H}_{33} - \Sigma^{\mathrm{1BA}}_{33}(\omega))\tilde{H}^2_{21}. \end{aligned}$$

E Impurities in the semiconducting core

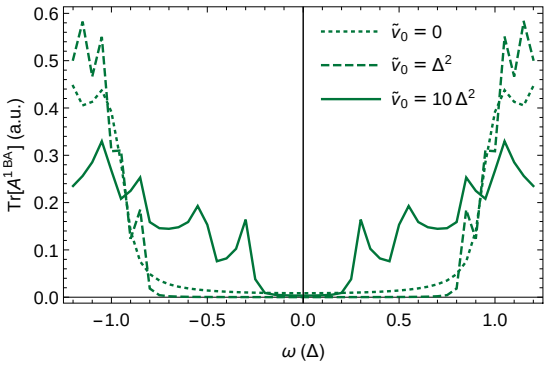

(a) $(\mu = 0.124\Delta, \alpha = 2.04\alpha_0)$, $m_J^{\max} = 62$

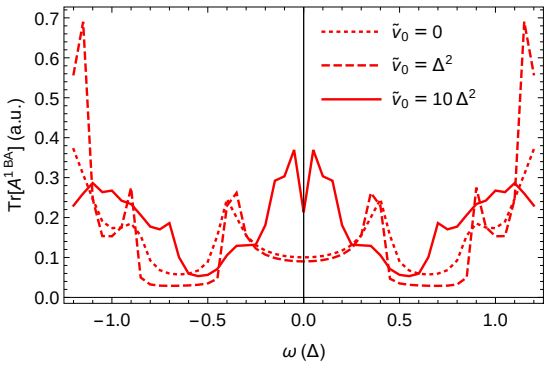

(b) $(\mu = 0.317\Delta, \alpha = 2.81\alpha_0)$, $m_J^{\max} = 62$

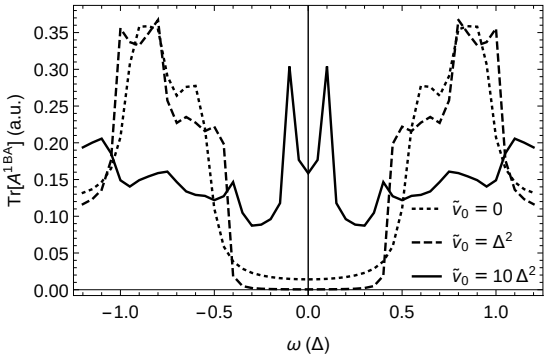

(c) $(\mu = 2.3\Delta, \alpha = 1.3\alpha_0)$, $m_J^{\max} = 62$

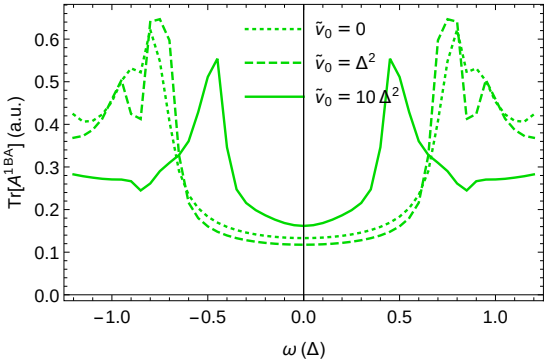

(d) $(\mu = 2.9\Delta, \alpha = 1.8\alpha_0)$, $m_J^{\max} = 32$

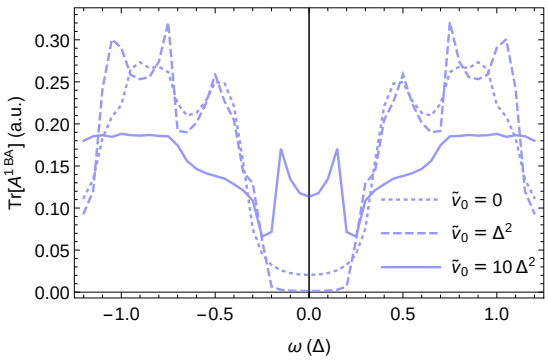

(e) $(\mu = 3.85\Delta, \alpha = 0.731\alpha_0)$, $m_J^{\max} = 62$

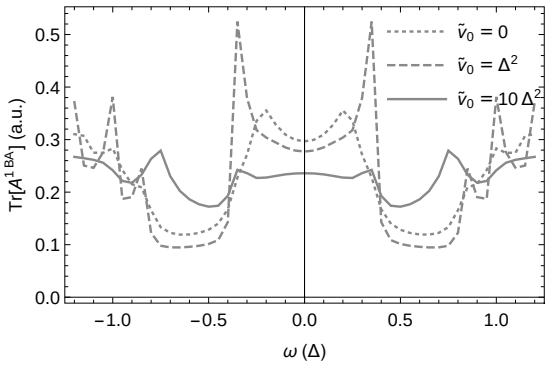

(f) $(\mu = 4.1\Delta, \alpha = 3.48\alpha_0)$, $m_J^{\max} = 42$

Figure E.1: Trace of the spectral function for the full-shell nanowire system described by $\sum_{m_J} \tilde{H}_{m_J,p_z}$ (Eq. (4.9)) with impurities of effective scattering strength $\tilde{v}_0$ in the semiconducting core. As previously, $m_J^{\max}$ denotes the absolute value of the limits on the m_J sums, which have been chosen from when the spectral functions would converge.

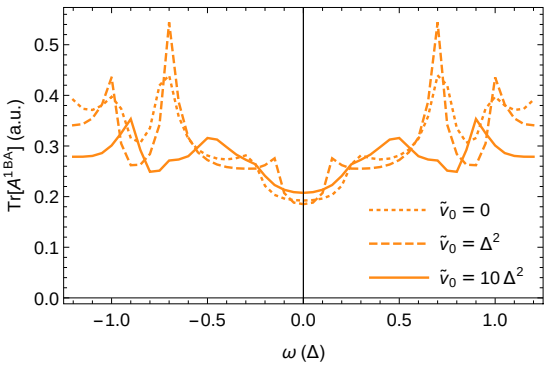

(a) $(\mu = 4.82\Delta, \alpha = 2.29\alpha_0)$, $m_J^{\max} = 32$

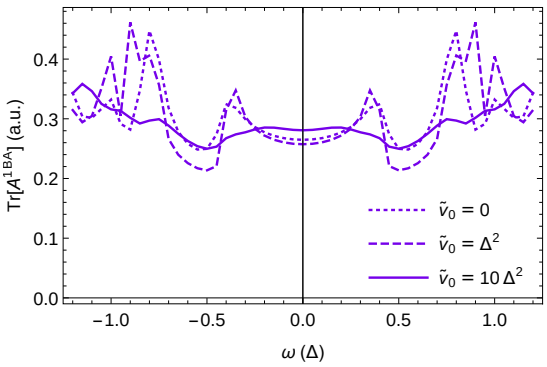

(b) $(\mu = 5.16\Delta, \alpha = 3.38\alpha_0)$, $m_J^{\max} = 32$

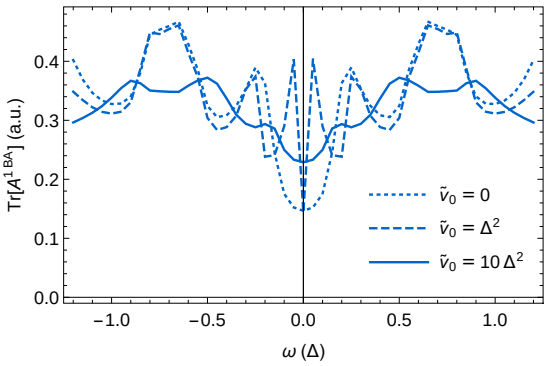

(c) $(\mu = 6.62\Delta, \alpha = 0.357\alpha_0)$, $m_J^{\max} = 32$

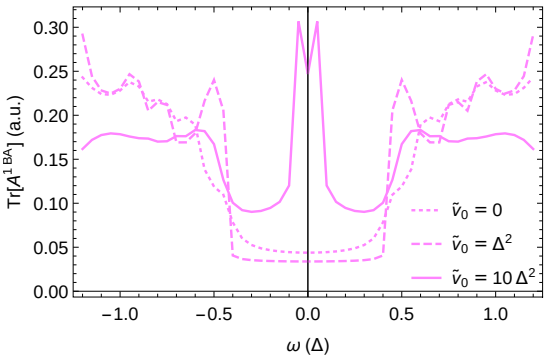

(d) $(\mu = 6.62\Delta, \alpha = 1.12\alpha_0)$, $m_J^{\max} = 62$

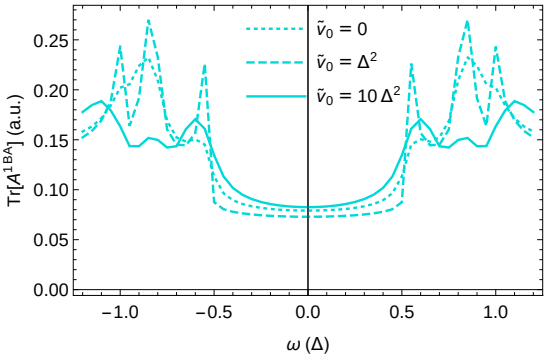

(e) $(\mu = 7.84\Delta, \alpha = 2.01\alpha_0)$, $m_J^{\max} = 52$

Figure E.2: Trace of the spectral function for the full-shell nanowire system described by $\sum_{m_J} \tilde{H}_{m_J,p_z}$ (Eq. (4.9)) with impurities of effective scattering strength $\tilde{v}_0$ in the semiconducting core. As previously, $m_J^{\max}$ denotes the absolute value of the limits on the m_J sums, which have been chosen from when the spectral functions would converge.

F Expression for the current of scattering states

Here we calculate the current of scattering states of type ζ from the left reservoir. The energy dependence of the wavenumbers $k_n(E)$ and the reflection coefficients $R_{\zeta' n',\zeta n}(E)$ is suppressed.

$$
\begin{aligned}
I_{L\zeta nE} &= \int_\Omega d\boldsymbol{r}_\perp \left(\psi_{L\zeta nE}(\boldsymbol{r}_\perp, z)\right)^\dagger \frac{1}{2mi}\left(\overrightarrow{\partial_z} - \overleftarrow{\partial_z}\right)\tau_z \left(\psi_{L\zeta nE}(\boldsymbol{r}_\perp, z)\right) \qquad (\boldsymbol{r}_\perp, z) \in L \\
&= \frac{1}{2mi}\int_\Omega d\boldsymbol{r}_\perp \left(\left(\phi^+_{L\zeta nE}\right)^\dagger + \left(\sum_{\zeta' n'} R_{\zeta' n',\zeta n}\phi^-_{L\zeta' n' E}\right)^\dagger\right)\left(\overrightarrow{\partial_z} - \overleftarrow{\partial_z}\right)\tau_z\left(\phi^+_{L\zeta nE} + \sum_{\zeta' n'} R_{\zeta' n',\zeta n}\phi^-_{L\zeta' n' E}\right) \\
&= \frac{1}{2mi}\int_\Omega d\boldsymbol{r}_\perp \Bigg[ik_n \left(\phi^+_{L\zeta nE}\right)^\dagger \tau_z \phi^+_{L\zeta nE} + \sum_{\zeta' n'} R_{\zeta' n',\zeta n}(-ik_{n'})\left(\phi^+_{L\zeta nE}\right)^\dagger \tau_z \phi^-_{L\zeta' n' E} \\
&\quad + ik_n \left(\sum_{\zeta' n'} R_{\zeta' n',\zeta n}\phi^-_{L\zeta' n' E}\right)^\dagger \tau_z \phi^+_{L\zeta nE} + \left(\sum_{\zeta' n'} R_{\zeta' n',\zeta n}\phi^-_{L\zeta' n' E}\right)^\dagger \tau_z \sum_{\zeta'' n''} R_{\zeta'' n'',\zeta n}(-ik_{n''})\phi^-_{L\zeta'' n'' E}\Bigg] \\
&\quad \frac{-1}{2mi}\int_\Omega d\boldsymbol{r}_\perp \Bigg[-ik_n \left(\phi^+_{L\zeta nE}\right)^\dagger \tau_z \phi^+_{L\zeta nE} - ik_n \left(\phi^+_{L\zeta nE}\right)^\dagger \tau_z \sum_{\zeta' n'} R_{\zeta' n',\zeta n}\phi^-_{L\zeta' n' E} \\
&\quad + \left(\sum_{\zeta' n'} R_{\zeta' n',\zeta n}(-ik_{n'})\phi^-_{L\zeta' n' E}\right)^\dagger \tau_z \phi^+_{L\zeta nE} \\
&\quad + \left(\sum_{\zeta' n'} R_{\zeta' n',\zeta n}(-ik_{n'})\phi^-_{L\zeta' n' E}\right)^\dagger \tau_z \sum_{\zeta'' n''} R_{\zeta'' n'',\zeta n}\phi^-_{L\zeta'' n'' E}\Bigg] \\
&= \frac{1}{2mi}\int_\Omega d\boldsymbol{r}_\perp \Bigg[\frac{ik_n}{k_n}\boldsymbol{v}^T_\zeta \tau_z \boldsymbol{v}_\zeta \chi^*_n(\boldsymbol{r}_\perp)\chi_n(\boldsymbol{r}_\perp) - \sum_{\zeta' n'} R_{\zeta' n',\zeta n}\frac{ik_{n'}}{\sqrt{k_n k_{n'}}}\boldsymbol{v}^T_\zeta \tau_z \boldsymbol{v}_{\zeta'}\chi^*_n(\boldsymbol{r}_\perp)\chi_{n'}(\boldsymbol{r}_\perp)e^{-i(k_n+k_{n'})z} \\
&\quad + \sum_{\zeta' n'} R^*_{\zeta' n',\zeta n}\frac{ik_n}{\sqrt{k_{n'}k_n}}\boldsymbol{v}^T_{\zeta'}\tau_z\boldsymbol{v}_\zeta\chi^*_{n'}(\boldsymbol{r}_\perp)\chi_n(\boldsymbol{r}_\perp)e^{i(k_{n'}+k_n)z} \\
&\quad - \sum_{\substack{\zeta' n' \\ \zeta'' n''}} R^*_{\zeta' n',\zeta n}R_{\zeta'' n'',\zeta n}\frac{ik_{n''}}{\sqrt{k_{n'}k_{n''}}}\boldsymbol{v}^T_{\zeta'}\tau_z\boldsymbol{v}_{\zeta''}\chi^*_{n'}(\boldsymbol{r}_\perp)\chi_{n''}(\boldsymbol{r}_\perp)e^{i(k_{n'}-k_{n''})z}\Bigg] \\
&\quad \frac{-1}{2mi}\int_\Omega d\boldsymbol{r}_\perp \Bigg[\frac{-ik_n}{k_n}\boldsymbol{v}^T_\zeta \tau_z \boldsymbol{v}_\zeta \chi^*_n(\boldsymbol{r}_\perp)\chi_n(\boldsymbol{r}_\perp) - \sum_{\zeta' n'} R_{\zeta' n',\zeta n}\frac{ik_n}{\sqrt{k_n k_{n'}}}\boldsymbol{v}^T_\zeta \tau_z \boldsymbol{v}_{\zeta'}\chi^*_n(\boldsymbol{r}_\perp)\chi_{n'}(\boldsymbol{r}_\perp)e^{-i(k_n+k_{n'})z} \\
&\quad + \sum_{\zeta' n'} R^*_{\zeta' n',\zeta n}\frac{ik_{n'}}{\sqrt{k_{n'}k_n}}\boldsymbol{v}^T_{\zeta'}\tau_z\boldsymbol{v}_\zeta\chi^*_{n'}(\boldsymbol{r}_\perp)\chi_n(\boldsymbol{r}_\perp)e^{i(k_{n'}+k_n)z} \\
&\quad + \sum_{\substack{\zeta' n' \\ \zeta'' n''}} R^*_{\zeta' n',\zeta n}R_{\zeta'' n'',\zeta n}\frac{ik_{n'}}{\sqrt{k_{n'}k_{n''}}}\boldsymbol{v}^T_{\zeta'}\tau_z\boldsymbol{v}_{\zeta''}\chi^*_{n'}(\boldsymbol{r}_\perp)\chi_{n''}(\boldsymbol{r}_\perp)e^{i(k_{n'}-k_{n''})z}\Bigg].
\end{aligned}
$$

$$
\begin{aligned}
I_{L\zeta nE} &= \frac{s(\zeta)}{2m} - \frac{s(\zeta)}{2m} R_{\zeta n,\zeta n} e^{-i2k_n z} + \frac{s(\zeta)}{2m} R^*_{\zeta n,\zeta n} e^{i2k_n z} - \sum_{\zeta' n'} R^*_{\zeta' n',\zeta n} R_{\zeta' n',\zeta n} \frac{s(\zeta')}{2m} \\
&\quad + \frac{s(\zeta)}{2m} + \frac{s(\zeta)}{2m} R_{\zeta n,\zeta n} e^{-i2k_n z} - \frac{s(\zeta)}{2m} R^*_{\zeta n,\zeta n} e^{i2k_n z} - \sum_{\zeta' n'} R^*_{\zeta' n',\zeta n} R_{\zeta' n',\zeta n} \frac{s(\zeta')}{2m} \\
&= \frac{1}{m} \left[s(\zeta) - \sum_{\zeta' n'} s(\zeta') R^*_{\zeta' n',\zeta n} R_{\zeta' n',\zeta n} \right].
\end{aligned}
$$

G Results for a finite full-shell nanowire

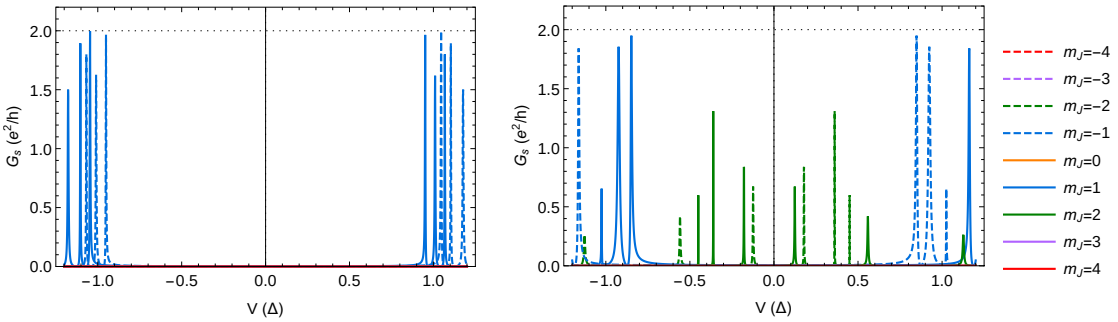

(a) $(\mu = 0.124\Delta, \alpha = 2.04\alpha_0)$ **(b)** $(\mu = 0.317\Delta, \alpha = 2.81\alpha_0)$

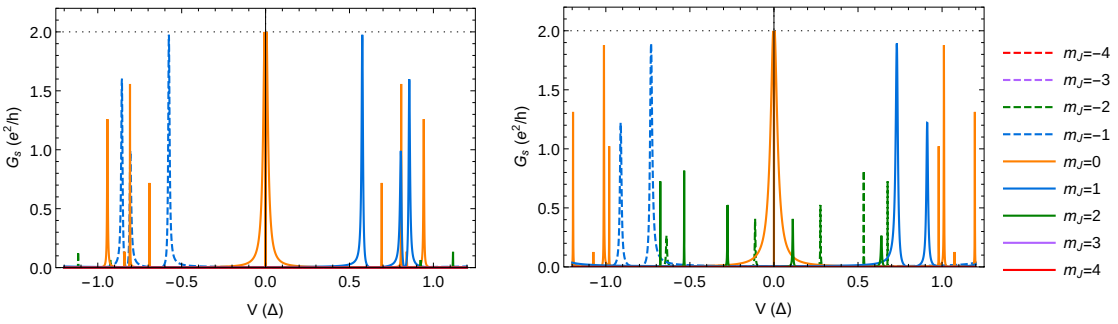

(c) $(\mu = 2.3\Delta, \alpha = 1.3\alpha_0)$ **(d)** $(\mu = 2.9\Delta, \alpha = 1.8\alpha_0)$

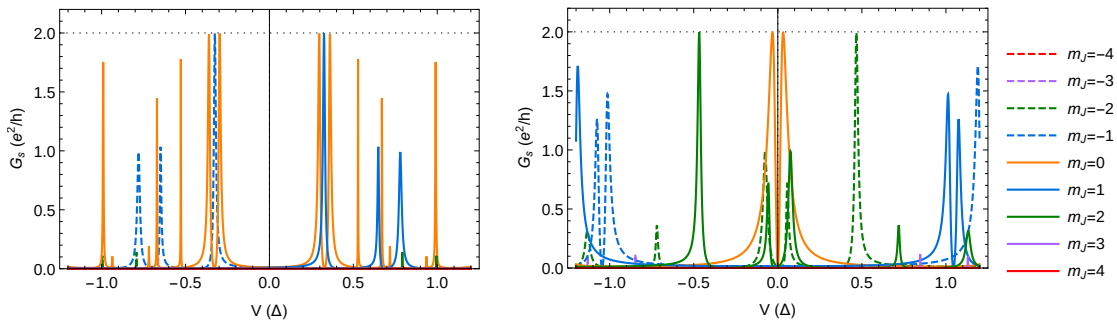

(e) $(\mu = 3.85\Delta, \alpha = 0.731\alpha_0)$ **(f)** $(\mu = 4.1\Delta, \alpha = 3.48\alpha_0)$

Figure G.1: Spectral conductance at different points in (μ, α) space for the discretised full-shell nanowire described by $\tilde{H}^{m_J}$ in Eq. (8.1). Also here we see that m_J bands mirror $-m_J$ bands. The calculations are made for a radius $R_2 = 0.5R_0$ and flux $\tilde{\Phi} = 0.5$.

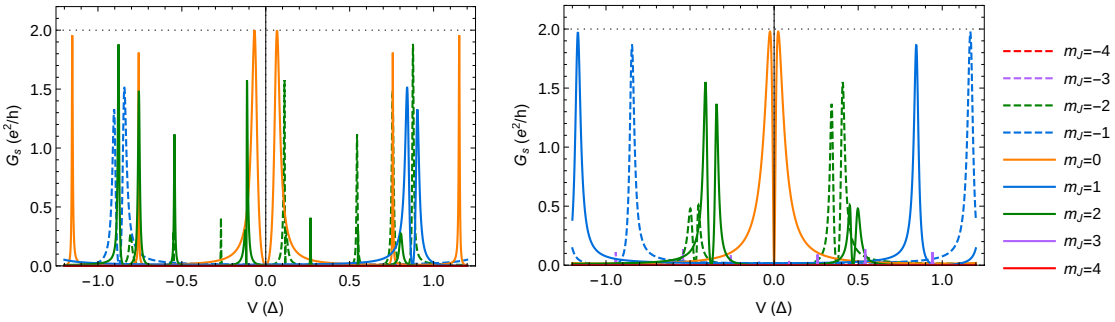

(a) $(\mu = 4.82\Delta, \alpha = 2.29\alpha_0)$ **(b)** $(\mu = 5.16\Delta, \alpha = 3.38\alpha_0)$

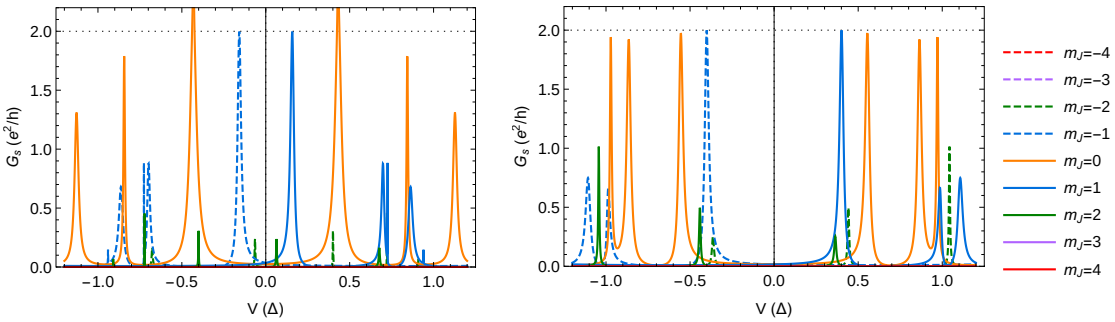

(c) $(\mu = 6.62\Delta, \alpha = 0.357\alpha_0)$ **(d)** $(\mu = 6.62\Delta, \alpha = 1.12\alpha_0)$

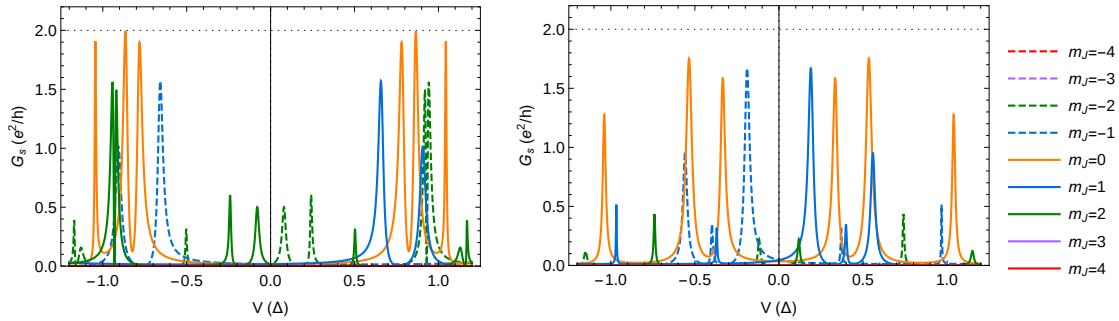

(e) $(\mu = 7.84\Delta, \alpha = 2.01\alpha_0)$ **(f)** $(\mu = 9.23\Delta, \alpha = 0.24\alpha_0)$

Figure G.2: Spectral conductance at different points in (μ, α) space as in Fig. G.1. The result in Fig. (d) does not appear to agree with the bulk calculations which found the gap to be closed at $(\mu = 6.62\Delta, \alpha = 1.12\alpha_0)$ without deformations. Also here $R_2 = 0.5R_0$ and $\tilde{\Phi} = 0.5$.

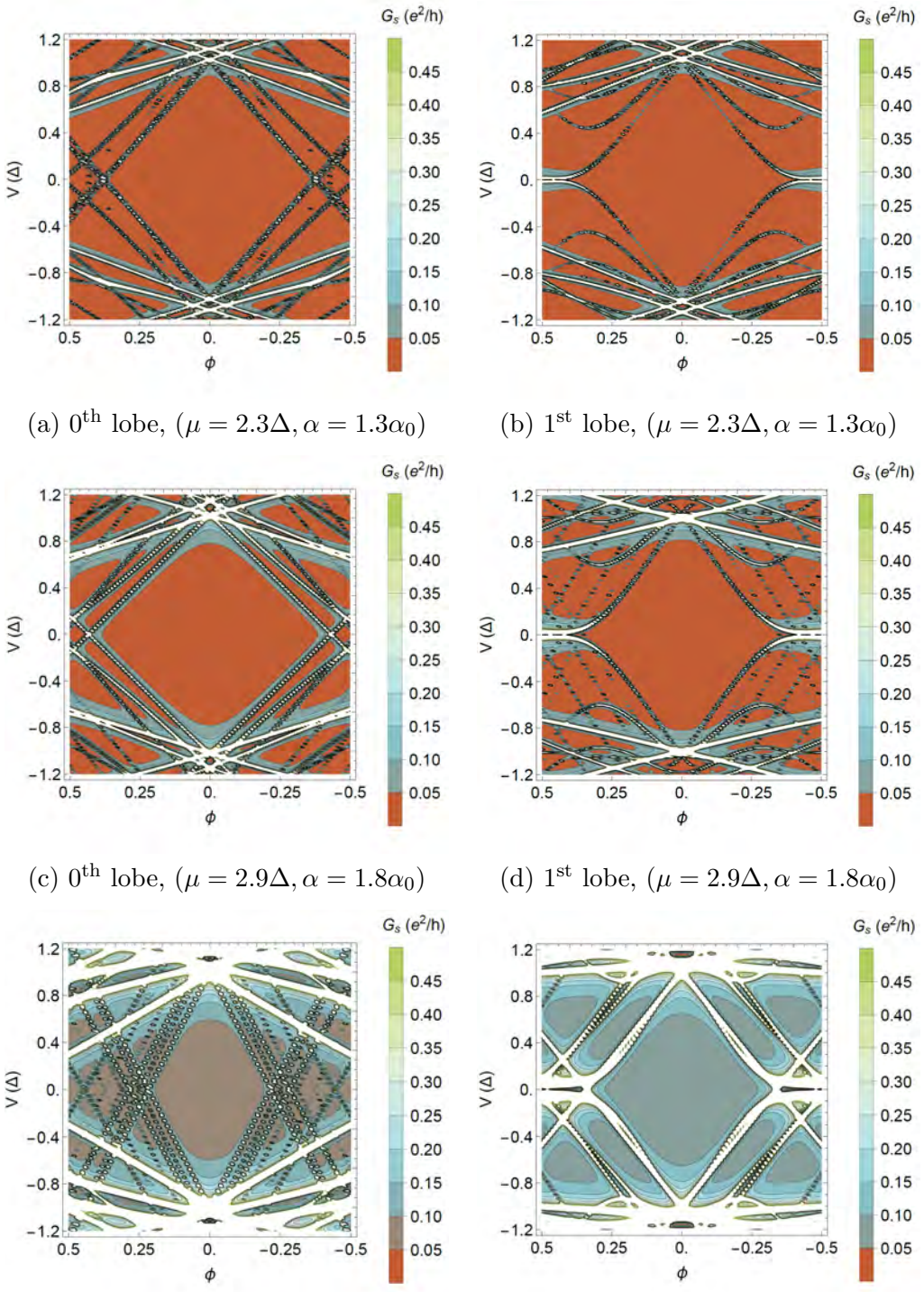

(a) 0^{th} lobe, $(\mu = 2.3\Delta, \alpha = 1.3\alpha_0)$

(b) 1^{st} lobe, $(\mu = 2.3\Delta, \alpha = 1.3\alpha_0)$

(c) 0^{th} lobe, $(\mu = 2.9\Delta, \alpha = 1.8\alpha_0)$

(d) 1^{st} lobe, $(\mu = 2.9\Delta, \alpha = 1.8\alpha_0)$

(e) 0^{th} lobe, $(\mu = 4.1\Delta, \alpha = 3.48\alpha_0)$

(f) 1^{st} lobe, $(\mu = 4.1\Delta, \alpha = 3.48\alpha_0)$

Figure G.3: Conductance as function of the reduced flux $n - \tilde{\Phi} = \phi$ and bias voltage V in the zeroth and first Little-Parks lobes. These are made for points inside the $V_{\text{Z}}^2 = \mu_{m_J=0}^2 + \Delta^2$ parabola with radius $R_2 = 0.5R_0$ and $B_{\text{Z}} = 0$.

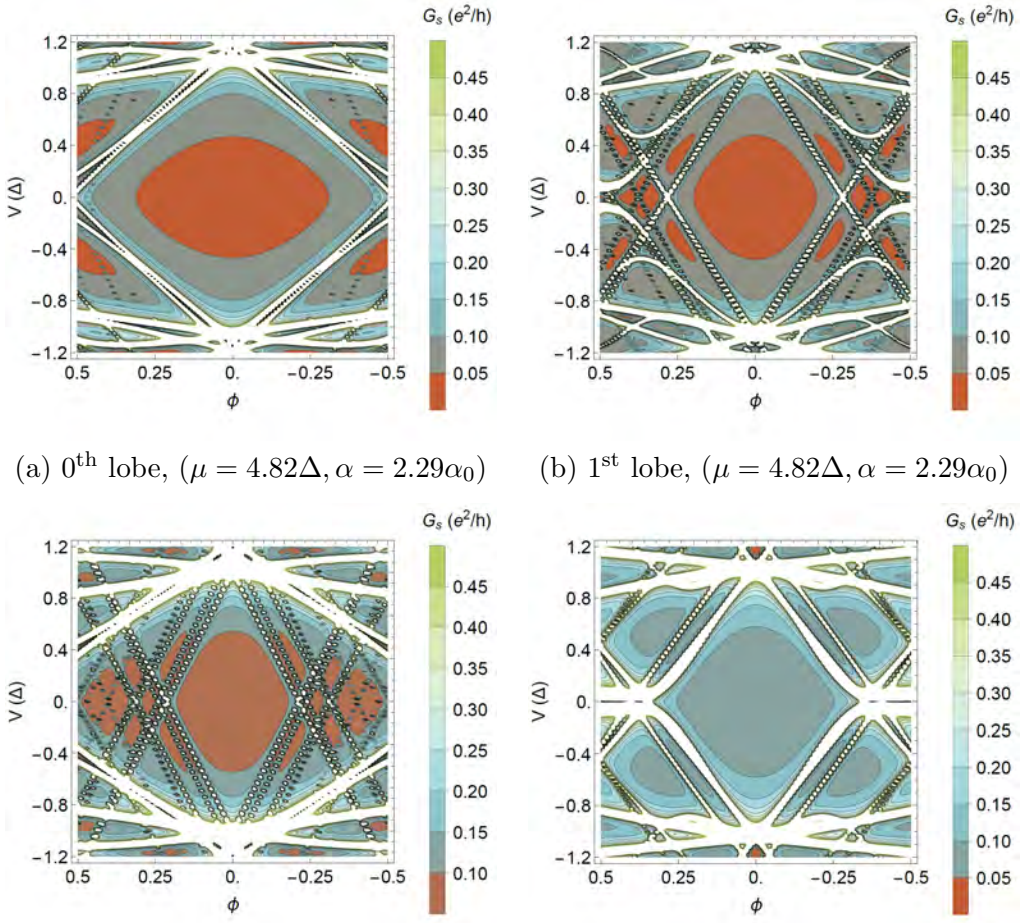

(a) 0^{th} lobe, $(\mu = 4.82\Delta, \alpha = 2.29\alpha_0)$

(b) 1^{st} lobe, $(\mu = 4.82\Delta, \alpha = 2.29\alpha_0)$

(c) 0^{th} lobe, $(\mu = 5.16\Delta, \alpha = 3.38\alpha_0)$

(d) 1^{st} lobe, $(\mu = 5.16\Delta, \alpha = 3.38\alpha_0)$

Figure G.4: Conductance as function of the reduced flux $n - \tilde{\Phi} = \phi$ and bias voltage V in the zeroth and first Little-Parks lobes. These are made for points inside the $V_{\text{Z}}^2 = \mu_{m_J=0}^2 + \Delta^2$ parabola with radius $R_2 = 0.5R_0$ and $B_{\text{Z}} = 0$.

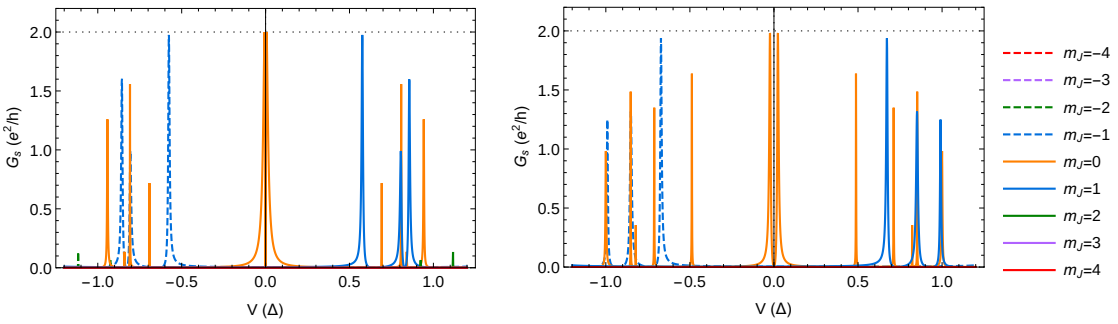

(a) $\tilde{\Phi} = 0.5$ **(b)** $\tilde{\Phi} = 0.6$

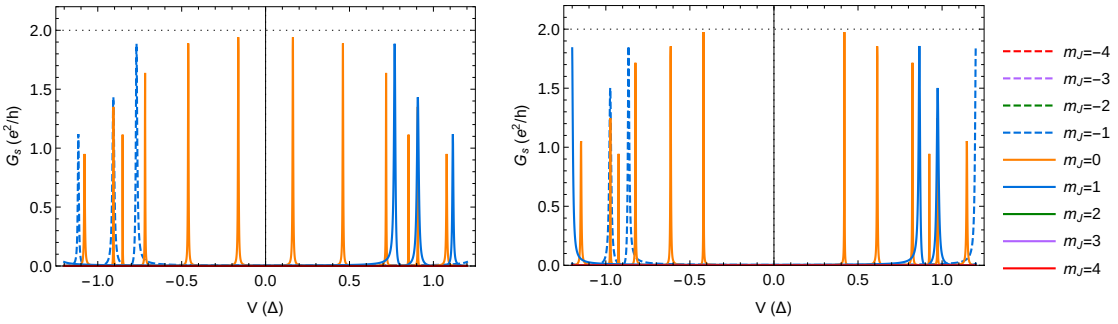

(c) $\tilde{\Phi} = 0.7$ **(d)** $\tilde{\Phi} = 0.8$

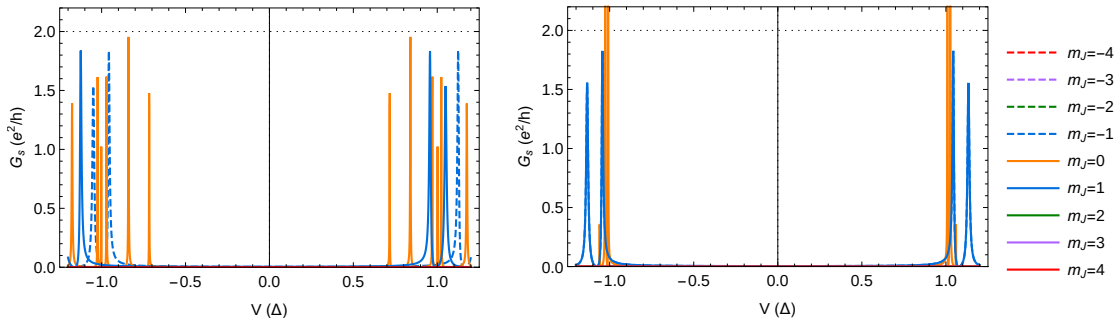

(e) $\tilde{\Phi} = 0.9$ **(f)** $\tilde{\Phi} = 1.0$

Figure G.5: Differential conductance in point $(\mu = 2.3\Delta, \alpha = 1.3\alpha_0)$ through the first half of the 1st Little-Parks lobe with $R_2 = 0.5R_0$. The zero-bias beak is seen to split up and the gap becomes 1Δ at one flux quantum.

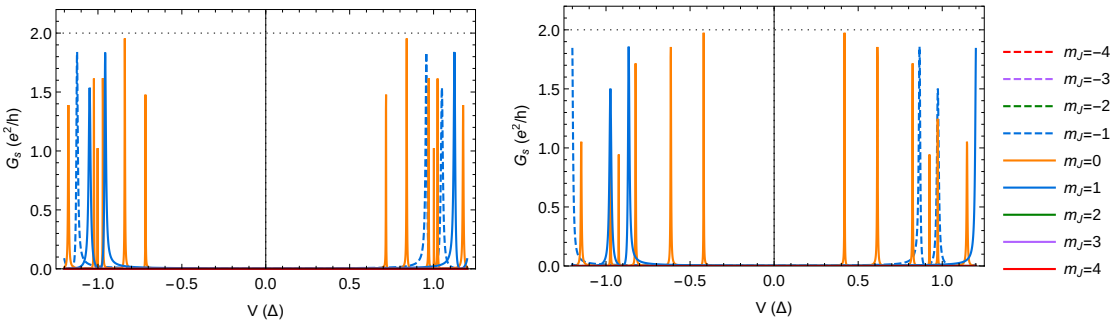

(a) $\Phi/\Phi_0 = 1.1$ **(b)** $\tilde{\Phi} = 1.2$

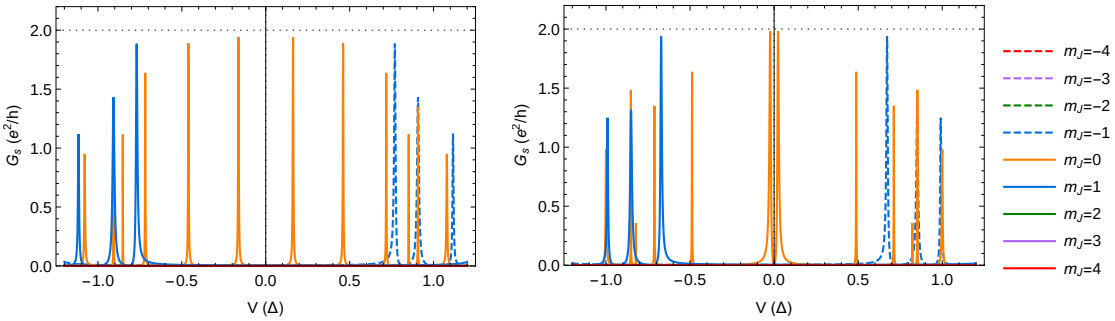

(c) $\tilde{\Phi} = 1.3$ **(d)** $\tilde{\Phi} = 1.4$

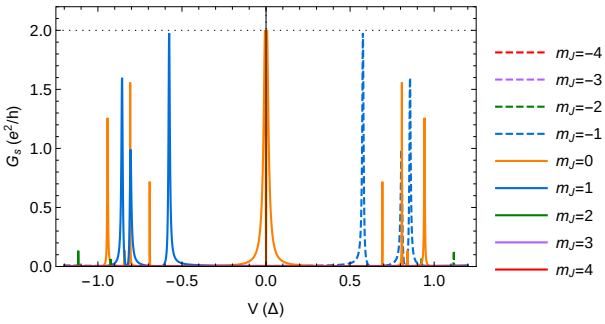

(e) $\tilde{\Phi} = 1.5$

Figure G.6: Differential conductance in point $(\mu = 2.3\Delta, \alpha = 1.3\alpha_0)$ through the second half of the 1st Little-Parks lobe with $R_2 = 0.5R_0$. Compared to $\tilde{\Phi} \leq 1$ the m_J and $-m_J$ bands are switched. Apart from that, the conductance is symmetric around one flux quantum.

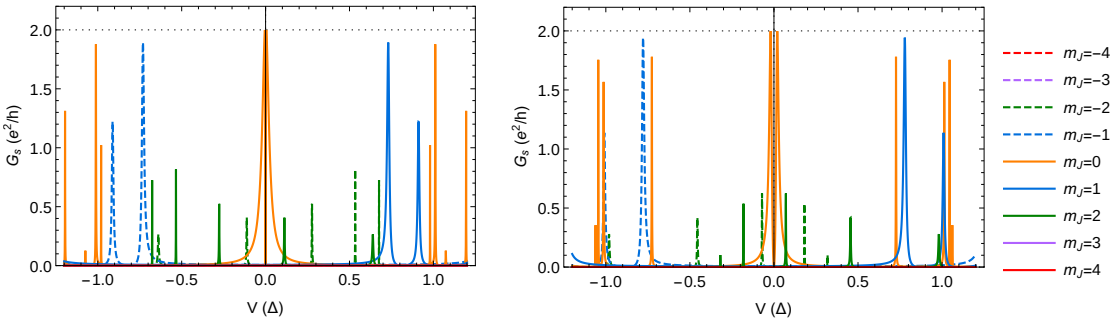

(a) $\tilde{\Phi} = 0.5$ **(b)** $\Phi/\Phi_0 = 0.6$

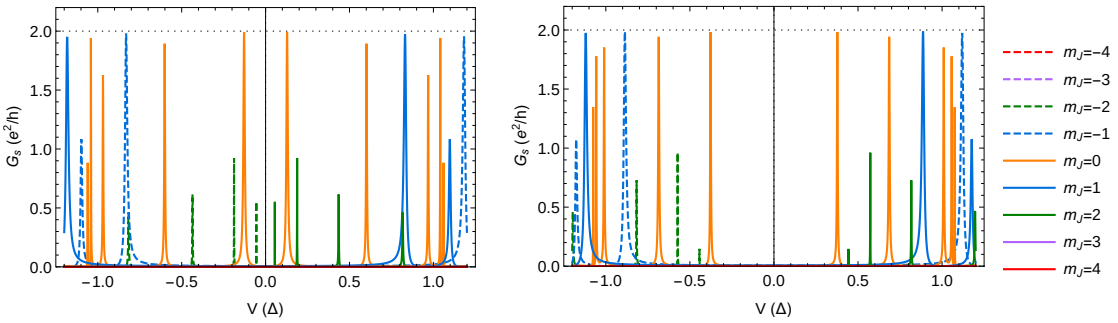

(c) $\tilde{\Phi} = 0.7$ **(d)** $\tilde{\Phi} = 0.8$

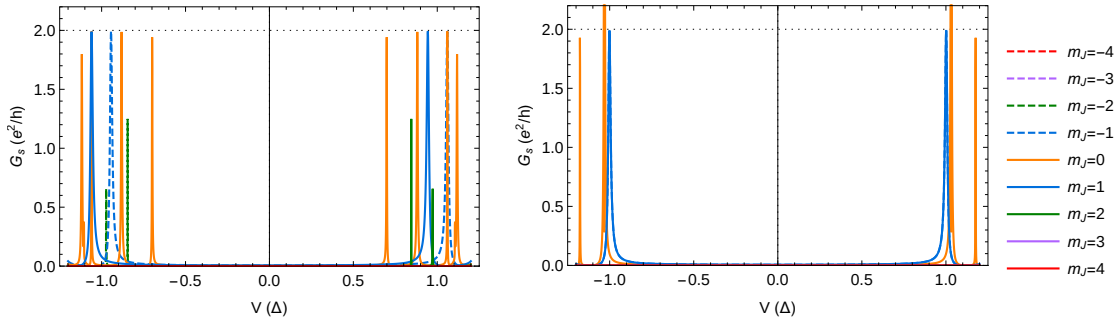

(e) $\tilde{\Phi} = 0.9$ **(f)** $\tilde{\Phi} = 1.0$

Figure G.7: Conductance in point $(\mu = 2.9\Delta, \alpha = 1.8\alpha_0)$ through the first half of the 1$^{\text{st}}$ Little-Parks lobe. As in Fig. G.5 the peak at zero bias voltage is not stable and the gap becomes 1Δ at one flux quantum. The conductance is symmetric around $\tilde{\Phi} = 1$ except for the interchange of $\pm m_J$ sectors.